UNIVERSITY OF LIVERPOOL

THE MECHANICAL PROPERTIES OF NOVEL LIGHTWEIGHT STRUCTURES BASED ON CORRUGATED-CORES

Thesis submitted in accordance with the requirement of the
University *of* Liverpool for the degree of
Doctor of Philosophy

By
Mohd Ruzaimi Mat Rejab
October 2013

ACKNOWLEDGMENTS

In The Name of Allah, The Most Beneficent, The Most Merciful.

First, I would like to sincere thanks and appreciation to my primary supervisor, Professor Wesley Cantwell for supervising me as his PhD student. Besides the actual research, he also guides me to become a good and responsible academician. I really value his advice, support, encouragement, respect, comments and most importantly his patience throughout the years that I have been working with him. My special thanks to Dr Robert Mines and Associate Professor Dr Kuniharu Ushijima for their feedback and motivations throughout this journey.

My sincere gratitude to members of School of Engineering, including Mr Stephen Pennington, Mr Jijimon Mathew, Mr Dave Atkinson as well as my friends in Composite Research Group, including Dr Mohamad Zaki Hassan (UTM), Dr Rafidah Hasan (UTeM), Mrs Siti Hajar Sheikh Md Fadzullah (UTeM), Mr Mohd Zuhri Mohamed Yusoff (UPM), Miss Alia Ruzanna Aziz (UniKL), Major Mohamed Al-Tenaiji (UAE Army), Mr Amit Haldar (IIT Guwahati) and Lieutenant Commander Tawan Boonkongwathana (Royal Thailand Navy). I enjoy being with them. My appreciation is also due to all the staffs and friends in the university that I have been associating directly or indirectly during my stay at Liverpool.

I am delighted to the love and support of my family and my parents over the past years. Also, to my three beautiful princesses, Qystina, Qaisara and Qaireena for giving me the tears and joys all these years. A special dedication to my lovely wife, Nurulfadzilah Hasan, for her love, support, understanding and patience throughout the ups and downs in finishing this study.

And finally, I would also like to thank the Universiti Malaysia Pahang and the Government of Malaysia for sponsoring this PhD study.

LIST OF PUBLICATIONS

1. M.R.M.Rejab, W.J.Cantwell. Compression behaviour of Aluminium corrugated-core panels, 1st Annual UK-Malaysia-Ireland Engineering Science Conference 2010 (UMIES 2010), Northern Ireland, UK. June 2010.
2. M.R.M.Rejab, W.J.Cantwell. Mechanical behaviour of corrugated-core sandwich panels under compression, 32nd SAMPE EUROPE International Conference 2011 (SEICO 11), Paris, France, March 2011.
3. M.R.M.Rejab, W.J.Cantwell. Fracture modes in compression-loaded corrugated-core sandwich panels, 11th Annual Composites UK Conference, Manchester, UK, May 2011.
4. M.R.M.Rejab, M.M.Issa, W.J.Cantwell. Novel lightweight composites cores for aerospace applications, 33rd SAMPE EUROPE International Conference 2012 (SEICO 12), Paris, France, March 2012.
5. M.R.M.Rejab, W.J.Cantwell. The mechanical behaviour of corrugated-core sandwich panels. Composites Part B: Engineering. 2013;47:267-277.
6. M.R.M.Rejab, K.Ushijima, W.J.Cantwell. The shear response of lightweight corrugated core structures. Journal of Composite Materials. 2013; 0(0): 1-14.

ABSTRACT

The aim of this research work is to investigate the mechanical properties of corrugated-core sandwich structures under quasi-static and dynamic loading conditions and to determine the failure mechanisms and energy-absorbing characteristics of the corrugated-cores with different cell wall thickness and filled with a foam core.

Triangular corrugation structures were made from an aluminium alloy (AL), a glass fibre reinforced plastic (GFRP) and a carbon fibre reinforced plastic (CFRP). The composite corrugations were fabricated using a hot press moulding technique and then adhesively bonded to skins based on the same material, to produce a range of lightweight sandwich structures. The role of the number of unit cells, the thickness of the cell walls and the width in determining the mechanical behaviour of the structures was investigated. Buckling of the struts was identified as the initial failure mode in these corrugated systems. Continued loading resulted in plastic deformation in the aluminium system, in contrast, fibre fracture, matrix cracking and localised delamination in the composite systems, as well as debonding between the skins and the core were observed in the composites. The compression strength and modulus were shown to be dependent on the number of unit cells and the cell wall thickness, but independent of specimen width. Subsequent mechanical testing was undertaken using an Arcan rig capable of generating a range of loading conditions between pure shear and pure compression. The failure strength in the aluminium system was accurately represented using a two dimensional quadratic failure criterion. In contrast, due to the initation of delamination within the composite struts, the composite corrugated-cores were accurately predicted using a modified failure criterion.

Low velocity compression loading was subsequently performed on the sandwich structures, where the dynamic strength enhancement factor was shown to increase for all the corrugation systems. This was attributed to both a material strain-rate sensitivity and inertial stabilisation effects. The failure mechanisms in the sandwich structures were found to be similar under both quasi-static and dynamic loading conditions, where damage initiated due to buckling of the struts. To simulate the mechanical response of the corrugation systems, FE models have been developed using the Abaqus finite element package. The FE results were compared to measured responses, and good agreement was achieved. The failure modes predicted by the FE models show reasonably good agreement with the experimental observations.

Finally, foam filling the composite corrugation systems significantly improved the specific strength as well as specific energy-absorbing characteristics of the structures. The compression properties of the corrugated structures have been compared to those of other core materials, where the evidence suggests that these systems compare favourably with other cellular core materials.

TABLE OF CONTENTS

CHAPTER VII: CONCLUSIONS

APPENDICES

LIST OF FIGURES

LIST OF TABLES

CHAPTER I: INTRODUCTION

1.1 Overview

The development and use of materials for structural and other design purposes is changing rapidly. One of the most important aspects in structural studies is minimising the weight without sacrificing the strength of a structure. Therefore, this engineering challenge has led a number of researchers to design and manufacture lightweight structures that can offer a higher strength and absorb more energy under various loading conditions.

One of the ways to achieve weight savings is by replacing metals with composites. A composite is a material having two or more distinct constituents or phases, whereby both constituents are present in reasonable proportions, each having different properties, resulting in altogether different properties for the composite material produced. The constituent that is present in a continuous form and often but not always present in the greater quantity is termed the ómatrixô, such as polymeric materials. In general, polymers are known to have a poor strength and a low Youngôs modulus. The second constituent is termed as the reinforcing phase or the óreinforcementô, with the purpose of enhancing or reinforcing the mechanical properties of the matrix, such as the carbon fibre. In general, the reinforcement is stronger and stiffer than the matrix. Recently, composites have been widely used either in monolithic form or in a sandwich structure.

For more than a half-century, there has been a growing increase in the use of composites and sandwich structures in a wide range of applications. These applications include structures in the automotive, aerospace, naval and construction industries. For example, the largest airliner in the sky, the Airbus A380, is an excellent example of the evolution and the use of the composite materials [1]. In Figure 1.1, the distribution of composite materials in the A380, is shown. The increased use of carbon fibre reinforced plastic (CFRP) laminates has resulted in a drastic weight reduction in the A380. The major material improvements in the A380 are a CFRP composite centre wing box, which is a first in commercial aviation. CFRP has also replaced aluminium in the lateral panels and the secondary rib.

(a)

This text box is where the unabridged thesis included the following third party copyrighted material:

http://www.malaysiaairlines.com/my/en/mh-experience/our-fleet/airbus-a380-800.html

(b)

This text box is where the unabridged thesis included the following third party copyrighted material:

Federal Aviation Administration. Aircraft Rescue and Firefighting Strategies and Tactical Considerations for New Large Aircraft. A Technical Report from William J. Hughes Technical Center, New Jersey: Aviation Research Division; 2013. p. 82.

http://www.airporttech.tc.faa.gov/safety/downloads/tc-13-12.pdf

Figure 1.1: (a) An Airbus A380 airliner [2], and (b) distribution of composite materials and locations on the A380 [1].

A sandwich structure typically consists of two thin but stiff skins, made from a fully dense material, and separated by a thick and light core. The result of this construction is a structure with a high bending stiffness and strength with a low overall density. In fact, the bending stiffness and strength of a sandwich structure are always superior to that of a monolithic structure made from the same material and having the same weight.

The skin materials are one of the important components in sandwich structures. It can be divided into fibre reinforced composites and non-composites (metals, woods). For the non-composites, the most common skin material is an aluminium sheet metal. Its applications include refrigerated transportation containers and construction

panels. Most fibre reinforced composites are employed as the skins in a sandwich structure. The most common fibres include glass fibre, carbon fibre and aramid. The composite skin may compose of different architectures, such as chopped strand mat (CSM), unidirectional (UD) and woven roving (WR). UD skin has a high strength in one direction (fibre direction only), whereas a WR skin has moderate a strength in two-perpendicular directions. In general, composites skins have an excellent strength, stiffness, corrosion resistance, thermal properties and are lightweight in nature. However, composites are still more expensive than sheet metals and sometimes require complex manufacturing processes.

The second important component in a sandwich structures is the core material. The core in a sandwich structure may be of the various types cellular material, such as honeycomb, foam or wood. The most common foams are made from polymers. In general, polymeric foams are good as energy absorption devices and heat insulators. Unfortunately, polymeric foams offer a highly irregular cell structure, mostly closed channels and are very conservative. Sandwich structures with closed channel cellular materials may retain air and humidity. Humidity retention is one of the problems in aircraft sandwich construction. This problem may lead to an increase in the overall weight of the sandwich structure and degrading of the core properties. To overcome problems, Airbus [3] has developed the sandwich fuselage concept, called the Ventable Shear Core (VeSCo). Figure 1.2 shows schematically the VeSCo concept. This VeSCo concept provides a maximum weight saving, while still offering attractive protection against impact and noise. The outer skin provides the aerodynamic surface, while in between the two skins, an open channel core material is ventable in order to avoid moisture accumulation.

As mentioned before, traditional core materials such as polymeric foams and honeycomb cores exhibit poor air flow exchange, and therefore, a new core design that has a good strength-to-weight ratio in compression as well as shear loads, and an open channel will increase mechanical performance avoiding problems associated with humidity retention.

Figure 1.2: VeSCo concept [3].

1.2 Application of Corrugated-core Sandwich Structures

The following sections outline some of the potential applications for corrugated-core sandwich structures.

1.2.1 Packaging Applications

In the packaging industry, the corrugated box was initially used for packaging glass and pottery containers. This corrugated box is a paper-based material, consisting of a flute (core) corrugated sheet and one or two flat linerboards. The first corrugated paper design was patented in England in 1856 [4]. Today, packaging engineers design and develop corrugated boxes (shipping containers) to satisfy the particular needs of the product being shipped and the hazards of the shipping surroundings, i.e. shock, compression, moisture, vibration.

1.2.2 Marine Applications

Laser Beam Welded Corrugated Core (LASCOR) metallic sandwich panels are designed to reduce the weight of a shipôs deck, bulkheads and hatches without sacrificing strength and durability. Figure 1.3 shows the LASCOR sandwich panel. It is expected that the LASCOR panels will result in a weight reduction of between 15% and 30% over conventionally fabricated structures. For example, the LASCOR

panel was used for the radar platforms on the US Navy ship (USS *Mount Whitney*) since 1994, data is being collected on that assembly, for future work to replace conventional structures in other applications for both surface ships and submarines [5].

Figure 1.3: LASCO metallic sandwich panel [5].

1.2.3 Transport Applications

In high-speed railway lines, noise pollution concerns mean that increasing the speed of a train is becoming difficult. A bullet train, Shinkansen 700 series reduced noise inside the car body structure (see Figure 1.4) by using a low-noise and low-vibration superstructure [6]. The transmission of noise and vibration through the roof and sides is reduced because the space inside the superstructure (aluminium double-skin corrugated-core) has been filled with a foamed vibration isolator. In addition, the use of the double-skin corrugated-core increases the strength-to-weight ratio, and reduces the number of parts and weld lengths, since this superstructure is made via an extrusion process.

Figure 1.4: Car body structure of the Shinkansen 700 series. Double-skin corrugated-core has been adopted for the roof and the side structure of the train [6].

1.2.4 Aerospace Applications

In morphing applications, where large shape changes are expected, the design of a suitable application is a huge challenge and a key issue. In general, the wing structures are required to be stiff in order to withstand aerodynamic pressure loads, while being flexible for the underlying morphing wings. Corrugated composites have a great potential to replace the conventional wing. This is due to that corrugated composites have an anisotropic characteristic that shows stiffness in the fibre direction and flexibility in the transverse direction [7].

1.3 Motivation of the Research Work

The manufacture of strong and stiff cellular materials requires the correct selection of materials and topologies as shown in Figure 1.5. An appropriate combination can delay the onset of failure modes such as yielding or plastic buckling in metals, and delamination or fibre fracture in fibre reinforced composites. Since the majority of studies in the field of sandwich structures are on polymeric and honeycomb core materials, there is very little information in the open literature on corrugated-cores. Therefore, this research work aims to undertake an experimental, analytical and finite element investigation on corrugated-core sandwich structures subjected quasi-static and dynamic compression loading, with particular attention focused on triangular corrugation geometry.

Figure 1.5: A material property chart comparing the compression strength as a function of density, with various engineering materials and core designs [8].

1.4 Project Aim and Objectives

The principal aim of this research work is to investigate the mechanical properties of corrugated-core sandwich structures. The research focuses on metal (aluminium) and composites (glass fibre reinforced plastic and carbon fibre reinforced plastic) structures. Polyurethane foam will be used to reinforce the empty space within the corrugation core.

The project objectives are:

i) To design and manufacture triangular corrugations and sandwich structures.
ii) To investigate the mechanical performance of corrugated-core sandwich structures subjected to static compression, bi-axial loading, and dynamic compression loading.
iii) To characterise the failure mechanisms in corrugated-core sandwich structures subjected to different loading conditions.

iv) To model the mechanical response of corrugated-core sandwich structures using finite element techniques.
v) To study the effect of varying geometrical parameters (unit cell, thickness, width) and the properties of foam-filled structures.
vi) To propose suitable failure criteria to predict the failure strength of corrugations under combined compression-shear loading.

1.5 Thesis Outline

This thesis consists of a further six chapters as follows:

Chapter II: Literature Review; this chapter gives an overview of the design and manufacture of sandwich cores and the mechanical behaviour of sandwich cores under quasi-static and dynamic loading.

Chapter III: Experimental Procedure; this chapter describes the design and experimental procedure in this study, consists of specimen preparation, experimental testing (tensile test, compression test, Arcan test, low velocity impact test), and finally, failure and damage characterisation.

Chapter IV: Experimental Results; this chapter presents and discusses the experimental results and the failure mechanisms of the structures. The fundamental theories to support each of the experiments are given.

Chapter V: Finite Element Modelling; this chapter presents the finite element modelling and numerical predictions of corrugated-core sandwich structures and foam core, and compares the predicted values with experimental results.

Chapter VI: Discussion; this chapter discusses the effect of varying geometrical parameters, construction of failure envelopes, damage characterisation, and compares the novel corrugated-core sandwich structures with existing cores.

Chapter VII: Conclusions; this chapter summarises the overall findings and discussions alongside recommendations for future work.

1.6 References

[1] Federal Aviation Administration. Aircraft Rescue and Firefighting Strategies and Tactical Considerations for New Large Aircraft. A Technical Report from William J. Hughes Technical Center, New Jersey: Aviation Research Division; 2013. p. 1-138.

[2] Malaysia Airlines (MAS) - www.malaysiaairlines.com.

[3] Herrmann AS, Zahlen PC, Zuardy I. Sandwich structures technology in commercial aviation. Sandwich structures 7: Advancing with Sandwich Structures and Materials: Springer; 2005. p. 13-26.

[4] DeLassus PT, Brown WE, Howell BA, Brody AL, Marsh KS. Encyclopedia of Packaging Technology. John Wiley and Sons, Inc., New York, NY; 1997.

[5] Foutch M. Submarine Force Technology: Building a better way of life for the future. Undersea Warfare Magazine, vol. 87: U.S. Submarine Force; 2004.

[6] Matsumoto M, Masai K, Wajima T. New technologies for railway trains. Hitachi Review. 1999;48(3):134-138.

[7] Yokozeki T, Takeda S-I, Ogasawara T, Ishikawa T. Mechanical properties of corrugated composites for candidate materials of flexible wing structures. Composites Part A: Applied Science and Manufacturing. 2006;37(10):1578-1586.

[8] Wadley Research Group - www.virginia.edu/ms/research/wadley/celluar-materials.html.

CHAPTER II: LITERATURE REVIEW

2.1 Introduction

This chapter presents a review of relevant past and current research work on corrugated-core sandwich structures subjected to quasi-static and dynamic events, focusing on low velocity impact. A brief overview of the design and manufacture of sandwich cores is given. Other important aspects included in this review are sandwich cores under quasi-static and dynamic loading, and the influence of geometrical parameters on the behaviour of the cores. In addition, relevant studies on corrugated-core sandwich structures are discussed, with examples of published experimental and numerical works.

2.2 Design and Manufacture of Sandwich Cores

A range of sandwich cores have been produced with the objective of developing a lightweight structure, which is both strong and stiff. From balsa wood of the 'mosquito aircraft' to polymeric foams and honeycomb cores, and recently more researchers are investigating ideal lightweight cellular core candidates for sandwich structures. Ashby [1] reported that the mechanical properties of sandwich core materials are governed by three factors; the topology of the cellular materials, the properties of the parent material and the relative density, ρ^* defined by the volume fraction of solid material.

Several different cellular core topologies have been developed, with the aim to maximise the strength and minimise the density. Cellular materials can be classified as those with stochastic cells and periodic cells. These topologies are shown in Figure 2.1. Foam, with either open or closed-cells, have a random microstructure, falling in stochastic category [2]. On the contrary, periodic structures are constructed from a precise unit cell, which is repeated in an array, can either two-dimensional open channel or three-dimensional truss or textile based assemblies [3].

Figure 2.1: Classification of cellular materials. Cellular materials are divided into stochastic and periodic microstructures [3].

2.2.1 Cellular Foams

Different techniques are used for foaming diverse types of cellular foams, i.e. polymeric and metal foams. In manufacture polymeric foams, polymers are foamed by introducing gas bubbles into a liquid monomer or a hot polymer, allowing the bubbles to grow and stabilise, and then solidifying by cross-linking or cooling [4]. Meanwhile, metal foams are cellular structures consisting of a solid metal, and are frequently made from aluminium filled with gas pores [5]. In polymeric and metal foams, the pores can be either sealed (closed-cell, see Figure 2.2(a)) or have an interconnected network (open-cell, see Figure 2.2(b)).

The fabrication process and characteristics of polymeric foams are now established in industry and well documented in many research papers and books [1, 2, 6-10]. The defining characteristic of metal foams is their permeability; typically 75-90% of the volume consists of voids. The mechanical properties and manufacturing processes of metal foams have been extensively studied and are well documented in [5, 11, 12]. In general, polymeric foams have a lower density than metal foams. However, both foam materials are similar in sustaining large compressive strains and this makes them attractive for energy-absorbing applications.

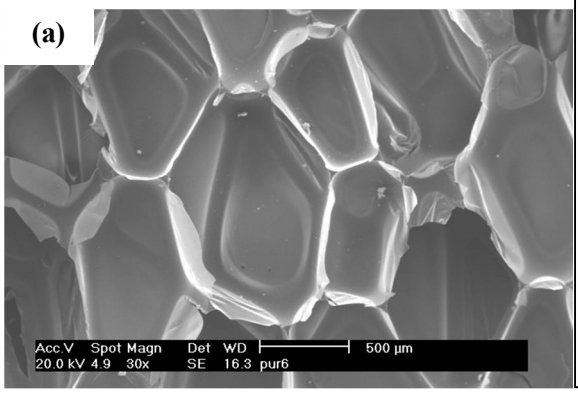

(b)

This text box is where the unabridged thesis included the following third party copyrighted material:

Kwon YW, Cooke RE, Park C. Representative unit-cell models for open-cell metal foams with or without elastic filler. Materials Science and Engineering: A. 2003;343(1–2):63-70.

http://dx.doi.org/10.1016/S0921-5093(02)00360-X

Figure 2.2: Examples of (a) Polyurethane foam with a closed-cell core [13] and (b) Aluminium metal foam with an open-cell core [14].

2.2.2 Two-dimensional Periodic Cores

Two-dimensional periodic cores can be divided into two categories: honeycomb and prismatic cores. Honeycombs are composed of plates or sheets that form the edge of unit cell. These can be arranged perpendicular to the face sheet to create a hexagonal structure. Other than the hexagonal shape, triangular, square or circular shapes can be used as honeycomb geometries. In contrast, prismatic cores are honeycombs, which are rotated 90^{o} about their horizontal axis. This forms a structure with open channels in one direction and a closed-cell structure in the second orthogonal direction. These periodic channels can offer a better cross-flow air/heat exchanger.

There are many innovative ways to manufacture a honeycombs core. Bratfisch *et al.* [15] invented and patented a thermoplastic folded honeycomb core from one single thermoplastic sheet using successive in-line operations. Square honeycomb and diamond cores can be assembled by cutting and slotting sheets as shown in Figure 2.3. For example, Zok *et al.* [16] used stainless steel, then brazed the core and the face sheets to make a sandwich panel. Later, Russell *et al.* [17] adopted the slotting technique for different material, i.e. woven carbon/epoxy composite. The slotted rectangles are assembled into a square honeycomb configuration and adhesively-bonded using a low viscosity epoxy resin.

(a)	(b)
This text box is where the unabridged thesis included the following third party copyrighted material: **Zok FW, Rathbun H, He M, Ferri E, Mercer C, McMeeking RM, Evans AG. Structural performance of metallic sandwich panels with square honeycomb cores. Philosophical Magazine. 2005;85(26-27):3207-3234.** http://dx.doi.org/10.1080/14786430500073945	This text box is where the unabridged thesis included the following third party copyrighted material: **Russell BP, Deshpande VS, Wadley HNG. Quasistatic deformation and failure modes of composite square honeycombs. Journal of Mechanics of Materials and Structures. 2008;3(7):1315-1340.** http://dx.doi.org/10.2140/jomms.2008.3.1315

Figure 2.3: (a) Sketch of method of square-honeycomb core assembly [16] and (b) photograph of composite square-honeycomb core [17].

In fabricating a metal corrugation, a sheet metal is bent in a continuous folding process [18] to the desired geometry i.e. a triangular or a navtruss structure. This technique is generally limited to metal systems since metallic materials have a good ductility performance. For composite materials, the compression moulding process is an alternative way to manufacture a corrugation geometry (see Figure 2.4). Here, the prepreg is placed between male and female moulds and then heated according to the recommended processing time [19, 20].

(a)	(b)
This text box is where the unabridged thesis included the following third party copyrighted material: **Kazemahvazi S, Tanner D, Zenkert D. Corrugated all-composite sandwich structures. Part 2: Failure mechanisms and experimental programme. Composites Science and Technology. 2009;69(7–8):920-925.** http://dx.doi.org/10.1016/j.compscitech.2008.11.035	

Figure 2.4: (a) Manufacturing route for composite trapezium-core and (b) 70^{o} inclined angle of carbon fibre corrugation [19].

2.2.3 Three-dimensional Periodic Cores

Truss and textile-based lattice materials are in same group of three-dimensional periodic cores. Trusses are composed of a network of interconnecting struts, which meet at nodes. Here, the word truss (sometimes referred to as a strut) refers to a rigidly-joined member, as opposed to a pin-jointed member, which is used in

structural mechanics. In 2000, tetrahedral and Kagome lattices were fabricated by investment casting [21]. However, due to limitations of the process, it requires a molten metal with a high fluidity, a continuous process was proposed by involving perforating and folding a plain metal sheet. Figure 2.5 shows the folding process for a pyramidal lattice core.

Figure 2.5: Manufacturing route for truss core [22].

In contrast, a textile lattice is an open cell structure, which consists of plain woven metal wires that are bonded to each other. Queheillalt and Wadley [23] manufactured a lattice by brazing an array of stainless steel tubes. They found that the strength of a truss core can be significantly increased at low relative densities, if the solid struts are replaced by hollow tubes. In latest development of lattice design, a Selective Laser Melting (SLM) technique was used by Smith *et al*. [24] and Gümrük *et al.* [25] to manufacture periodic metallic lattice structures. Figure 2.6 shows an array of stainless steel micro-lattice blocks manufactured using SLM technology.

(a) **(b)**

Figure 2.6: (a) A set of micro-lattice blocks and (b) the definition of lattice block for body centred cubic (BCC) [25].

Further research interests in there-dimensional periodic core geometries relate to egg-box and folded cores. Zupan *et al.* [26] fabricated an aluminium egg-box panel by cold pressing in a lubricated closed die. Deshpande and Fleck [27] reported that egg-box structures have similar energy-absorption characteristics to that of hexagonal honeycomb and superior to that of metal foams. Later, Chung *et al.* [28] investigated the deformation and energy-absorption characteristics of composite egg-box panels. The egg-box panels were fabricated from fabric prepreg sheets draped onto the lower mould, the upper mould was then closed, and breather and nylon films were wrapped to form a vacuum bag. Finally, the panels were cured in an autoclave. Figure 2.7 shows the egg-box panels made from metallic and composite materials.

(a)	**(b)**
This text box is where the unabridged thesis included the following third party copyrighted material: **Zupan M, Chen C, Fleck NA. The plastic collapse and energy absorption capacity of egg-box panels. International Journal of Mechanical Sciences. 2003;45(5):851-871.** http://dx.doi.org/10.1016/S0020-7403(03)00136-X	This text box is where the unabridged thesis included the following third party copyrighted material: **Chung JG, Chang SH, Sutcliffe MPF. Deformation and energy absorption of composite egg-box panels. Composites Science and Technology. 2007;67(11–12): 2342-2349.** http://dx.doi.org/10.1016/j.compscitech.2007.01.020

Figure 2.7: Egg-box core structures: (a) metal [26] and (b) composite [28].

In 2007, Movchan [29] proposed a folded core made from Nomex® aramid paper, and the design was called as M-crimp type. Based on experimental data, the author found that the failure energy of a panel with such cores is greater than that for a honeycomb core. Recently, this novel folded core has been further developed and investigated by Heimbs *et al.* [30-32]. The authors were focused on advanced cellular core materials by folding composite prepreg sheets to form three-dimensional open zigzag structures in an origami like-manner, for potential applications in future primary aircraft structures. The aims were to achieve lower fabrication costs and an improved impact performance. Figure 2.8 shows an innovative folded core structure made from carbon composite material.

Figure 2.8: A carbon fibre folded core with a zigzag geometry [32].

2.2.4 Multifunctional Cellular Materials

Cellular materials exhibit desirable qualities, such as a low density, a high strength, a high stiffness and high energy absorption. With careful design, these qualities can be combined as multifunctional components [33]. The potential for cellular materials to have multifunctional performance makes them even more attractive to researchers. For example, foldcores feature multifunctional properties, such as thermal insulation and good acoustic damping, in addition to their mechanical properties [31]. Furthermore, the problem of humidity accumulation in closed-cell sandwich core materials such as honeycombs can be solved. In general, the open cell design of prismatic, truss and textile cores permits ventability, resulting in improved an air flow.

Figure 2.9: Typical applications of cellular materials in automotive industry [34].

Zhu *et al.* [34] presented a diagram of the requirements of cellular–core sandwich structures in an automotive industry (see Figure 2.9). The region in the centre of the

figure, where all three circles overlap, is an idealised multifunctional performance, which fulfils all three specifications, i.e. ultra-light structures, energy absorbers and heat and a sound dissipation medium.

2.3 Corrugated-core Sandwich Structures

Corrugated-cores are a subset of two-dimensional periodic cores. In Figure 2.10, Buannic *et al.* [35] reported that corrugated-cores can be divided into four conventional geometries; straight, hat-type or trapezium, triangular and curvilinear. The authors then compared the properties of the four core geometries to a reference stiffened panel, to determine the equivalent membrane and pure bending characteristics of periodic plates.

Figure 2.10: Traditional corrugated-core sandwich panels [35].

2.3.1 Curvilinear Corrugated-core

Amongst the four cores above, curvilinear or sinusoidal was the most common core shape in the corrugated-core sandwich panels. This type of geometry has been extensively studied, especially for use in the packaging industry. Nordstrand and Carlsson [36-38] studied the compression, shear and buckling behaviour of five different corrugated boards. The experimental data were then compared to finite

element analysis and analytical predictions. Lu *et al*. [39-42] studied the compression behaviour of corrugated board panels. The mechanical response and failure mechanisms of corrugated sandwich panels subjected to lateral compression were examined in a combined theoretical and experimental study. Minimum weight also was considered in optimising the corrugated panels. Biancolini *et al*. [43-45] investigated the compression and buckling behaviour of corrugated board packages. Pre-buckling and post-buckling behaviour of the panels were evaluated, in order to quantify the effect of design parameters on the strength of the panels. Aboura *et al.* [46] proposed an analytical model related to the assessment of the equal elastic behaviour of corrugated cardboard. Yokozeki *et al.* [47] and Ge *et al*. [48] proposed that sinusoidal corrugated structures are candidate materials for flexible morphing wing structures (see Figure 2.11). Numerical modelling and challenges in optimising the sinusoidal corrugated-core are documented in [49-52].

(a) **(b)**

This text box is where the unabridged thesis included the following third party copyrighted material:

Yokozeki T, Takeda S-I, Ogasawara T, Ishikawa T. Mechanical properties of corrugated composites for candidate materials of flexible wing structures. Composites Part A: Applied Science and Manufacturing. 2006;37(10):1578-1586.

http://dx.doi.org/10.1016/j.compositesa.2005.10.015

Figure 2.11: (a) Carbon fibre corrugated-core structure and (b) geometry of flexible core for candidate material of morphing wing [47].

2.3.2 Straight Corrugated-core

Straight-core sandwich panels are practically good in compression direction, but very weak in shear. Therefore, to have a good combination between the compression and shear response, the straight trusses should be inclined at appropriate angles. Kazemahvazi and Zenkert [20] analysed the effect of shear modulus by increasing the corrugation angles. In Figure 2.12, the authors found that a maximum shear modulus was clearly achieved at 45^{o} angle, in contrast, the modulus at 0^{o} and 90^{o} (straight-core) angles was nearly to zero.

(a) **(b)**

This text box is where the unabridged thesis included the following third party copyrighted material:

Kazemahvazi S, Zenkert D. Corrugated all-composite sandwich structures. Part 1: Modeling. Composites Science and Technology. 2009;69(7–8):913-919.

http://dx.doi.org/10.1016/j.compscitech.2008.11.030

Figure 2.12: (a) Free-body diagram of the corrugated-core and (b) shear modulus as function of corrugation angle [20].

2.3.3 Hat-type Corrugated-core

A hat-type corrugated-core or navtruss has a trapezium cross-section shape. This trapezium corrugated-core has been studied as an alternative to conventional plate-beam metallic structures in selected areas of ships. Knox *et al.* [53] fabricated an adhesively-bonded steel trapezium corrugated-core sandwich construction suitable for marine applications. They found that the fatigue performance of adhesively-bonded construction in the low stress, high-cycle fatigue regime is superior to an equivalent laser-welded construction. Liang *et al.* [54] investigated the optimum design of trapezoid metallic corrugated-core sandwich panels subjected to blast loads using combined algorithms. The authors found that the corrugation leg, corrugation angles and core thickness are most important for the core component. Chang and Krauthammer [55] developed an elastic-plastic analysis of trapezium corrugated-core sandwich panels. The analysis was based on the incremental theory of plasticity, with the initial incremental plastic moments being calculated by an iterative procedure. Liang *et al.* [56] improved the theoretical method by combining on plastic analysis and a beam model. By using normality theory and simplified beam theory, a theoretical method was built to evaluate the relationship between the central deflection of a corrugated panel and an external uniformly distributed pressure load.

Recently, Kazemahvazi *et al.* [19, 20, 57] studied the mechanical response of a trapezium carbon fibre corrugated-core subjected to quasi-static and dynamic

loading. The conventional (monolithic core member) corrugated-cores were compared to hierarchical (sandwich core member) sandwich structures. The authors concluded that the difference in strength arises mainly from the increase in buckling resistance of the sandwich core members compared to monolithic version. Note that in Figure 2.13, this hierarchical concept was introduced by Deshpande *et al.* [58], where from the experimental investigation it was confirmed that the strength of the second order truss (hierarchical) is about ten times greater than that of a first order (monolithic) of the same relative density. Other researchers, Dayyani *et al.* [59, 60] manufactured and investigated the mechanical properties of glass fibre trapezium corrugated-core for morphing skins. A high degree of correlation was observed which showed the suitability of the numerical analysis for predicting the mechanical behaviour of the corrugated laminated panels.

(a) **(b)**

This text box is where the unabridged thesis included the following third party copyrighted material:

Kooistra GW, Deshpande V, Wadley HNG. Hierarchical corrugated core sandwich panel concepts. Journal of Applied Mechanics. 2007;74:259-268.

http://dx.doi.org/10.1115/1.2198243

Figure 2.13: (a) Monolithic corrugated-core (1st order) and (b) hierarchical corrugated-core (2nd order) [58].

2.3.4 Triangular Corrugated-core

For the triangular geometry shape, most of available literature discusses the mechanical properties of metallic corrugated-core sandwich structures. Côté *et al.* [61] manufactured triangular corrugated and diamond lattice cores by slotting together stainless steel sheets in a $\pm 45^{o}$ and then brazing together the assembly. Three different experiments, out-of-plane compression, transverse shear and longitudinal shear tests were conducted and the authors found that the compression strengths were sensitive to the aspect ratio length-to-width, and are below the analytical prediction due to imperfections. Tilbrook *et al.* [62] and Rubino *et al.* [63, 64] manufactured a triangular corrugated-core by CNC folding, and the core was

then laser-welded to two identical face sheets. The core comprised ten struts inclined at 60°. The sandwich plates were loaded dynamically by metal projectiles under three different test conditions: out-of-plane compression, end-clamped and clamped rectangular sandwich plates. Wadley *et al.* [65] investigated the projectile penetration of an extruded aluminium alloy corrugated-core sandwich panel, with a web inclination angle of 60°. Interestingly, the authors compared sandwich panels that were empty and alumina filled, and found that inserting ballistic-grade alumina prisms in the triangular cross-section spaces significantly increased the panels's ballistic resistance.

To date, little research has been done on triangular composite corrugated-core sandwich structures. Recently, Russell *et al.* [66] fabricated a novel triangular corrugated-core from E-glass fibre, filled with triangular prisms of PVC foam to form the corrugations. The apex of theses corrugations were then stitched to the S2-glass face sheet with a Kevlar thread. The whole assembly was then vacuum-bagged and cured in an autoclave at 72°C for 6 hours. Finally, the sample was fabricated with a strut inclination angle of approximately 64°. The mechanical response of the structures was measured from quasi-static to dynamic rates.

Figure 2.14: Sketch of the procedure used to assemble a dry corrugated-core [66].

Malcom *et al.* [67] extended the above experimental investigation with micromechanical predictions. Good agreement was observed between the experimental results and the micromechanical predictions over the wide range of core densities.

2.4 Mechanical Performance of Corrugated-core Sandwich Structures

This section presents the mechanical response under static and dynamic compression tests, static shear test and combined compression-shear loading of the corrugated-core sandwich structures.

2.4.1 Mechanical Response under Static Compression Test

The mechanical response and failure modes observed in corrugated-core sandwich structures can be studied by uniaxial compression tests under distributed uniform loading. This method is commonly used to assess the load-carrying capacity and energy-absorption characteristic of sandwich structures with novel cores [34].

Lu and Chen [39] investigated the mechanical behaviour and failure mechanisms in corrugated board panels. Two types of specimens were considered, FCT (Flat Crush Test) and CMT (Concorra Medium Test). Uniaxial compression tests were conducted on two types of commercially-available corrugated board panel to assess the validity of the analytical predictions. The effect of boundary conditions, geometrical parameters, material properties and geometrical imperfections were studied. They found that if a perfect board panel deforms symmetrically relative to the loading axis, and the strain hardens until densification region. The panel then is stiffest and strongest when the initially sinusoidal core deforms into a square wave pattern. However, the presence of small geometrical imperfections in the core significantly softens the post-yield strength of the panel, accompanied by non-symmetrical deformation about the loading axis. Moreover, the out-of-plane compression response of the panel was dominated by the geometrical and material properties of the core.

The compressive responses of a metallic corrugated-core were measured by Côté *et al.* [61]. A 304 stainless steel was used as the core material, and tested in out-of-plane compression at the three relative densities, $\rho^* = 0.036$, 0.05 and 0.10. Figure 2.15 shows photos at different levels of compression, indicating that the peak load was governed by buckling of the constituent struts, while the subsequent softening was associated with post-buckling response.

Figure 2.15: Deformation images of the $\rho^* = 0.05$ corrugated-core in out-of-plane compression [61].

Figure 2.16: A comparison of the experimental and predicted values of out-of-plane compressive strength of stainless steel corrugated-core panels [61].

A comparison between the experimental data and FE predictions is shown in Figure 2.16, where an imperfection of magnitude, ζ = 0.25 predicts the peak stress accurately. The figure also shows that the peak stress increases systematically with increasing ρ^* and the analytical solution over-predicts the peak strength because the equation does not include any imperfection. The analytical predictions were based on the Euler elastic buckling analysis and the Shanley plastic bifurcation stresses [68], as in Equation 2.1:

$$\sigma_c = \begin{cases} \dfrac{k^2\pi^2 E_s}{12(1-\upsilon^2)}\left(\dfrac{t}{l}\right)^2 & \text{if} \quad \dfrac{t}{l} < \sqrt{\dfrac{8\sqrt{3}(1-\upsilon^2)\sigma_y}{\pi^2 k^2 E_s}} \\ \dfrac{2\sigma_y}{\sqrt{3}} \end{cases} \qquad 2.1$$

where k is a boundary condition factor (k = 2 if built-in), E_s is the Young's modulus, σ_y is the yield stress, υ is a Poisson's ratio and (t/l) is an aspect ratio of thickness and a length of a strut. Note that the buckling behaviour is a common failure mode in metallic truss structure, and this failure mode under quasi-static loading also reported in [62].

Kazemahvazi *et al.* [19, 20] performed an experimental and theoretical study on the behaviour of composite corrugations. All of the corrugations were made using unidirectional carbon fibre laminates with the fibre directions along the corrugation. The uniaxial compression tests were conducted at two different corrugation angles, 45^o and 70^o, respectively. They observed that the struts tended to fail in a combined splitting, buckling and compressive material failure. The splitting failure mode was obvious in the test since all the corrugations were made from unidirectional laminates. Figure 2.17 shows that the peak load for 70^o corrugation is greater than 45^o corrugation, at the same struts thickness. However, the predicted failure load was approximately 20% below the theoretical critical buckling load of a clamped strut. The authors believed that the initial imperfection induces larger bending moments on the strut which lead to material failure at lower load than the theoretical bifurcation load. This study was limited to a single unit cell with a same cell wall thickness.

(a) **(b)**

This text box is where the unabridged thesis included the following third party copyrighted material:

Kazemahvazi S, Tanner D, Zenkert D. Corrugated all-composite sandwich structures. Part 2: Failure mechanisms and experimental programme. Composites Science and Technology. 2009;69(7–8):920-925.

http://dx.doi.org/10.1016/j.compscitech.2008.11.035

Figure 2.17: Compression response of a single unit cell of (a) 70^{o} and (b) 45^{o} monolithic corrugations. The peak load at angle of 70^{o} ($P^{70^{\circ}} \approx 1.05$ kN) is greater than the peak load at angle of 45^{o} ($P^{45^{\circ}} \approx 0.90$ kN). Note dashed line show analytical predictions [19].

To improve the buckling resistance of corrugated-core sandwich structures under uniaxial compression, a number of reinforcement materials or hierarchical architectures can be used.

Hierarchical construction is expected to delay elastic buckling in the web of the sandwich truss core. The work of Deshpande *et al.* [58] in Figure 2.18 shows a comparison between monolithic and hierarchical corrugated-cores.

(a) **(b)**

This text box is where the unabridged thesis included the following third party copyrighted material:

Kooistra GW, Deshpande V, Wadley HNG. Hierarchical corrugated core sandwich panel concepts. Journal of Applied Mechanics. 2007;74:259-268.

http://dx.doi.org/10.1115/1.2198243

Figure 2.18: Photographs showing the failure modes of a (a) monolithic corrugated-core (1^{st} order) and (b) hierarchical corrugated-core (2^{nd} order) [58].

The deformation of the monolithic corrugated-core was controlled by elastic buckling and the peak strength was approximately 0.08 MPa. In contrast, the hierarchical corrugated-core achieved an initial peak strength of 1.0 MPa, where first face wrinkling was observed, resulting in a sharp drop in stress. Following this, the stress increased until a second wrinkle formed at approximately 0.8 MPa. The two wrinkles are clearly seen in Figure 2.18.

Kazemahvazi *et al.* [19, 20] extended the above work by combining the strut with a polymethacrylimide (PMI) foam, where the foam becomes part of truss core member (hierarchical). In the study, a hierarchical corrugation core was manufactured in the same way as the monolithic corrugation, and the hierarchical configurations have the same foam thickness in the truss core member. In Figure 2.19, the results show that the peak stress is approximately three times higher than its monolithic counterpart. Different failure modes were observed, where the 45^{o} configuration failed through core member face fracture, while the 70^{o} configuration failed through local buckling or core shear buckling. Neither global buckling nor splitting failure modes were observed in the experiment.

(a) **(b)**

This text box is where the unabridged thesis included the following third party copyrighted material:

Kazemahvazi S, Tanner D, Zenkert D. Corrugated all-composite sandwich structures. Part 2: Failure mechanisms and experimental programme. Composites Science and Technology. 2009;69(7–8):920-925.

http://dx.doi.org/10.1016/j.compscitech.2008.11.035

Figure 2.19: Compression response of a single unit cell of (a) 70^{o} and (b) 45^{o} hierarchical corrugations. Note that dashed line show analytical predictions [19].

Alternatively, the properties of the corrugated-core could be by reinforcing with a foam core [69]. Such research was done by Malcom *et al.* [67] which shows that the peak strength of the foam-filled cores was 3 to 7 MPa higher than that the open core structure, where the foam-filled just increased relative density of the overall

composite structure by about 15% to 40%, as shown in Figure 2.20. They found that the strength of struts with a thickness to length ratio (t/l) of 0.07 or less was governed by Euler buckling. It is possible that the foam stabilised the strut by providing lateral pressure to the cell wall during buckling, leading to an increase in the critical buckling strength. All structures with $t/l > 0.07$ failed by microbuckling, and it is unlikely that the foam used in the structures significantly impeded this failure mode. An expression to peak strength of open core (unfilled) composite corrugated-core is expected to be set by either the Euler buckling or the microbuckling of the struts, by:

$$\sigma_p = \begin{cases} \frac{\pi^2}{6}\left(\frac{t}{l}\right)^3 \frac{h}{H} E_s & if \quad \frac{\sigma_s}{E_s} > \frac{\pi^2}{12}\left(\frac{t}{l}\right)^2 \\ 2\frac{t}{l}\frac{h}{H}\sigma_s \end{cases} \qquad 2.2$$

where h is a height of the core and H is a length of an unit cell.

(a) **(b)**

This text box is where the unabridged thesis included the following third party copyrighted material:

Malcom AJ, Aronson MT, Deshpande VS, Wadley HNG. Compressive response of glass fiber composite sandwich structures. Composites Part A: Applied Science and Manufacturing. 2013;54(0):88-97.

http://dx.doi.org/10.1016/j.compositesa.2013.07.007

Figure 2.20: Compressive strength measurements and predictions for corrugated composite core as a function of relative density; (a) unfilled core and (b) foam-filled core [67].

The work above highlighted the advantages of using a foam-filled core to increasing the peak strength, delay the onset of buckling and improve the energy-absorption characteristics. However, the construction process of the foam-filled sandwich core was impractical as the foam core must be cut precisely into triangular prisms, and then inserted to form triangular topology.

2.4.2 Mechanical Response under Static Shear Test

A static shear test presents a suitable way to determine the shear strength and stiffness of a corrugated-core sandwich structure. Such tests are carried out according to the ASTM C273 standard [70].

Aboura *et al.* [46] investigated the transverse shear moduli, G_{xz} and G_{yz} respectively. The corrugated paper board was bonded to loading blocks and tested according to standard shear test [70]. They found that the shear modulus in the cross-direction (CD) is greater than in machine-direction (MD), $G_{yz} > G_{xz}$. From the MD shear load-displacement curve in Figure 2.21, four phases can be observed before failure. Firstly, the linear elastic phase, followed by failure of the flutings (cores) under shear effect. Next, when the fluting-skins interfaces takes place, the load increases again. Finally, the fourth stage represents total damage of the specimen. In contrast, only a linear elastic phase was observed in the CD direction before reaching failure, since the flutings detached. A theoretical analysis of shear stiffness for a sinusoidal corrugated-core was reported in [71] and an analytical prediction for the shear buckling was reported in [72].

Figure 2.21: Shear load-displacement curve in MD direction [46].

Transverse and longitudinal shear responses of a metallic corrugated-core were performed in [61]. Figure 2.22 shows photos at different levels of engineering shear strain, suggesting that the peak load is controlled by plastic buckling in one of the adjacent struts.

Figure 2.22: Deformation images of the $\rho^* = 0.05$ corrugated-core in transverse shear [61].

Figure 2.23: A comparison of the experimental and predicted values of transverse shear strength of stainless steel corrugated-core panels [61].

A comparison between the experimental data and the FE predictions for transverse shear strength is shown in Figure 2.23, where an imperfection of magnitude, $\zeta = 0.25$ predicted the peak stress accurately. In longitudinal shear, the authors found that the peak stresses exceeded those in compression or transverse shear.

In assessing the transverse shear performance of a carbon fibre corrugated-core, Kazemahvazi *et al.* [19] showed that the shear peak load for a 45^o corrugation is greater than 70^o corrugation, for the same struts thickness. Figure 2.24 shows the shear peak load for the 45^o corrugation is double the value of the 70^o corrugation. This proves that at an inclination angle of 45^o, the shear strength is a maximum as well as the shear stiffness.

Figure 2.24: Shear response of a single unit cell of (a) 70^o and (b) 45^o monolithic corrugations. The peak shear load at angle of 45^o ($P^{45^\circ} \approx 5.1$ kN) is greater than the peak shear load at angle of 70^o ($P^{70^\circ} \approx 2.2$ kN). Note that dashed line show analytical predictions [19].

2.4.3 Mechanical Response under Combined Loading

Sandwich structures are often subjected to complex service loading conditions, in which two or three dynamic or static principal stresses may exist [73], e.g. a sandwich fuselage side panel subjected to combined bending and torsion. In the literature, there are several test methods used to investigate the behaviour of sandwich cores under combined loading, except for the triangular corrugated-core.

2.4.3.1 Cylindrical Combined Loading

Patel *et al.* [74] studied the effect of biaxial loading on corrugated board cylinders. Three different loading conditions were applied to the cylinders, axial compression (F), torsion (T) and external pressure (P), as shown in Figure 2.25 (a).

(a) **(b)** **(c)**

This text box is where the unabridged thesis included the following third party copyrighted material:

Patel P, Nordstrand T, Carlsson LA. Local buckling and collapse of corrugated board under biaxial stress. Composite Structures. 1997;39(1):93-110.

http://dx.doi.org/10.1016/S0263-8223(97)00130-X

Figure 2.25: (a) Coordinate systems and loading of a corrugated cylinder. Failure envelopes for the corrugated cylinder; (b) the axial compression and torsion quadrant and (c) the torsion and external pressure quadrant [74].

The authors observed that the failure modes were mostly dominated by local buckling from the inner facing of the corrugated board. However, for torsion (T) and externally-pressurised (P) cylinders, the cylinders buckled globally in the collapse mode before local buckling or material failure occurred. It was noted that the experimental failure stresses are approximately one quarter of the predicted values. The combined failure loads were presented as failure locus in stress space. Figure 2.25 (b) shows the experimental collapse stress closely follows the Tsai-Wu failure criterion [75] for combined pure axial compression and torsion. However, in Figure 2.25(c), the experimental data fall well below the Tsai-Wu predictions. As noted previously, Tsai-Wu failure criterion over-predicts the collapse stresses, due to the cylinders appeared to fail by a global buckling.

2.4.3.2 Combined Shear-Compression Loading

Kintscher *et al.* [76] presented a methodology and a test fixture construction for quasi-static combined out-of-plane shear and compression tests on sandwich core materials. They tested and discussed the stiffness and failure behaviour of folded core structures. Figure 2.2.6 shows schematic assembly of multi-axial test rig and data acquisition. Note that this test assembly was proposed in reference [77].

Figure 2.26: Schematic data acquisition [76].

From the experiment, the author found that the experimental data were quite scattered. It was shown that the larger the original shear deformation, the smaller was the residual compression stiffness. This was due to initial shear deformation, the cell walls of the folded core were deformed against the original position.

Figure 2.27: Stresses at failure of folded core material under shear and compression loading [76].

For the scatter experimental data in Figure 2.27, the authors approximated a reasonable linear failure criterion prediction as:

$$\frac{\sigma_3}{R_3^{(-)}} + \frac{|\tau_5|}{R_5} = 1 \qquad 2.3$$

where σ_3 and τ_5 are the current transverse compression and shear stresses for a given stress state, and $R_3^{(-)}$ and R_5 are the compression and shear strength. However, this is a simply way to describe the interaction between the transverse compression and shear stresses, and it might not be universally valid for all folded core or prismatic cores.

In contrast to the simple approximation in the Equation 2.3, Besant *et al.* [77] investigated the interaction between the compressive-shear stresses, for an aluminium honeycomb core at the same multi-axial test fixture. They proposed a modified quadratic failure criterion of the form:

$$\left(\frac{\sigma}{\sigma_u}\right)^n + \left(\frac{\tau_l}{\tau_{lu}}\right)^n + \left(\frac{\tau_t}{\tau_{tu}}\right)^n = 1 \qquad 2.4$$

where σ, τ_l and τ_t are the compressive stress and the through-thickness shear stresses in the longitudinal and transverse directions respectively, and σ_u, τ_{lu} and τ_{tu} are the corresponding yield stresses. Note that the failure component in the normal direction is $\left(\frac{\sigma}{\sigma_u}\right)^n$, while $\left(\frac{\tau_l}{\tau_{lu}}\right)^n$ is the second component in the tangential direction and the additional component in out-of-plane direction is $\left(\frac{\tau_t}{\tau_{tu}}\right)^n$. Figure 2.28 shows the value of n required to force the model to fit the experimental data was found to be dependent on the material type, with values of n = 1.5 in Equation 2.4 produces a very good fit to experimental data. For simplicity, a value of n = 2 still provides a good fit.

Figure 2.28: Failure curves of the aluminium honeycomb core [77].

2.4.3.3 Bi-axial Arcan Test

Petras and Sutcliffe [78] constructed the compressive-shear failure locus for an aluminium honeycomb. Instead of using two load cells to simultaneously measure the mechanical response of the sandwich cores, the authors used the Arcan test method [79] to characterise the compression and shear responses. With this technique, they observed that the failure envelopes can be represented by a linear failure criterion (Equation 2.3), the exception was a honeycomb with density of 128 kg/m^3 (see Figure 2.29). No clear evidence on discrepancy for a 128 kg/m^3 honeycomb core was reported here.

Figure 2.29: Strength-to-failure criterion for honeycomb cores; (a) ρ = 64 kg/m^3 and (b) ρ = 128 kg/m^3. Note that the dashed lines correspond to the linear failure criterion [78].

Mohr and Dyoyo [80-83] studied the mechanical responses of honeycomb cores with the used of the Arcan test method.

Figure 2.30: Localisation of deformation in an aluminium honeycomb specimen under combined normal and shear loading in the *T*-*W* plane [82].

Figure 2.30 shows the deformation of the core under combined loading. Based on global static equilibrium, the mean shear and normal stresses, τ_{TW} and σ_T are calculated from the vertical force that acts on the specimen:

$$\sigma_T = \frac{F_V}{A}\sin\theta \qquad 2.5$$

$$\tau_{TW} = \frac{F_V}{A}\cos\theta \qquad 2.6$$

where F_V is a vertical force, θ is a bi-axial loading angle and A is a cross-section area. The authors found that some issues associated with the Arcan testing must have to take into consideration, especially the effects of mounting configurations [84]. Figure 2.31(a) shows the standard configuration or single pin joint in the test rig. This condition allows rotation of the fixture at the joint and eliminates any transverse load (horizontal force, $F_H = 0$) on the actuator. Therefore, the Equations 2.5 and 2.6 are only valid for this standard configuration.

(a) **(b)**

This text box is where the unabridged thesis included the following third party copyrighted material:

Mohr D, Doyoyo M. Analysis of the Arcan apparatus in the clamped configuration. Journal of Composite Materials. 2002;36(22):2583-2594.

http://dx.doi.org/10.1177/002199802761405303

Figure 2.31: Mounting conditions between the uniaxial testing machine and the Arcan grips for the (a) standard and (b) clamped configuration [80].

For the second condition, shown in Figure 2.31(b), the multiple-pin or clamped configuration do not allow any rotation between the Arcan grips and the testing machine, and thus F_H can take non-zero values. The expressions for the normal and shear stresses must be corrected by adding a term that takes the effect of the horizontal force into account [80]:

$$\sigma_T = \frac{F_V}{A}\sin\theta - \frac{F_H}{A}\cos\theta \qquad 2.7$$

$$\tau_{TW} = \frac{F_V}{A}\cos\theta + \frac{F_H}{A}\sin\theta \qquad 2.8$$

Some authors ignored the measurement of the horizontal force, since to measure the value of F_H required an additional load cell. The standard load cell of a universal testing machine can only measure F_V, but not F_H. Mohr and Dyoyo [80] concluded that the F_H must be measured for the clamped configuration, otherwise significant errors will arise in the stresses, i.e. they found that for unidirectional composites, maximum relative errors in the shear stresses of 1000% are observed.

One of the ways to measure F_H without an additional load cell was introduced by Lamb *et al.* [85]. The authors characterised the hexagonal honeycomb core using an Arcan apparatus, and found that the failure mechanism was similar to those observed by Mohr and Dyoyo [82]. The value of F_H was determined by a simple pre-calibration test to measure the transverse compliance of the test rig, at a loading angle of 45^o. With this calibration, the value of F_H acting at the grips was measured, and then the value can be used in Equations 2.7 and 2.8.

2.4.3.4 Bi-axial Failure Envelopes

Under compression-shear loading, the failure stresses and mechanisms differ depending on the loading angle. Mines and Jones [86] stated that four different failure envelope models can be used to characterise the response of a core structure. Model 1 uses the von-Mises yield criterion, including strain-hardening and is given by:

$$\left(\frac{\sigma}{\sigma_e}\right)^2 + \left(\frac{\tau}{\tau_e}\right)^2 = 1 \qquad 2.9$$

where σ_e and τ_e are the effective stresses with σ and τ being related through $\sigma = \tau\sqrt{3}$.

In Model 2, it is assumed that no strain-hardening occurs as a result of the transverse shear stress component and hence:

$$\left(\frac{\sigma}{\sigma_e}\right)^2+\left(\frac{\tau}{\tau_f}\right)^2=1 \qquad 2.10$$

where τ_f is the shear strength of the core, i.e. the shear stress at initial crush.

In the third model it is assumed that a linear relationship exists between the direct and shear stress components:

$$\left(\frac{\sigma}{\sigma_e}\right)+\left(\frac{\tau}{\tau_e}\right)=1 \qquad 2.11$$

Meanwhile, Model 4 represents a hybrid interaction criterion, in which the von-Mises criterion is assumed to apply up to the initial crush condition ($\sigma_e = \sigma_f$ and $\tau_e = \tau_f$) with and thereafter, a linear relationship apply.

The four models discussed above were used as guides to construct the failure envelope of a sandwich core [87]. Surprisingly, even for the same core material, the failure criterion model to be used can be different. For example, Benderly and Putter [88] constructed a failure envelope for Rohacell foam, and the data were well-fitted by a quadratic equation (Equation 2.10). A linear relationship (Equation 2.11) was not appropriate, unlike that reported in [89] for the same foam core. The argument for this difference in the applicability of the failure model was unclear.

2.4.4 Mechanical Response under Dynamic Loading

This section presents the classification of impact response, the dynamic compression of corrugated-core sandwich structures and related topics on dynamic effects and impact testing.

2.4.4.1 Classification of Impact Response

To understand the mechanical responses of sandwich structures under dynamic loading, Chai and Zhu [90] presented two criteria for the classification of impact response, as shown in Figure 2.32. These criteria are based on structural deformation

and damage, and structural response. Stronge [91] explained that plastic deformation is localised around the contact area for low velocity impact, but a large area of deformation or damage around the contact area for high velocity impact. However, the impact mass, M should be take into account as well as the impact velocity [92]. In addition to the impact velocity and mass, impact duration, t, is also considered as a key parameter in distinguishing between a high and a low velocity impacts [93].

Figure 2.32: Solution methods for different categories of impact. Note that M is mass of impactor, m_p is mass of specimen and (M/m_p) is impactor mass ratio [90].

Cantwell and Morton [94] classified low velocity impact as an impact response up to 10 m/s. The authors summarised that under low velocity impact, the energy absorption capability is dependent on the shape and size of the specimen, whilst at high velocity impact, which involves a localised form of specimen response, and where damage is independent to specimen geometry.

High velocity and ballistic impact is not of primary interest in this thesis, and only relevant literature on low velocity impact of corrugated-core sandwich structures will be discussed below.

2.4.4.2 Dynamic Effects

The dynamic response of a periodic cellular core can be significantly different from its quasi-static loading response, due to three fundamental effects:

a) Material strain-rate sensitivity

   The constituent material of the core may show a strain-rate dependence, i.e. the yield strength of mild steel increases with increasing strain-rate [95].

b) Inertia stabilisation

   Since cellular cores are buckling-dominated, inertial effects can delay the onset of buckling and change the wavelength of the buckling mode. This effect can be important under low velocity impact, for which wave propagation effects are negligible [96].

c) Wave propagation

   Wave propagation effects become important as the impact velocity is increased. Propagation of elastic, plastic and bending waves can be transmitted through the core which can affect the macroscopic properties of the structure. For example, consider a metal column loaded dynamically in compression, if the impact velocity is greater than the plastic wave speed, the column does not buckle and material accumulates at the impacted end [97].

2.4.4.3 Dynamic Compression of Corrugated-core Sandwich Structure

When a sandwich structure is loaded dynamically, some energy is absorbed by crushing the core. Therefore, the dynamic performance of a sandwich structures is highly dependent on the compressive response of the core [98].

Tilbrook *et al.* [62] investigated the dynamic out-of-plane compressive response of a stainless steel corrugated-core sandwich structure at impact velocities ranging from quasi-static to 200 m/s. They used two unit cells corrugated-core sandwich structure and the dynamic compression responses of the structure were measured using a strain-gauged Kolsky bar. Under low velocity impact at 10 m/s, direct observational evidence was provided for inertial stabilisation against elastic buckling, as in Figure 2.33. They found that the peak stress increased seven times above quasi-static values, due to dynamic stabilisation against the buckling modes.

Figure 2.33: High speed video images of the deformation at a striker velocity of 10 m/s [62].

Latter, Rubino *et al.* [63, 64] continued the work of Tilbrook *et al.* [62], and assessed the dynamic responses of corrugated-core sandwich structures in two different boundary conditions: end-clamped and clamped rectangular sandwich plate. A different measuring technique was used. They used Alporas aluminium foam as a projectile which was fired from a gas gun (v_o = 30 - 426 m/s) to impact the structures.

Recently, Russell *et al.* [66] carried out a series of dynamic compressive tests on filled and unfilled triangular corrugated-core sandwich structures. The specimens were manufactured in 'stocky under compression' with an aspect ratio (t/l) of 0.219 and relative density of $\rho^* \approx 33\%$, and measured using Kolsky bar apparatus. The

idea of the stocky strut was to measure responses of the material rather than structural behaviour (Euler buckling). They found that the measured peak strength of filled and unfilled specimens were almost identical, where deformation is more localised near the impacted face with the corrugated-core 'stubbing' against the impacted face. In Figure 2.34, they plotted a bi-linear relationship of the strength with impactor velocity, and concluded that the rate-sensitivity of the high relative density corrugated-core is controlled by the rate-sensitivity of the parent cell wall material and is not significantly affected by inertial stabilisation against elastic buckling. Note that the rate-sensitivity of the parent material indicated two different zones of deformation, microbuckling of the strut (v_o < 50 m/s) and compressive crushing at higher strain rate.

Figure 2.34: Bi-linear relationship of the measured peak stresses in the filled and unfilled corrugated-core specimens as a function of impact velocity and applied strain-rate [66].

Figure 2.35: Range of failure mechanisms at different velocities and for different core member aspect ratios. Note that the number displayed in the small box is a buckle mode shape [57].

Most recently, with the same test apparatus of a Kolsky bar, Kazemahvazi *et al.* [57] extended the work on the dynamic out-of-plane compressive responses of the corrugated-cores. A single unit cell of trapezium shape geometry with three different

aspect ratios (t/l) of 0.015, 0.03 and 0.06, was dynamically loaded at impact velocities ranging from 5 m/s to 35 m/s. They evaluated the failure mechanisms at different velocities and for different core member aspect ratios. In Figure 2.35, the authors observed that the order of the buckling modes rises dramatically with increasing velocity. They concluded that the dynamic strength enhancements from inertial stabilisation achieved factors of up to 9 for the most slender geometry (t/l = 0.015) and for the most stubby strut (t/l = 0.06), can achieved by factors of 2.5.

2.4.4.4 Instrumented Dynamic Compression Test

The above literature is mostly uses the instrumented Kolsky bar to measure the dynamic compression properties. Additionally, an instrumented drop-weight tower has been used to characterise the dynamic compression properties of a novel structure [98]. Here, the impact force was measured directly using a piezoelectric load cell positioned between the striker and weight of the impactor. The impactor was released from heights up to 300 mm to produce the desired impact velocity. The velocity of the impactor during the impact test was measured using a Laser Doppler Velocimeter. However, in the Kolsky bar test, the specimens were impacted with an impactor bar, the impact forces on the rear of the specimens were measured by inferring the stress in the transmitter bar through strain gauges. Very strict protocols have to be followed including the calibration procedure, to receive reliable impact force data [99]. Figure 2.36 shows the drop-weight tower and the Kolsky bar.

(a)	(b)
This text box is where the unabridged thesis included the following third party copyrighted material: **McKown S, Shen Y, Brookes WK, Sutcliffe CJ, Cantwell WJ, Langdon GS. The quasi-static and blast loading response of lattice structures. International Journal of Impact Engineering. 2008;35(8):795-810.** http://dx.doi.org/10.1016/j.ijimpeng.2007.10.005	This text box is where the unabridged thesis included the following third party copyrighted material: **Lee S, Barthelat F, Hutchinson JW, Espinosa HD. Dynamic failure of metallic pyramidal truss core materials – Experiments and modeling. International Journal of Plasticity. 2006;22(11):2118-2145.** http://dx.doi.org/10.1016/j.ijplas.2006.02.006

Figure 2.36: (a) A free-fall instrumented drop-weight tower [98] and (b) an instrumented direct impact Kolsky bar set up [99].

2.5 Modelling of Sandwich Structures

This section describes the background of the finite element method, the modelling of corrugated-core sandwich structures and other issues involved in static and dynamic FE modelling.

2.5.1 Background of Finite Element Method

Understanding the foreign object impact to lightweight aircraft constructed from polymer composite sandwich structure requires the quantification of impact energy absorption of the structure as it deforms. This is a very complex problem given the variety of candidate composite materials for such structures, and given possibility of many different material and structural failure modes. Also, the analytical model includes a large number of simplifications and assumptions, and in order to make progress in this field the use of a computer is indispensable.

Finite Element Method (FEM) is a numerical technique for finding approximate solutions that can be used for analysing the behaviour of complicated structures where such analyses may not be feasible theoretically and the cost of laboratory testing limits the amounts of tests possible. In recent years, the use of FEM in a

computer-aided engineering (CAE) tool for technical analysis has become more common. There are several commercial FE packages available on the market these days, e.g. Abaqus, LS-Dyna, ANSYS, CosmosM, ALGOR, MSC.Nastran, etc. Displacement method is the most widely used as FEM approach and is suitable for most technical problems. In this method, displacements are obtained by inversion of the stiffness matrix so that stresses and strains can be derived.

Since the FEM technique is already established, researchers and industry are the end-users of commercial FE packages. Although the area is already established one would require a good level of understanding in order to apply the right procedure and to utilise it to its optimum level. With a good understanding of FEM, the end-user is able to produce detailed visualisations in CAE, showing the stresses and strains and deformation of the structural components. Therefore, FEM can give a high level of confidence for the performance of structural components, before the components are manufactured.

2.5.2 Modelling of Corrugated-core Sandwich Structures

Côté *et al.* [61] used FE analysis to predict the quasi-static response of the triangular corrugated and diamond lattice cores in Abaqus/Standard. A single corrugation was modelled using three-dimensional linear shell element (S4R) and elastic-plastic property of the stainless steel was inputted to predict the mechanical response of the core. An imperfection in the shape of the buckling mode was imposed onto reach strut, where the first eigenmode and maximum amplitude equal to 25% of the sheet thickness was specified in the FE model. They concluded that by including geometric imperfection, this FE model is in good agreement with the experimental result.

Tilbrook *et al.* [62] simulated quasi-static and dynamic responses of the stainless steel corrugated-core sandwich structures using Abaqus/Explicit. Two-dimensional FE models were created using four-noded plane strain quadrilateral element with reduced integration (CPE4R), with the same geometry as measured in the corresponding experimental specimens. The material behaviour was modelled as rate-dependent J2-flow theory for an elastic-plastic solid. Perfect bonding between the core and the face sheet was assumed in all cases and a hard contact interaction

was enforced between all contacting surfaces. Geometric imperfections were introduced in the FE geometries of the specimen, in form of the first static eigenmode of elastic buckling. The maximum amplitude of the imperfections was set equal to sheet thickness. Figure 2.37(a) shows comparisons of the measured and numerical predictions of the quasi-static response showed good agreement throughout the collapse response. Dynamic simulations showed that a higher order buckling mode in the corrugated-core was triggered. For dynamic compression at v_o = 50 and 100 m/s, initial deformation was concentrated near the impacted end of the corrugated-core. The FE models also showed that the material strain-rate effects have a negligible effect on the dynamic compressive response of the laboratory-scale core specimens, as shown in Figure 2.37(b). They concluded that laboratory-scale specimens tested were adequate to reveal the dynamic strengthening mechanism of full-scale corrugated sandwich core.

(a) **(b)**

Figure 2.37: (a) A comparison between the observed and FE predictions of the quasi-static deformation mode of the corrugated-core specimens and (b) FE predictions of the dynamic strength enhancement with and without material strain-rate sensitivity [62].

Rubino *et al.* [63, 64] developed FE models to simulate the response of sandwich structures with corrugated and Y-frame cores, under dynamic compression loading. The models aimed to gain further insight into the failure mechanisms and to understand the role the boundary conditions; end-clamped and clamped around the

edges. Numerical simulations were performed using Abaqus/Explicit and employed four-noded shell elements (S4R) for the both the face sheets and the core. Perfect bonding between the core and the face sheets was assumed. The uniaxial tensile true stress versus equivalent plastic strain curve at plastic strain rates of 10^{-3} $s^{-1} \leq \dot{\varepsilon}^{p} \leq 10^{4}$ s^{-1} were tabulated to define the strain hardening and strain-rate behaviour of the material (AISI 304 stainless steel). Over the range of impact velocities considered in this study, thermal effects were neglected throughout the numerical simulations. The 'general contact' option in Abaqus was employed to simulate contact between all adjacent surfaces, which enforced hard, frictionless contact interaction using a penalty algorithm. Comparisons of the simulations and measurements show good agreement for predicting the plate permanent deflections for corrugated-core, however the FE calculations under-predict the core compression in the Y-frame sandwich plates. The authors attributed this discrepancy to the fact that tearing between the Y-frame leg and the back face sheet. They concluded that theses sandwich constructions have potential for significantly enhancing the dynamic performance of structures.

Qin *et al.* [100] modelled a three-dimensional metal corrugated-core sandwich structure subjected to heavy mass with low impact. The FE model was performed with Abaqus/Explicit and employed eight-noded linear brick element with reduced integration (C3D8R) for both face sheets and core. Due to the symmetry of the beam struck at midspan, half length of the sandwich panel was considered in analysis with symmetry boundary conditions imposed at midspan. Elastic and plastic strain hardening properties were used to simulate the behaviour of the structure. They concluded that the dynamic response of the sandwich panel outperforms monolithic solid plate of the same mass.

Vaziri *et al.* [101] used Abaqus/CAE software to develop models for clamped-end metal sandwich plates with two different sandwich cores (square honeycomb and folded cores) subjected to quasi-static and impulsive loading. One of the main studies was to investigate enhancement of the buckling resistance of the webs due to lateral support of foam. Brick elements with reduced integration (C3D8R) were employed to all components (face sheet, core webs and polymeric foams). Classical flow theory based on the von-Mises yield surface and isotropic hardening was

employed in the computations. All the computations were performed using the explicit time integration (Abaqus/Explicit), both for dynamic and quasi-static events. They explained that for the models of foam-filled cores, the displacement of the steel core and polymeric foam coincide at nodal points on shared interfaces. When analysed with implicit version (Abaqus/Standard), the problems addressed with convergence difficulty, because of the complexity of the geometry and variation of the material behaviour. For that reason, Abaqus/Explicit was utilised to simulate each field and history output of empty and foam-filled cores. From the quasi-static FE model, they found that the foam enhances the core crushing resistance by providing lateral support of the core webs (see Figure 2.38).

Figure 2.38: Deformed configuration of the empty and fully-filled sandwich plates at $\delta_{punch} / L = 0.25$. Note that the polymeric foam components are not shown and v_s is volume fraction of steel [101].

To date, only one research paper has discussed a modelling procedure for composite corrugated-core sandwich structures. Kazemahvazi and Zenkert [20] used the FE method to validate the linear elastic response of CFRP corrugated-core sandwich structures as well as the stress predictions calculated from an analytical model. A non-linear geometry model of a single unit cell was generated in Abaqus/Standard. Each strut was modelled using a four-noded linear shell element with reduced integration (S4R). The loading and boundary conditions were detailed in the paper, however the constitutive model used in the simulation was not presented. A very good correlation was found between the analytical model and the FE model.

In the commercial finite element code Abaqus, in-built progressive damage models for elastic-brittle material, based on Hashin's failure theory are able for predicting failure and post-failure behaviour in fibre-reinforced composite materials. It was noted that this failure theory in Abaqus can only be applied to conventional shell or continuum shell element. Details for simulating an anisotropic damage model suitable for composite materials are presented in [102].

2.5.3 Imperfections

Zhang *et al.* [103] studied the crushing behaviour of four different types of corrugated-cores (Y-type, U-type, X-type and Y-type core). The authors ignored imperfection issues in numerical modelling with MSC.Dytran, and consequently, the numerical results over-predicted the stiffness and peak load of the core structures. For example in Figure 2.39, the prediction of peak load is about three times above the measured response of V-type core sandwich panel.

Heimbs *et al.* [30] stated that the imperfections in cellular core structures can be divided into two categories: global and local imperfections.

a) Global imperfections

   Due to irregular cell geometry, uneven or pre-buckled cell walls.

b) Local imperfections

   i) Macro level (e.g. surface roughness, wall thickness variation, deviation of fibre angles, resin accumulation in cell wall corners).

   ii) Micro level (e.g. cracks, pores, variation of fibre volume fraction).

Both the imperfections in hexagonal honeycombs and folded cores were due to fabrication process, i.e. the folding process. Therefore, FE models without imperfections will always lead to an over-prediction of the stiffness and strength values [99].

(a) **(b)**

Figure 2.39: (a) A load-displacement curves of measured and numerical prediction of V-type core sandwich panel (b) a V-type core panel made from mild steel [103].

To account for imperfection issues, a FE buckling analysis procedure is presented in [104] while Sarawit *et al.* [105] presented an imperfection sensitivity study for two types of imperfections, local and distortional modes obtained from the buckling eigenvalue analysis. The modes were superposed in the model to give the initial geometric imperfection.

2.6 Summary of Chapter II

Chapter II presented a review of relevant past and current research work on corrugated-core sandwich structures subjected to quasi-static and dynamic compression loading. A brief overview of the classification of cellular materials e.g. foams, periodic cores, is given. Then, the mechanical response of corrugated-core sandwich structures under compression, shear and combined loading has been reviewed, with some relevant examples. Following this, the impact test response of the corrugated-core sandwich structures has been discussed. Finally, procedures for modelling the response of these sandwich structures using commercially-available codes, and numerical modelling techniques have been reviewed, with examples of published numerical work. To date, limited literature is available on triangular corrugated-core sandwich structures, especially those made from composite materials. A summary of the relevant work is given in Table 2.1.

Therefore, this research work aims to contribute to the manufacture and evaluation of the mechanical properties of triangular corrugated-core sandwich structure, made from metallic and composite materials. A range of quasi-static tests, from out-of-plane compression to combined compression-shear loading are presented. These tests aim to understand the mechanical response, energy absorption and failure modes in the structures. An analytical model and a finite element model are developed to predict the strength and stiffness of the structures, both in quasi-static as well as under low velocity compression loading.

Table 2.1: A summary of relevant research works on corrugated-core sandwich structures.

Author	Year	Design	Core Material	Manufacturing Process	Corrugation Angles	Investigation
Knox *et al.* [53]	1998	Trapezium	Mild steel	Folding and adhesive bonding	18^o, 20^o, 25^o, 30^o	Experimental and FE analysis - Static bending test
Liang *et al.* [54]	2001	Trapezium	Steel	N/A	N/A	Analytical and Computer programming - Blast test
Côté *et al.* [61]	2006	Corrugated and Diamond Lattice	Stainless Steel 304	Slotting and brazing the assembly	$\pm 45^o$	Analytical, Experimental and FE analysis - Static compression and shear tests
Deshpande *et al.* [58]	2007	Trapezium - Monolithic and Hierarchical (sandwich corrugated-core)	Aluminium Alloy 6061-T6	Folding and brazing the assembly	60^o	Analytical analysis, Experimental - Static compression test
Tilbrook *et al.* [62]	2007	Triangular corrugated-core and Y-frame core	Stainless Steel 304	Folding and brazing the assembly	60^o	Experimental and FE analysis - Static and dynamic compression tests. Impact velocity, v_o = 2 m/s to 200 m/s
Rubino *et al.* [63]	2008	Triangular corrugated-core and Y-frame core	Stainless Steel 304	Folding and brazing the assembly	60^o	Experimental and FE analysis - Dynamic three point bending test, end-clamped. Impact velocity, v_o = 30 m/s to 426 m/s

Kazemahvazi and Zenkert [20]	2009	Trapezium - Monolithic and Hierarchical	Unidirectional CFRP (T700, Gurit)	Compression moulding and adhesive bonding	45°, 70°	Analytical, FE analysis - Static compression and shear tests
Kazemahvazi *et al.* [19]	2009	Trapezium - Monolithic and Hierarchical (sandwich foam core)	Unidirectional CFRP (T700, Gurit)	Compression moulding and adhesive bonding	45°, 70°	Experimental and Analytical analysis - Static compression and shear tests
Rubino *et al.* [64]	2009	Triangular corrugated-core and Y-frame core	Stainless Steel 304	Folding and brazing the assembly	60°	Experimental and FE analysis - Dynamic penetration test, clamped plates. Impact velocity, v_o = 94 m/s to 451 m/s
Russell *et al.* [66]	2010	Triangular corrugated-core (fully-filled and unfilled foam)	Woven E-glass (3WEAVE fabric, 3tex. Inc)	Stitching	64°	Analytical analysis, Experimental - Static and dynamic compression test. Impact velocity, v_o = 25 m/s to 175 m/s
Kazemahvazi *et al.* [57]	2012	Trapezium	Unidirectional CFRP (T700, Gurit)	Compression moulding and adhesive bonding	70°	Experimental - Dynamic compression test. Impact velocity, v_o = 5 m/s to 35 m/s
Wadley *et al.* [65]	2013	Triangular corrugated-core (fully-filled and unfilled foam)	Aluminium Alloy 6061-T6	Extrusion process	60°	Experimental - Ballistic test, clamped plates. Projectile velocity, v_o = 500 m/s to 1500 m/s

Note: N/A = information is not given

2.7 References

[1] Ashby MF. The properties of foams and lattices. Philosophical Transactions of the Royal Society A: Mathematical, Physical and Engineering Sciences. 2006;364(1838):15-30.

[2] Gibson LJ, Ashby MF. Cellular Solids: Structure and Properties. 2nd Edition ed: Cambridge Solid State Science Series; 1999.

[3] Wadley HNG. Multifunctional periodic cellular metals. Philosophical Transactions of the Royal Society A: Mathematical, Physical and Engineering Sciences. 2006;364(1838):31-68.

[4] Suh KW. Foamed plastics. Kirk-Othmer Encyclopedia of Chemical Technology. 1980.

[5] Ashby MF. Metal foams: a design guide: Butterworth-Heinemann; 2000.

[6] Zenkert D. An Introduction to Sandwich Construction: Engineering Materials Advisory Services Limited; 1995.

[7] Kabir ME, Saha MC, Jeelani S. Tensile and fracture behavior of polymer foams. Materials Science and Engineering: A. 2006;429(1–2):225-235.

[8] Ramsteiner F, Fell N, Forster S. Testing the deformation behaviour of polymer foams. Polymer Testing. 2001;20(6):661-670.

[9] Saint-Michel F, Chazeau L, Cavaillé J-Y. Mechanical properties of high density polyurethane foams: II Effect of the filler size. Composites Science and Technology. 2006;66(15):2709-2718.

[10] Viot P, Shankar K, Bernard D. Effect of strain rate and density on dynamic behaviour of syntactic foam. Composite Structures. 2008;86(4):314-327.

[11] Brothers AH, Scheunemann R, DeFouw JD, Dunand DC. Processing and structure of open-celled amorphous metal foams. Scripta Materialia. 2005;52(4):335-339.

[12] Orbulov IN, Ginsztler J. Compressive characteristics of metal matrix syntactic foams. Composites Part A: Applied Science and Manufacturing. 2012;43(4):553-561.

[13] Rejab MRM. Polymeric Foam as Core of Side-door Impact Beam, MSc Thesis, Universiti Teknologi Malaysia, 2004.

[14] Kwon YW, Cooke RE, Park C. Representative unit-cell models for open-cell metal foams with or without elastic filler. Materials Science and Engineering: A. 2003;343(1–2):63-70.

[15] Bratfisch JP, Vandepitte D. Development and validation of a continuous production concept for thermoplastic honeycomb. Journal of Sandwich Structures and Materials. 2007;9(2):113-122.

[16] Zok FW, Rathbun H, He M, Ferri E, Mercer C, McMeeking RM, Evans AG. Structural performance of metallic sandwich panels with square honeycomb cores. Philosophical Magazine. 2005;85(26-27):3207-3234.

[17] Russell BP, Deshpande VS, Wadley HNG. Quasistatic deformation and failure modes of composite square honeycombs. Journal of Mechanics of Materials and Structures. 2008;3(7):1315-1340.

[18] Metal Sandwich Technology - www.metawell.de.

[19] Kazemahvazi S, Tanner D, Zenkert D. Corrugated all-composite sandwich structures. Part 2: Failure mechanisms and experimental programme. Composites Science and Technology. 2009;69(7–8):920-925.

[20] Kazemahvazi S, Zenkert D. Corrugated all-composite sandwich structures. Part 1: Modeling. Composites Science and Technology. 2009;69(7–8):913-919.

[21] Wallach JC, Gibson LJ. Mechanical behavior of a three-dimensional truss material. International Journal of Solids and Structures. 2001;38(40–41):7181-7196.

[22] Zok FW, Waltner SA, Wei Z, Rathbun HJ, McMeeking RM, Evans AG. A protocol for characterizing the structural performance of metallic sandwich panels: application to pyramidal truss cores. International Journal of Solids and Structures. 2004;41(22):6249-6271.

[23] Queheillalt DT, Wadley HNG. Cellular metal lattices with hollow trusses. Acta Materialia. 2005;53(2):303-313.

[24] Smith M, Guan Z, Cantwell WJ. Finite element modelling of the compressive response of lattice structures manufactured using the selective laser melting technique. International Journal of Mechanical Sciences. 2013;67(0):28-41.

[25] Gümrük R, Mines RAW, Karadeniz S. Static mechanical behaviours of stainless steel micro-lattice structures under different loading conditions. Materials Science and Engineering: A. 2013;586(0):392-406.

[26] Zupan M, Chen C, Fleck NA. The plastic collapse and energy absorption capacity of egg-box panels. International Journal of Mechanical Sciences. 2003;45(5):851-871.

[27] Deshpande VS, Fleck NA. Energy absorption of an egg-box material. Journal of the Mechanics and Physics of Solids. 2003;51(1):187-208.

[28] Chung JG, Chang SH, Sutcliffe MPF. Deformation and energy absorption of composite egg-box panels. Composites Science and Technology. 2007;67(11–12):2342-2349.

[29] Movchan GV. Analysis of folded structures for impact resistance. Russian Aeronautics. 2007;50(4):439-441.

[30] Heimbs S. Virtual testing of sandwich core structures using dynamic finite element simulations. Computational Materials Science. 2009;45(2):205-216.

[31] Heimbs S. Foldcore Sandwich Structures and Their Impact Behaviour: An Overview. Dynamic Failure of Composite and Sandwich Structures: Springer; 2013. p. 491-544.

[32] Heimbs S, Middendorf P, Kilchert S, Johnson AF, Maier M. Experimental and numerical analysis of composite folded sandwich core structures under compression. Applied Composite Materials. 2007;14(5-6):363-377.

[33] Evans AG, Hutchinson JW, Fleck NA, Ashby MF, Wadley HNG. The topological design of multifunctional cellular metals. Progress in Materials Science. 2001;46(3–4):309-327.

[34] Zhu F, Lu G, Ruan D, Wang Z. Plastic deformation, failure and energy absorption of sandwich structures with metallic cellular cores. International Journal of Protective Structures. 2010;1(4):507-541.

[35] Buannic N, Cartraud P, Quesnel T. Homogenization of corrugated core sandwich panels. Composite Structures. 2003;59(3):299-312.

[36] Nordstrand TM. Parametric study of the post-buckling strength of structural core sandwich panels. Composite Structures. 1995;30(4):441-451.

[37] Nordstrand TM, Carlsson LA. Evaluation of transverse shear stiffness of structural core sandwich plates. Composite Structures. 1997;37(2):145-153.

[38] Nordstrand T. On buckling loads for edge-loaded orthotropic plates including transverse shear. Composite Structures. 2004;65(1):1-6.

[39] Lu TJ, Chen C, Zhu G. Compressive behaviour of corrugated board panels. Journal of Composite Materials. 2001;35(23):2098-2126.

[40] Lu TJ, Hutchinson JW, Evans AG. Optimal design of a flexural actuator. Journal of the Mechanics and Physics of Solids. 2001;49(9):2071-2093.

[41] Lu TJ, Zhu G. The elastic constants of corrugated board panels. Journal of Composite Materials. 2001;35(20):1868-1887.

[42] Tian YS, Lu TJ. Optimal design of compression corrugated panels. Thin-walled structures. 2005;43(3):477-498.

[43] Biancolini ME, Brutti C. Numerical and experimental investigation of the strength of corrugated board packages. Packaging Technology and Science. 2003;16(2):47-60.

[44] Biancolini ME. Evaluation of equivalent stiffness properties of corrugated board. Composite Structures. 2005;69(3):322-328.

[45] Biancolini ME, Brutti C. Analysis of corrugated board panels under compression load. Steel and Composite Structures. 2009;9(1):1-17.

[46] Aboura Z, Talbi N, Allaoui S, Benzeggagh ML. Elastic behavior of corrugated cardboard: experiments and modeling. Composite Structures. 2004;63(1):53-62.

[47] Yokozeki T, Takeda S-I, Ogasawara T, Ishikawa T. Mechanical properties of corrugated composites for candidate materials of flexible wing structures. Composites Part A: Applied Science and Manufacturing. 2006;37(10):1578-1586.

[48] Ge R, Wang B, Mou C, Zhou Y. Deformation characteristics of corrugated composites for morphing wings. Frontiers of Mechanical Engineering in China. 2010;5(1):73-78.

[49] Gilchrist AC, Suhling JC, Urbanik TJ. Nonlinear finite element modeling of corrugated board. ASME Applied Mechanics Division. 1998;231:101-106.

[50] Krusper A, Isaksson P, Gradin P. Modeling of out-of-plane compression loading of corrugated paper board structures. Journal of Engineering Mechanics. 2007;133(11):1171-1177.

[51] Kress G, Winkler M. Corrugated laminate homogenization model. Composite Structures. 2010;92(3):795-810.

[52] Bartolozzi G, Pierini M, Orrenius U, Baldanzini N. An equivalent material formulation for sinusoidal corrugated cores of structural sandwich panels. Composite Structures. 2013;100:173-185.

[53] Knox EM, Cowling MJ, Winkle IE. Adhesively bonded steel corrugated core sandwich construction for marine applications. Marine Structures. 1998;11(4-5):185-204.

[54] Liang C-C, Yang M-F, Wu P-W. Optimum design of metallic corrugated core sandwich panels subjected to blast loads. Ocean Engineering. 2001;28(7):825-861.

[55] Chang W-S, Krauthammer T, Ventsel E. Elasto-Plastic Analysis of Corrugated-Core Sandwich Plates. Mechanics of Advanced Materials and Structures. 2006;13(2):151-160.

[56] Liang YH, Louca LA, Hobbs RE. A simplified method in the static plastic analysis of corrugated steel panels. The Journal of Strain Analysis for Engineering Design. 2006;41(2):135-149.

[57] Kazemahvazi S, Russell BP, Zenkert D. Impact of carbon fibre/epoxy corrugated cores. Composite Structures. 2012;94(11):3300-3308.

[58] Kooistra GW, Deshpande V, Wadley HNG. Hierarchical corrugated core sandwich panel concepts. Journal of Applied Mechanics. 2007;74:259-268.

[59] Dayyani I, Ziaei-Rad S, Salehi H. Numerical and experimental investigations on mechanical behavior of composite corrugated core. Applied Composite Materials. 2012;19(3-4):705-721.

[60] Dayyani I, Ziaei-Rad S, Friswell MI. The mechanical behavior of composite corrugated core coated with elastomer for morphing skins. Journal of Composite Materials. 2013;0(0):1-14.

[61] Côté F, Deshpande VS, Fleck NA, Evans AG. The compressive and shear responses of corrugated and diamond lattice materials. International Journal of Solids and Structures. 2006;43(20):6220-6242.

[62] Tilbrook MT, Radford DD, Deshpande VS, Fleck NA. Dynamic crushing of sandwich panels with prismatic lattice cores. International Journal of Solids and Structures. 2007;44(18):6101-6123.

[63] Rubino V, Deshpande VS, Fleck NA. The dynamic response of end-clamped sandwich beams with a Y-frame or corrugated core. International Journal of Impact Engineering. 2008;35(8):829-844.

[64] Rubino V, Deshpande VS, Fleck NA. The dynamic response of clamped rectangular Y-frame and corrugated core sandwich plates. European Journal of Mechanics - A/Solids. 2009;28(1):14-24.

[65] Wadley HNG, Dharmasena KP, O'Masta MR, Wetzel JJ. Impact response of aluminum corrugated core sandwich panels. International Journal of Impact Engineering. 2013;62(0):114-128.

[66] Russell B, Malcom A, Wadley H, Deshpande V. Dynamic compressive response of composite corrugated cores. Journal of Mechanics of Materials and Structures. 2010;5(3):477-493.

[67] Malcom AJ, Aronson MT, Deshpande VS, Wadley HNG. Compressive response of glass fiber composite sandwich structures. Composites Part A: Applied Science and Manufacturing. 2013;54(0):88-97.

[68] Shanley FR. Inelastic column theory. Journal of the Aeronautical Sciences 1947;14(5):261-268.

[69] Cartie DD, Fleck NA. The effect of pin reinforcement upon the through-thickness compressive strength of foam-cored sandwich panels. Composites Science and Technology. 2003;63(16):2401-2409.

[70] ASTM. Standard Test Method for Shear Properties of Sandwich Core Materials. C273, 1998.

[71] Nordstrand T, Carlsson LA, Allen HG. Transverse shear stiffness of structural core sandwich. Composite Structures. 1994;27(3):317-329.

[72] Rao KP. Shear buckling of corrugated composite panels. Composite Structures. 1987;8(3):207-220.

[73] Chen AS, Matthews FL. A review of multiaxial/biaxial loading tests for composite materials. Composites. 1993;24(5):395-406.

[74] Patel P, Nordstrand T, Carlsson LA. Local buckling and collapse of corrugated board under biaxial stress. Composite Structures. 1997;39(1):93-110.

[75] Tsai SW, Wu EM. A general theory of strength for anisotropic materials. Journal of Composite Materials. 1971;5(1):58-80.

[76] Kintscher M, Kärger L, Wetzel A, Hartung D. Stiffness and failure behaviour of folded sandwich cores under combined transverse shear and compression. Composites Part A: Applied Science and Manufacturing. 2007;38(5):1288-1295.

[77] Besant T, Davies GAO, Hitchings D. Finite element modelling of low velocity impact of composite sandwich panels. Composites Part A: Applied Science and Manufacturing. 2001;32(9):1189-1196.

[78] Petras A, Sutcliffe MPF. Indentation failure analysis of sandwich beams. Composite Structures. 2000;50(3):311-318.

[79] Arcan M, Hashin Z, Voloshin A. A method to produce uniform plane-stress states with applications to fiber-reinforced materials. Experimental Mechanics. 1978;18(4):141-146.

[80] Mohr D, Doyoyo M. Analysis of the Arcan apparatus in the clamped configuration. Journal of Composite Materials. 2002;36(22):2583-2594.

[81] Mohr D, Doyoyo M. A new method for the biaxial testing of cellular solids. Experimental Mechanics. 2003;43(2):173-182.

[82] Mohr D, Doyoyo M. Large plastic deformation of metallic honeycomb: orthotropic rate-independent constitutive model. International Journal of Solids and Structures. 2004;41(16):4435-4456.

[83] Doyoyo M, Mohr D. Microstructural response of aluminum honeycomb to combined out-of-plane loading. Mechanics of Materials. 2003;35(9):865-876.

[84] Greer Jr JM, Galyon Dorman SE, Hammond MJ. Some comments on the Arcan mixed-mode (I/II) test specimen. Engineering Fracture Mechanics. 2011;78(9):2088-2094.

[85] Lamb AJ, Pickett AK, Chaudoye F. Experimental characterisation and numerical modelling of hexagonal honeycomb cellular solids under multi-axial loading. Strain. 2011;47(1):2-20.

[86] Mines RAW, Jones N. Approximate elastic-plastic analysis of the static and impact behaviour of polymer composite sandwich beams. Composites. 1995;26(12):803-814.

[87] Abrate S. Criteria for yielding or failure of cellular materials. Journal of Sandwich Structures and Materials. 2008;10(1):5-51.

[88] Benderly D, Putter S. Characterization of the shear/compression failure envelope of Rohacell foam. Polymer Testing. 2004;23(1):51-57.

[89] Li QM, Mines RAW, Birch RS. The crush behaviour of Rohacell-51WF structural foam. International Journal of Solids and Structures. 2000;37(43):6321-6341.

[90] Chai GB, Zhu S. A review of low-velocity impact on sandwich structures. Proceedings of the Institution of Mechanical Engineers, Part L: Journal of Materials Design and Applications. 2011;225(4):207-230.

[91] Stronge WJ. Impact mechanics: Cambridge University Press; 2004.

[92] Abrate S. Impact on composite structures: Cambridge University Press; 2005.

[93] Olsson R. Mass criterion for wave controlled impact response of composite plates. Composites Part A: Applied Science and Manufacturing. 2000;31(8):879-887.

[94] Cantwell WJ, Morton J. The impact resistance of composite materials—a review. Composites. 1991;22(5):347-362.

[95] Jones N. Structural impact: Cambridge University Press; 1989.

[96] Calladine CR, English RW. Strain-rate and inertia effects in the collapse of two types of energy-absorbing structure. International Journal of Mechanical Sciences. 1984;26(11):689-701.

[97] Taylor G. The use of flat-ended projectiles for determining dynamic yield stress. I. Theoretical considerations. Proceedings of the Royal Society of London Series A Mathematical and Physical Sciences. 1948;194(1038):289-299.

[98] McKown S, Shen Y, Brookes WK, Sutcliffe CJ, Cantwell WJ, Langdon GS. The quasi-static and blast loading response of lattice structures. International Journal of Impact Engineering. 2008;35(8):795-810.

[99] Lee S, Barthelat F, Hutchinson JW, Espinosa HD. Dynamic failure of metallic pyramidal truss core materials – Experiments and modeling. International Journal of Plasticity. 2006;22(11):2118-2145.

[100]Qin QH, Zhang JX, Wang TJ. Low velocity impact response of lightweight metal sandwich panel with corrugated core. Materials Research Innovations. 2011;15(1):198-200.

[101]Vaziri A, Xue Z, Hutchinson JW. Metal sandwich plates with polymer foam-filled cores. Journal of Mechanics of Materials and Structures. 2006;1(1):97-127.

[102]Lapczyk I, Hurtado JA. Progressive damage modeling in fiber-reinforced materials. Composites Part A: Applied Science and Manufacturing. 2007;38(11):2333-2341.

[103] Zhang YC, Zhang SL, Wang ZL. Crush behavior of corrugated cores sandwich panels. Advanced Materials Research. 2011;217:1584-1589.

[104]Kueh C, Navaranjan N, Duke M. The effect of in-plane boundary conditions on the post-buckling behaviour of rectangular corrugated paperboard panels. Computers and Structures. 2012;104:55-62.

[105]Sarawit AT, Kim Y, Bakker MCM, Peköz T. The finite element method for thin-walled members-applications. Thin-walled Structures. 2003;41(2–3):191-206.

CHAPTER III: EXPERIMENTAL PROCEDURE

3.1 Introduction

This chapter focuses on the experimental procedures used in this study to investigate the mechanical properties of the different types of material studied here. The test methods used in this study include both static and dynamic compression tests. Tests were conducted on an aluminium alloy, a glass fibre reinforced plastic (GFRP) and a carbon fibre reinforced plastic (CFRP). Initial tests focused on the influence of the number of unit cells on the fracture properties of the sandwich structure. Following this, tests were conducted on corrugations with increasing wall thicknesses, at both static and dynamic loading rates. The study also investigates the influence of filling the corrugated-core structures with foam core in order to increase their energy absorption capability. An overview of the materials and fabrication procedures used in this project is also given in this chapter. Details of the tests, including the tensile tests, shear tests, Arcan tests and static and dynamic compression tests are also reported.

3.2 Design and Fabrication of Corrugated-core

The corrugated-cores were prepared using a 45^{o} triangular profile with a 210 mm by 240 mm effective area of fabrication. Figures 3.1 and 3.2 show the mould which was made from mild steel. Each unit cell had a nominal height of 10 mm and a length of 20 mm. The cores using the corrugated 45^{o} profile, as the female mould (lower profile) to hold the composite prepreg (or flat material) and as the male mould (upper profile) pressed the material to form the shape of a triangular profile.

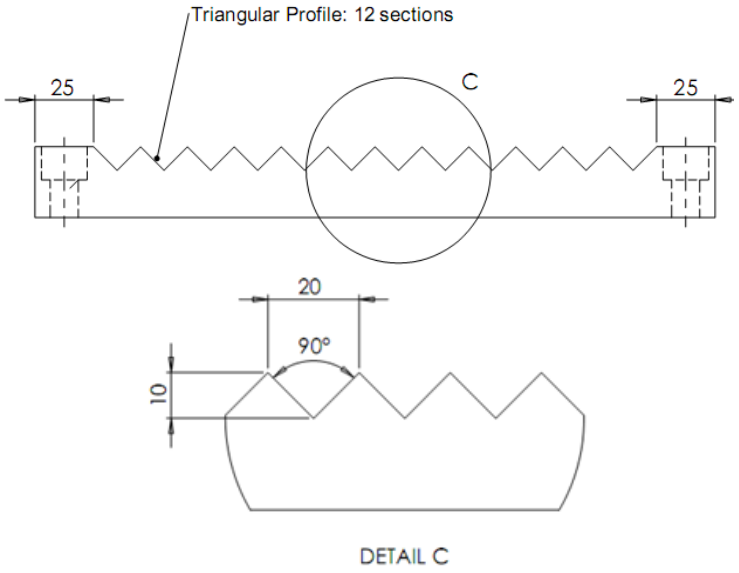

Figure 3.1: Drawing of corrugated mould design.

The mould was manufactured to a high precision using a computer-controlled numerical milling machine (CNC). The apex of each triangular unit in the mould was relatively sharp, having an average diameter of approximately 0.1 mm, as shown in Figure 3.3. This does result in a small region of resin enrichment in the corners, however, this was not deemed to be significant. A 45^{o} corrugation was selected since it gives an optimum shear modulus with respect to tensile and bending stiffness of the core structure [1]. Appendix A shows the detailed drawings of the mould.

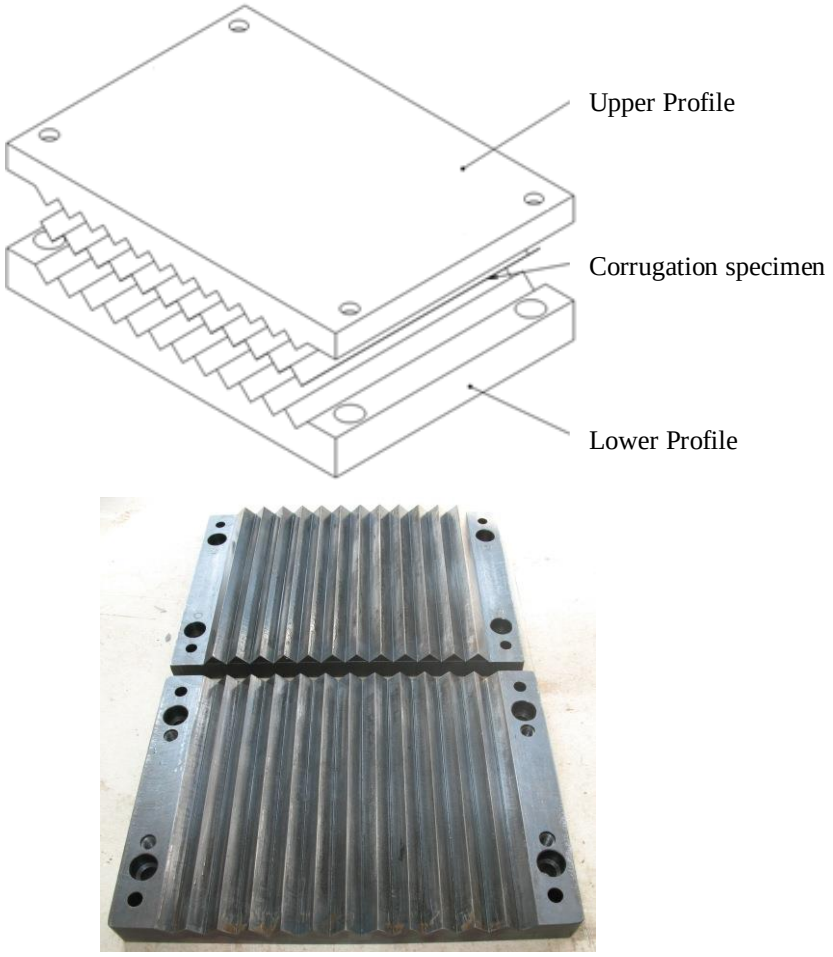

Figure 3.2: Assembly drawing and photograph of the corrugated mould.

A precise fabrication procedure was followed to control the quality of the corrugated-core specimens. A roll of composite prepreg was taken out from the freezer and then placed on a clean flat surface as shown in Figure 3.4. The prepreg was cut according to 200 mm x 150 mm in warp and weft directions, respectively.

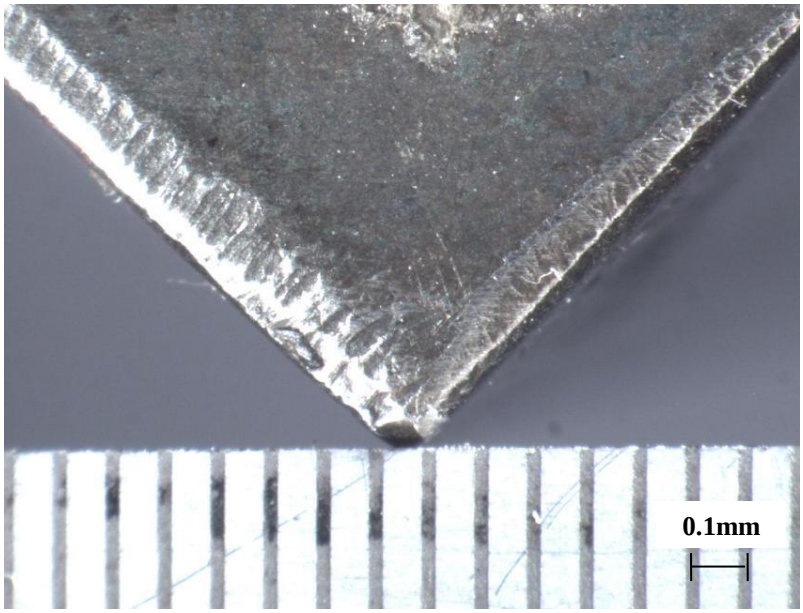

Figure 3.3: The apex of the triangular unit in the mould.

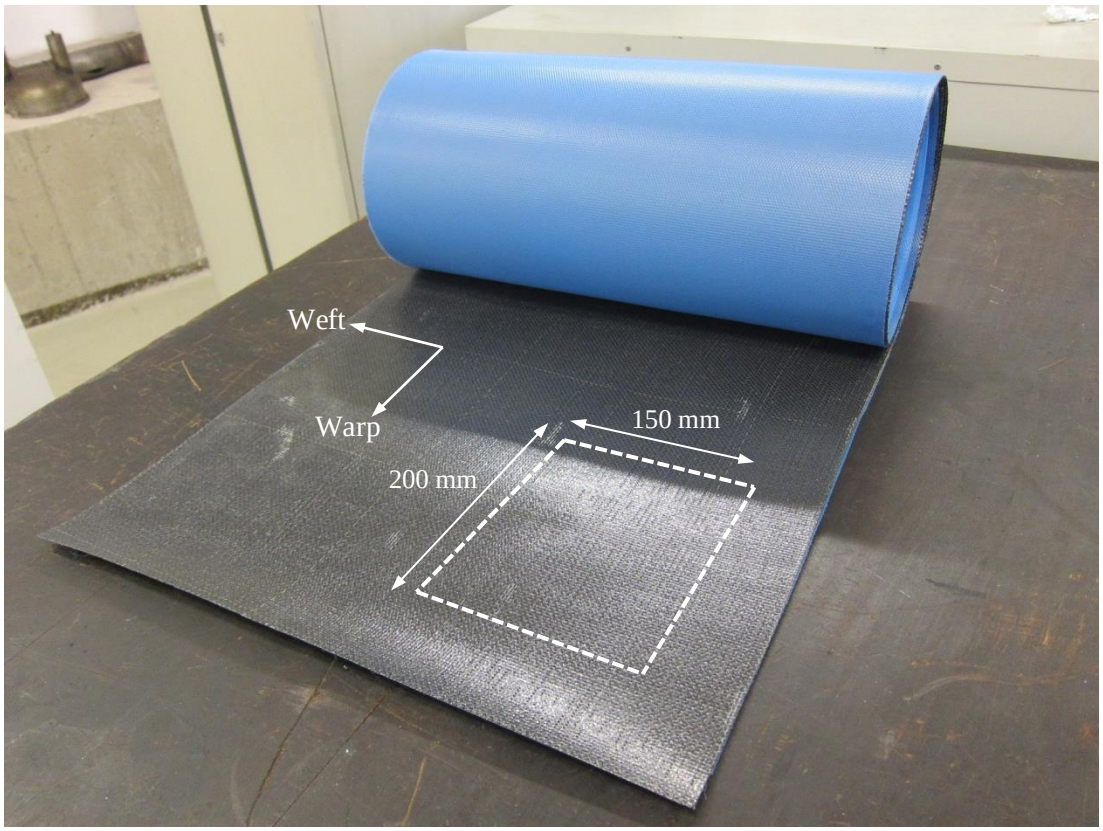

Figure 3.4: A roll of composite prepreg in the as-received condition before cutting to size of 200 mm by 150 mm.

During manufacture, the prepreg was placed between the upper and lower moulds, and separated with a sheet of thin polypropylene (PP) film (Xiro Collano AG). The PP film was used to separate the prepreg and the mould surfaces to ensure easy demoulding at the end after curing. The prepreg was then cured in a hot press at a curing temperature, T_C, with a dwell time of t_{dwell} minutes, before cooling down to room temperature, T_R, or 60°C according to the manufacturer's recommended processing cycle, as illustrated in Figure 3.5. After the corrugated-core profile was fully cured, it was taken out from the mould and then bonded to two skins using an epoxy adhesive. Then, the sandwich structure was heated in the oven at 120°C for 60 minutes, to cure the adhesive. The structure was then cut to the required specimen dimensions for testing.

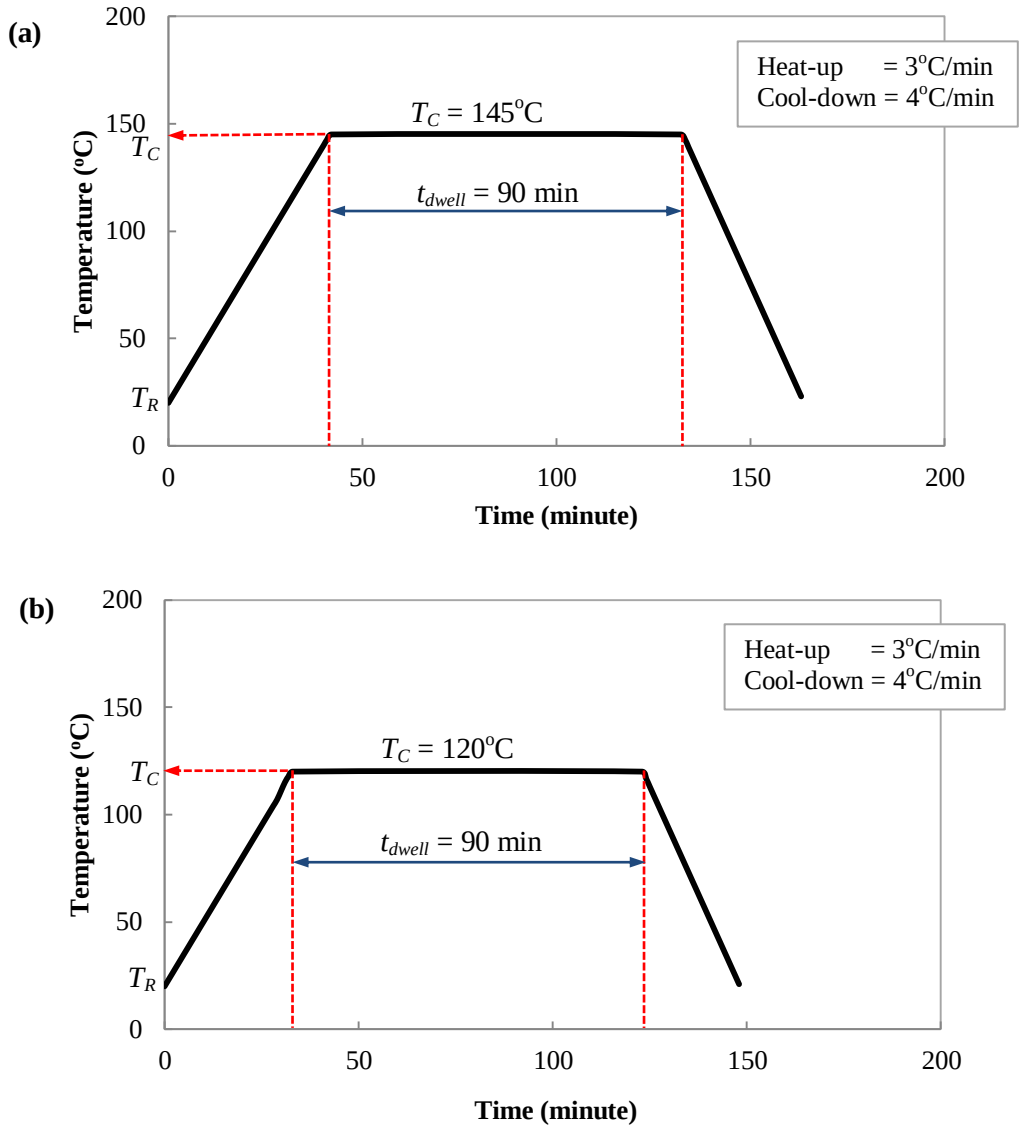

Figure 3.5: Curing profile for (a) GFRP and (b) CFRP prepregs.

Figure 3.6 shows the Meyer hot press machine used for manufacturing the test specimens.

Figure 3.6: Photograph of the Meyer hot press machine.

3.2.1 Aluminium Alloy

Aluminium alloy 2024 is an aluminium alloy with copper and magnesium as the alloying elements. It has been used in many applications, such as in aerospace primary structures, requiring a high strength to weight ratio, as well as a good fatigue resistance. In this study, the aluminium alloy 2024-O (AL) was used. The general properties of aluminium reported in the literature [2] are a density of 2780 kg/m^3, with a melting point of approximately 550^{o}C, a tensile strength of 185 MPa, an elastic modulus of 73.1 GPa and a strain of failure between 20% to 22%. To ensure that the raw material was not damaged during the fabrication process, the plain aluminium sheet was fed one unit cell at a time across whilst pressing after each step until a complete corrugation profile was achieved. The corrugated-core specimens were then measured to ensure that they satisfied the required dimensions. Note that springback effects were noted in the aluminium following the fabrication process. These effects were neglected in this study.

3.2.2 Glass Fibre Reinforced Plastic

The glass fibre reinforced plastic (GFRP) used here was supplied by Gurit AG (Stesapreg EP127-44-40). Note that density of a laminated GFRP is 1750 kg/m^3. Prior to manufacture, the woven prepreg (four harness satin or Crowfoot) was cut to dimensions of 150 mm x 200 mm and then layed up, to give the required thickness. Sheets of thin (PP) films were then placed on each surface of the prepreg. The prepreg was subsequently placed in a hot press (Meyer hot press machine) and heated to a temperature of 145^{o}C under a pressure of 6 bar for 90 minutes. The temperature was monitored by a digital thermocouple inserted between the prepreg plies.

3.2.3 Carbon Fibre Reinforced Plastic

A woven carbon fibre reinforced plastic (CFRP) supplied by Gurit AG (EP121-C15-53) was also used in the study. Note that density of a laminated CFRP is 1390 kg/m^3. During the manufacturing process, the plain woven prepreg was cut into dimensions 150 mm x 200 mm and placed between two 60 µm thick PP films. The prepreg was then placed in a hot press and heated to a temperature of 120^{o}C under a pressure of 6 bar for 90 minutes. The temperature was monitored by thermocouples inserted between the prepreg plies.

3.3 Specimen Preparation

In fabrication method adopted here, the material was placed between the male and female moulds, and then cured using the hot press according to the manufacturer's recommended processing cycle, as previously discussed.

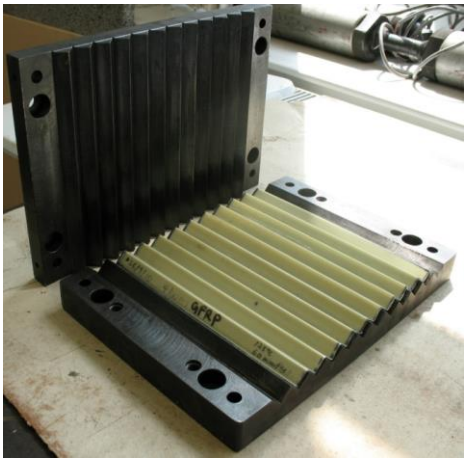

Figure 3.7: Photograph of specimens following removal from the mould.

Figure 3.7 shows a corrugated composite core after curing, and removal from the mould. The upper and lower skins of the sandwich structures were made from the same material as the core. Figure 3.8 shows a schematic of stacking orientation and cutting direction of the composite specimens. A summary of the thicknesses of the corrugations and the processing time to manufacture the skins is given in Table 3.1. For the CFRP and GFRP specimens, the skins were removed from the mould after the hot press had cooled to a temperature below 60^{o}C and then visually inspected for any defects.

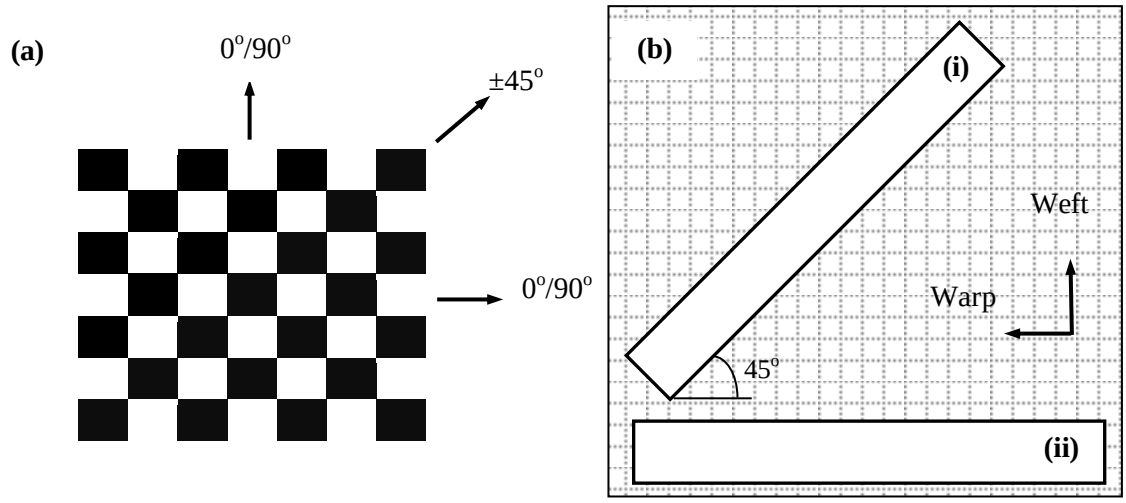

Figure 3.8: (a) Schematic of the stacking orientations of the woven composite and (b) cutting the cured specimen into (i) ±45^{o} and (ii) 0^{o}/90^{o} layers.

Table 3.1: Summary of processing parameters used for manufacturing the skins of the sandwich structures.

Material	**No. of plies**	**Average Thickness (mm)**	**Heating Temperature (^{o}C)**	**Pressure (bar)**	**Curing Time (min.)**	**Cool-down rate (^{o}C/min.)**
AL	1	0.5 ± 0.01				
GFRP	4	0.4 ± 0.03	145	4	90	4
CFRP	2	0.5 ± 0.05	120	4	90	4

The core was then bonded to the two skins using an epoxy adhesive. The Araldite 420 A/B structural adhesive used here was supplied by Hunstman Advanced Materials GmbH and has a lap shear strength (LSS) of 43 MPa. It is recommended

for both metal and polymer bonding. The adhesive was laid on the apex of the core, followed by the upper and lower skins. A moderate weight was placed on top of the sandwich structure to ensure good contact between the core and skins, as well as aligning the skins parallel to each other. The sandwich structure was then heated in an oven at a temperature of 120^{o}C for approximately one hour to cure the adhesive. The structure was then cut into specimens with dimensions of 100 mm length and 25 mm width.

Figure 3.9 shows a corrugated-core specimen consisting of five repetitions of an identical unit cell. The consistency of the dimensions in each unit cell after fabrication is clearly important. An exact measurement and consistent identity of unit cell are important to ensure the reliability of the repeated experimental results.

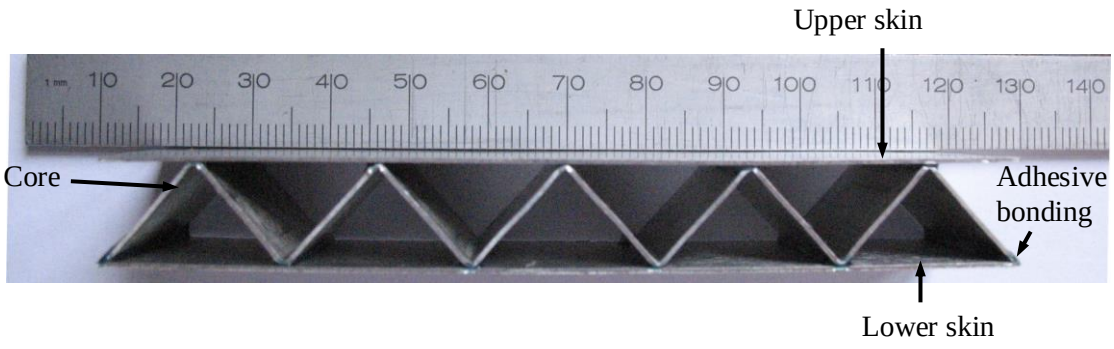

Figure 3.9: Five identical unit cells of an AL corrugated-core sandwich structure.

The corrugated-core unit cell is based on a triangular profile. The geometric parameters shown in Figure 3.10 are annotated as follows: θ and β are the internal angles of a unit cell in the corrugated-core sandwich structure; h_c is the height of the core; L is the length of the strut member; H_U and H_L are thicknesses of upper and lower of the skins, respectively; H is the average thickness of the inclined core members and is therefore equal to the wall thickness; x is the length of the core; and w is the width of the specimen. Due to the predetermined mould design, the value of x was 20 mm while θ and β were set equal to 45^{o} and 90^{o}, respectively.

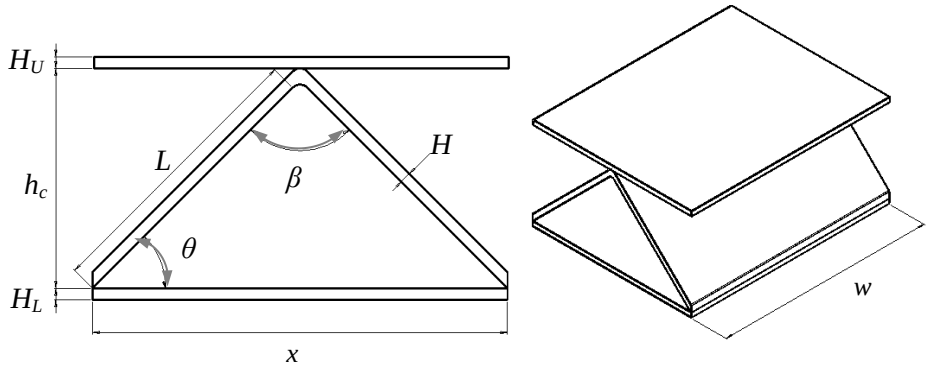

Figure 3.10: The geometry of unit cell of the corrugated-core sandwich structure.

In preparation of the test specimens, the value of w was set equal to 25 mm width. The corrugated-cores were cut to yield specimens with five different numbers of unit cells, as shown in Figure 3.11.

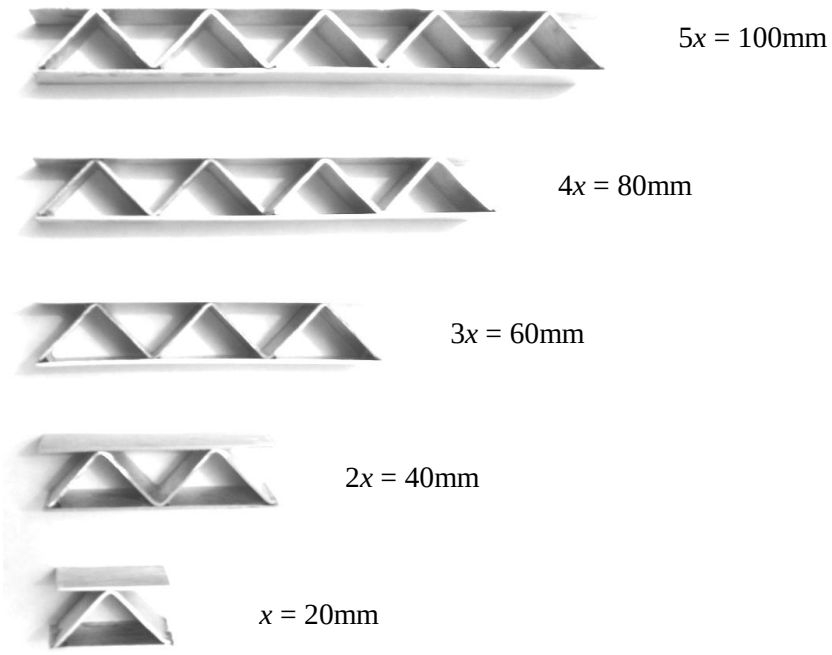

Figure 3.11: Photographs of the five different number of unit cells in the AL sandwich specimens.

To investigate the influence of filling the corrugations with foam, a liquid polyurethane (PU) rigid foam, LDP40 supplied by Polycraft Ltd., was introduced into the core. The use of the liquid foam chemical to fill the empty spaces of

corrugated-core area is more practical than cutting foam sheets into a triangular shape and then inserting the resulting prism blocks between the unit cells. Two chemical components are used to manufacture the foam. Component A is termed a polyol blend (clear liquid) and component B is called Isocyanate (brown liquid). Here, both chemical components were mixed manually, and then poured into the five unit cells. Figure 3.12 shows a conventional corrugation as well one with a semi-filled core and one with a fully-filled core.

Figure 3.12: Carbon fibre corrugated-core sandwich structures (a) without foam, (b) semi-filled foam and (c) fully-filled with foam.

In order to investigate the properties of the PU foam, the foam was cut into 25 mm cubes. The density of the foam was measured according to the ASTM D1622 standard [3]. Figure 3.13 shows the free-rise rigid PU foam following manufacture and also a cube-shaped specimen with a measured density of 40 ± 5 kg/m^3.

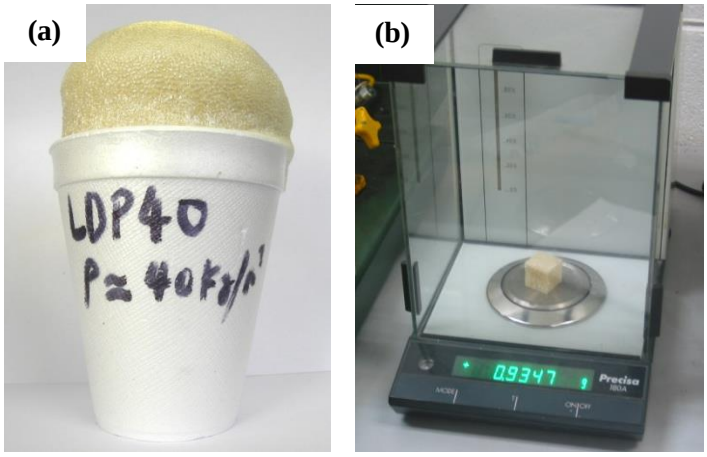

Figure 3.13: (a) Free-rise in the rigid PU foam and (b) a cube-shaped foam block on the weight scale.

3.4 Mechanical Properties of Materials

The material properties of the constituent materials are one of the most important factors in determining the deformation characteristics of a structure. The material properties of corrugated-cores are commonly obtained from a standard tensile test. This type of test generally involves axially loading a specimen at both ends at a constant strain rate. In the present study, all of the static tests are conducted on an Instron 4204 testing machine. This machine is an electromechanical universal testing machine in which the forces are applied by a moving crosshead movement driven by a screw mechanism. Load-displacement traces are directly plotted from the measured loads and displacements.

3.4.1 Tensile Test on the Aluminium Alloy

A standard dog-bone shaped aluminium specimen of length, L_c was prepared based on the BS 10002-1[4] as illustrated in Figure 3.14. The dimensions of the specimen were 20 mm x 140 mm and a nominal thickness of 0.5 mm. The tensile tests were carried out at a crosshead speed of 1 mm per minute up to fracture. An extensometer with the original gauge length, GL = 50 mm was placed onto the specimen to record the extension. At least three tests were performed in order to obtain reliable data.

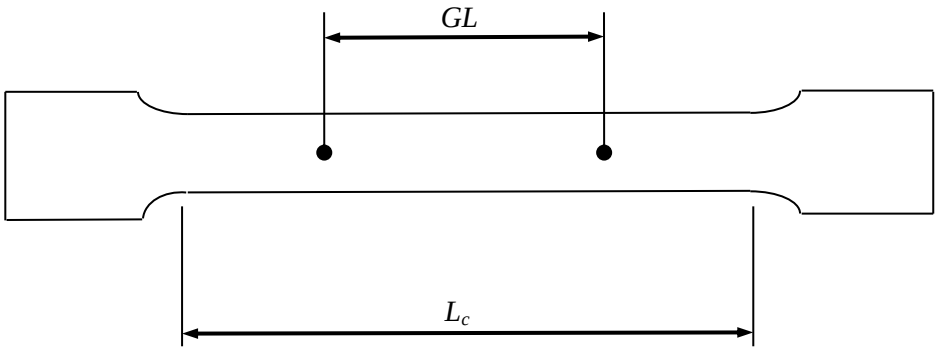

Figure 3.14: Tensile test geometry of the metal specimen.

3.4.2 Tensile Tests on the Composites

Tensile tests were also conducted on the GFRP and CFRP composite laminates in accordance with the standard BS 527-4 [5]. The specimens were prepared by bonding aluminium end-tabs as shown in Figure 3.15.

Figure 3.16 shows the tensile and in-plane shear test specimens, using a minimum of three test specimens (dimensions: 250mm length x 25 mm width x 1 mm thick). The

tensile tests were performed using the Instron 4204 testing machine. Again an extensometer with a gauge length, *GL* = 50 mm was attached to the specimen in the longitudinal direction. Tests were undertaken at a constant crosshead speed of 1 mm per minute.

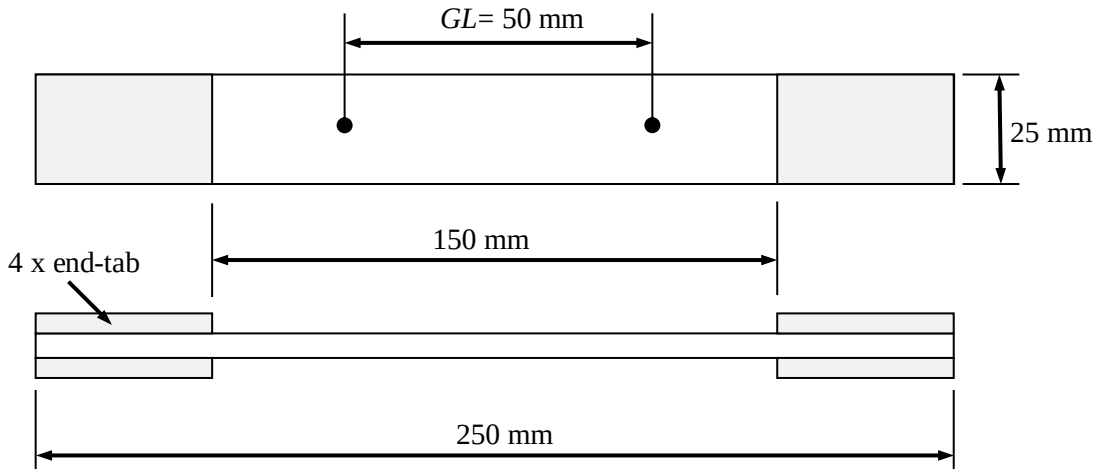

Figure 3.15: Tensile test geometry for a composite specimen.

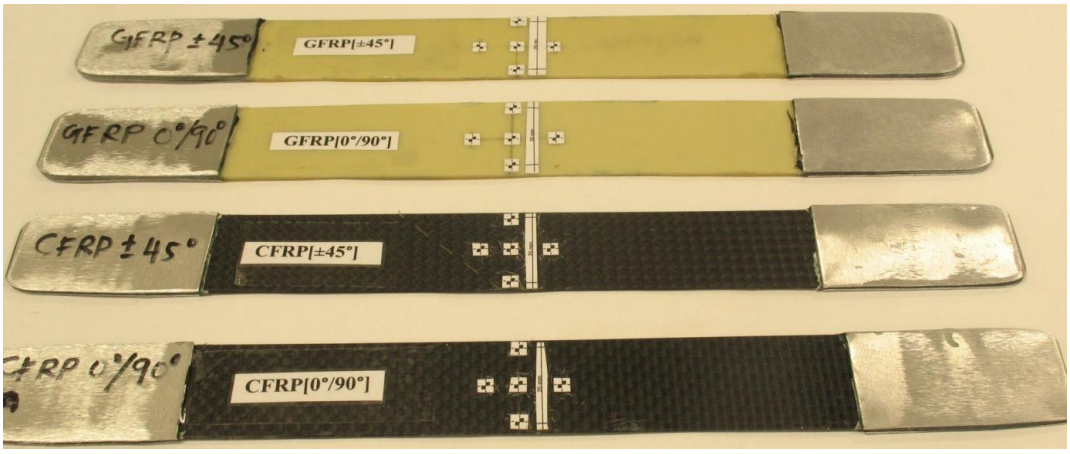

Figure 3.16: Composite specimens for tensile and in-plane shear tests.

In order to measure the Poisson's ratio, a digital camera was placed in front of the tensile specimen to capture the relative displacements in the longitudinal and transverse directions from four targets placed at the target. A digital NIKON D5000 camera was programmed using a personnel computer to capture images at a frequency of one frame per second to synchronise with an Instron machine recording data at the same frequency.

The images were processed using the motion analysis software, ProAnalyst. This digital technique was used to avoid using 90° bi-axial strain gauges to measure the Poisson's ratio. Figure 3.17 (a) shows the set-up for a tensile test on a CFRP specimen and (b) the positioning of the target points in the *x* and *y* directions. Two target points were fixed in the longitudinal direction (T_3 and T_4), and two target points were fixed in transverse direction (T_1 and T_2). The targets were positioned 20 mm apart in the *x* and *y* directions.

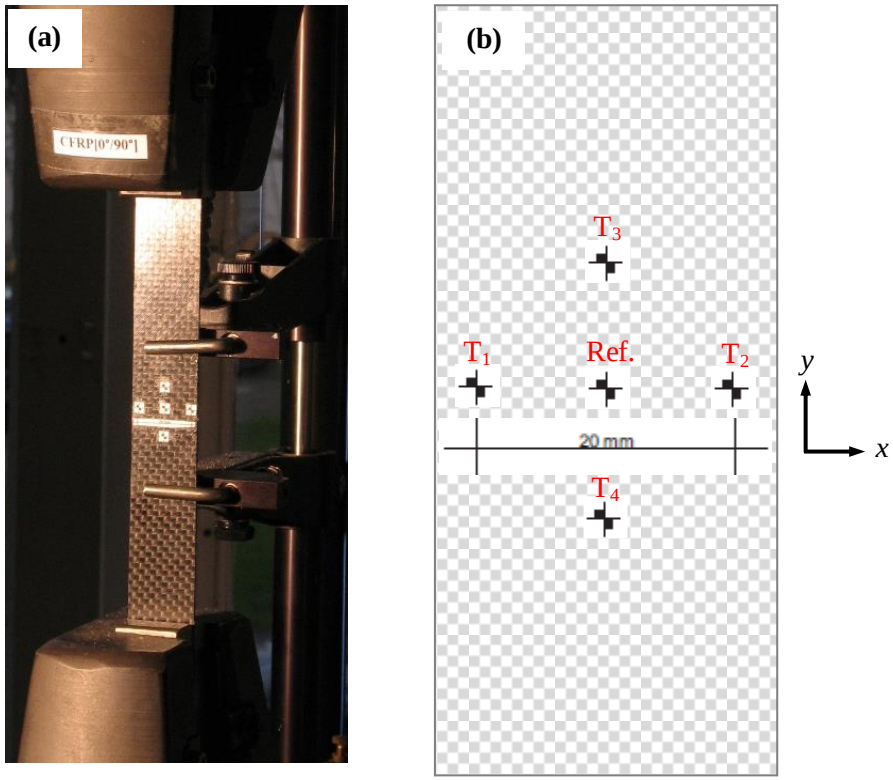

Figure 3.17: (a) Tensile test set-up and (b) the configuration of the five target and tracking points in the longitudinal and transverse directions. The middle target point is the reference point.

3.4.3 In-plane Shear Test on Composites

A series of in-plane shear tests were undertaken on the composites to obtain the shear strength and shear modulus values. The tests were conducted on an Instron 4204 in the tensile direction. The specimens were prepared by orientating the plies at ±45° and cut to similar dimensions as the standard tensile test coupon. The test procedure was similar to that adopted for the tensile specimens discussed above. Figure 3.18 shows the set-up for the in-plane shear test.

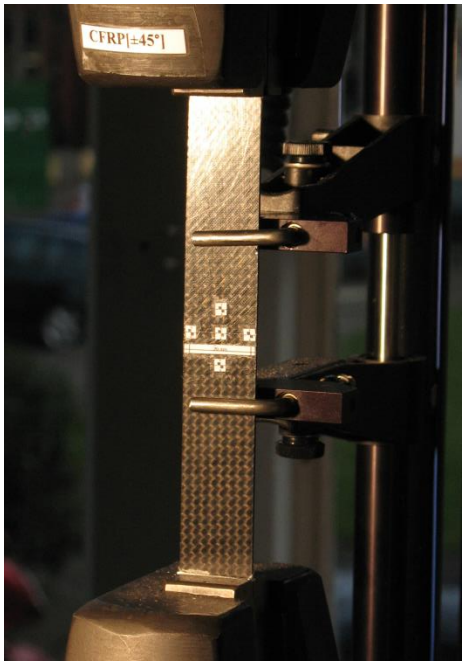

Figure 3.18: Photo of an in-plane shear test on a composite specimen.

3.4.4 Compression Tests on the Rigid PU Foam

Compression tests on the rigid PU foam were conducted using an Instron 4204 testing machine according to the ASTM D1621 standard [6]. All specimens were cubic in form with overall dimensions of 25 mm x 25 mm x 25 mm. Figure 3.19 shows a typical specimen placed between the platens of the test machine. The specimens were deformed at a static loading rate of 1 mm per minute.

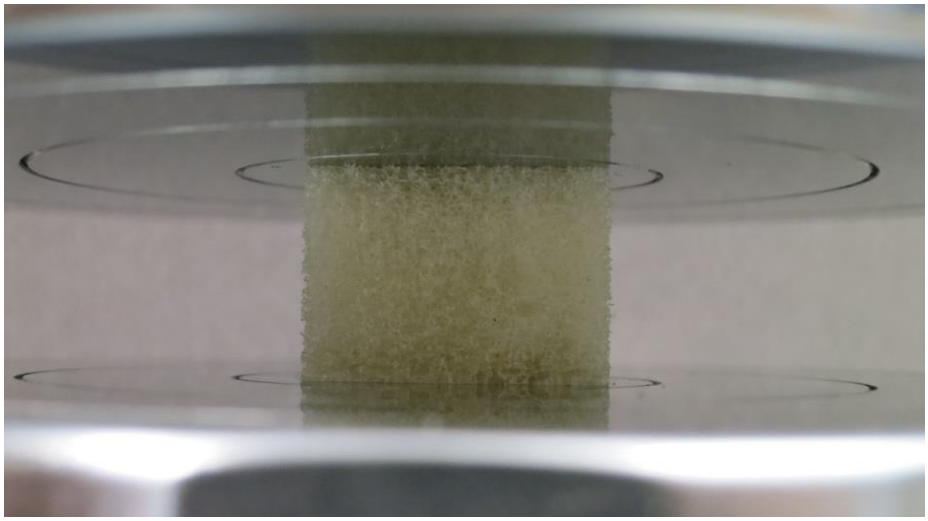

Figure 3.19: The rigid PU foam under compression loading.

3.5 Static Compression Testing

The static compression tests on the corrugated-core sandwich structures were conducted using an Instron 4204 testing machine. All of the test specimens were prepared in a rectangular form, being based on differing numbers of unit cells and thicknesses, a summary of sandwich specimens tested in this research is shown in Table 3.2.

The specimen was placed between the platens of the machine as shown in Figure 3.20 and was deformed by applying a uniform lateral compressive load at a quasi-static rate of 1 mm per minute. At least three tests were carried out on each specimen type. Since the main area of interest was in the deformation behaviour of the structures, a high-resolution displacement measurement system was used to record the displacement data as well as to identify the failure modes. The previous method used to record the displacement data was adopted in this testing, with the frequency being set to one frame per second. As before, the images were processed using the ProAnalyst software package.

Here, a digital camera was located in front of the sandwich structure to capture displacement of six targets, with three targets being located equally spread on the upper and lower platens. The first three targets (T_1, T_2 and T_3) correspond to the moving points and the targets attached at the lower platen (T_4, T_5 and T_6) are the reference points. Three targeted points were used to validate the displacement in the vertical direction relative to machine displacement, and to monitor any sliding motion (shear displacement) that occurred in contributing initial failure of the struts. The load-displacement trace from the testing machine was recorded until the specimen had been fully crushed.

Table 3.2: Summary of the aluminium alloy 2024-O, GFRP and CFRP structures investigated during the quasi-static compression study.

Material	**Core ID**	**No. of unit cell**	**No. of plies**	**Average core width, *w* (mm)**	**Average core length, *x* (mm)**	**Average wall thickness, *H* (mm)**	**Average panel density, ρ(kg/m^3)**
Aluminium Alloy 2024-O	AL1	1		25	20	0.50	459
	AL2	2		25	40	0.50	459
	AL3	3		25	60	0.50	459
	AL4	4		25	80	0.50	459
	AL5	5		25	100	0.50	459
Glass Fibre Reinforced Plastic	GF2U1	1	2	25	20	0.19	228
	GF2U2	2	2	25	40	0.19	218
	GF2U3	3	2	25	60	0.19	213
	GF2U4	4	2	25	80	0.19	210
	GF2U5	5	2	25	100	0.19	202
	GF3U5	5	3	25	100	0.31	220
	GF4U5	5	4	25	100	0.43	238
	GF5U5	5	5	25	100	0.50	261
	GF7U5	5	7	25	100	0.77	292
	GF10U5	5	10	25	100	0.98	363
	GF2W50	5	2	50	100	0.19	214
	GF2W75	5	2	75	100	0.19	205
	GF2W100	5	2	100	100	0.19	202
Carbon Fibre Reinforced Plastic	CF2U1	1	2	25	20	0.50	260
	CF2U2	2	2	25	40	0.50	259
	CF2U3	3	2	25	60	0.50	256
	CF2U4	4	2	25	80	0.50	248
	CF2U5	5	2	25	100	0.50	244
	CF3U5	5	3	25	100	0.89	296
	CF4U5	5	4	25	100	1.03	340
	CF5U5	5	5	25	100	1.10	350
	CF6U5	5	6	25	100	1.25	390
	CF2W50	5	2	50	100	0.50	249
	CF2W75	5	2	75	100	0.50	247
	CF2W100	5	2	100	100	0.50	243

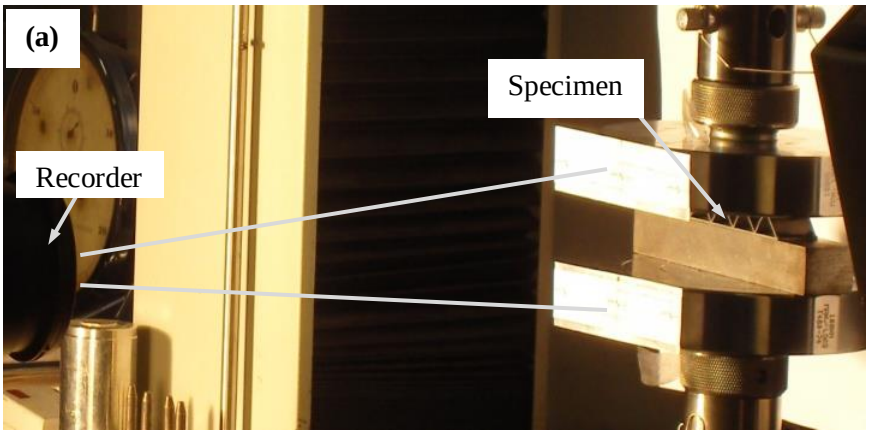

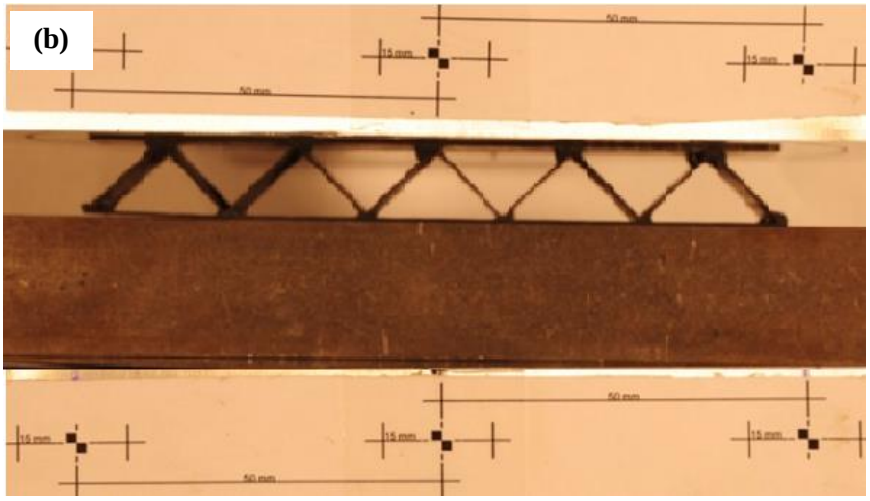

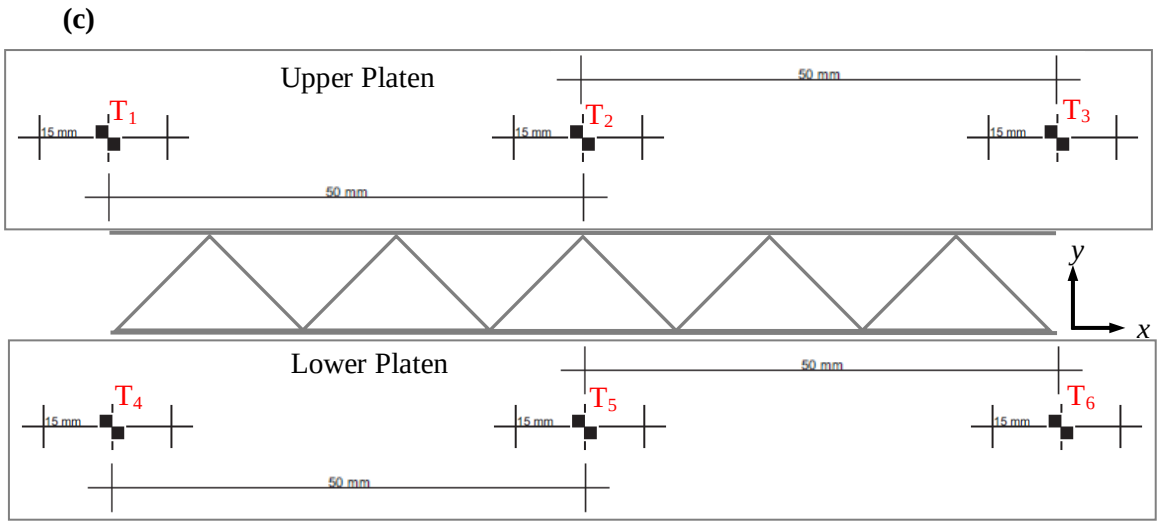

Figure 3.20: (a) Photograph of the compression test set-up and the displacement measurement system, (b) front view of the specimen test set-up, (c) schematic of target points for measuring the displacement during the quasi-static compression test.

Additionally, in order to study the effect of strain rate, several AL, GFRP and CFRP structures with H = 0.5 mm were subjected to compression at three crosshead displacement rates of 1, 10 and 100 mm per minute, respectively. Table 3.3 summarises the specimen geometry and machine speeds. Table 3.4 presents the dimensions of the composite corrugated-core specimens with or without filled foam.

Table 3.3: Summary of the aluminium alloy 2024-O, GFRP and CFRP structures used for test at three different compression strain rates.

Material	**Core ID**	**Crosshead speed (mm/minute)**	**No. of plies**	**Average core width, *w* (mm)**	**Average core length, *x* (mm)**	**Average wall thickness, *H* (mm)**	**Average panel density, ρ(kg/m^3)**
AL	ALS1	1		25	100	0.5	459
	ALS10	10		25	100	0.5	459
	ALS100	100		25	100	0.5	459
GFRP	GFS1	1	5	25	100	0.5	261
	GFS10	10	5	25	100	0.5	261
	GFS100	100	5	25	100	0.5	261
CFRP	CFS1	1	2	25	100	0.5	244
	CFS10	10	2	25	100	0.5	244
	CFS100	100	2	25	100	0.5	244

Table 3.4: Summary of the GFRP and CFRP corrugated sandwich structures filled with PU foam used for quasi-static compression testing.

Material	**Core ID**	**Foam core**	**No. of plies**	**Average core width, *w* (mm)**	**Average core length, *x* (mm)**	**Average wall thickness, *H* (mm)**	**Average panel density, ρ(kg/m^3)**
GFRP	GFXPU	-	5	25	100	0.5	261
	GFPUS	Semi	5	25	100	0.5	280
	GFPUF	Full	5	25	100	0.5	310
CFRP	CFXPU	-	2	25	100	0.5	244
	CFPUS	Semi	2	25	100	0.5	260
	CFPUF	Full	2	25	100	0.5	281

3.6 Arcan Test

The Arcan test [7, 8] was used to investigate the failure behaviour of corrugated-core specimens under combined shear and compression/tensile loading. The test was used to derive a new bi-axial loading failure criterion under for the corrugated-cores. The rig consists of two pairs of plane semi-circular loading plates with non-symmetric cutouts, as shown in Figure 3.21.

The specimen was attached to these plates via loading platens. The two pairs of loading plates were loaded by the universal test machine in the compression loading direction. The array of bolt holes in the loading plates allows the loading plates to be attached to the grips at different orientations. This allows a range of values of the angle α (from 0^o to 90^o with 11.25^o increments for each bolt hole) between the plane of the specimen and the loading direction, and hence a variation in the ratio $\tan(\alpha)$ of compression to shear loads applied to the specimen.

Due to limitations in the dimensions of the 100 mm x 80 mm loading platen, the corrugated-core specimens were prepared by cutting the core to 25 mm wide and 90 mm long, as shown in Figure 3.22. Although the aim of the test is to examine the behaviour of the corrugated-core only, the skins were not bonded to the core during the test. Therefore, the skins do not affect the behaviour of the core in the rig, as the loading platens acted as real skins. The core was bonded inside five grooves (with a 0.1 mm depth) in each loading platen, using epoxy adhesive Araldite 420A/B. The grooves were introduced to firmly hold the sharp edges of the core, and to ensure a consistent thickness of the adhesive. The specimen was then placed in an oven at 120^oC for 60 minutes in order to cure the adhesive. After cooling to room temperature, the upper and lower platens were bonded to the test specimen and then fixed to the semi-circular loading plates. Loading was monotonic up to failure, at a quasi-static rate of 0.5 mm per minute.

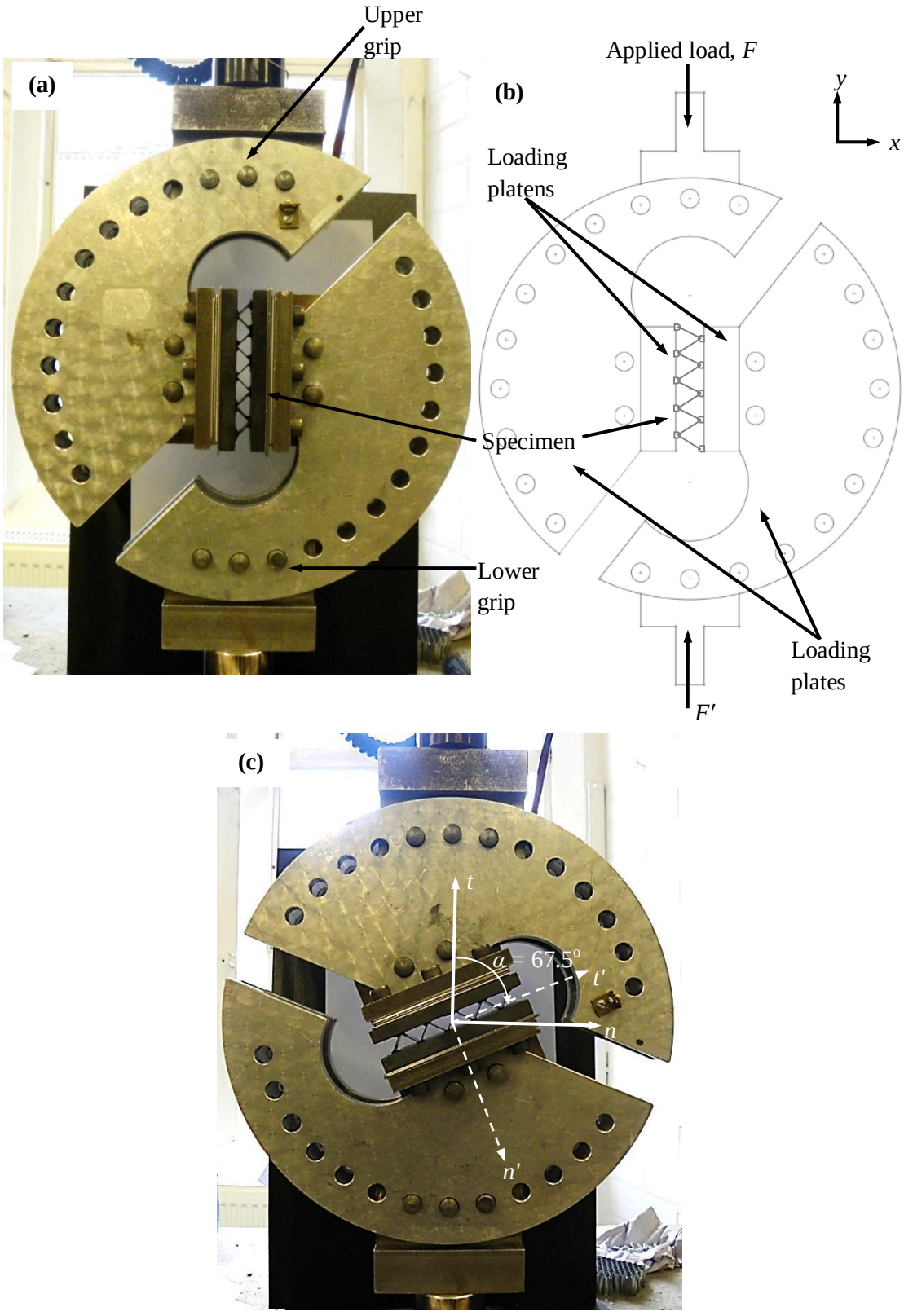

Figure 3.21: (a) Photo of the modified Arcan test rig, (b) a schematic diagram of the arrangement for a pure shear ($\alpha = 0^o$) Arcan test, and (c) at a 67.5° rotation to give a combined compression-shear loading condition.

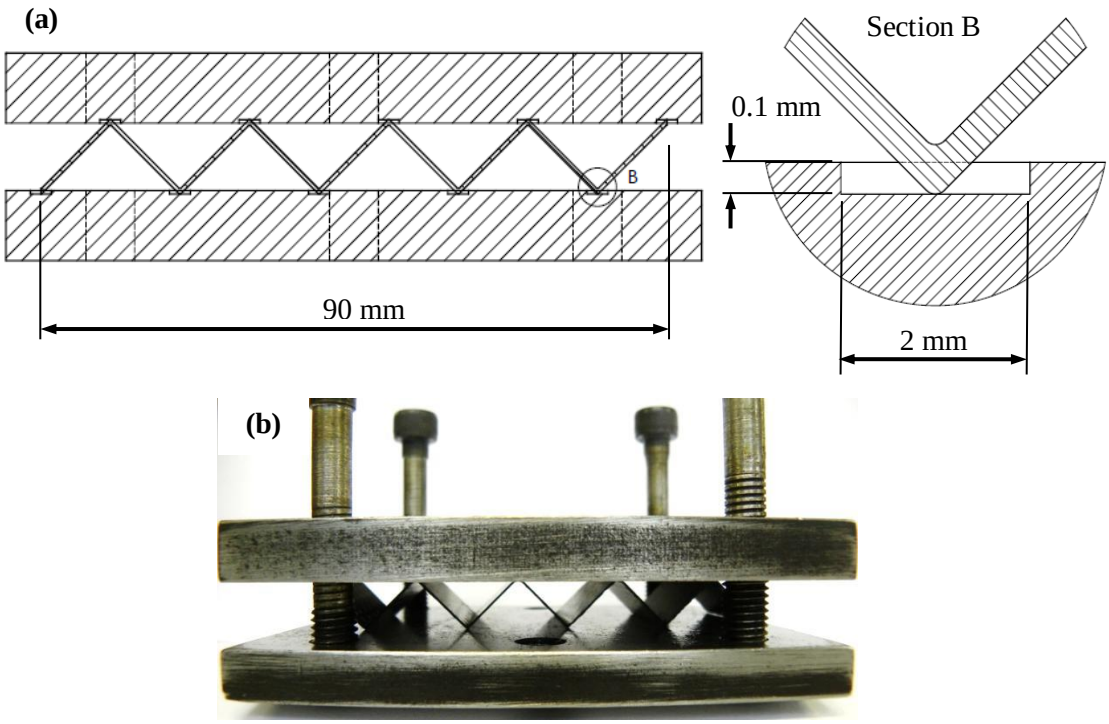

Figure 3.22: (a) Cross-section showing the bonding areas of the specimen to the loading platens, (b) a photo of a CFRP specimen bonded between two loading platens.

In order to cover a wide range of loading conditions from pure shear to pure compression, the tests were undertaken at five different angles, those being of $\alpha = 0^o$, 22.5^o, 45^o, 67.5^o and 90^o. At least three tests were carried out at each angle. A summary of the Arcan test procedure is given in Table 3.5.

Table 3.5: A summary of the specimen configurations for the Arcan tests.

Angle, α	**AL, H = 0.5 mm**	**5-ply GFRP, H = 0.5 mm**	**2-ply CFRP, H = 0.5 mm**
0^o	ALS0	GFS0	CFS0
22.5^o	ALS22.5	GFS22.5	CFS22.5
45^o	ALS45	GFS45	CFS45
67.5^o	ALS67.5	GFS67.5	CFS67.5
90^o	AL90	GF90	CF90

Two calibration tests were carried out prior to undertaking the Arcan test programme. To measure the initial stiffness accurately, a compliance test of the machine was used. Here, the two loading platens were bonded together using the same epoxy adhesive as used to bond the core structure to the loading platens. Load was applied until the adhesive failed. This test was then used to generate a linear load-displacement calibration curve, which was then subtracted from each test result to correct for unwanted displacements due to the elastic stiffness of the adhesive as well as that associated with the compliance of the test machine. A FORTRAN computer program was developed and used to get the corrected curves by means of subtracting the compliance curve (see Appendix B). All the displacement correction tests were conducted before commencing of the actual test specimen.

Next, the joint between the Arcan grips and the Instron testing machine included three pins, ensuring that both the horizontal and vertical displacement are controlled, as well as ensuring that the rotation of the grip is zero. Since the Arcan fixture is in a fully clamped configuration, rotations at the connecting points are prohibited. As a result, a horizontal load (P_h) is generated which needs to be accounted for in the analysis [9]. To measure the value of P_h, the vertical load applied to the corrugated core was measured directly from the machine load cell. The horizontal force was determined by conducting a simple pre-calibration exercise to obtain the transverse compliance of the rig [10].

Figure 3.23 shows the case where the compression load is applied with the loading platens set at 45^o and separated by a 0.08 mm-thick Teflon film (a nearly frictionless layer) to allow free sliding of the two platen surfaces. Two digital dial gauges were positioned at both sides of the loading plates to measure the relative horizontal displacement (d_h). With this test arrangement, the imposed vertical force and the generated horizontal load acting at the grips are equal and a relationship between the P_h and d_h can be established. Thus, it is a straightforward transformation exercise to establish the horizontal force that was developed during the test.

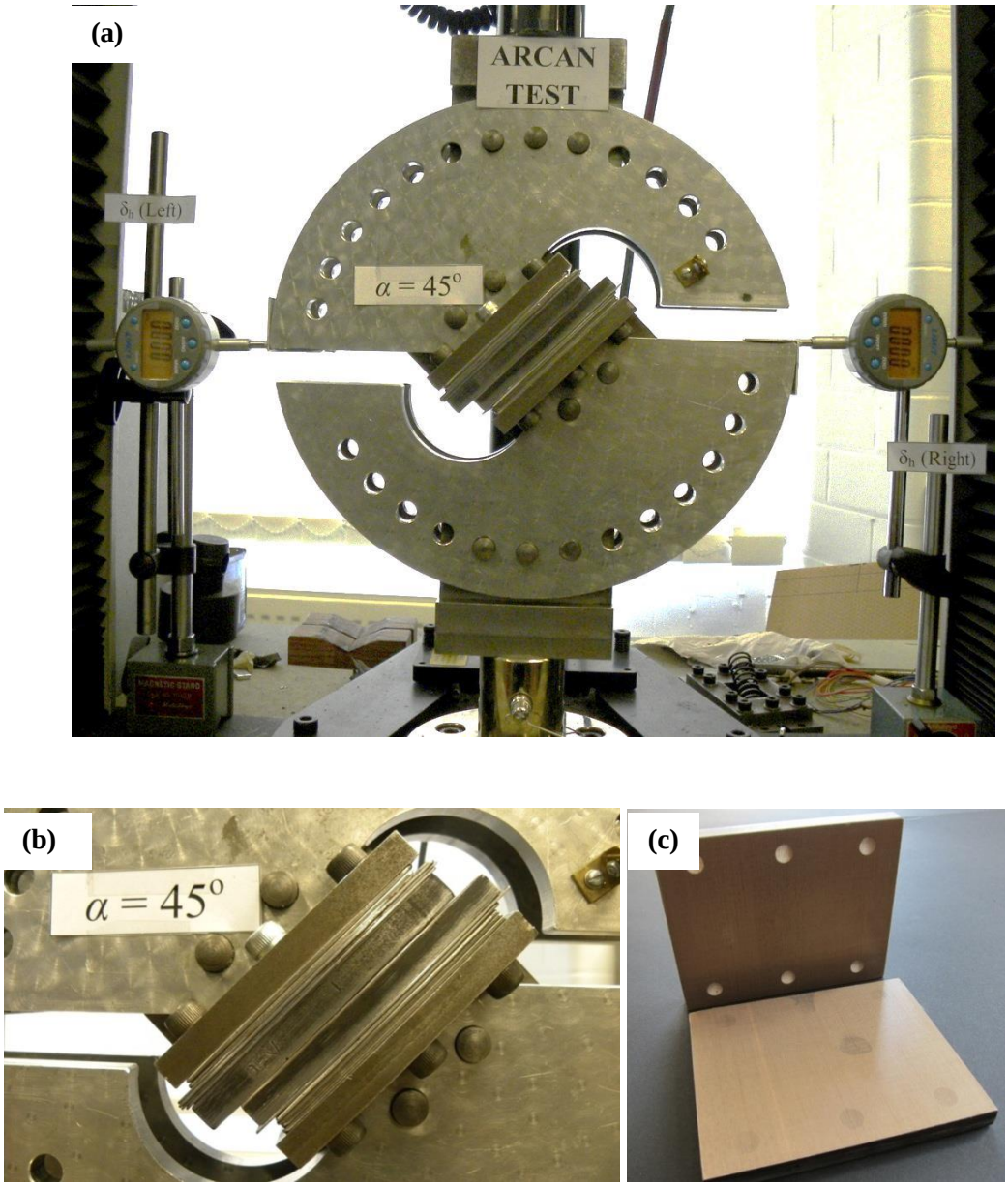

Figure 3.23: (a) Experimental test arrangement for the calibration test involving contact between two frictionless surfaces. The horizontal displacements are measured using two digital dial gauges, (b) close-up of the contact zone between the two frictionless platens and (c) the platen surfaces are covered with a Teflon film.

3.7 Low Velocity Impact Test

The low impact response of the corrugated-core sandwich structures were assessed using an instrumented drop-weight impact rig as shown in Figure 3.24. The impact test relies on the free fall of a known mass to supply the energy required to crush the specimen. The kinetic energy of the impactor can be adjusted by varying its drop height or its mass. In this study, a 1.247 kg impactor, *M* was used over a range of velocities of 0.99 ~ 4.43 m/s in order to characterise the dynamic response of the structures. A flat rectangular impactor, with dimensions of 120 mm x 80 mm, was used to strike the specimens.

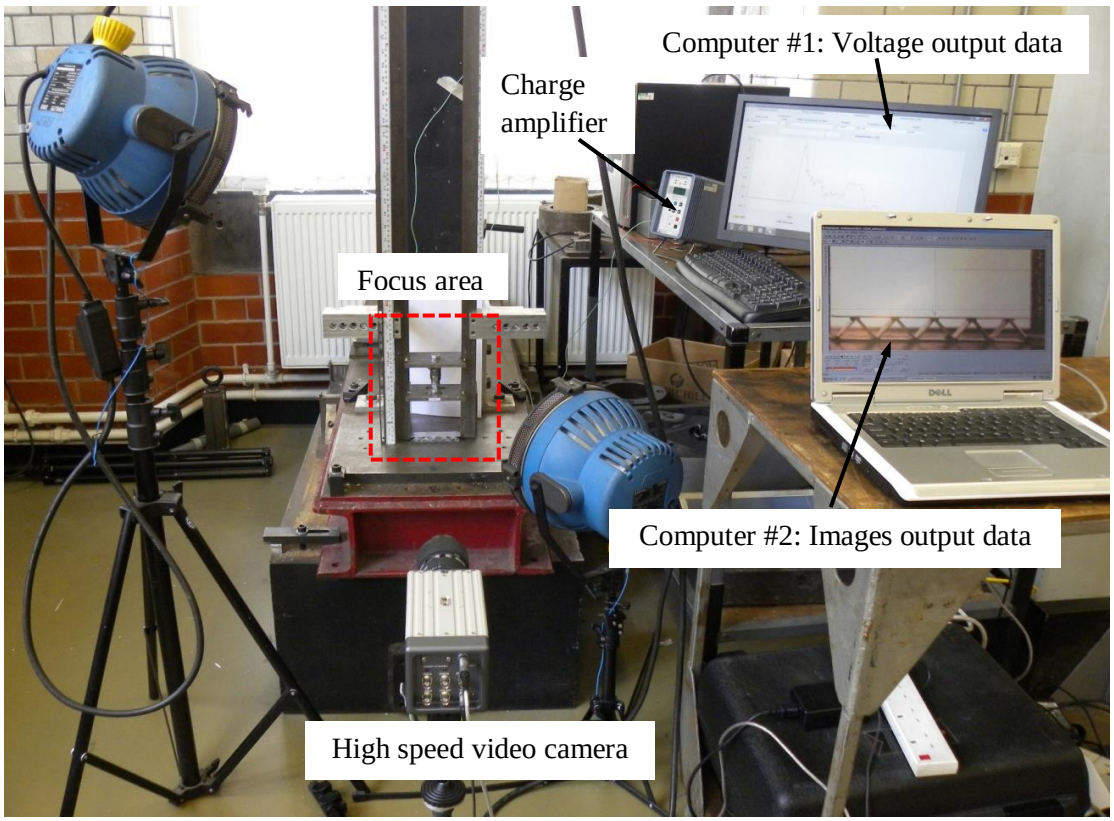

Figure 3.24: The instrumented drop-weight impact test set-up adopted for testing the corrugated-core sandwich structures.

The movement of the impactor was restricted by two rails with a ±0.5 mm clearance and was covered with grease from both sides of the rail. Note that frictionless contact was assumed between the guide rails and the impactor. When the impactor came in contact with the top surface, the specimen progressively crushed to the bottom. By neglecting the small rebound energy, it is assumed that the kinetic energy is completely absorbed by the specimen.

A 10 kN piezoelectric load cell (Kistler type 9321A) was used to measure the force-time histories during the impact events. The load cell was connected to a charge amplifier (Kistler type 5011) using an insulated coaxial cable. The load cell was initially held between two bolts to give pre-compression mode and then placed between the upper and lower steel plates, as shown in Figure 3.25.

Impacting the specimen initiated a signal to the load cell. The voltage signal generated by the load cell was amplified and filtered using the charge amplifier. The signal was then converted from an analog to a digital signal by a DAQ device (Measurement Computing, USB 1208HS) and recorded using the computer. The voltage was then converted to force (N) using a scale factor supplied by the manufacturer, as given in Table 3.6.

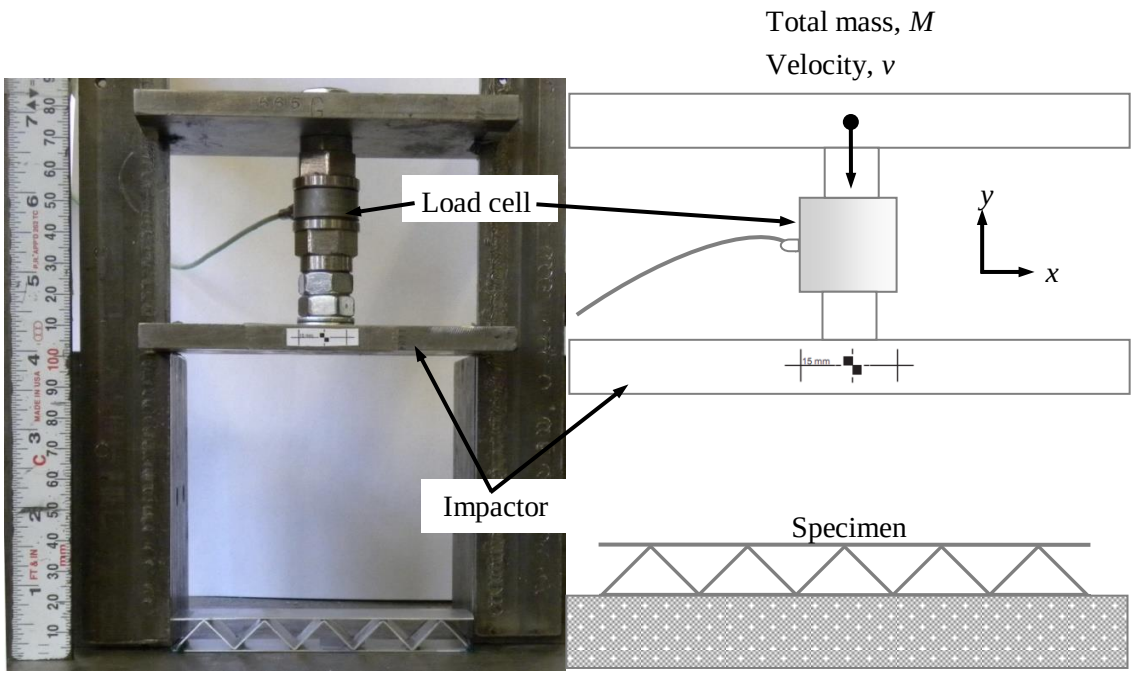

Figure 3.25: (a) A closer view of the test set-up for a drop-weight impact test, (b) a schematic diagram illustrating the test assembly, showing how the load cell is connected between the impactor and the mass.

A high-speed video camera (MotionPro X4, model no. X4CU-U-4) was used to capture the velocity and displacement of the impactor. The frequency of the video camera was set to 10,000 frames per second. The video camera was positioned in front of the impact tower in order to track the movement of the impactor by the

target, and to capture the deformation of the structures during the impact event. A MotionPro software, Version 2.30.0, was used to record the images into a video file.

Table 3.6: Details of the piezoelectric load cell (Kistler type 9321A).

Setting	**Value (Unit)**
Transducer sensitivity	3.97 (pC/N)
Measurement range	0 -10 (V)
Maximum load	10 000 (N)
Scaling factor	1 000 (N/V)

The captured images were analysed using the motion analysis software, ProAnalyst, where the images were calibrated and processed, from the information in pixels to the required parameter for example the displacement, velocity or acceleration of the impactor. In this study, only the displacement and velocity data in the *y*-direction were considered. All of the specimens were fabricated as described in Section 3.2. A summary of the parameter adopted for the low velocity impact test studies is given in Table 3.7.

Table 3.7: A summary of the corrugated-core impact test specimens undertaken at five different velocities.

Material	**No. of plies**	**Average wall thickness, *H* (mm)**	**Initial velocity, *v* (m/s)**	**Impact energy, (J)**
AL		0.5	0.99	0.61
			1.40	1.22
GFRP	5	0.5	1.98	2.45
			3.13	6.12
CFRP	2	0.5	4.43	12.23

3.8 Failure Mechanisms and Damage Characterisation

Finally, a microscopy study, using an optical microscope camera (Infinity 2, Lumenera Corporation) as shown in Figure 3.26, was performed to elucidate the failure mechanisms during the tests.

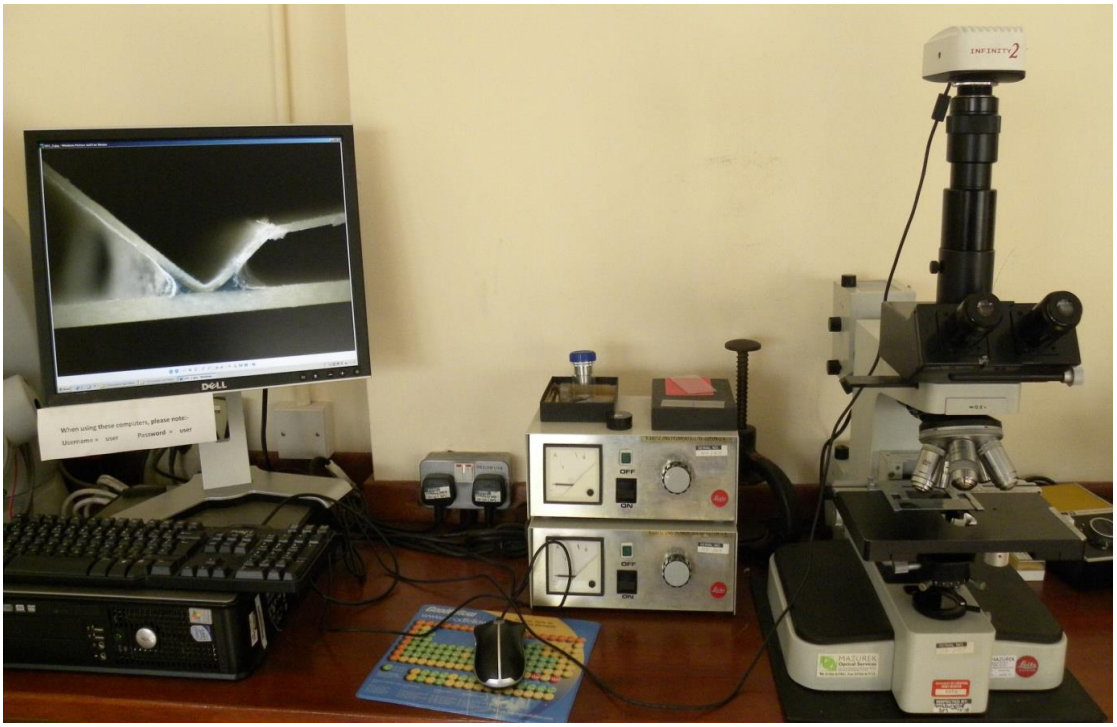

Figure 3.26: Optical microscope equipment that was used in the study.

After testing, the sandwich specimens were removed, sectioned and polished to a 1200 grit finish using silicon carbide paper. The specimens were then viewed under the microscope to investigate changes in the failure mechanisms as a function of thicknesses, number of unit cells following testing at quasi-static tests and selected specimens from dynamics events.

3.9 Summary of Chapter III

Chapter III presented details of the fabrication of the mould and the corrugated-core sandwich structures, the experimental set-up as well as the testing procedure for both quasi-static and dynamic loading. In this chapter, the corrugated-core sandwich structures were fabricated from three different materials, these being aluminium, a woven GFRP and a woven CFRP. The fabrication process and the specimen geometries were explained in detail. The basic mechanical properties of the materials were examined via tensile, in-plane shear for the AL, GFRP and CFRP corrugations. The Arcan test procedure was used to investigate complex loading conditions. Finally, the corrugated sandwich structures were filled with a low density rigid PU foam in order to investigate the effect of applying an additional internal support (i.e. the foam) on the compression response of these novel corrugations.

3.10 References

[1] Kazemahvazi S, Zenkert D. Corrugated all-composite sandwich structures. Part 1: Modeling. Composites Science and Technology. 2009;69(7–8):913-919.

[2] Mondolfo LF. Aluminum and its Alloys: Structure and Properties. London and Boston: Butterworth Company; 1976.

[3] ASTM. Standard Test Method for Apparent Density of Rigid Cellular Plastics. D1622, 1998.

[4] BS. Metallic Materials - Tensile Testing. Part 1: Method of test at ambient temperature, vol. EN 10002-1:2001 E Brussels: European Commitee for Standardisation; 2001.

[5] BS. Plastics - Determination of Tensile Properties. Part 4: Test conditions for isotropic and orthotropic fibre-reinforced plastic composites, vol. EN ISO 527-4 Brussels: European Commitee for Standardization; 1997.

[6] ASTM. Standard Test Method for Compressive Properties Of Rigid Cellular Plastics. D1621, 2000.

[7] Voloshin A, Arcan M. Pure shear moduli of unidirectional fibre-reinforced materials (FRM). Fibre Science and Technology. 1980;13(2):125-134.

[8] Voloshin A, Arcan M. Failure of unidirectional fiber-reinforced materials-New methodology and results. Experimental Mechanics. 1980;20(8):280-284.

[9] Mohr D, Doyoyo M. Analysis of the Arcan apparatus in the clamped configuration. Journal of Composite Materials. 2002;36(22):2583-2594.

[10] Lamb AJ, Pickett AK, Chaudoye F. Experimental characterisation and numerical modelling of hexagonal honeycomb cellular solids under multi-axial loading. Strain. 2011;47(1):2-20.

CHAPTER IV: EXPERIMENTAL RESULTS

4.1 Introduction

This chapter presents the experimental results obtained during this research work. Here, the results from a series of tensile and in-plane shear tests will be evaluated and analysed. Subsequently, the results of tests on the sandwich structures under lateral quasi-static and dynamic compression tests will be discussed. Following this, the behaviour of the structures under combined loading (shear and compression) will also be discussed. Finally, the failure mechanisms observed in the structures during and after the tests will be presented and characterised.

4.2 Mechanical Properties of Materials

This section discusses the results obtained from a series of tensile, in-plane shear and Arcan tests on the AL, the GFRP and the CFRP laminates.

4.2.1 Tensile Tests on the Aluminium Alloy

When loaded in tension, the AL will undergo elastic and plastic deformation phases. Initially, the specimen tested here deformed elastically, giving a linear relationship between load and extension. These two parameters were then used to calculate the engineering stress versus engineering strain curves, such as that shown in Figure 4.1. Here, the engineering stress and strain were calculated using:

$$\sigma = \frac{P}{A_o} \tag{4.1}$$

$$\varepsilon = \frac{L_f - L_o}{L_o} = \frac{\Delta L}{L_o} \tag{4.2}$$

where σ is the engineering stress, ε is the engineering strain, P is the external axial load, A_o is the original cross-sectional area of the specimen, L_o is the original length of the specimen and L_f is the final length of the specimen.

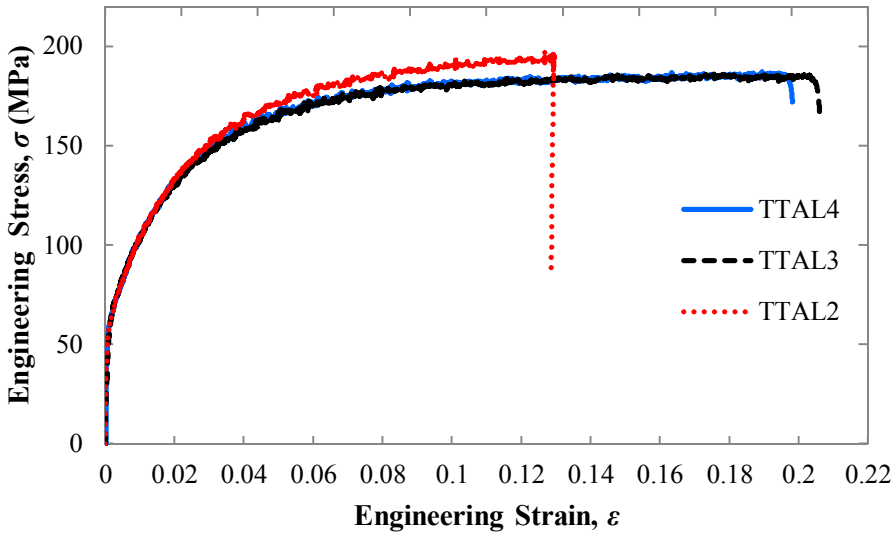

Figure 4.1: Engineering stress-strain curves for the aluminium alloy (AL 2024-O), following three tensile tests.

Since the specimen dimensions can potentially change significantly from their original values during the test, the engineering stress-strain curve must be interpreted with caution beyond the elastic limit. Here the true stress, $\sigma_t = P/A$ gives a more direct measure of the material response in the plastic flow range, where A is the specimen cross-sectional area. The true strain, ε_t is calculated by dividing the incremental displacement dL by the instantaneous length L:

$$d\varepsilon_t = \frac{dL}{L} \rightarrow \varepsilon_t = \int_{L_o}^{L} \frac{1}{L} dL = \ln \frac{L}{L_o} \tag{4.3}$$

where ratio L/L_o is the extension ratio. The relationships between the true and engineering values of tensile stress and strain can be shown to be:

$$\sigma_t = \sigma(1+\varepsilon) \tag{4.4}$$

$$\varepsilon_t = \ln(1+\varepsilon) \tag{4.5}$$

Figure 4.2 shows the true stress-strain curve for an aluminium alloy specimen in which the graph is plotted using the true engineering values of stress and strain given in Equations 4.4 and 4.5.

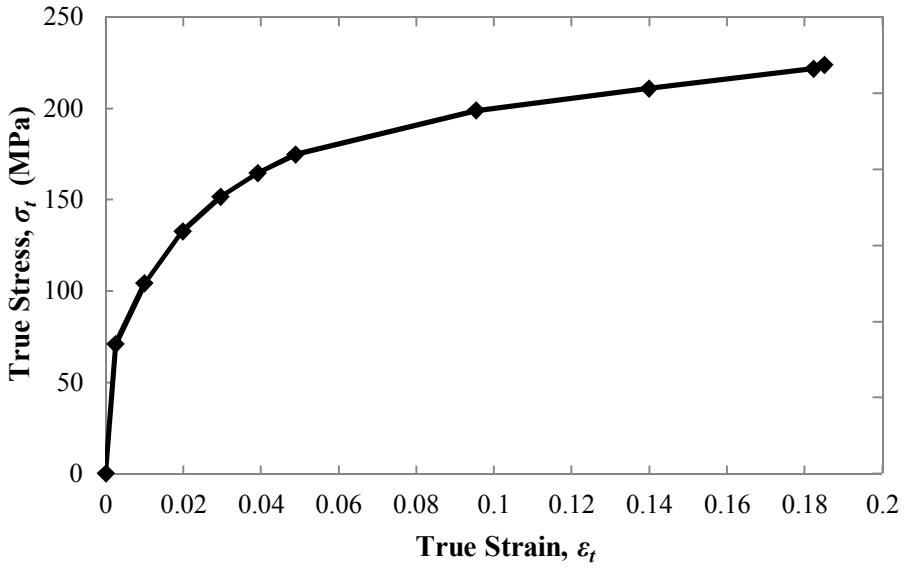

Figure 4.2: True tensile stress-strain curve for an aluminium alloy specimen (TTAL3).

For purposes of numerical modelling, the plastic strain response, ε_p is required for the isotropic-strain hardening material model. A summary of the data for the aluminium alloy is given in Table 4.1. The plastic strain data is obtained from:

$$\varepsilon_p = \varepsilon_t - \left(\frac{\sigma_t}{E}\right) \qquad 4.6$$

From the tensile test results, specimen TTAL3 shows a high degree of ductility. The fracture characteristics in this specimen are shown in Figure 4.3.

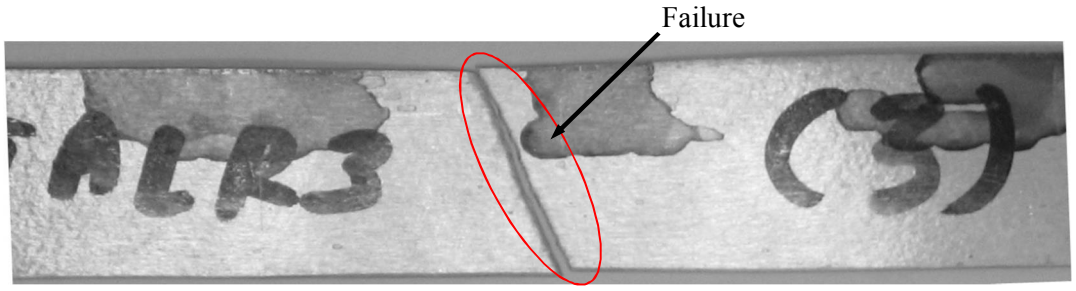

Figure 4.3: Tensile failure at approximately 40^o to the loading axis (specimen TTAL3).

Necking initiated when the stress-strain curve passed the maximum point, where plastic deformation is no longer uniform. Just prior to fracture, a shear plane at approximately 40^o to tensile axis formed in the specimen.

Table 4.1: Tensile stress-strain data for the aluminium alloy.

Engineering Stress, σ (MPa)	**Engineering Strain, ε**	**True Stress, σ_t (MPa)**	**True Strain, ε_t**	**Plastic Strain, ε_p**
70.8	0.0026	71.0	0.0026	0
103.1	0.01	104.1	0.0100	0.0085
130.1	0.02	132.7	0.0198	0.0179
147.3	0.03	151.7	0.0296	0.0275
158.3	0.04	164.7	0.0392	0.0369
166.5	0.05	174.8	0.0489	0.0464
180.7	0.10	198.8	0.0953	0.0925
183.4	0.15	210.9	0.1398	0.1368
184.9	0.20	221.8	0.1823	0.1792
186.1	0.2033	223.9	0.1851	0.1819

4.2.2 Tensile Tests on the Composites

Typical stress-strain curves for the GFRP and CFRP are given in Figures 4.4 and 4.5, respectively. Here, the composite laminates exhibited a roughly linear response up to the maximum stress value. At this point, the composite failed in a catastrophic manner across the width of the sample, as shown in Figure 4.6, provoking a rapid drop in the stress-strain curve. The CFRP specimens exhibited a higher tensile strength (X^T = 550 MPa) and a more brittle response (strain to failure, ε_f = 0.013) than the GFRP specimen (X^T = 320 MPa , ε_f = 0.024).

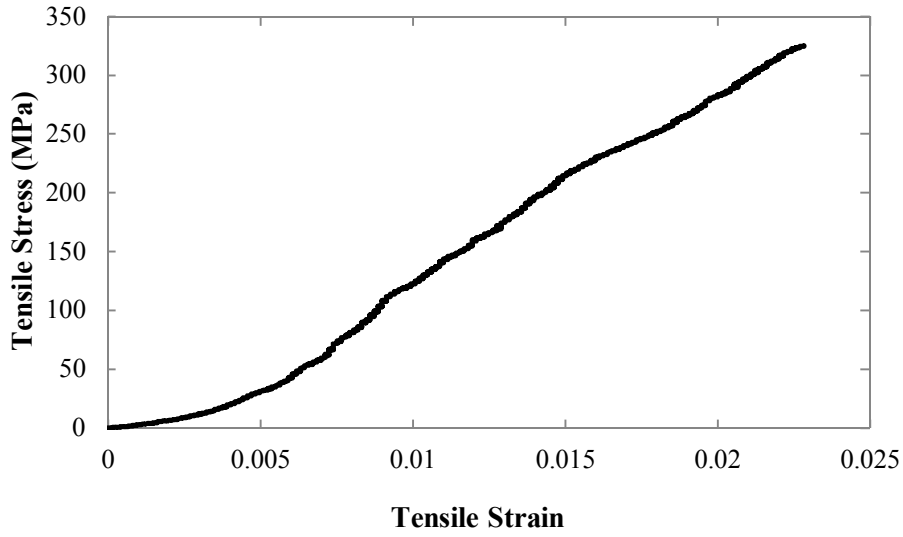

Figure 4.4: Typical tensile stress-strain curve for a GFRP specimen.

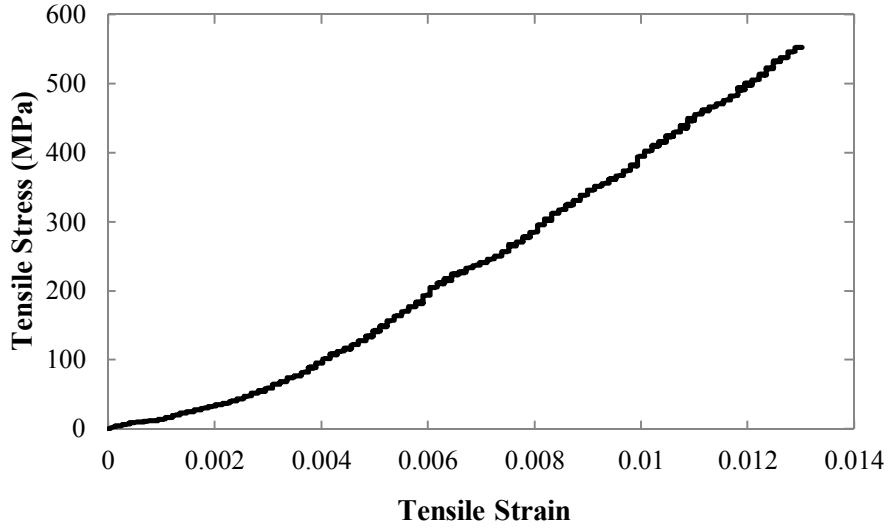

Figure 4.5: Typical tensile stress-strain curve for a CFRP specimen.

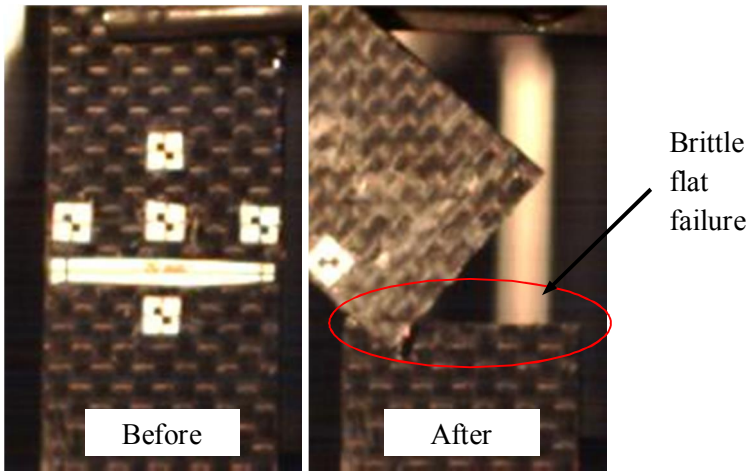

Figure 4.6: Typical tensile failure modes in the woven composite (CFRP specimen) following tensile testing.

The Poisson's ratio was subsequently calculated from the tracking displacement data using:

$$\upsilon = -\frac{d\varepsilon_x}{d\varepsilon_y} \qquad 4.7$$

From the analysis, the Poisson's ratios for the CFRP and GFRP specimens are shown in Figures 4.7 and 4.8, respectively.

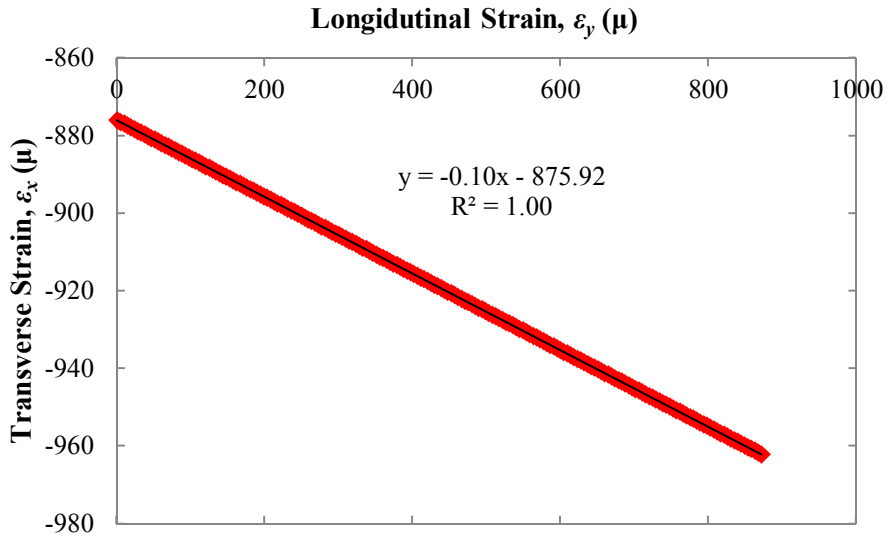

Figure 4.7: Plot of the strain in transverse x-direction versus strain in the longitudinal y-direction. The slope of the line gives the value of the Poisson's ratio for this woven CFRP specimen, i.e. $\upsilon = 0.10$.

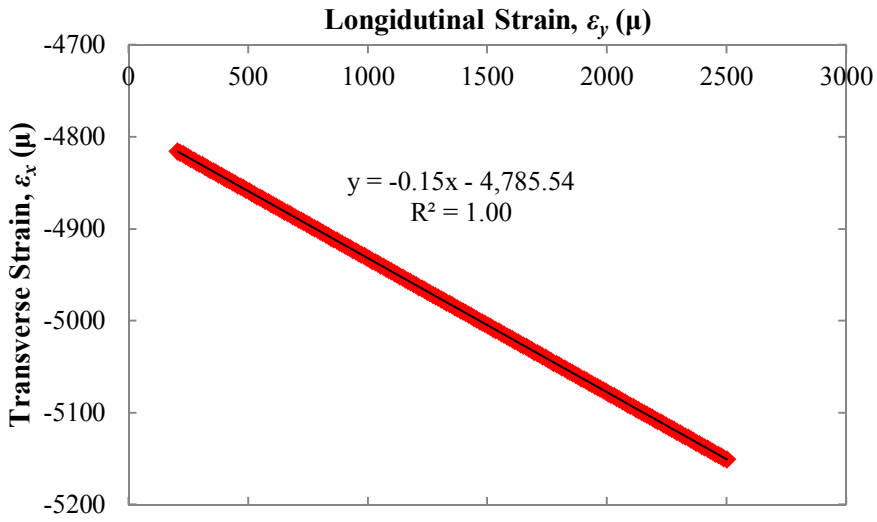

Figure 4.8: Plot of the strain in transverse x-direction versus strain in the longitudinal y-direction taken from the relative displacement images analysis. The slope of the line gives the value of the Poisson's ratio for this woven GFRP specimen, i.e. υ = 0.15.

4.2.3 In-plane Shear Tests on the Composites

For the ±45° tensile specimens, the shear stress-strain values were determined according to:

$$\tau_{12} = \frac{\sigma_y}{2} \tag{4.8}$$

$$\gamma_{12} = \varepsilon_y - \varepsilon_x \tag{4.9}$$

where τ_{12} is the shear stress, σ_y is the tensile stress in the specimen, γ_{12} is the shear strain, ε_y is the strain in the loading direction and ε_x is the strain at 90° to the loading direction. The in-plane shear-stress versus strain curves exhibit a non-linear response throughout the loading range. Figures 4.9 and 4.10 show the shear stress-strain curves for the GFRP and CFRP specimens, respectively. Here, the CFRP specimen exhibits a higher shear strength (S^L = 120 MPa) and ultimate shear strain compared to the GFRP specimen (S^L = 100 MPa).

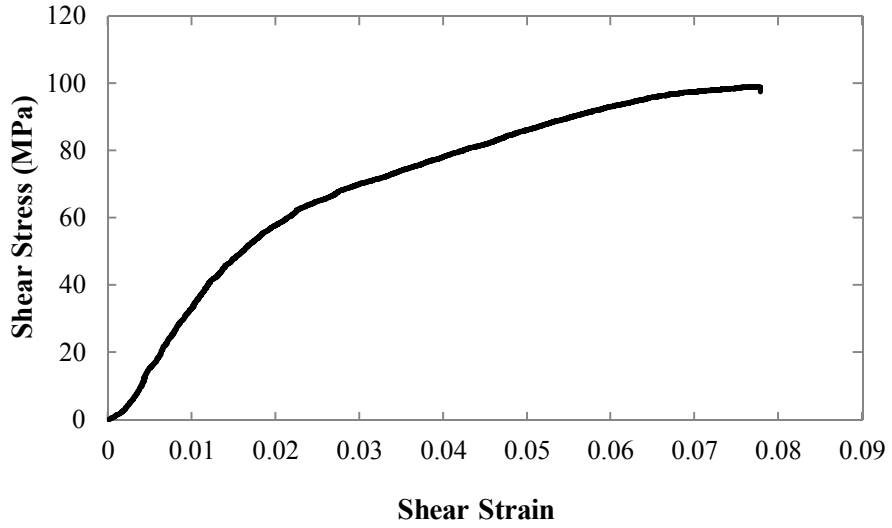

Figure 4.9: Typical in-plane shear stress-strain curve for a GFRP specimen.

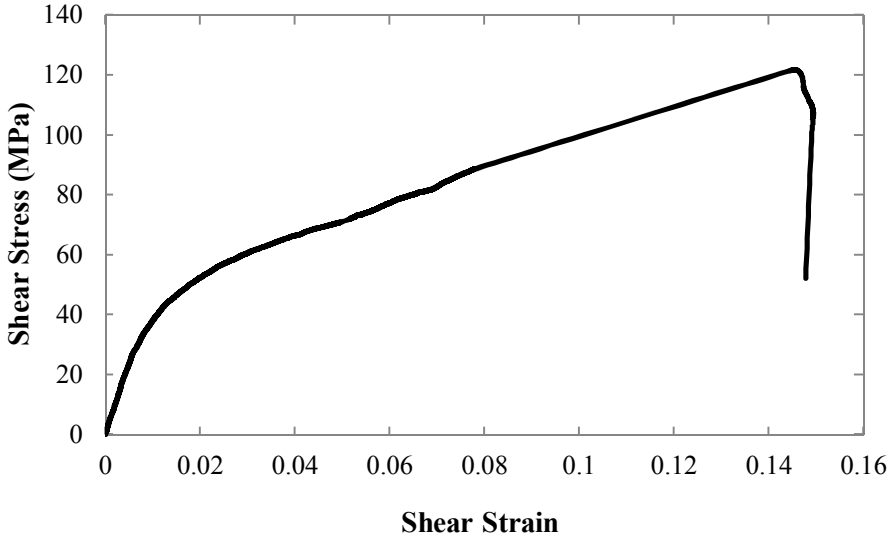

Figure 4.10: Typical in-plane shear stress-strain curve for a CFRP specimen.

4.2.4 Relative Density

When characterising the mechanical properties of a corrugated-core specimen, it is appropriate to determine its specific properties by dividing the density of the corrugated-core, ρ by the overall density of the core, ρ_s. As discussed in Section 3.3, using the geometrical parameters given in Figure 3.8, a derivation of the relative density of the core ρ^* is:

$$\rho^* = \frac{\rho}{\rho_s} = \frac{2H}{L\sin 2\theta} \qquad 4.10$$

4.2.5 Compression Tests on the Rigid Polyurethane Foam

The rigid polyurethane (PU) foam used in the study was manufactured from two liquid chemical components. Prior to use, it is necessary to determine the behaviour of the foam, its modulus of elasticity, its compressive strength and its energy absorption characteristics.

Figure 4.11 shows the mechanical response during a uniaxial compression test. Compression in the rigid PU foam gives rise to the three phases of response, each corresponding to distinct deformation mechanisms. The initial linear elastic response was controlled by elastic axial compression and bending of cell edges, stretching of cell faces and compression of the gas within closed cells [1]. Deformation during this phase was small and uniformly distributed throughout the specimen. In the plastic plateau region, the cells collapse via buckling, plastic deformation or rupture of the cell walls and edges. Final densification was associated with completely collapsed cells being compacted against one another. Plastic collapse caused the cells to crumple in the compressive direction and the foam to become thin. Deformation was uniformly distributed and the stress rises steeply as the material is compressed. The compression stress is determined by dividing the load by cross-sectional area of the foam and the energy absorption was calculated from the area under the curve up to the point of densification, typically at 60% of strain.

Anisotropy can sometimes be very significant in some types of foam. Alias *et al.* [2] reported that the compression yield values varied slightly but the elastic modulus remained almost constant in the three different principal directions. In this study, it is assumed that the rigid PU foam behaves as an isotropic material, therefore the compression response is uniform in all principle directions.

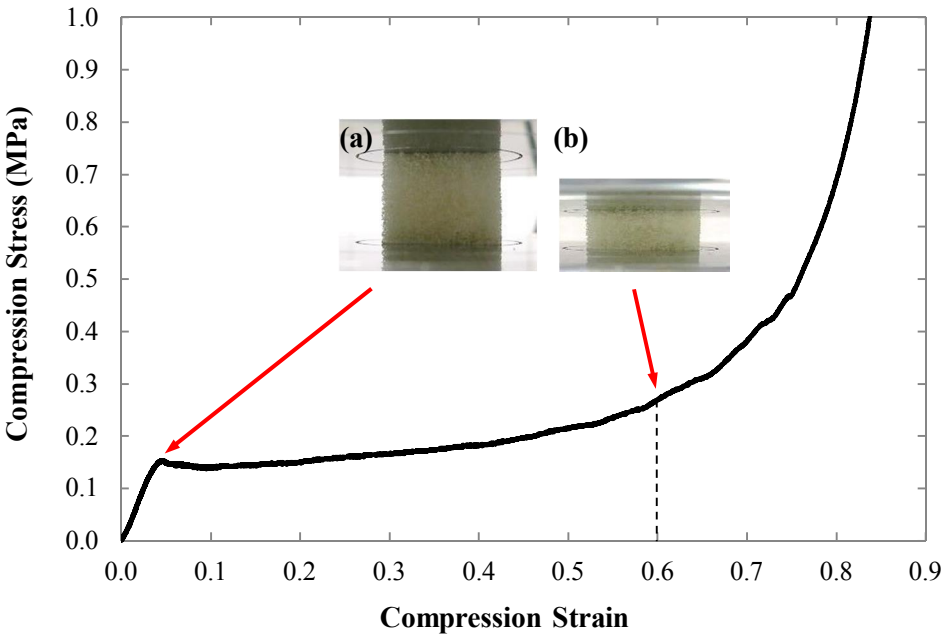

Figure 4.11: Typical compression stress-strain behaviour of a rigid PU foam; (a) at the yield point and (b) at 60% strain where the densification begins.

4.3 Static Compression Test

Quasi-static compression tests were carried out to determine the compression strength and stiffness of the specimens under lateral compression loading.

4.3.1 Model of the Compressive Response of the Corrugated-core Sandwich Structures

Consider a model of a corrugated-core with geometrical quantities as specified in Figure 4.12 subjected to an applied load. When the sandwich structure is subjected to a compressive load 5P, it is assumed that all of the unit cells are subjected to the same load, as shown in Figure 4.12(b). As a result of symmetry of the triangular profile, each of the core members can be considered as a cantilever beam subjected to the same axial compression load N, bending moment M and shear load R, as illustrated in Figure 4.12(c). Here, no deformation is permitted at end of the lower core member.

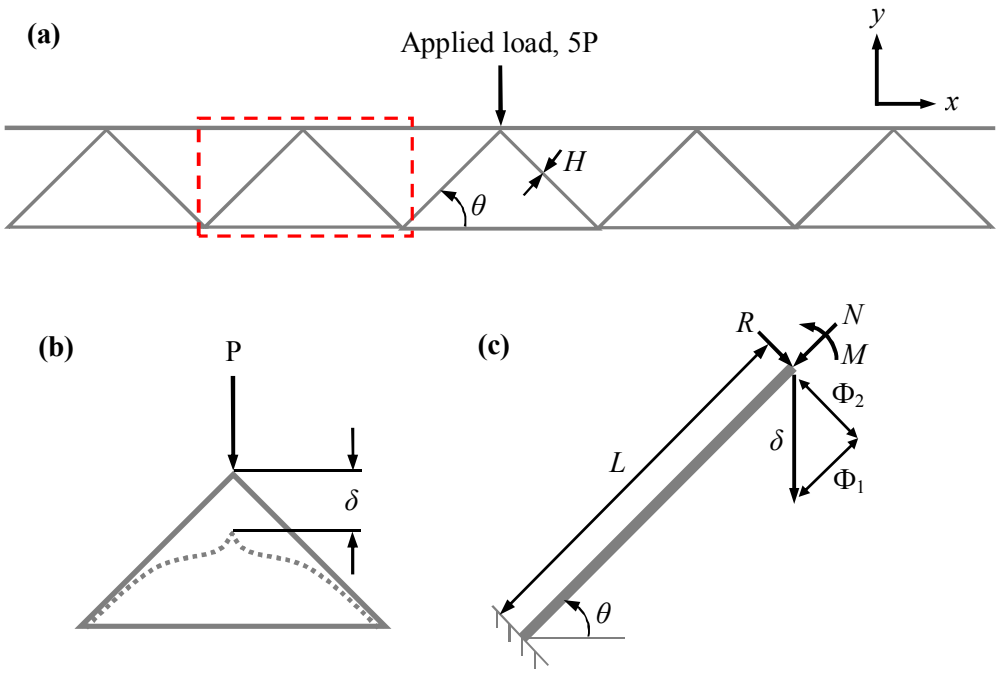

Figure 4.12: (a) A five unit cell sample under compression loading, (b) a single unit cell showing the deformed behaviour (dashed-line), (c) a free-body diagram of a compression loaded core member.

Considering equilibrium of loads in the *y*-direction, it can be shown that:

$$N\sin\theta + R\cos\theta = \frac{\mathrm{P}}{2} \tag{4.11}$$

The bending moment M and the shear load R are related through:

$$M = \frac{RL}{2} \tag{4.12}$$

The deformation δ then can be written in terms of the displacement parameters of Φ_1 and Φ_2 as:

$$\Phi_1 \sin\theta + \Phi_2 \cos\theta = \delta \tag{4.13}$$

where the relationship between the Φ_1 and Φ_2 is:

$$\Phi_1 = \Phi_2 \tan\theta \tag{4.14}$$

Using classical beam theory, the relationship between the displacement parameters and the loads acting on the core member can be written as follows:

$$\Phi_1 = \frac{NL}{EA} \tag{4.15}$$

$$\Phi_2 = \frac{RL}{12EI} \tag{4.16}$$

where A is the cross-sectional area (= wH), I is the moment of inertia (= $wH^3/12$) and E is the Young's modulus of the core.

By substituting Equations 4.14 to 4.16 into Equation 4.13, and then solving the resulting expression using Equation 4.11, the relationship between the load P and the deformation δ can be shown to be:

$$\mathrm{P} = \frac{2EHw(L^2 \sin^2\theta + H^2 \cos^2\theta)}{L^3}\delta \tag{4.17}$$

As noted previously, this analysis assumes specific boundary conditions, which in turn assumes symmetry and full constraint at the apex.

In contrast, if debonding occurs between the core and the skins during the initial stages of compression loading, the core can be assumed to be pin-jointed to the skins [3], and then the load-displacement relationship is given by:

$$\mathrm{P} = \frac{5EHw}{L}\delta \tag{4.18}$$

In predicting the strength of a corrugated-core, Kazemahvazi and Zenkert [4] reported that Euler buckling and core shear buckling are two possible modes of local elastic buckling in the inclined cell wall under lateral compression loading. Here, the Euler buckling load P_E, can be estimated from classical buckling theory [5, 6] using:

$$\mathrm{P}_E = \frac{\lambda^2 \pi^2 EI}{L^2} \tag{4.19}$$

where λ is a factor dependant on the boundary conditions, e.g. $\lambda = 2$ for a beam with built-in ends. Assuming perfect bonding between the core and the skins, the value of

P_E for a corrugated structure can be expressed as:

$$P_E = \frac{n\lambda^2\pi^2 EwH^3\left(L^2\sin^2\theta + H^2\cos^2\theta\right)}{6L^4\sin\theta} \quad 4.20$$

Since $\theta = 45^o$ in this study, Equation 4.20 can be simplified to:

$$P_E = \frac{nEwH^3}{6\sqrt{2}}\left(\frac{\lambda\pi}{L}\right)^2\left\{1+\left(\frac{H}{L}\right)^2\right\} \quad 4.21$$

When considering core shear buckling, Xiong *et al.* [7] stated that it is reasonable to neglect the shear stiffness of the skins and assume that the shear rigidity of the sandwich structure is approximately equal to that of the corrugated-core. Therefore, the core shear buckling load $P_S \approx G_c wx\sin\theta$, where G_c is the effective shear modulus of the corrugated-core, which can be approximated by [3]:

$$G_c = \frac{E\rho^*}{4}\sin^2 2\theta \quad 4.22$$

substituting Equation 4.10 into Equation 4.22, gives:

$$G_c = \frac{EH}{2L}\sin 2\theta \quad 4.23$$

Thus,

$$P_S = \frac{xwEH}{2L}\sin 2\theta\sin\theta \quad 4.24$$

If the two buckling loads associated with macro-buckling in the sandwich structure, P_E and P_S differ greatly, then Equations 4.21 and 4.24 can be used to estimate the critical buckling load, P_{cr}, (i.e. if $P_S > P_E$, then $P_{cr} \approx P_E$, and vice-versa). However, if the Euler and core shear buckling loads are of similar magnitude, interaction

between buckling modes must be considered. In this case, the critical buckling load can be estimated from [8]:

$$\frac{1}{P_{cr}} = \frac{1}{P_E} + \frac{1}{P_S} \qquad 4.25$$

4.3.2 The Compression Behaviour of the Aluminium Corrugated-Core Sandwich Structures

A typical load-displacement trace for an aluminium corrugated-core sandwich structure is presented in Figure 4.13.

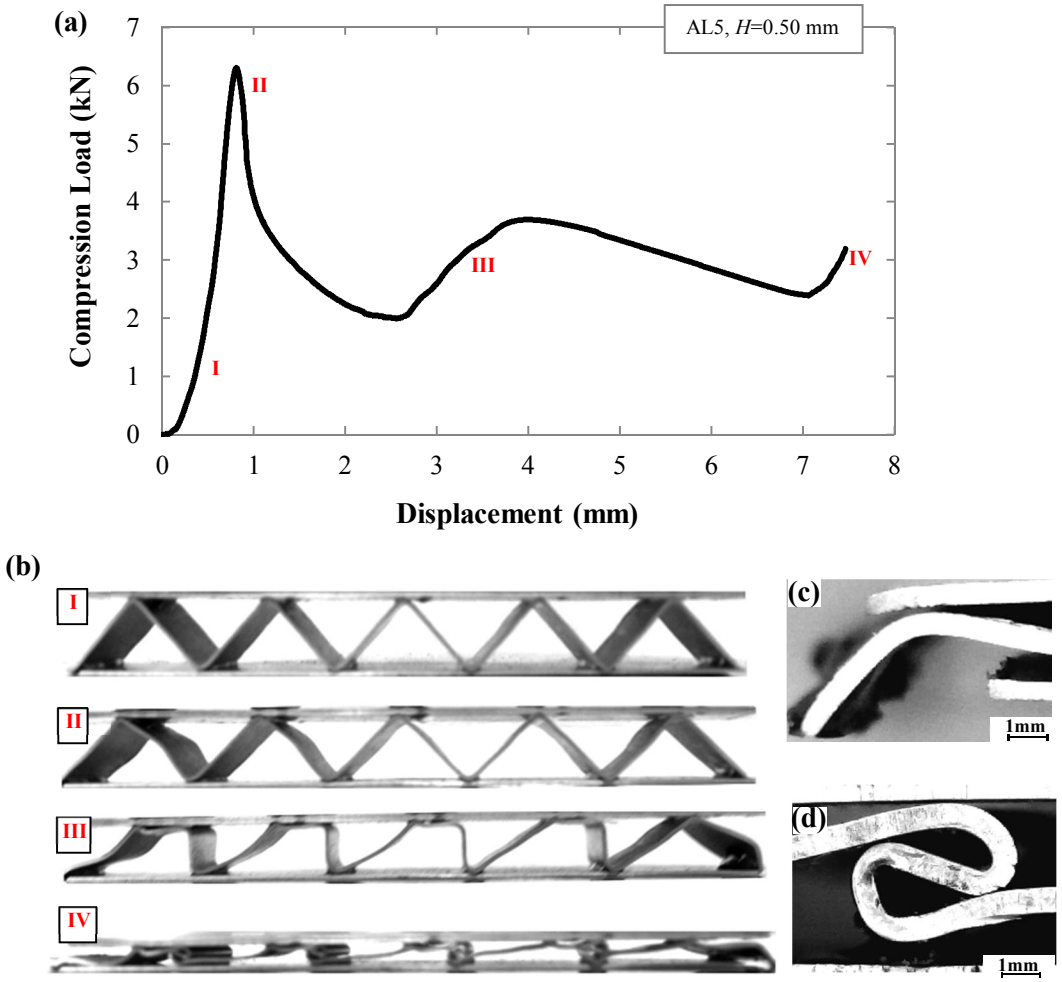

Figure 4.13: (a) Typical load-displacement curves for the AL sandwich corrugated-core structures. (b) Photographs of progressive damage development in structures based on five unit cells in (a). (c) Debonding at an end of the core after loading (b – III). (d) Crumpling after the corrugated-core has been almost completely flattened.

The deformed shapes of this ductile specimen, at various levels of prescribed displacement were recorded using a high speed video camera. Upon loading, the specimen exhibited an initial non-linear response. This may be due to effects associated with the machine compliance and, perhaps due to the fact that the skins may not be fully parallel to each other. As a result, the initial deformation of the structure is likely to be influenced by the effective flattening of the specimen. After this initial "stiffening", the specimen responds in a linear fashion (Region I) up to the first peak in the trace, with deformation being symmetrical about the axis of loading. After reaching the peak load, one of the struts in the corrugated-core was partially bent and as a result, the overall stiffness of the specimen decreased. The load required to further deform the sample gradually decreases due to the propagation of localised buckling across the width of the corrugated-core.

The response then becomes progressively nonlinear (Region II). This is followed by a sudden drop in the applied load as the structure loses stability due to plastic buckling. In Region III, the corrugated-core takes on a trapezium shape and the applied load starts to increase again due to interactions between the surfaces of the cell walls and the uppermost skin. Finally, in Region IV the corrugated-core has been completely densified, resulting in certain cases, in debonding at the edges of the specimen. This debonding occurs since the level of adhesion between the core and skin is not sufficient to transmit the shear force to the core. The evidence from these tests on the aluminium corrugations indicates that elastic buckling, plastic deformation and the formation of plastic hinges are the dominant failure mode in this material.

Figure 4.14 shows the load-displacement traces following compression tests on AL sandwich specimens based on one to five unit cells. It is clear that all of the specimens deformed in an acceptable fashion except for one unit cell. From the investigation, the five unit cells specimen withstands a higher compression load and offers a higher energy absorption capability (larger area under the curve) compared to the other specimens.

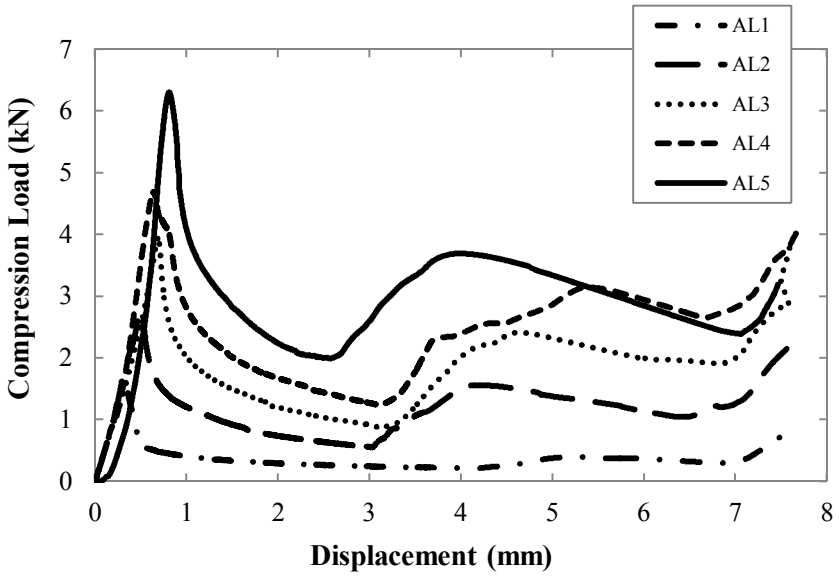

Figure 4.14: Comparison of the load-displacement traces for AL sandwich specimens based on 1, 2, 3, 4 and 5 unit cells.

However, for a single unit cell specimen, after reaching the maximum peak load, the strut buckled and then debonding occurred at the edge, leading to a less of contact between the midsurface and the upper skin. Under further loading, the load remains constant until all of the constituents of the structure (upper skin, core and lower skin) become in contact and then the core is densified.

4.3.3 The Compression Behaviour of the GFRP Corrugated-Core Sandwich Structures

Typically, the load-displacement traces for the GFRP corrugated-core sandwich structures exhibited a brittle type of behaviour, involving extensive crushing as shown in Figure 4.15.

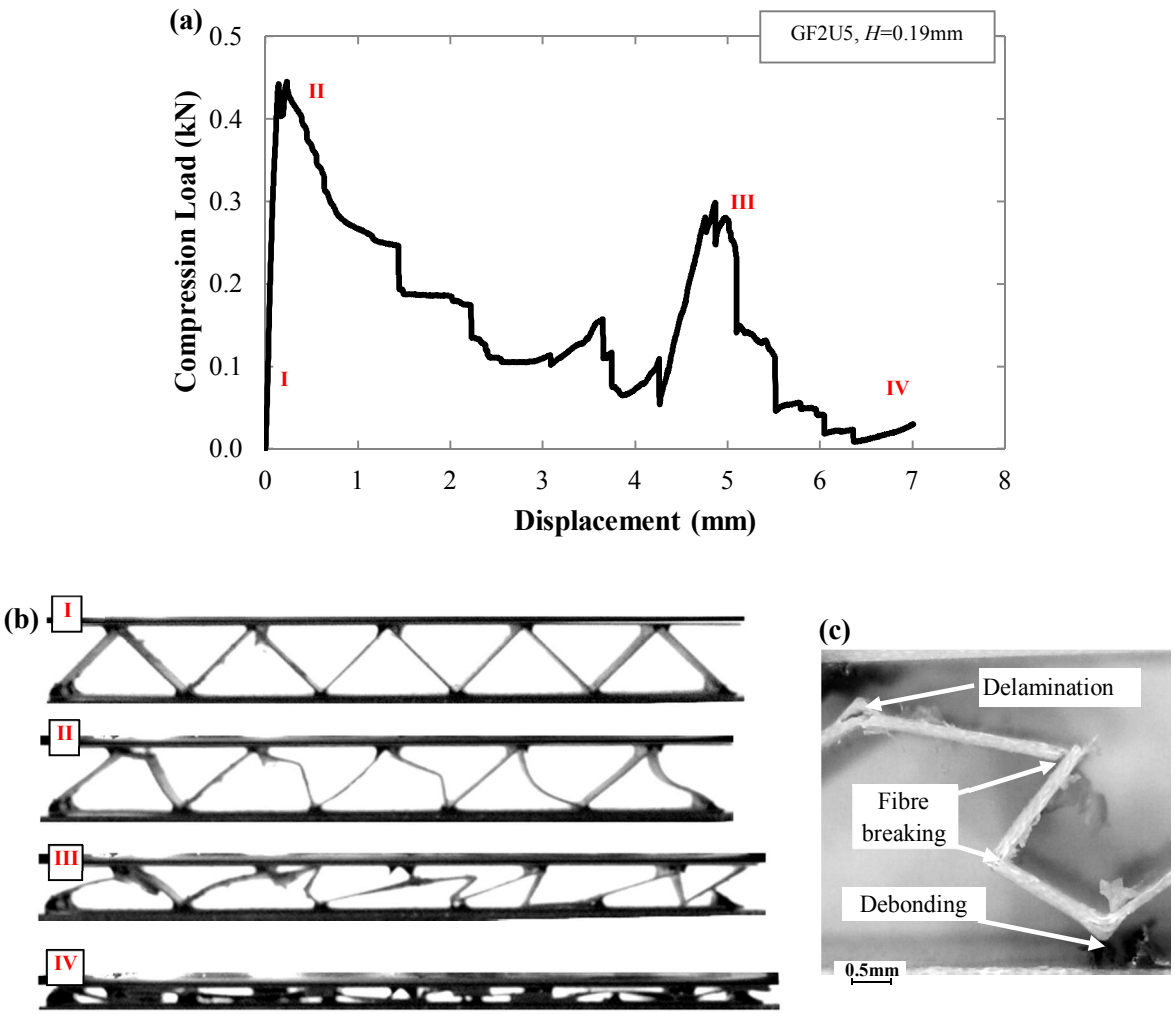

Figure 4.15: (a) Typical load-displacement curve for a GFRP sandwich corrugated-core structure. (b) Photographs of progressive damage development in a five unit cell specimen in (a). (c) Failure mode images after crushing process.

The load increases linearly up to the first peak, with deformation in the core being symmetrical about the axis of loading. In Region II, initial cell wall buckling was visible, followed by compressive failure at the peak load. The load then progressively decreases as fibres begin to fracture in the middle of individual struts. Subsequent failure involved the formation of hinges in the middle of the cell wall and then progressive crushing at the cell wall close to lower skin, as evidenced in Region III. Finally, in Region IV the corrugated-core is completely crushed, and the core is fully flattened. An examination of the failed samples in Figure 4.15(c) indicates that additional failure mechanisms involved in the crushing process include delamination between the plies and debonding of the adhesive between the core and

skin surfaces. Meanwhile, based on the observations of different numbers of unit cells, elastic buckling was the dominant initial failure mode for this type of material.

In order to further investigate the mechanical response of the cores, the load-displacement traces are compared following tests on specimens with differing number of unit cells (η_x), cell wall thicknesses (η_H) and different widths (η_w).

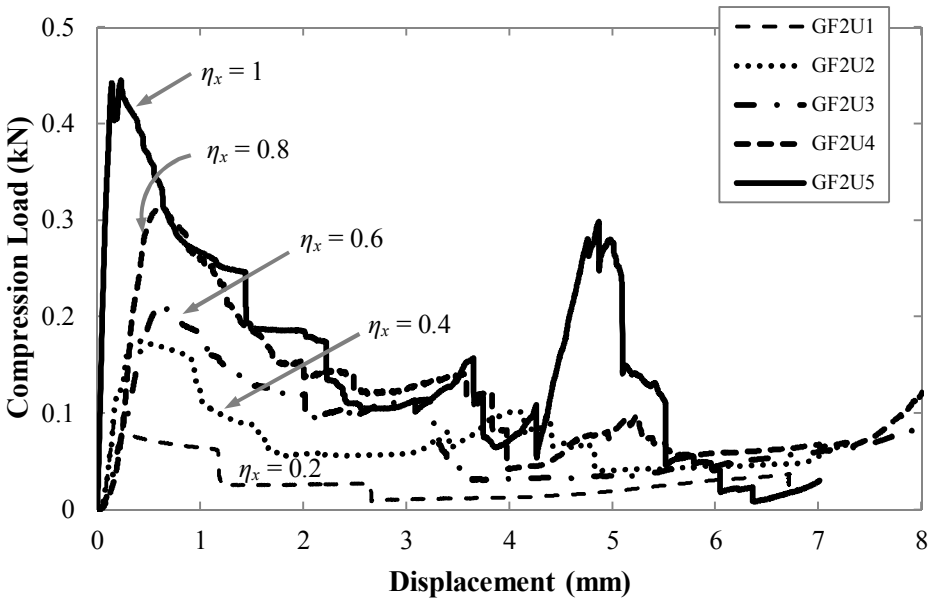

Figure 4.16: Comparison of load-displacement traces for GFRP sandwich specimens based on 1, 2, 3, 4 and 5 unit cells. (Note that these are GFRP specimens of 2-ply thickness. The term of η_x is an aspect ratio based on the number of unit cells in *x*-direction relative to a specimen having 5 unit cells, GF2U5).

Figure 4.16 shows the compression responses of the GFRP sandwich specimens. Based on these observations, it was evident that just after the peak load, the fibres starts to fracture, and the crushing process continues until densification region. With an increase in the number of unit cells, the compression loads rise significantly. Clearly the core based on five unit cells (GF2U5) has a higher strength than the other specimens.

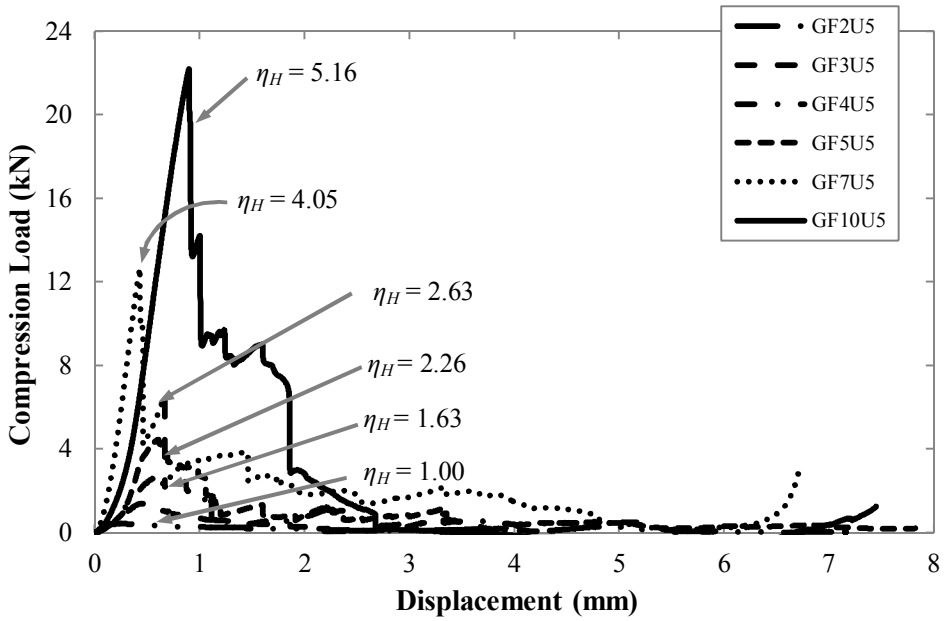

Figure 4.17: Comparison of load-displacement traces following tests on five unit cell sandwich structures based on between 2 and 10 plies of GFRP. (Note that the term of η_H is a normalised average thickness of the corrugated-cores relative to the 2-ply specimen, GF2U5).

Figure 4.17 shows that the compression strength increases with increasing cell wall thickness in the core, η_H. The thickest core (GF10U5) exhibited a combination of fracture mechanisms immediately after the sudden load drop, as the composite layers delaminated and the edges of the specimen debonded. However, at displacements between 1 mm and 2 mm, the struts progressively crush and above a displacement of 3 mm, all of the cores are flattened.

Here, the five unit cell GFRP specimen based on two plies is taken as a reference to compare the influence of different specimen widths, η_w. Figure 4.18 shows that the wider specimen with $\eta_w = 4$ (GF2W100) is approximately six times stronger than the reference specimen and capable of absorbing more energy than the other widths.

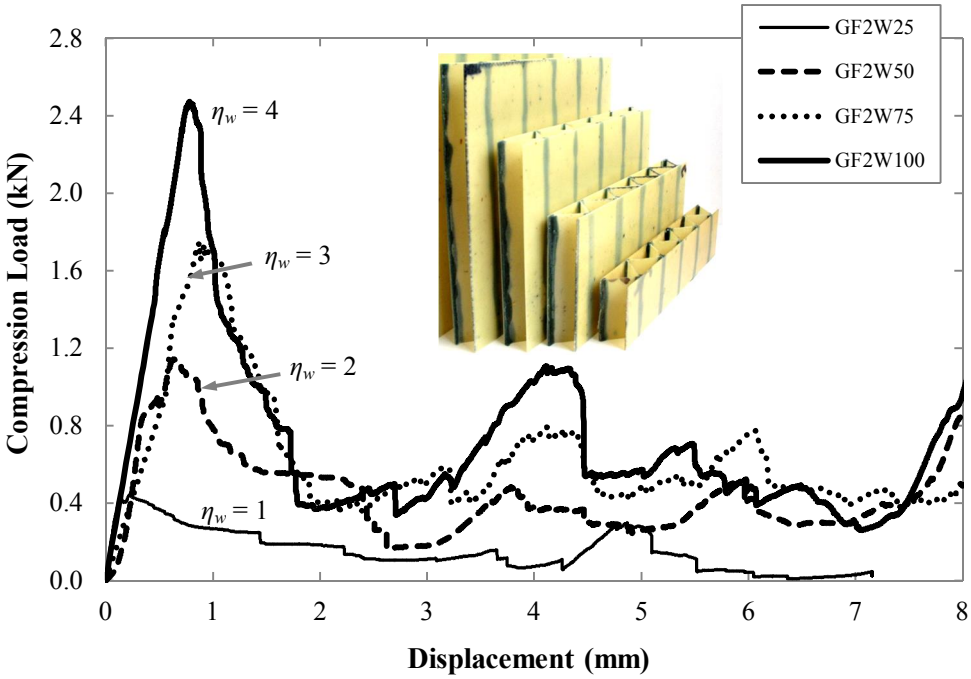

Figure 4.18: Comparison of the load-displacement traces for the GFRP corrugated-core sandwich specimens based on spans of 25, 50, 75 and 100 mm, respectively. (Note that these GFRP specimens are based on 2-ply cores with 5 unit cells. The width aspect ratio η_w is relative to a 25 mm wide specimen, GF2W25).

4.3.4 The Compression Behaviour of the CFRP Corrugated-Core Sandwich Structures

The failure processes in the CFRP corrugated-core are shown in Figure 4.19, where initial failure was dominated by cell wall buckling. Generally, the load-displacement plot is steeper than that for the AL corrugated-core and the post-damage failure modes are similar to the GFRP corrugated-core sandwich structure. Following the initial linear response, the structure buckles and load in the cell wall drops gently (Regions I-II). Subsequent failure involves fibre fracture, delamination and debonding between the core and the skin (Regions III-IV). Figure 4.19(c) shows the failure modes after the crushing process is complete involving the formation of hinges in the middle of the cell wall after fibre fracture, delamination and debonding at both ends. As before, elastic buckling was the dominant initial failure mode in these CFRP specimens.

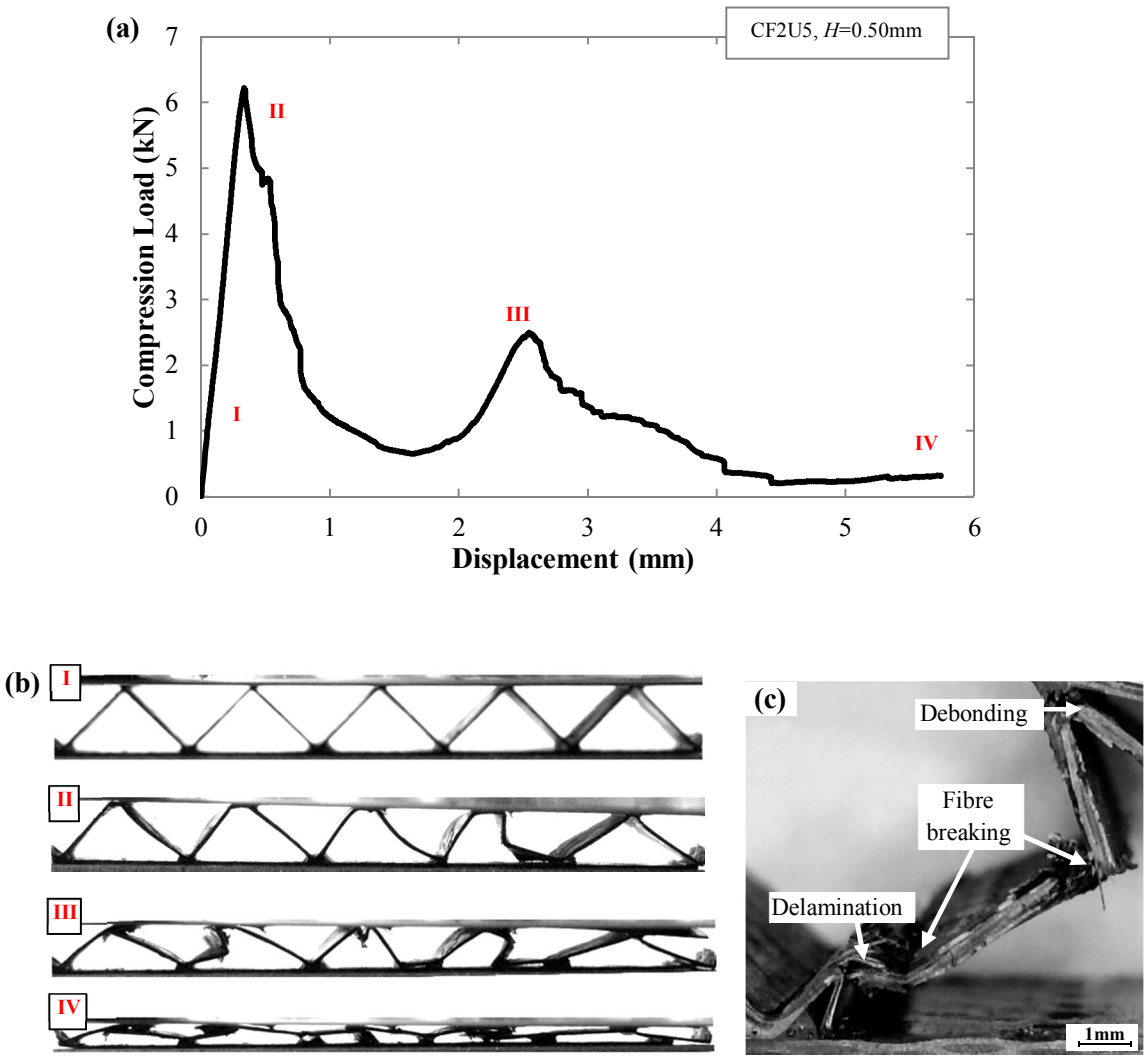

Figure 4.19: (a) Typical load-displacement curve for a CFRP sandwich corrugated-core structure. (b) Photographs of progressive damage development in five unit cell corrugations in (a). (c) Failure modes after crushing process.

Figure 4.20 shows that the strength of the CFRP sandwich structure increases significantly as the number of unit cells increases. Similarly, Figure 4.21 shows that the structure with the greatest cell wall thickness (CF6U5) is capable of carrying a load of approximately 35 kN. Finally, with increasing width, the maximum load trends to increase. Here the CF2W100 specimen is approximately six times greater than the reference structure (CF2W25), as shown in Figure 4.22.

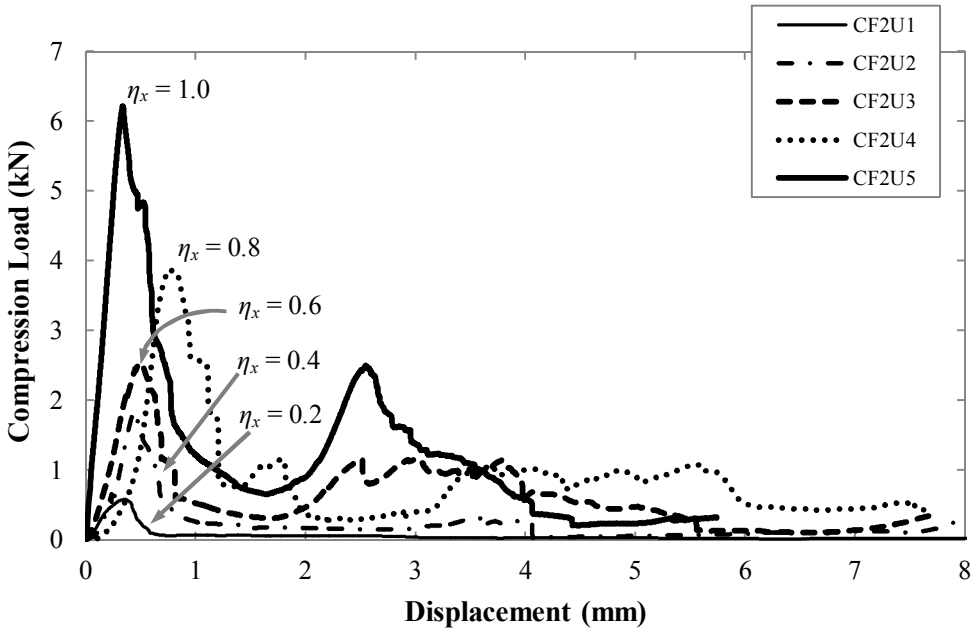

Figure 4.20: Comparison of load-displacement traces for CFRP sandwich specimens based on 1, 2, 3, 4 and 5 unit cells. (Note that these are CFRP specimens based on 2 plies and the term of η_x is an aspect ratio based on the number of unit cells in *x*-direction relative to 5 unit cells, CF2U5).

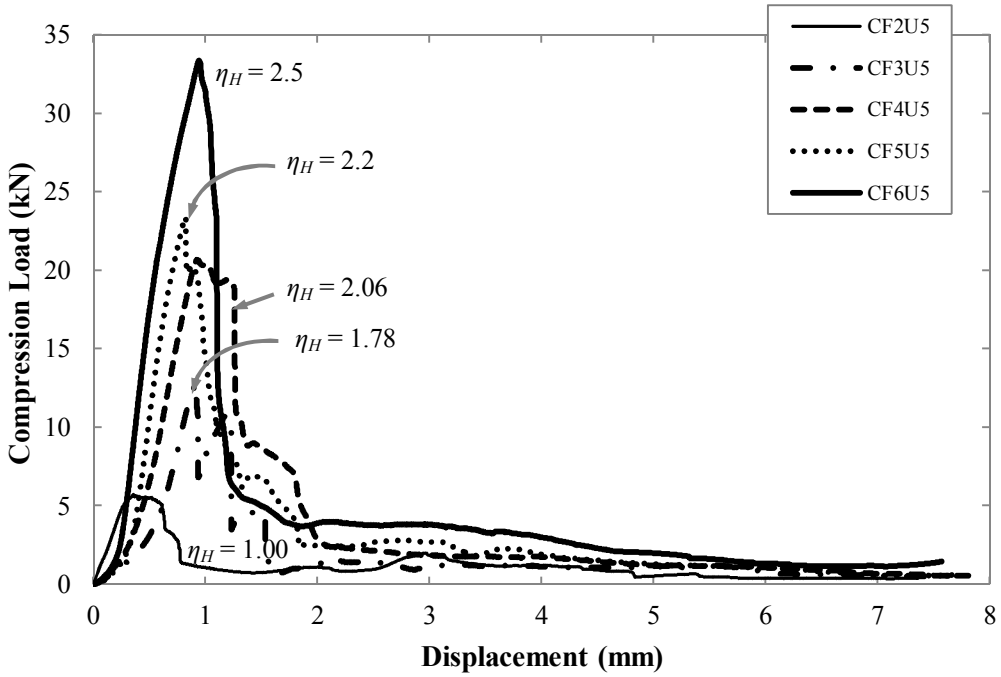

Figure 4.21: Comparison of load-displacement traces for CFRP specimens based on between 2 plies and 6 plies. (Note that these CFRP specimens contained 5 unit cells and η_H is a normalised average thickness of the corrugated-cores relative to the 2-ply specimen, CF2U5).

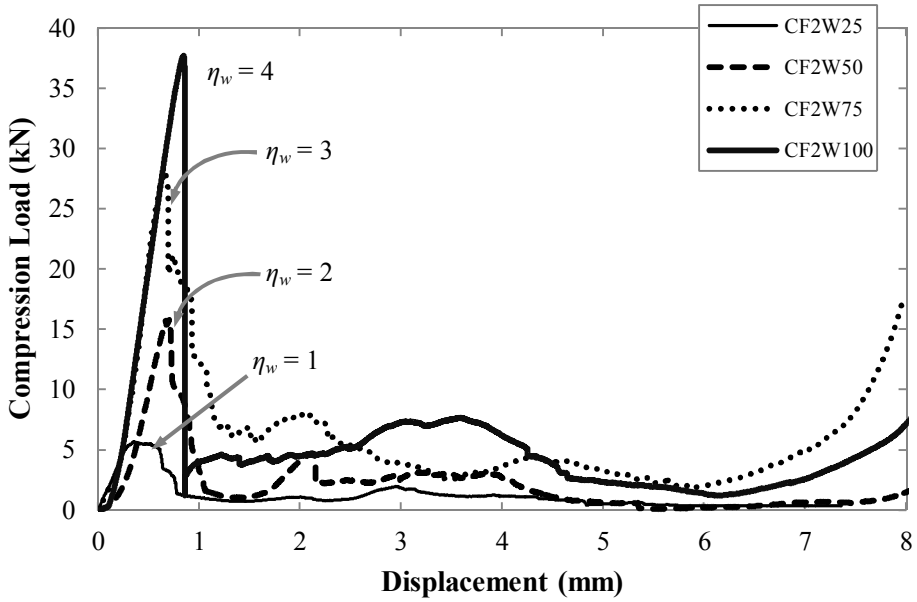

Figure 4.22: Comparison of the load-displacement traces of CFRP corrugated-core sandwich specimens based on spans of 25, 50, 75 and 100 mm, respectively. (Note these specimens are based on 2 plies with 5 unit cells. The aspect ratio of the width, η_w is relative to a width of 25 mm, CF2W25).

4.3.5 The Influence of Crosshead Displacement Rates

The influence of varying the compression displacement rate was investigated by changing the crosshead speed of the testing machine. In Figure 4.23, the resulting load-displacement curves of the specimens show an increasing peak load. The strength of the CFRP specimens in Figure 4.23(c) significantly increased from a crosshead speed of 1 to 100 mm per minute. The damage modes were similar to those observed earlier in the AL, GFRP and CFRP specimens, since compression displacement rates up to 100 mm per minute are still considered as being in the quasi-static loading range.

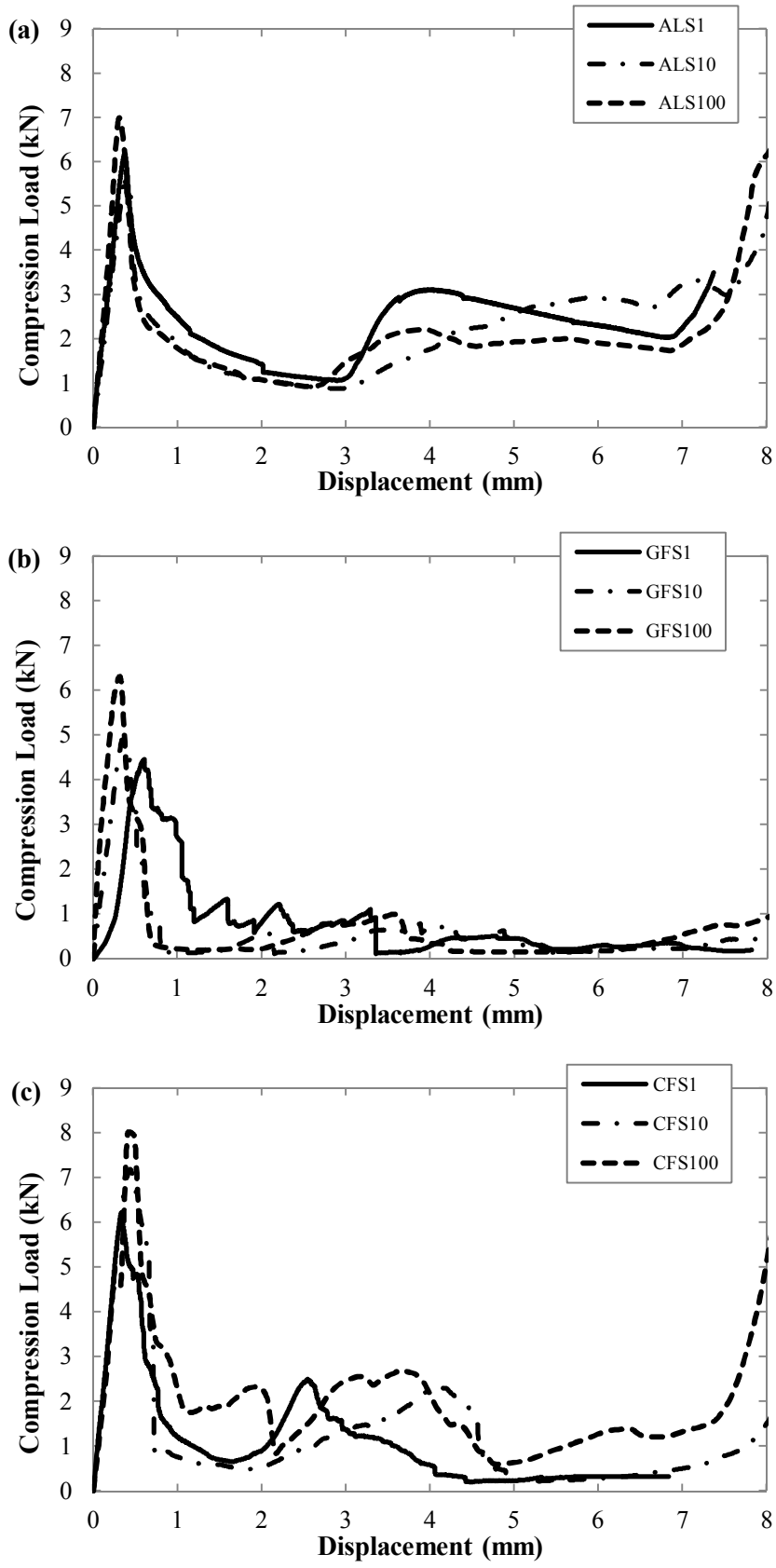

Figure 4.23: Comparison of load-displacement traces of corrugated-core specimens following testing at different compression displacement rates of 1, 10 and 100 mm per minute; (a) AL, (b) GFRP and (c) CFRP.

4.3.6 The Behaviour of the Composite Sandwich Structures filled with the Rigid Polyurethane Foam

The load-displacement traces for the GFRP and CFRP corrugated-core sandwich structures with and without foam are presented in Figures 4.24 and 4.25, respectively.

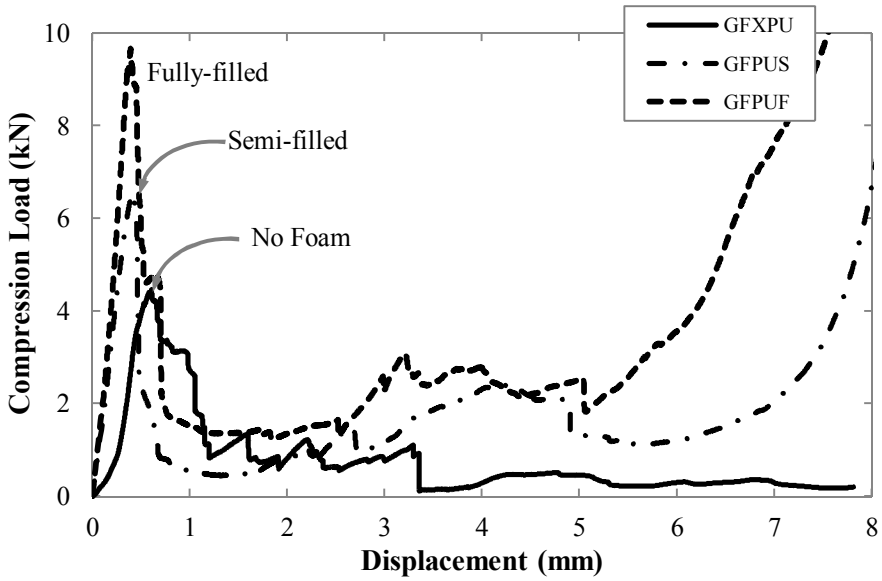

Figure 4.24: Comparison of load-displacement traces for the GFRP corrugated-core specimens for three different foam-filled core configurations.

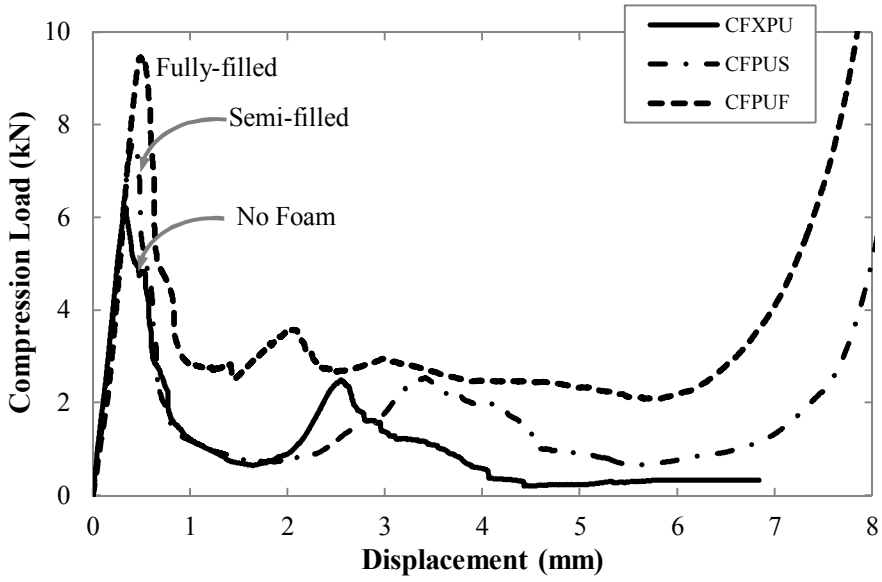

Figure 4.25: Comparison of load-displacement traces for the CFRP corrugated-core specimens for three different foam-filled core configurations.

From the figures, it is clear that the corrugated-core sandwich structures completely filled with foam (GFPUF and CFPUF) exhibit higher compression loads compared to the conventional corrugated-core and the semi-filled core (GFPUS and CFPUS).The load initially increases linearly up to the first peak, with deformation in the core being symmetrical about the axis of loading, as shown in Figure 4.26(a). The triangular corrugations were restrained by the upper and lower foam cores holding the struts during this early stage. In Figure 4.26(b), buckling in the five struts is observable, followed by compressive failure at peak load. The load then progressively decreases as fibres begin to fracture in the middle of individual struts and the foam is being compressed. Failure involved the formation of hinges in the middle of the cell wall and progressive crushing at the cell wall close to lower skin, as shown in Figure 4.26(c). Finally, the sandwich structure is completely crushed, and the core is fully flattened. This evidence indicates that the peak load almost doubles, reducing the sudden drops after peak load and increasing the energy absorption as a result of the interaction between the triangular corrugation and the inserted foam.

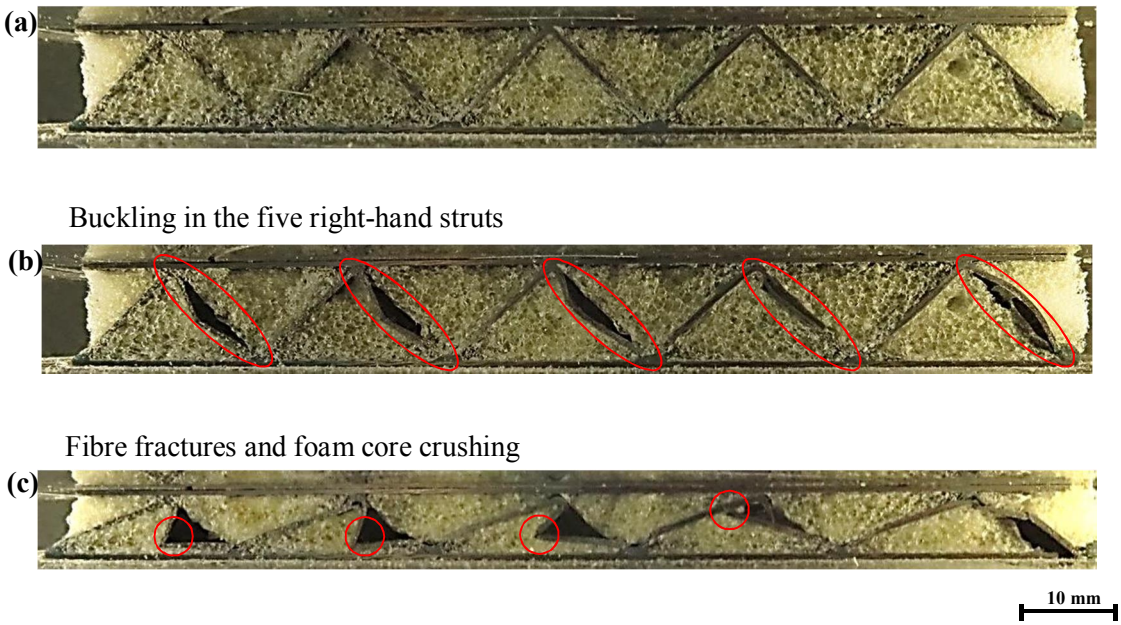

Figure 4.26: Photographs of progressive damage development in the CFPUF sandwich structure during (a) initial compression, (b) buckling in the cell wall structure and (c) core crushing.

Figure 4.27 shows the progressive damage development in the semi-filled corrugated-core sandwich structure. An observation of the structure during testing showed the once buckling of the middle strut had occurred, the buckled strut propagated easily into the unfilled area, see Figure 4.27(b). Further loading resulted in the structure collapsing as the lower foam compressed and debonding occurred at both ends. Delamination also occurred as the compression load progressively crushed the cores, as shown in Figure 4.27(c). This semi-filled configuration offers a peak load that is higher than the conventional corrugated-core (GFXPU). After the struts break, interactions between the surfaces of the cell walls and the lower foam increase the compression load again. Such interaction increases the energy absorption capability of the structure.

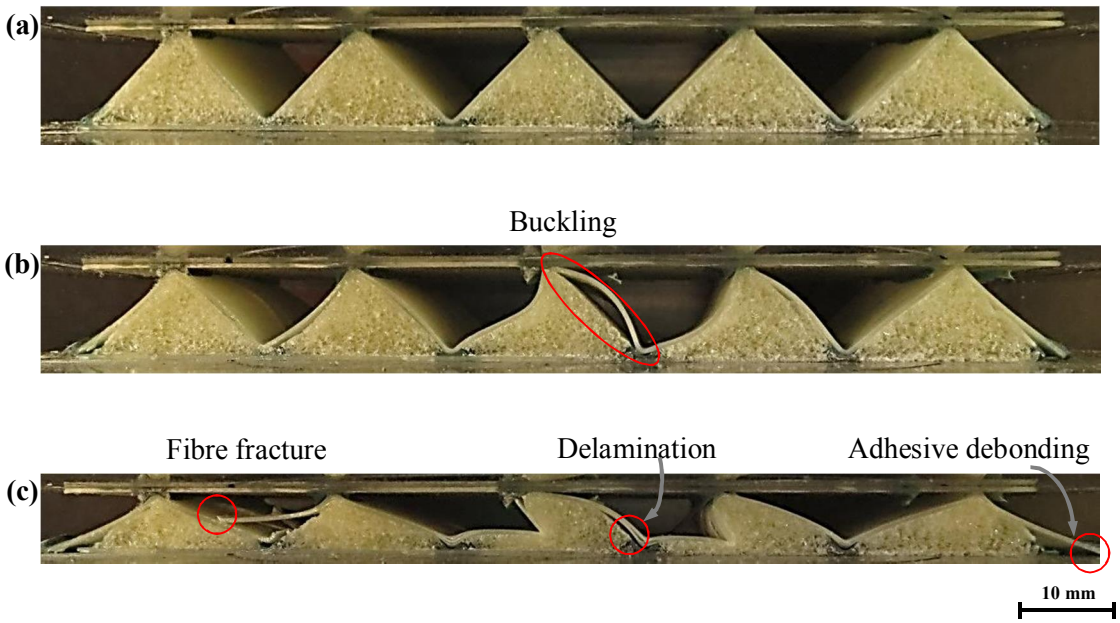

Figure 4.27: Photographs of progressive damage development in the GFPUS sandwich structure during (a) initial compression, (b) the buckling process and (c) the final stages of testing.

4.4 Arcan Tests

The Arcan tests were carried out to determine the mechanical responses of the specimens under mixed-mode loading conditions.

4.4.1 Model of Compressive-Shear Response of the Corrugated-core Structure

Consider a model of a corrugated-core with geometrical quantities as specified in Figure 4.28. Figure 4.28(a) shows a schematic diagram of the combined normal (n) and tangential (t) loading conditions on the top of one of the platens. The figure is characterised by a mixed-mode loading angle α, and the resultants of displacement δ, and an applied load P. The corrugated-cores investigated in this study can be considered as consisting of nine thin plates with a thickness to length ratio (H/L) of 0.035 and a thickness to width ratio (H/w) of 0.02. Given these values, the contribution to overall stiffness from bending of the constituent plates is negligible compared to that from stretching, as noted previously by Côté *et al.*[3].

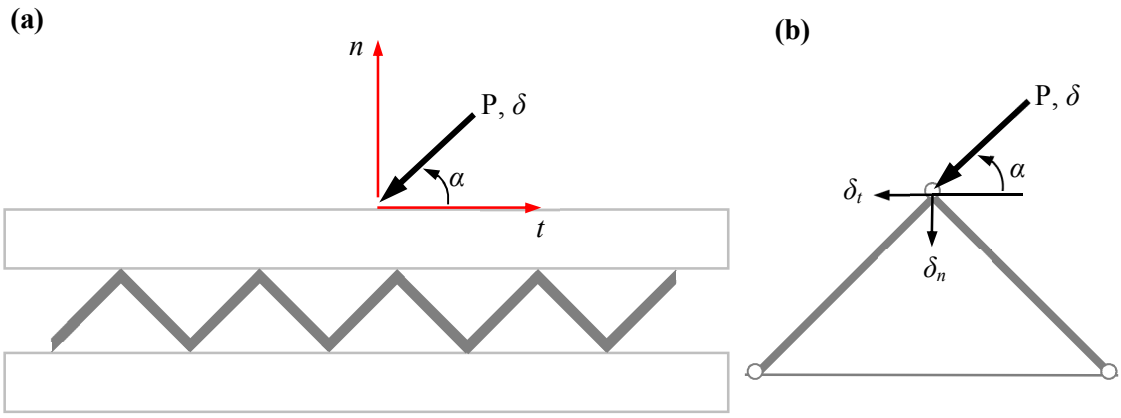

Figure 4.28: (a) A schematic of a mixed-mode loading condition on a corrugated-core structure, (b) a free body diagram of a single unit cell of the corrugated-core.

In Figure 4.28(b) it is assumed that the connections between adjacent plates can be regarded as pin-jointed. Now, for the case where the single unit model is subjected to an inclined load P at an angle α, the relationships between the applied load P and the tangential and normal displacements, δ_t and δ_n, can be shown to be equal to:

$$\begin{cases} \delta_t = \dfrac{\mathrm{P}L}{EHw}\cos\alpha \\ \delta_n = \dfrac{\mathrm{P}L}{EHw}\sin\alpha \end{cases} \qquad 4.26$$

The deflection in the direction of the applied load $\delta = \sqrt{\delta_t^{\,2} + \delta_n^{\,2}}$, and the initial stiffness (P/δ) is therefore given as;

$$\frac{\mathrm{P}}{\delta} = \frac{EHw}{L} \tag{4.27}$$

Figure 4.28(b) shows a schematic of the corrugated-core geometry considered in this study. For those cases where the load is either pure shear or pure compression, i.e. the angle α = 0° or 90° respectively, in-plane stretching or compression deformation occurs in all of the plates. For these two cases, the initial stiffness P/δ can be re-written as:

$$\frac{\mathrm{P}}{\delta} = \frac{9EHw}{2L} \tag{4.28}$$

In contrast, when a mixed form of loading is applied, i.e. for cases in which the loading angle α lies between 0° and 90°, the axial deformation in the right-hand plate becomes small and equals zero when the angle α = 45°. In such cases, the stiffness of the corrugated structure decreases and can now be approximated by:

$$\frac{\mathrm{P}}{\delta} = \frac{5EHw}{L} \tag{4.29}$$

Further, if the loading angle is increased beyond 90^{o}, the right-hand plate begins to carry the load and when α = 135°, the load in the left-hand plate is equal to zero, therefore the stiffness can be estimated by:

$$\frac{\mathrm{P}}{\delta} = \frac{4EHw}{L} \tag{4.30}$$

In transforming the load-displacement results to stress-strain data, the average compression and shear stresses, considering the horizontal load P_h acting along the top boundary in the normal and tangential directions can be calculated as follows:

$$\sigma = \frac{P \sin \alpha}{A_e} - \frac{P_h \cos \alpha}{A_e} \quad 4.31$$

$$\tau = \frac{P \cos \alpha}{A_e} + \frac{P_h \sin \alpha}{A_e} \quad 4.32$$

where A_e = the equivalent contact area = *w.x,* where *w* is width and *x* is the length of the specimen.

4.4.2 Pre-calibration of the Arcan Test Rig

Two calibration tests were conducted to correct the Arcan test raw data and give a high degree of confidence in the overall test results. Figure 4.29 shows typical raw data, a compliance curve and the corrected curve for an Arcan test on a corrugated-core structure. Here, the example of the compliance curve for a CFRP corrugated-core structure at a loading angle of 45° is shown. The compliance curve significantly corrects the raw data. A summary of the percentage correction from the compliance test is given in Table 4.2. The table shows that the greater level of correction in the pure shear (α = 0°) is due to the initial displacement of the adhesive as well as the machine stiffness. Such errors reduce when the loading angle is increased to 90°.

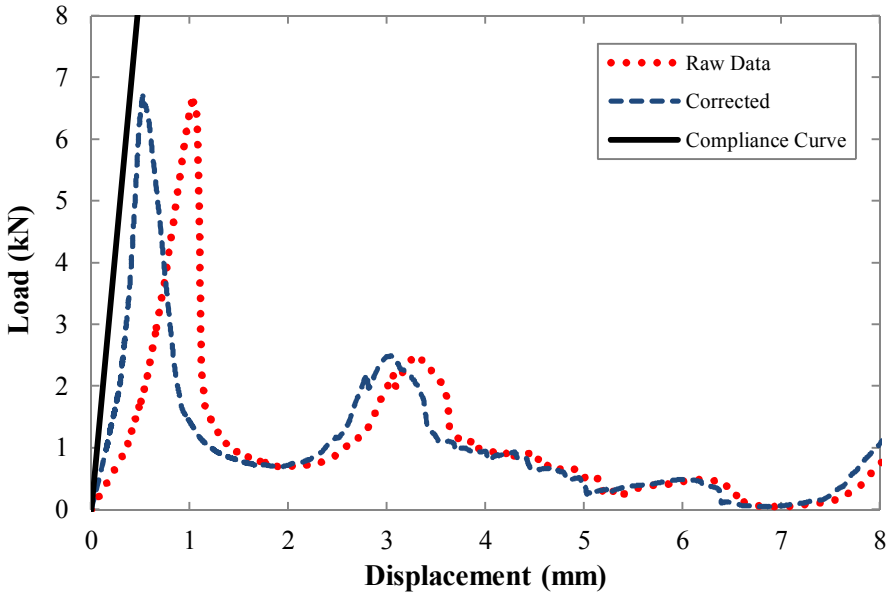

Figure 4.29: Typical load versus displacement trace for a corrugated-core structure (CF45 at 45° loading angle). The unwanted displacement is removed from the Arcan mixed-mode test data.

Table 4.2: A summary of the average initial stiffness values of the corrugated-core structures. The table includes the experimental data, the corrected data and the error between the raw data and the corrected data.

Materials	Loading angle, α	Raw data (kN/mm)	Corrected data (kN/mm)	Percentage Error (%)
AL	0^o	6.7	21.3	217.9
	45^o	10.6	27.5	159.4
	90^o	23.6	24.6	4.2
GFRP	0^o	6.8	15.7	130.9
	45^o	9.1	19.5	114.3
	90^o	15.2	16.8	10.5
CFRP	0^o	6.6	18.8	184.8
	45^o	10.8	22.6	109.3
	90^o	16.7	18.6	11.4

Figure 4.30 shows the results from multiple calibration tests on the Arcan fixture to obtain the transverse compliance of the test rig. The results show that the horizontal displacement of the Arcan test rig is consistent. It is then a straightforward transformation exercise to convert vertical and horizontal loads to determine the normal and shear loads acting on the specimen. The horizontal load (P_h) determined from the best fit curve and used in Equations 4.31 and 4.32, to calculate the normal and shear stresses.

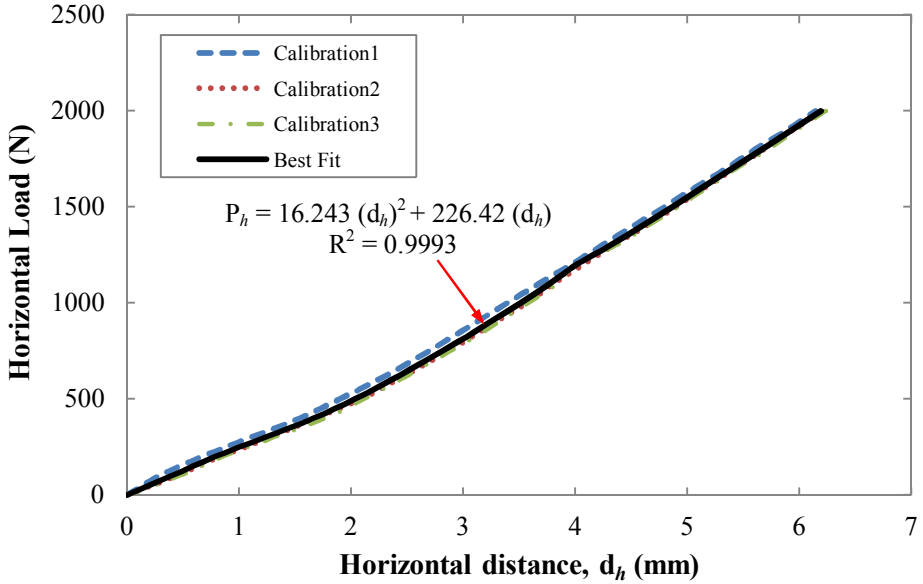

Figure 4.30: Calibration data of the horizontal load-displacement relationship for the Arcan test rig.

4.4.3 Arcan Tests on the Aluminium Corrugated-core Structure

Typical load-displacement traces following compression, shear and mixed-mode loading at 45° on the aluminium corrugated core structure are presented in Figure 4.31.

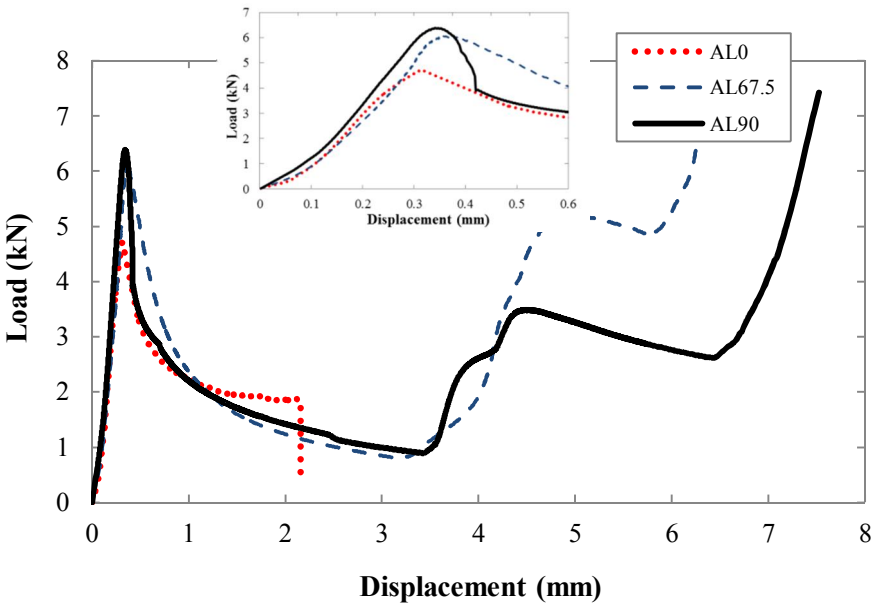

Figure 4.31: Typical load-displacement traces for the aluminium corrugation subjected to pure compression (AL90), pure shear (AL0) and mixed compression-shear (AL67.5). The inset shows the initial stiffness in the elastic deformation region for three different loading angles.

Under uniaxial compression, the specimen (AL90) exhibits a linear response up to peak load, at which point one of the struts in the corrugation is bent, leading to a reduction in stiffness. The load required to further deform the specimen gradually decreases due to the propagation of localised buckling across the width of the core. The mechanical response then becomes progressively non-linear and the force drops rapidly as the structure loses stability due to plastic buckling. At intermediate displacements, the specimen takes on a trapezium shape and the applied load starts to increase again due to interactions between the cell walls and the loading platen. In the final phase of deformation, the corrugated-core was fully crushed, which, in certain cases, resulted in debonding between the loading platens and the core at the edges of the specimen. Under pure shear loading (AL0), it is apparent that the specimen stiffness is lower, and strain-to-failure is much lower by about ~24%, compared to that measured in pure compression. Buckling phenomena were

observed in the strut during the test. Debonding between the adhesive and the apex of the core was one of the failure modes that influenced the peak loads, instead of shear buckling.

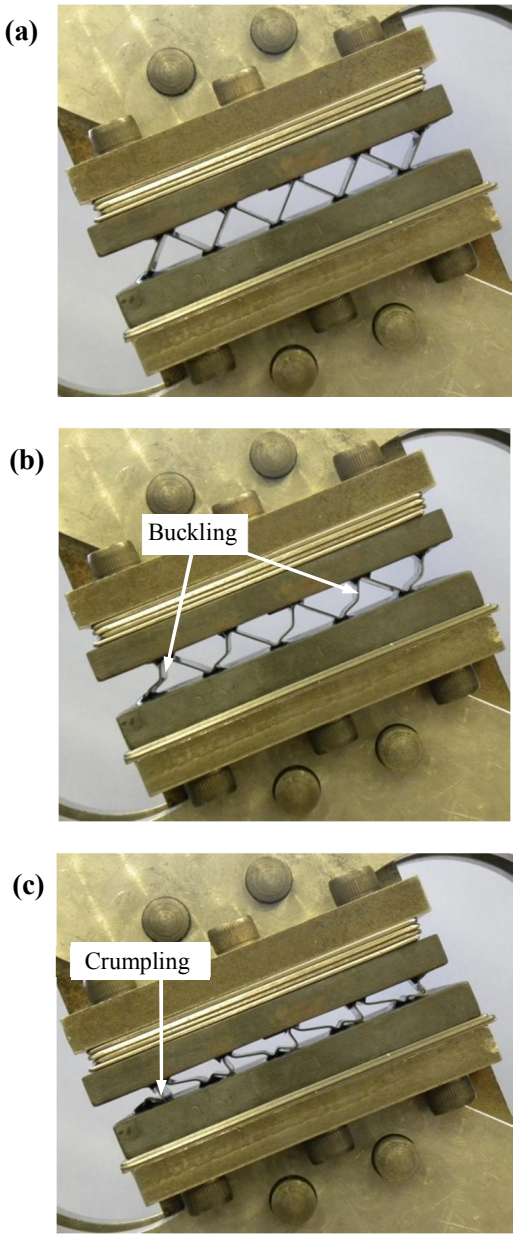

Figure 4.32: Photos of an aluminium corrugation at three different stages of compression-shear loading at 67.5^{o} loading angle; (a) unloaded, (b) initial buckling, and (c) crumpling at high displacements.

For the case of mixed-mode loading (specimen AL67.5) the load-displacement characteristics (stiffness and peak load) lie between those recorded following tests on the AL0 and AL90 specimens. The failure mechanisms observed during mixed-mode

loading are shown in Figure 4.32, for the case of $\alpha = 67.5^{o}$. Combined loading results in the progression of buckling deformation in middle of the loading process leading to crumpling at end of the test.

4.4.4 Arcan Tests on the GFRP Corrugated-core Structure

The load-displacement traces for the GFRP corrugated core structure generally exhibited a brittle type of behaviour, involving extensive crushing as shown in Figure 4.33.

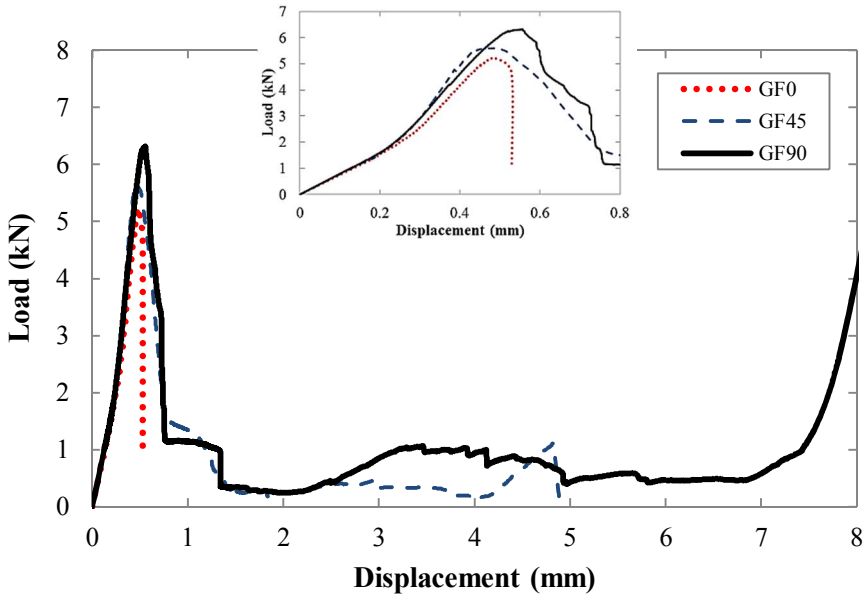

Figure 4.33: Typical load-displacement traces for the GFRP corrugation subjected to pure compression (GF90), pure shear (GF0) and mixed compression-shear (GF45). The inset shows the initial stiffness in the elastic deformation region for three different loading angles.

In the uniaxial compression response, the load increases linearly up to the first peak, with deformation in the core being symmetrical about the axis of loading. Cell wall buckling was initially observed, followed by compressive failure at the peak load. The load then progressively decreased as fibres begin to fracture in the middle of individual struts. Subsequent failure involved the formation of hinges in the middle of the cell wall and then progressive crushing at the cell wall close to the lower platen. During the final stages of the test, the core was fully crushed leading to it being flattened. In contrast, in shear, loading was linear up to the peak load at which point it dropped abruptly as a result of failure at the platens. Further investigation of

the specimens indicated that failure had occurred as a result of debonding between the core and the support, Figure 4.34. Under mixed-mode loading, the average stiffness and failure load lie between those associated with pure shear and pure compression loading conditions. It is clear that the failure strain along the bonding line is dependent on the shear loading contribution; for this glass/epoxy corrugation structure (at $\alpha = 45^{o}$), it is approximately 51%.

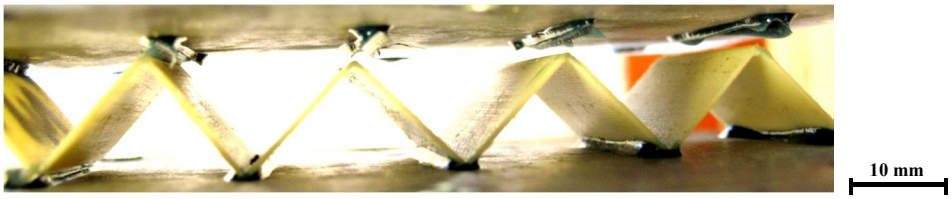

Figure 4.34: Photograph of one of the failure modes for the case where the corrugated-core was debonded from the loading platens.

4.4.5 Arcan Tests on the CFRP Corrugated-core Structure

The load-displacement responses for the CFRP corrugated structures are shown in Figure 4.35, where initial failure in pure compression was dominated by cell wall buckling.

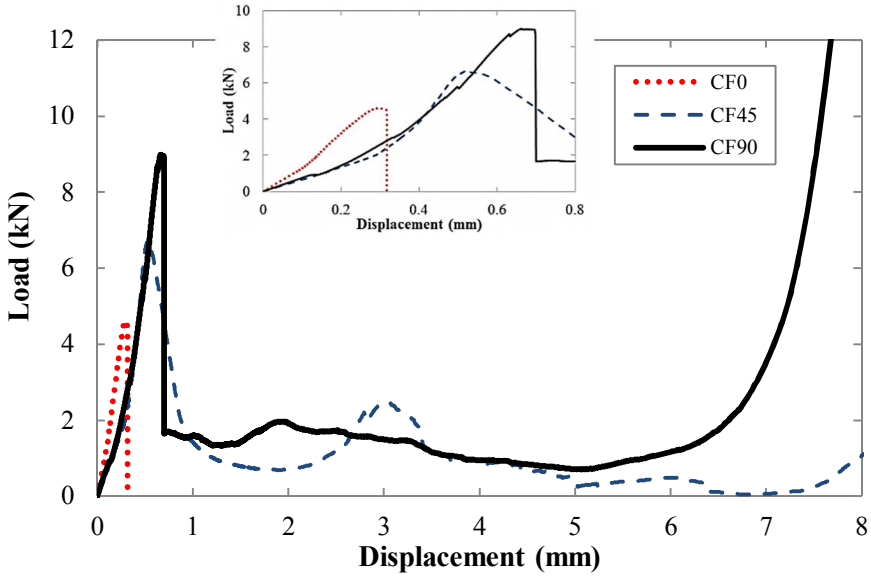

Figure 4.35: Typical load-displacement traces for the CFRP corrugation subjected to pure shear (CF0), pure compression (CF90) and mixed compression-shear (CF45). The inset shows the initial response in the elastic region for three different loading angles.

The load-displacement plot is steeper than that for the aluminium core and the failure modes are similar to the GFRP corrugated core structures. Following the initial linear response, the core buckles and the load drops suddenly. Subsequent failure involves fibre fracture, delamination and debonding between the core and the facings. Figure 4.36 shows the deformation process under mixed-mode loading at $\alpha = 45^{o}$, where the cell walls initially start to buckle, followed by fibre breaking in parts of the unit cell.

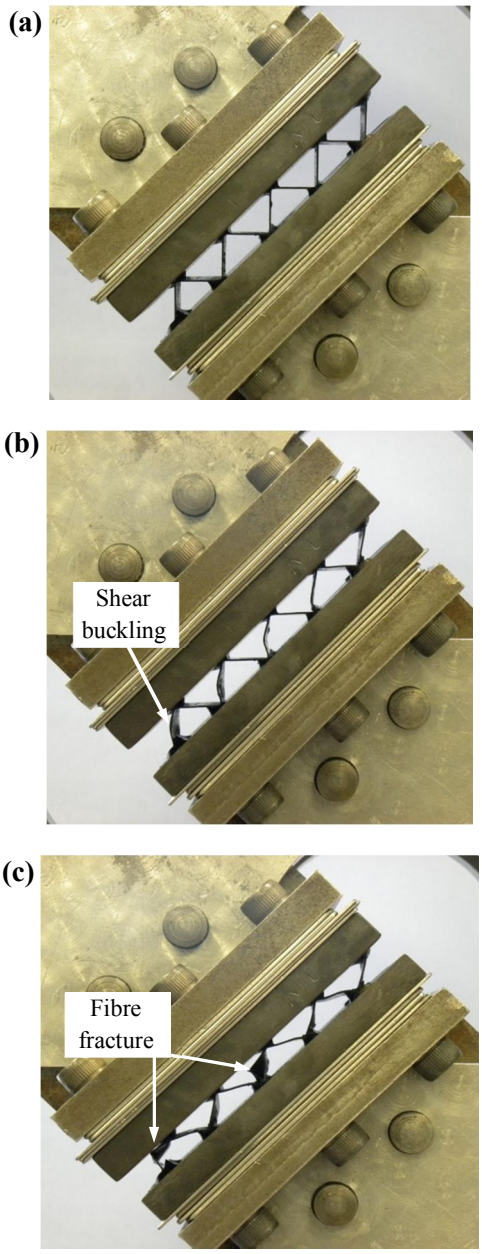

Figure 4.36: Photos of the CFRP composite corrugation at three stages of deformation under mixed-mode loading at 45^{o}; (a) unloaded, (b) initial cell wall buckling, and (c) fibre fracture in the unit cells.

Interestingly, instead of buckling in a two dimensional out-of-plane mode, as was the case in the aluminium and GFRP materials, the CFRP structure failed in a three dimensional mode, as shown in Figure 4.37. This different failure mode led to a reduction in the failure load and larger errors.

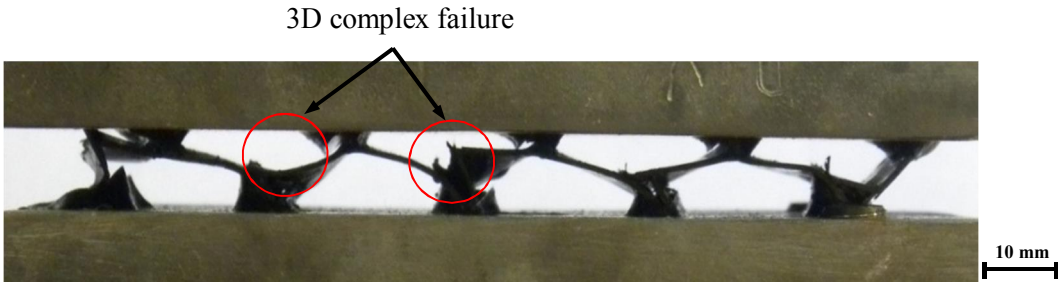

Figure 4.37: Failure mode in a CFRP corrugated-core structure showing 3D complex cell wall crushing.

A summary of the failure data for the aluminium, GFRP and CFRP corrugated-core structures are presented in Table 4.3.

Table 4.3: Experimental data at failure for the aluminium, GFRP and CFRP corrugation specimens. Note that standard deviations are given in the brackets.

Loading angle, α	Aluminium			GFRP			CFRP		
	Failure load, P (kN)	**Compression stress, σ (MPa)**	**Shear Stress, τ (MPa)**	**Failure load, P (kN)**	**Compression stress, σ (MPa)**	**Shear Stress, τ (MPa)**	**Failure load, P (kN)**	**Compression stress, σ (MPa)**	**Shear Stress, τ (MPa)**
0^o	5.20 (0.71)	-	2.31	6.09 (0.05)	-	2.70	8.46 (1.21)	-	3.76
22.5^o	5.41 (0.44)	0.92	2.22	5.85 (0.23)	1.00	2.40	7.27 (0.81)	1.24	2.98
45^o	5.93 (0.08)	1.86	1.86	5.89 (0.36)	1.85	1.85	7.99 (0.37)	2.51	2.51
67.5^o	6.36 (0.49)	2.61	1.08	6.20 (0.28)	2.55	1.05	8.65 (1.01)	3.55	1.47
90^o	6.80 (0.14)	3.02	-	6.48 (0.24)	2.88	-	10.29 (1.86)	4.57	-

4.5 Low Velocity Impact Tests

Impact tests were carried out to determine the dynamic compression responses of the specimens at different velocities.

4.5.1 Impact Test

A free-fall model of a low velocity impact test was used to determine the maximum impact force at various drop heights. Figure 4.38 shows the free body diagram for the test setup.

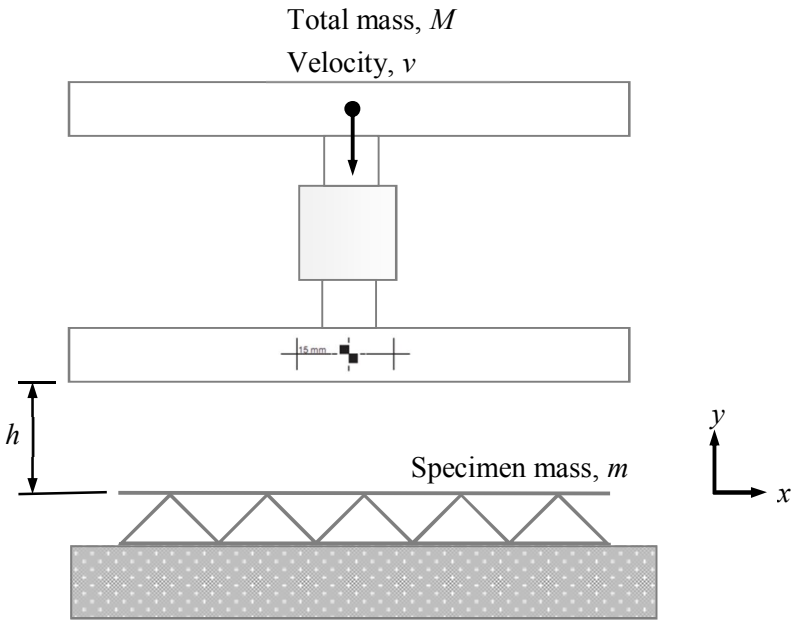

Figure 4.38: The schematic diagram showing the impact test setup.

The impactor mass, M was released from a height, h to strike the specimen. Here, the impact energy, E_i from the free-falling impactor can be calculated as:

$$E_i = Mgh \tag{4.33}$$

where g is the gravitational constant (9.81m/s^2) and h is the height of fall of the impactor. It is assumed that all of the potential energy is converted into kinetic energy. Therefore the impact energy is given as:

$$E_i = \frac{1}{2} M v^2 \tag{4.34}$$

where v is the velocity of the impactor before striking the specimen. Equating Eqs. 4.33 and 4.34, the initial or striking velocity, v is defined as:

$$v = \sqrt{2gh} \tag{4.35}$$

In principle, the impact or contact force is derived as:

$$F = Mg - f = M\frac{dv}{dt} = Ma \tag{4.36}$$

with f is a frictional force.

In this study, the contact force, F on the specimen was obtained directly from the load cell, after converting the voltage-time (v-t) history to a force-time (F-t) curve. Meanwhile, the captured images from the high speed video camera were analysed and then converted to a displacement-time (d-t) history. Contact force-displacement (F-d) traces were produced by synchronising the time histories from the F-t and d-t diagrams. From the F-d curve, the energy absorption of the specimen was calculated by integrating the area under the curve, as below:

$$E_a = \int_0^{d_{\max}} F.dy \tag{4.37}$$

where y is vertical displacement and $d_{\max}$ is the maximum displacement in the test.

Note that this is a large mass impact response [9] with the mass ratio, $\mathbf{m}^*=M/m > 2$. Next, all of the output results presented here used a filtering frequency of 10 kHz.

4.5.2 Impact Response at Low Energies

The corrugated-core sandwich specimens were tested at five different velocities, as outlined in Table 3.7.

Figure 4.39 shows typical contact force and displacement against time traces for the specimens in which the impact energy, E_i is less than the energy to break the

specimen, E_b. The contact force and displacement against time traces are smooth, and have the same total contact duration, t_{total}. The maximum contact force shows the F_{max} is at the highest point on the curve, and where t_{peak} which indicates the time to reach F_{max}. Here, the maximum displacement d_{max} is at the same contact time as t_{peak}.

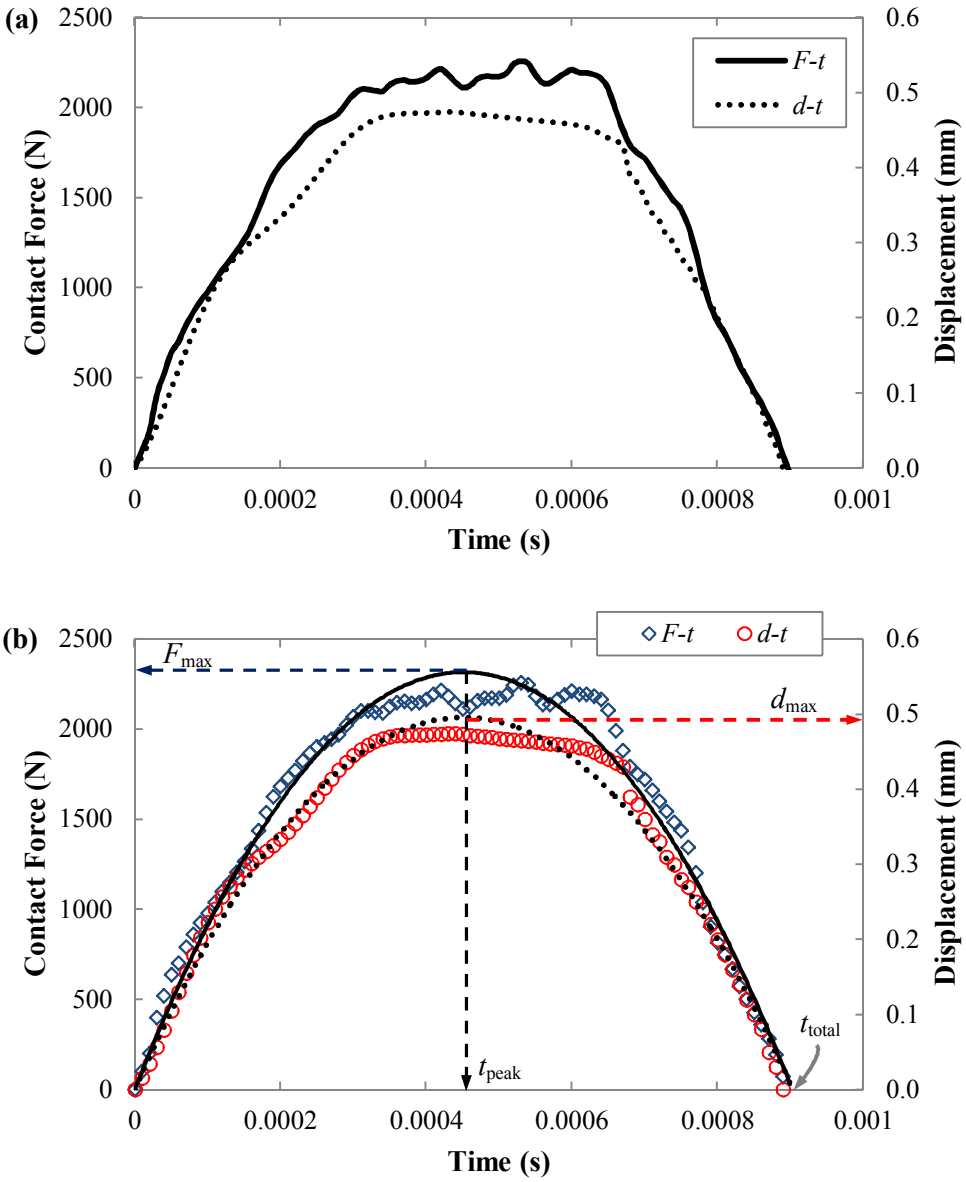

Figure 4.39: Typical *F-t* and *d-t* histories for an impact energy below that to break the specimen, (a) experimental data and (b) best fit curves showing that the maximum contact force and the maximum displacement happen at the same time, t_{peak} when F_{max} occurs. Data taken from an AL corrugated-core specimen at a drop height, h = 50 mm.

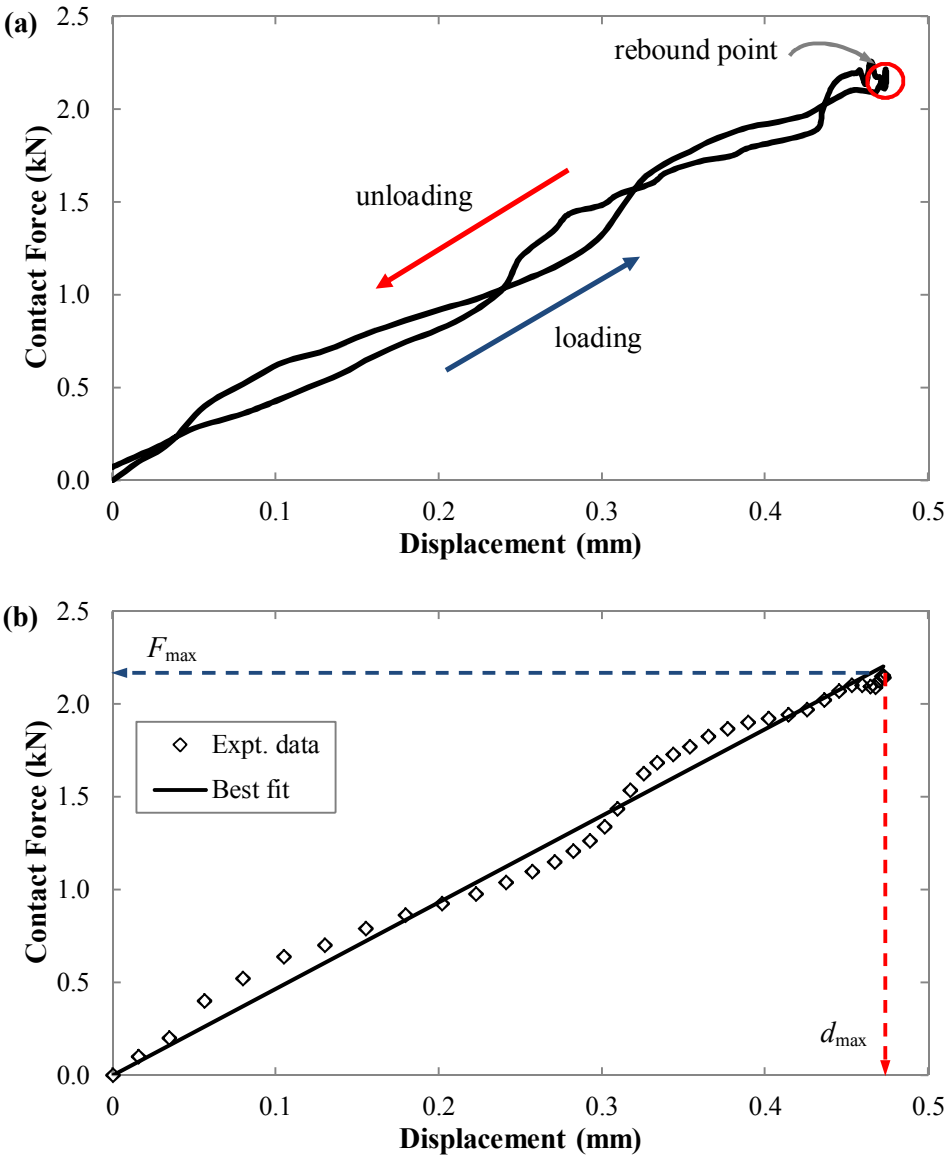

Figure 4.40: Typical *F-d* traces for an impact energy less below that to break the specimen, (a) loading and unloading response and (b) best fit line to illustrate the contact force is proportional to displacement in the elastic regime.

In Figure 4.40, the *F-d* curve shows the loading and unloading responses in the linear deformation region when $E_i < E_b$. It is clear that the contact force increases proportionally with displacement. No sign of damage was observed either in the AL or the composites specimens at release heights of 50 and 100 mm. For these cases, the F_{max} and d_{max} values occurred at the same time, t_{peak}. The impactor then bounces back, as shown in Figure 4.41.

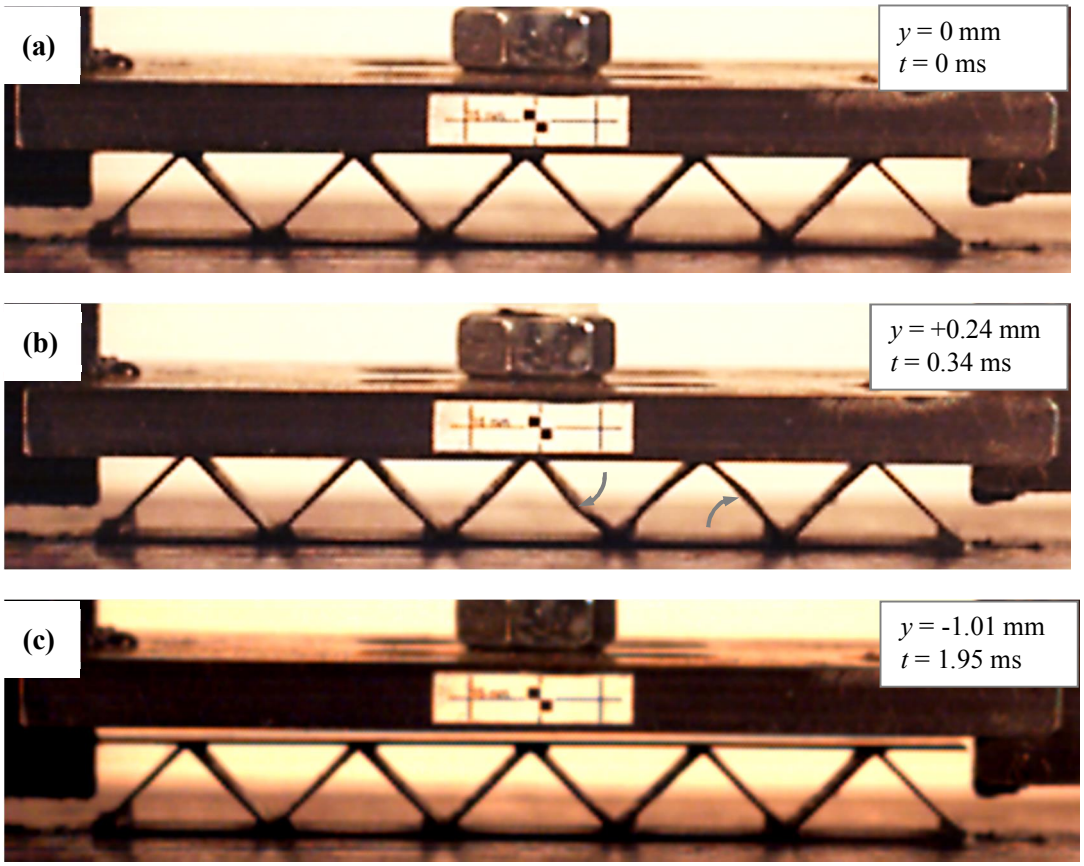

Figure 4.41: Impact images for an initial velocity, v of 0.99 m/s, (a) just before contact with the top surface of the specimen, (b) elastic bending of the struts at the maximum impactor displacement, d_{max} and (c) the specimen returns to its original position and the impactor rebounds. Impact on a CFRP corrugated-core specimen from a drop height, h = 50 mm. The impactor mass ratio, **m*** =173.

4.5.3 Impact Responses beyond Threshold Energy to Break the Specimens

Figures 4.42 and 4.43 show the impact response of the corrugated core structure when the impact energy exceeds the threshold energy for the metal and composite specimens.

Figure 4.42(a) shows the *F-t* and the *d-t* histories for the AL corrugated-core sandwich specimen, and it was found that the d_{max} occurs at a very different contact duration, t_{peak} than F_{max}. Combining the *F-t* data with the *d-t* data yield the contact force-displacement curve for the impactor, as shown in Figure 4.42(b). Three important points are identified in the *F-d* curve for this ductile specimen. The first point (P1) is the point on the curve that has the highest contact force before the struts collapse. After P1, the fluctuating force gradually decreases under the buckling

collapse mechanism until the bent strut and the top surface of the skin became in contact with each other. Here, P2 is the second peak point on the curve, and the final point, P3 is the rebound point. This is the maximum deformation, d_{max} in the *F-d* curve. This point P3 corresponds to the instant at which the curve starts to move leftwards signifying impactor rebounding with a negative velocity.

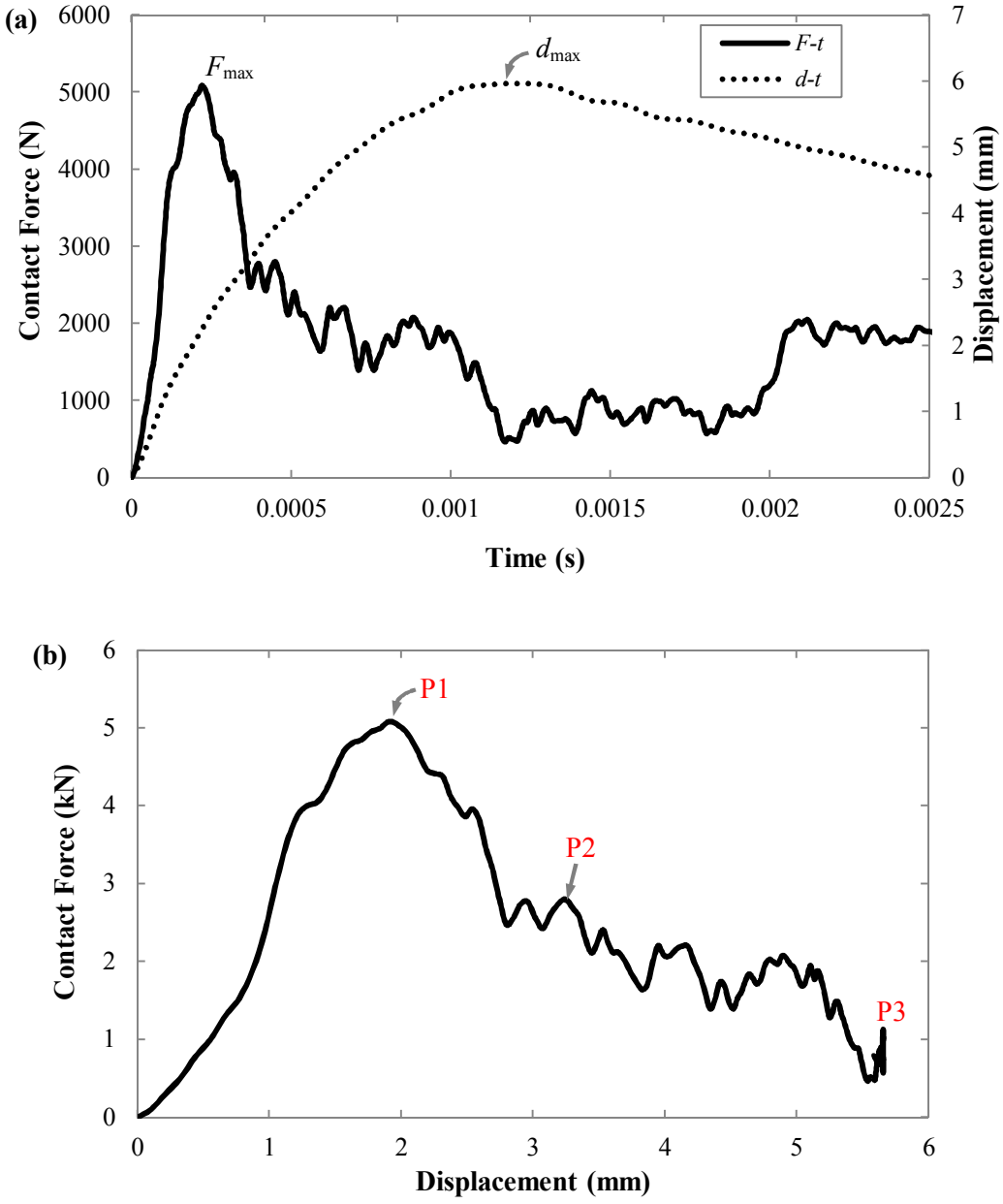

Figure 4.42: (a) Typical *F-t* and *d-t* histories for the AL corrugated-core sandwich specimen above its threshold absorb energy and (b) the *F-d* traces during the impact tests at a drop height, h = 1000 mm.

Furthermore, initial collapse in the AL corrugated-core specimens was characterised by a buckling phenomena. Two buckling modes were observed. Figure 4.43(a) shows the first buckling mode shape. As in the quasi-static compression test, the core members always buckle in an asymmetric manner with respect to the centre of the unit cell: one strut buckles to the right or left and other strut remains in the same position. This response contrasts with the behaviour at higher velocities. Figure 4.43(b) shows the combination of asymmetry and symmetry buckling mode shapes in the core. According to Vaughn and Hutchinson [10], this symmetry is due to the stabilising effect of core inertia on buckling.

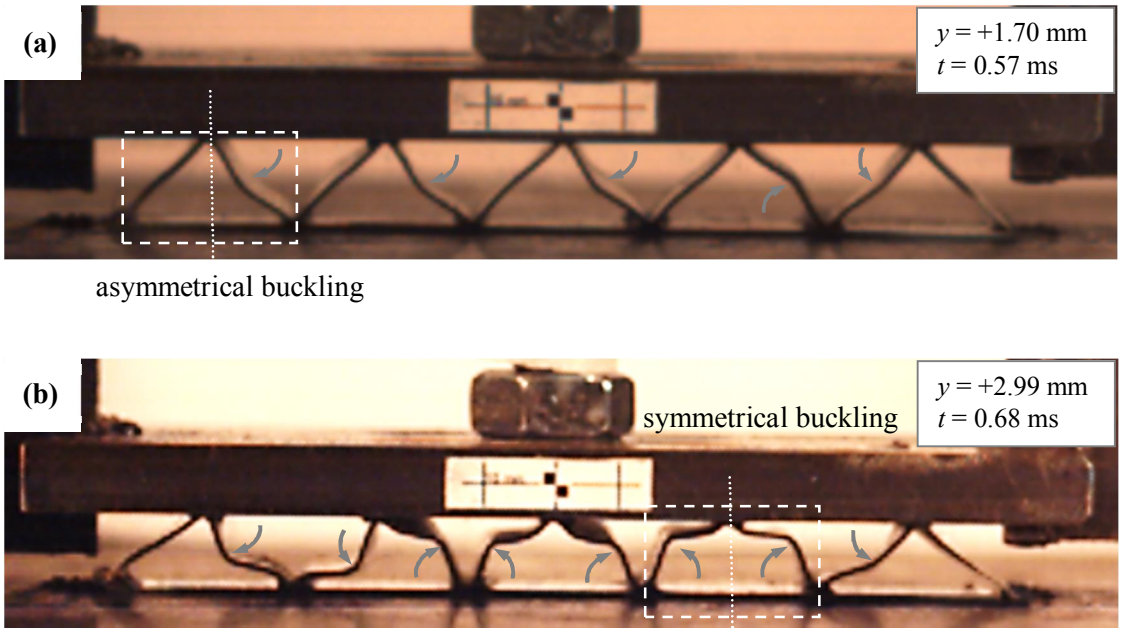

Figure 4.43: Two different buckling phenomena observed during testing: (a) asymmetrical buckling commonly found in out-of-plane compression loading (at v = 3.13 m/s) and (b) combination of two different buckling patterns, symmetrical and asymmetrical behaviour at an impact velocity of 4.43 m/s.

Given the elastic brittle behaviour of the composite specimens, an assumption based on the superposition of stresses is reasonable, where the struts loaded within the core are subjected to a combination of axial compression and bending loads [9]. Figure 4.44(a) shows the *F-t* and the *d-t* histories for the composite corrugated-core sandwich specimen, and Figure 4.44(b) is a typical *F-d* curve after combining the force versus time and the displacement versus time histories. Four points are indicated at the *F-d* curve for this type of brittle specimen. After reaching the

maximum contact force (P1), the force progressively decreases to crush the cell wall until the bent strut and the top surface of the skin become in contact with each other. P3 is a second peak on the curve. The core is now fully crushed and is no longer capable of resisting the force. The force subsequently oscillates until the rebound point, P4.

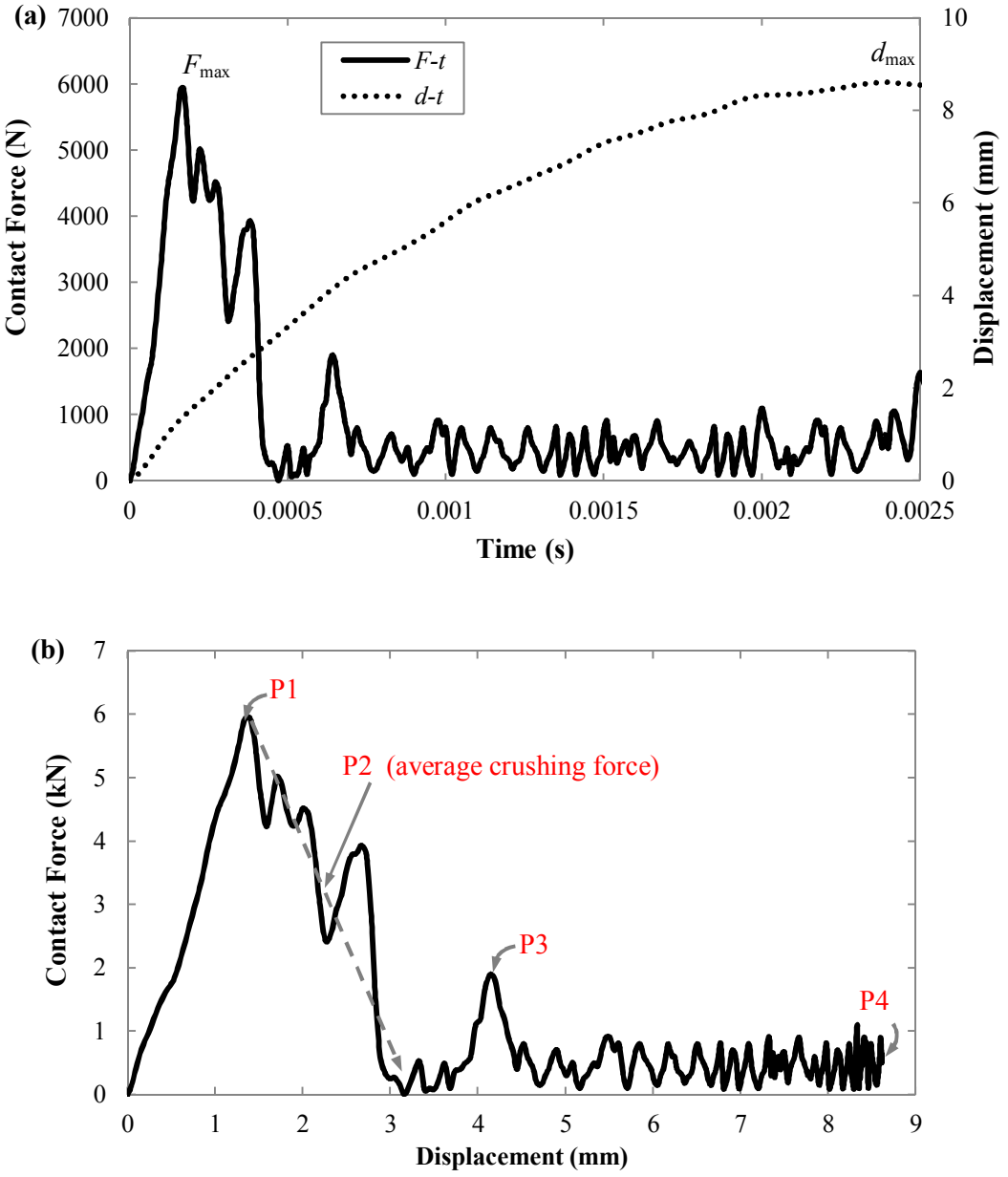

Figure 4.44: (a) Typical *F-t* and *d-t* histories for the CFRP corrugated-core sandwich specimen above its threshold impact energy and (b) the *F-d* curve following the impact test from a drop height, h = 1000 mm.

For both GFRP and CFRP materials, the progressive failure mechanisms involved in the crushing process include symmetric and asymmetric buckling, delamination between the plies and debonding of the adhesive between the core and the skin. Kazemahvazi *et al.* [9] also reported that the buckling modes in the corrugated-core specimens rise dramatically with increasing velocity. The failure mode shape for the composite struts with an aspect ratio, H/L = 0.035 at an impact velocity of 5 m/s is a Mode 2 sine wave. Typical impact sequences of buckling progression up to failure are shown in Figure 4.45. Table 4.4 summarises the maximum contact force, peak time, maximum displacement and energy absorption for all of the test specimens.

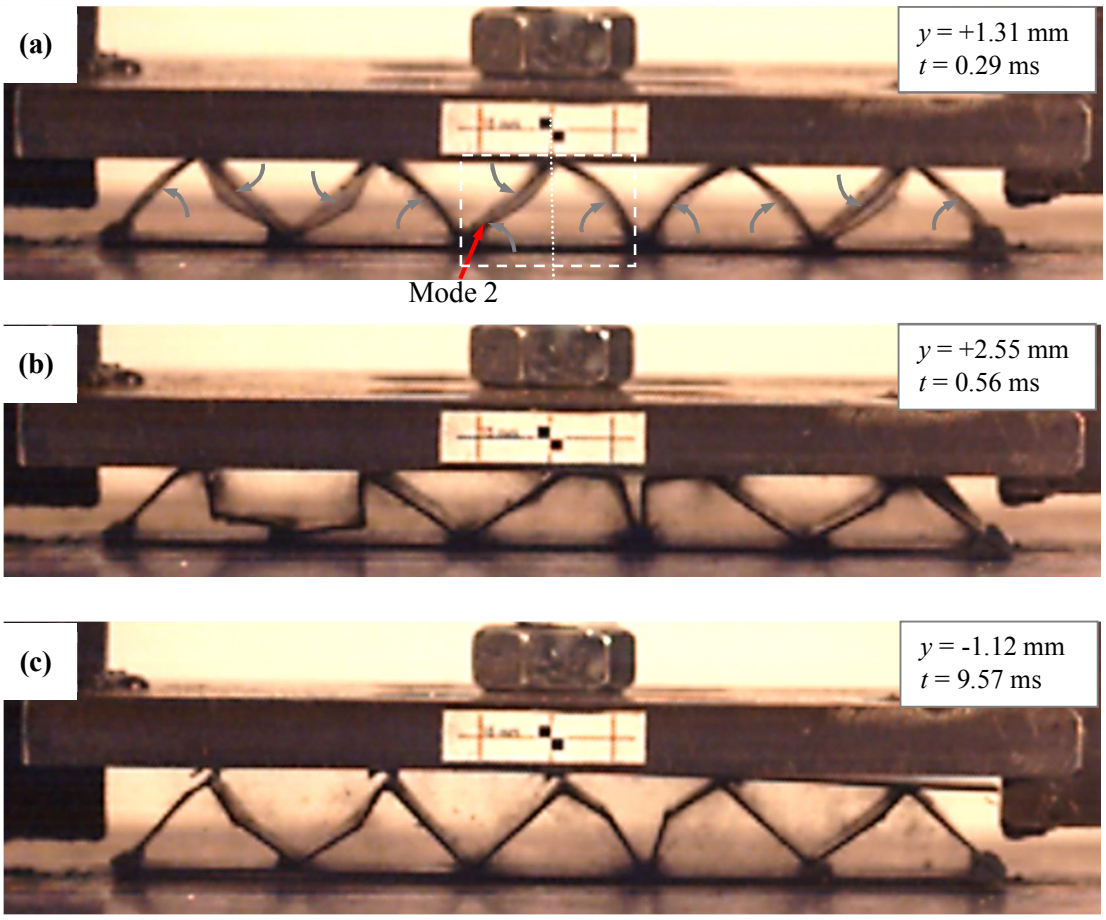

Figure 4.45: Impact images of the composite (CFRP) corrugated-core sandwich specimen at an impact velocity of 4.43 m/s, (a) initial failure is dominating by buckling (combined mode shapes of 1 and 2), (b) failures (fibre fracture, matrix cracking) and (c) rebound of the impactor as the top skin debonds from the core.

Table 4.4: Summary of the results of impact tests on the three corrugated-core sandwich materials; AL, GFRP and CFRP.

		Aluminium				GFRP				CFRP			
Impact velocity, v (m/s)	**Impact energy, E_i (J)**	**Max. contact force, F_{max} (kN)**	**Max. disp., d_{max} (mm)**	**Contact time at peak force, t_{peak} (ms)**	**Energy absorbed, E_a (J)**	**Max. contact force, F_{max} (kN)**	**Max. disp., d_{max} (mm)**	**Contact time at peak force, t_{peak} (ms)**	**Energy absorbed, E_a (J)**	**Max. contact force, F_{max} (kN)**	**Max. disp., d_{max} (mm)**	**Contact time at peak force, t_{peak} (ms)**	**Energy absorbed, E_a (J)**
0.99	0.61	2.51	0.30	0.48	0.36	3.47	0.53	0.39	0.48	3.18	1.46	0.34	0.23
1.40	1.22	6.31	0.39	0.31	0.88	3.99	0.65	0.25	0.81	7.35	2.91	0.30	0.92
1.98	2.45	7.09	0.88	0.26	1.83	6.11	1.07	0.25	1.61	7.54	4.01	0.28	2.22
3.13	6.12	7.37	1.70	0.24	5.67	5.89	3.55	0.21	6.05	6.53	3.32	0.24	6.04
4.43	12.24	6.24	5.96	0.24	11.26	5.83	9.01	0.20	10.01	6.74	8.61	0.16	12.16

Note:
For AL: **m*** = 98, E_a at the first peak in the quasi-static compression test is 1.23 J.
For GFRP: **m*** = 170, E_a at the first peak in the quasi-static compression test is 1.15 J.
For CFRP: **m*** = 173, E_a at the first peak in the quasi-static compression test is 1.09 J.

4.6 Summary of Chapter IV

Chapter IV presented the experimental results for the aluminium alloy 2024-O, GFRP and CFRP corrugated-core materials. Firstly, the mechanical properties of the materials were characterised during tensile and in-plane shear tests. The data for the corrugated-core sandwich specimens under quasi-static and dynamic compression tests, and combined compression-shear loading were presented and the failure mechanisms were discussed in detail. The fundamental theories to support each of the tests were derived and explained. Further discussion and analysis with additional experimental results will be presented in Chapter VI.

4.7 References

[1] Gibson LJ, Ashby MF. Cellular Solids: Structure and Properties. 2nd Edition ed: Cambridge Solid State Science Series; 1999.

[2] Alias A, Mines RAW, Birch RS, Li QM, Close JA. On the measurement of the crush behaviour of structural foams. 11th International Conference on Experimental Mechanics, Oxford;1998.

[3] Cote F, Deshpande VS, Fleck NA, Evans AG. The compressive and shear responses of corrugated and diamond lattice materials. International Journal of Solids and Structures. 2006;43(20):6220-6242.

[4] Kazemahvazi S, Zenkert D. Corrugated all-composite sandwich structures. Part 1: Modeling. Composites Science and Technology. 2009;69(7–8):913-919.

[5] Bleich F. Buckling Strength of Metal Structures. London: McGraw-Hill Book Company; 1952.

[6] Turvey GJ. Buckling and Postbuckling of Composite Plates: Springer; 1995.

[7] Xiong J, Ma L, Wu L, Liu J, Vaziri A. Mechanical behavior and failure of composite pyramidal truss core sandwich columns. Composites Part B: Engineering. 2011;42(4):938-945.

[8] Zenkert D. An Introduction to Sandwich Construction: Engineering Materials Advisory Services Limited; 1995.

[9] Kazemahvazi S, Russell BP, Zenkert D. Impact of carbon fibre/epoxy corrugated cores. Composite Structures. 2012;94(11):3300-3308.

[10] Vaughn DG, Hutchinson JW. Bucklewaves. European Journal of Mechanics - A/Solids. 2006;25(1):1-12.

CHAPTER V: FINITE ELEMENT MODELLING

5.1 Introduction

In this chapter, both the numerical modelling theory as well as techniques used to model the response of the specimens under static and dynamic loading are presented. The numerical predictions are compared to corresponding experimental results in order to validate the numerical models, using a commercial finite element analysis (FEA) package, Abaqus.

Abaqus/CAE Version 6.12 was used for creating, submitting, monitoring and visualising the results for both the static as well as dynamic models. The input files generated by Abaqus/CAE were submitted to the designated solvers, i.e. either Abaqus/Standard or Abaqus/Explicit. The static analyses were conducted using Abaqus/Standard, whereas Abaqus/Explicit was used for the dynamic problems.

In general, Abaqus/Standard is a general-purpose analysis product that can solve a wide range of linear and nonlinear problems involving the static, dynamic, thermal and electrical and electromagnetic response of components. The analysis solves a system of equations implicitly at each solution 'increment'. In contrast, Abaqus/Explicit marches a solution forward through time in small time increments without solving a coupled system of equation at each increment (or even forming a global stiffness matrix). In other words, the explicit solver is a special-purpose analysis package that uses an explicit dynamic finite element formulation. It is suitable for modelling brief, transient dynamic events, such as impact and blast problems, and is also very efficient for highly nonlinear problems involving changing contact conditions, such as forming simulations [1].

5.2 Constitutive Models for the Aluminium Alloy

This section presents the constitutive models for the aluminium alloy (AL 2024-O) that was used to manufacture the corrugated-core structure. To model the metal specimen, an isotropic elasto-plasticity model was chosen to predict elastic and plastic behaviour. This material model is commonly used for metal plasticity analyses, either as a rate-dependent or rate-independent model, and has a simple form [2].

5.2.1 Elasticity

An isotropic linear elasticity model was used to generate the elastic response of the material in the numerical model. For materials that exhibit linear elastic behaviour, the total stress is defined from the total elastic strain as:

$$\sigma = D^{el}\varepsilon^{el} \tag{5.1}$$

where σ is the total stress, D^{el} is the fourth order elasticity tensor and ε^{el} is the total elastic strain [3].

From Equation 5.1, the stress-strain relationship for isotropic linear elasticity is given as:

$$\begin{bmatrix}\sigma_{11}\\ \sigma_{22}\\ \sigma_{33}\\ \sigma_{12}\\ \sigma_{13}\\ \sigma_{23}\end{bmatrix} = \frac{E}{(1+\upsilon)(1-2\upsilon)}\begin{bmatrix} 1-\upsilon & \upsilon & \upsilon & 0 & 0 & 0 \\ \upsilon & 1-\upsilon & \upsilon & 0 & 0 & 0 \\ \upsilon & \upsilon & 1-\upsilon & 0 & 0 & 0 \\ 0 & 0 & 0 & \frac{(1-2\upsilon)}{2} & 0 & 0 \\ 0 & 0 & 0 & 0 & \frac{(1-2\upsilon)}{2} & 0 \\ 0 & 0 & 0 & 0 & 0 & \frac{(1-2\upsilon)}{2} \end{bmatrix}\begin{bmatrix}\varepsilon_{11}\\ \varepsilon_{22}\\ \varepsilon_{33}\\ 2\varepsilon_{12}\\ 2\varepsilon_{13}\\ 2\varepsilon_{23}\end{bmatrix} \tag{5.2}$$

The Young's modulus, E, and the Poisson's ratio, υ, were well-defined in Equation 5.2. Note that $2\varepsilon_{ij} = \gamma_{ij}$, and γ is the shear strain.

The inverse relationship can be expressed as:

$$\begin{bmatrix}\varepsilon_{11}\\ \varepsilon_{22}\\ \varepsilon_{33}\\ \gamma_{12}\\ \gamma_{13}\\ \gamma_{23}\end{bmatrix} = \begin{bmatrix} \frac{1}{E} & \frac{-\upsilon}{E} & \frac{-\upsilon}{E} & 0 & 0 & 0 \\ \frac{-\upsilon}{E} & \frac{1}{E} & \frac{-\upsilon}{E} & 0 & 0 & 0 \\ \frac{-\upsilon}{E} & \frac{-\upsilon}{E} & \frac{1}{E} & 0 & 0 & 0 \\ 0 & 0 & 0 & \frac{1}{G} & 0 & 0 \\ 0 & 0 & 0 & 0 & \frac{1}{G} & 0 \\ 0 & 0 & 0 & 0 & 0 & \frac{1}{G} \end{bmatrix}\begin{bmatrix}\sigma_{11}\\ \sigma_{22}\\ \sigma_{33}\\ \sigma_{12}\\ \sigma_{13}\\ \sigma_{23}\end{bmatrix} \tag{5.3}$$

where G is the shear modulus; $G = \frac{E}{2(1+\upsilon)}$

The elastic material properties for the aluminium alloy (AL 2024-O) used in the numerical models were taken from experimental data, as previously discussed in Section 4.2.1. From the experimental results, the Young's modulus, E = 70.6 GPa and the Poisson's ratio, υ = 0.3.

5.2.2 Yielding

A von Mises yield surface was used for isotropic yielding. The Mises yield surface assumes that yielding of the metal is independent of the equivalent hydrostatic stress where this observation is confirmed experimentally for most metals under positive pressure stress. However it may be inaccurate for metals under conditions of high triaxial tension, when voids may nucleate and grow in the material [1].

5.2.3 Plasticity

Beyond the yield point, isotropic hardening was used to define the plastic behaviour of the AL material. To describe isotropic hardening, the yield stress, σ^0, is given as a tabular function of the plastic strain. Interpolation of the yield stress at any plastic strain state is done from the data table. It remains constant until plastic strain reaches the last value given in the table.

Decomposition of the total increment of strain is defined as:

$$d\varepsilon = d\varepsilon^{el} + d\varepsilon^{pl} \tag{5.4}$$

For a rate-dependent material, the relationship of the equivalent plastic strain rate, $\dot{\bar{\varepsilon}}^{pl}$, follows the uniaxial flow rate definition as:

$$\dot{\bar{\varepsilon}}^{pl} = \psi(q, \bar{\varepsilon}^{pl}, \theta_T) \tag{5.5}$$

where ψ is a known function, q is the von Mises equivalent stress, $\bar{\varepsilon}^{pl}$ is an equivalent plastic strain and θ_T is the temperature.

The plastic material properties for the aluminium alloy (AL 2024-O) used in the numerical models were obtained from experimental data, and are tabulated in Table 4.1.

5.2.4 Failure Criteria

The development of progressive damage and failure for ductile material were used to model the damage behaviour the aluminium material. Abaqus/Explicit offers two material failure models to account for damage and failure in ductile metals, using *SHEAR FAILURE and *TENSILE FAILURE or a combination of both. To calculate failure, the shear and tensile failure models use an equivalent plastic strain and a hydrostatic cut-off stress, respectively. Removing failed elements from meshes is possible for both failure models.

5.2.4.1 Damage for Ductile Metals

Two damage mechanisms for ductile metals were used in this study, these being the ductile damage and shear damage models.

The ductile fracture or ductile damage initation criterion is a model for predicting the onset of damage due to nucleation, growth and the combination of voids. This model activates when the following condition is satisfied:

$$\omega_D = \int \frac{d\bar{\varepsilon}^{pl}}{\bar{\varepsilon}_D^{pl}(\eta, \dot{\bar{\varepsilon}}^{pl})} = 1 \qquad 5.6$$

where ω_D is a state variable that increases monotonically with plastic deformation. The model assumes that the equivalent plastic strain at the onset of damage, $\bar{\varepsilon}_D^{pl}$, is a function of the stress triaxiality, $\eta = -p/q$, and the equivalent plastic strain rate, $\dot{\bar{\varepsilon}}^{pl}$. Note that p is the pressure stress and q is the Mises equivalent stress.

The second model, shear damage model is a shear fracture due to shear band localisation in ductile metals. This model will activate if the following condition is satisfied:

$$\omega_s = \int \frac{d\bar{\varepsilon}^{pl}}{\bar{\varepsilon}_s^{pl}(\theta_s, \dot{\bar{\varepsilon}}^{pl})} = 1 \qquad 5.7$$

where ω_s is a state variable that increases monotonically with plastic deformation and is relative to the incremental change in equivalent plastic strain, $\bar{\varepsilon}^{pl}$. The model assumes that the equivalent plastic strain at the onset of damage, $\bar{\varepsilon}_s^{pl}$, is a function of the shear stress ratio, $\theta_s = (q + k_s p)/\tau_{\max}$, and the equivalent plastic strain rate, $\dot{\bar{\varepsilon}}^{pl}$. Note that $\tau_{\max}$ is the maximum shear stress and k_s is a material parameter ($k_s = 0.3$ for the aluminium alloy [4]).

A linear damage evolution law based on effective plastic displacement was used in the study. This evolution will trigger when the condition of damage initation is reached, then the effective plastic displacement, $\bar{\varepsilon}^{pl}$, is defined by the evolution equation as:

$$\dot{\bar{u}}^{pl} = L_e \dot{\bar{\varepsilon}}^{pl} \qquad 5.8$$

where L_e is the characteristic length of the element.

5.2.4.2 Failure in Ductile Metals

Two failure models for ductile metals were considered in this study, these being shear and tensile failure models. Both models are applicable mainly to high-strain-rate and truly dynamic problems.

*SHEAR FAILURE damage parameter, ω is defined as:

$$\omega = \frac{\bar{\varepsilon}_0^{pl} + \sum \Delta\bar{\varepsilon}^{pl}}{\bar{\varepsilon}_f^{pl}} \qquad 5.9$$

where $\bar{\varepsilon}_0^{pl}$ is any initial value of the equivalent plastic strain, $\Delta\bar{\varepsilon}^{pl}$ is an increment of the equivalent plastic strain and $\bar{\varepsilon}_f^{pl}$ is the equivalent plastic strain at failure. Failure is assumed to occur when the damage parameter exceeds 1.

*TENSILE FAILURE is supposed to occur when the pressure stress, p becomes more tensile than the user-specified hydrostatic cut-off stress. This model is suitable for modelling dynamic spall or a pressure cut-off. In this study, the input value for the hydrostatic cut-off stress was set to 279 MPa [5].

In general, element deletion occurs if one of the failure models is met at an integration node, all the stress components will be set to zero and the node fails. When all of the nodes at any element fail, then the element will be removed from the mesh.

5.3 Constitutive Models for the Composites

This section presents the constitutive models for the composite materials, i.e. for the glass fibre reinforced plastic and carbon fibre reinforced plastics. To model these materials in the corrugated-core structures, a transversely isotropic material model was chosen to predict their elastic response. In-built progressive damage models for elastic-brittle behaviour, proposed by Hashin and Rotem [6], Hashin [7-9], Matzenmiller *et al.* [10], and Camanho and Davila [11] were used for predicting the onset of failure and the post-failure response of the fibre-reinforced composites.

5.3.1 Elasticity

As discussed in Section 3.2, a woven-type prepreg was used to manufacture the corrugated-core specimens. Here, it is assumed that the top plane of the woven laminate is the 1-2 plane. The 1-2 plane is a plane of material isotropy in one of the principal planes of an orthotropic body [12]. Hence, the Young's modulus of $E_{11} = E_{22} = E_{ip}$, the shear modulus of $G_{13} = G_{23} = G_{tt}$, and the Poisson's ratio of $\upsilon_{13} = \upsilon_{31} = \upsilon_{23} = \upsilon_{32} = \upsilon_{tt}$ directions where the lower terms of the *ip* and *tt* denote the 'in-plane' and 'through-thickness', respectively.

If the 3-direction is normal to the plane of isotropy (1-2 plane), the stress-strain relationship for transverse isotropy is given as:

$$\begin{bmatrix} \varepsilon_{11} \\ \varepsilon_{22} \\ \varepsilon_{33} \\ \gamma_{12} \\ \gamma_{13} \\ \gamma_{23} \end{bmatrix} = \begin{bmatrix} \frac{1}{E_{ip}} & \frac{-\upsilon_{ip}}{E_{ip}} & \frac{-\upsilon_{tt}}{E_{tt}} & 0 & 0 & 0 \\ \frac{-\upsilon_{ip}}{E_{ip}} & \frac{1}{E_{ip}} & \frac{-\upsilon_{tt}}{E_{tt}} & 0 & 0 & 0 \\ \frac{-\upsilon_{tt}}{E_{ip}} & \frac{-\upsilon_{tt}}{E_{ip}} & \frac{1}{E_{tt}} & 0 & 0 & 0 \\ 0 & 0 & 0 & \frac{2(1+\upsilon_{ip})}{E_{ip}} & 0 & 0 \\ 0 & 0 & 0 & 0 & \frac{1}{G_{tt}} & 0 \\ 0 & 0 & 0 & 0 & 0 & \frac{1}{G_{tt}} \end{bmatrix} \begin{bmatrix} \sigma_{11} \\ \sigma_{22} \\ \sigma_{33} \\ \sigma_{12} \\ \sigma_{13} \\ \sigma_{23} \end{bmatrix} \qquad 5.10$$

With this stiffness matrix, the total number of independent elastic constants of orthotropic system is reduced from nine to five. The mechanical properties of the GFRP and CFRP were obtained from a series of the tests, as discussed in Section 4.2. Table 5.1 gives a summary of the elastic properties for the GFRP and CFRP composites that were used in the FE analysis.

Table 5.1: Summary of the elasticity properties of the GFRP and CFRP materials.

Symbol	**Value (GFRP)**	**Value (CFRP)**	**Property**
E_{11}	23 GPa	48 GPa	Young's modulus in longitudinal direction
E_{22}	23 GPa	48 GPa	Young's modulus in transverse direction
E_{33}	5 GPa**	10 GPa*	Young's modulus in thickness direction
G_{12}	5 GPa	9 GPa	In-plane shear modulus
G_{13}, G_{23}	5 GPa**	9 GPa*	Through-thickness shear modulus
υ_{12}	0.15	0.1	In-plane Poisson's ratio
υ_{13}, υ_{23}	0.15**	0.1*	Through-thickness Poisson's ratio

*Assumption

**Data taken from reference [5]

5.3.2 Damage Development Model for the Fibre-Reinforced Composites

The progressive damage models for composites are based on combination models from the degradation of the stiffness matrix coefficients [10] before degradation at a material point based on four damage initation mechanisms [6-9]. This is followed by damage propagation in the post-damage initation phase, based on the evolution law of the damage variable [11].

Prior to damage initation, the material stiffness is given by:

$$\sigma = C_d \varepsilon \tag{5.11}$$

where C_d is the damaged elasticity matrix, which has the form of:

$$C_d = \frac{1}{D}\begin{bmatrix} (1-d_f)E_1 & (1-d_f)(1-d_m)\upsilon_{21}E_1 & 0 \\ (1-d_f)(1-d_m)\upsilon_{12}E_2 & (1-d_m)E_2 & 0 \\ 0 & 0 & (1-d_s)GD \end{bmatrix} \tag{5.12}$$

where $D = 1 - (1 - d_f)(1 - d_m)\ \upsilon_{12}\ \upsilon_{21}$, E_1 is the Young's modulus in the fibre direction, E_2 is the Young's modulus perpendicular to the fibre direction, d_f is the current state of fibre damage, d_m is the current state of matrix damage and d_s reflects the current state of shear damage.

Four different damage initation mechanisms were considered in the analysis, these are based on Hashin's damage model. These four initation criteria are:

Fibre tension $(\hat{\sigma}_{11} \geq 0)$:

$$F_f^t = \left(\frac{\hat{\sigma}_{11}}{X^T}\right)^2 + \xi\left(\frac{\hat{\sigma}_{12}}{S^L}\right)^2 \tag{5.13}$$

Fibre compression $(\hat{\sigma}_{11} < 0)$:

$$F_f^c = \left(\frac{\hat{\sigma}_{11}}{X^C}\right)^2 \tag{5.14}$$

Matrix tension $(\hat{\sigma}_{22} \geq 0)$:

$$F_m^t = \left(\frac{\hat{\sigma}_{22}}{Y^T}\right)^2 + \left(\frac{\hat{\sigma}_{12}}{S^L}\right)^2 \quad 5.15$$

Matrix compression $(\hat{\sigma}_{22} < 0)$:

$$F_m^c = \left(\frac{\hat{\sigma}_{22}}{2S^T}\right)^2 + \left[\frac{Y^C}{2S^T} - 1\right]\frac{\hat{\sigma}_{22}}{Y^C} + \left(\frac{\hat{\sigma}_{12}}{S^L}\right)^2 \quad 5.16$$

Note that $\hat{\sigma}_{ij}$ are the components of the effective stress tensor, and ξ is a coefficient that determines the contribution of the shear stress to the fibre tensile initation criterion. Table 5.2 presents the damage initation data for the GFRP and CFRP corrugated-core specimens.

Table 5.2: Summary of the damage initation data for the GFRP and CFRP materials.

Symbol	**Value (GFRP)**	**Value (CFRP)**	**Property**
X^T	320 MPa	550 MPa	Longitudinal tensile strength
X^C	260 MPa*	150 MPa*	Longitudinal compressive strength
Y^T	320 MPa	550 MPa	Transverse tensile strength
Y^C	260 MPa*	150 MPa*	Transverse compressive strength
S^T	100 MPa	120 MPa	Transverse shear strength
S^L	100 MPa	120 MPa	Longitudinal shear strength

*Assumption

Once a damage initation criterion is satisfied, further loading of the specimen will cause degradation of the material stiffness coefficients. The decrease in the stiffness coefficient is monitored by damage variables that assume values between 0 and 1; undamaged to a fully damage state. The damage variable corresponding to a specific failure mode is given by following expression:

$$d = \frac{\delta_{eq}^{f}(\delta_{eq} - \delta_{eq}^{0})}{\delta_{eq}(\delta_{eq}^{f} - \delta_{eq}^{0})} \qquad 5.17$$

where δ_{eq}^{0} is initial value of the equivalent displacement at which the initation criterion for the particular mode is met and δ_{eq}^{f} is the displacement when damaged.

Here, a linear damage evolution law based on the fracture energy dissipated during the damage process was introduced in the numerical model. The fracture energy values were set before running the FE analysis. Table 5.3 gives the fracture energies for the various failure modes.

Table 5.3: Summary of the fracture energy data for the GFRP and CFRP materials.

Symbol	**GFRP (J/m^2)**	**CFRP (J/m^2)**	**Failure mode**
G_{ft}^{C}	40000*	50000**	Fibre tension
G_{fc}^{C}	60000*	45000**	Fibre compression
G_{mt}^{C}	40000*	50000**	Matrix tension
G_{mc}^{C}	60000*	45000**	Matrix compression

*Data taken from reference [5]

**Data taken from reference [13]

5.4 Static Finite Element Modelling

This section presents details of the numerical modelling procedures for the corrugated-core structures under static compression and combined Arcan mixed-mode loading. Uniaxial compression of the rigid PU foam was also studied before modelling the corrugated sandwich structures filled with the foam. These three dimensional numerical simulations with six degrees of freedom were performed using Abaqus/Standard.

5.4.1 Modelling of Compression Corrugated-core Sandwich Structure

In this section, the FE modelling procedures for the corrugated-core sandwich structures based on three different types of materials are presented. The numerical results will be verified using experimental data at the end of this section.

5.4.1.1 Selection of Parts and Elements

The response of the corrugated-core sandwich structures under compression loading was modelled using the Kirchhoff shell element. This element was selected because it can be used to accurately model the behaviour of the metal and composite structures, which have a section thickness that is small relative to the overall dimensions of the components [3]. The S4R shell element is defined by four nodal points. These nodes show the spatial position of the element and define the normal direction of the shell using the right-hand rule. This S4R shell element is a general purpose element, and can be used in thin or thick shells. The element code relates to the following:

S4R – **S**tress/displacement element, **4** nodes, **R**educed integration.

In modelling the specimen, a deformable shell geometry was used to draw the shape of the unit cell in an in-plane view, and then extrude the geometry with the desired width, for example w = 25 mm to generate the triangular corrugated-core specimen. The edges of the triangular corrugations were modelled as perfect, this might influence both the strength and stiffness predictions. In these compression test simulations, the skins do not carry significant load and it was therefore sufficient to model the cores without skins, whilst applying the appropriate boundary conditions. Figure 5.1 shows the core with five unit cells between the upper and lower platens.

The compression platen was defined as a rigid body. There are two techniques to model a rigid body, either by an analytical rigid or a discrete rigid surface. Here, the circular compression platen was modelled using the analytical rigid surface. The analytical rigid surface is a geometric surface with profiles that can be described using straight and curved line segments [1]. Using this analytical rigid surface instead of discrete rigid surface formed by element faces reduces computational costs associated with the contact algorithm. The platen model does not undergo any deformation during the test, but can undergo large rigid body motions.

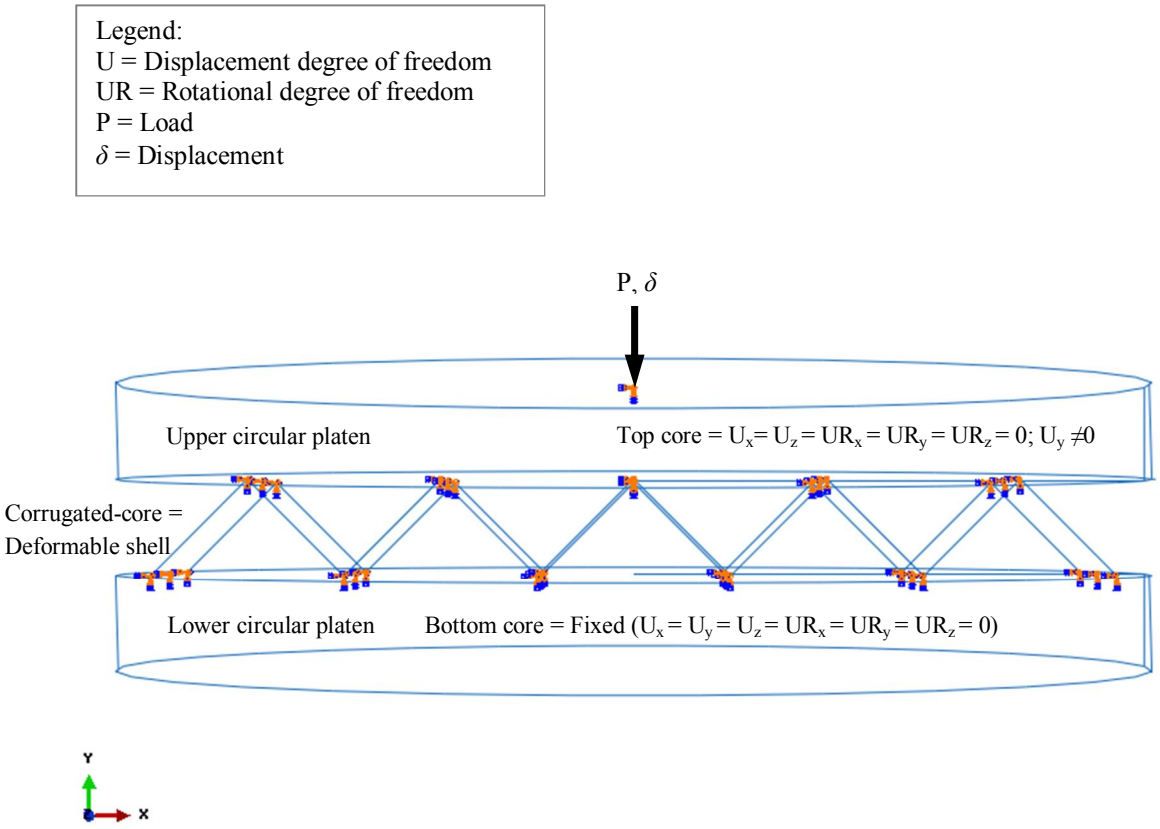

Figure 5.1: Loading direction, boundary conditions and assembly of the corrugated-core model between two platens.

5.4.1.2 Loading and Boundary Conditions

When establishing the boundary conditions, the nodes along the upper and lower edges were fully constrained, except in y-direction ($U_y \neq 0$) at the upper edge. This to allowed the upper edge to move downwards. A displacement boundary condition was applied uniformly to the nodes at the apex of the unit cells to progressively crush the unit cells. This displacement boundary condition was assigned to the reference

point, placed at the centre of the upper platen, and this was set to displace the platen downwards in vertical direction at a constant rate. The reference point was used to record the displacement and reaction load from the core.

5.4.1.3 Interaction Properties

The core and the platen were connected using a contact interaction formulation. A contact pair algorithm was used to model the interaction behaviour of the corrugated-core structures. In Abaqus/CAE, the user can refer to a contact property. In normal behaviour, a hard contact pressure-overclosure relationship and a frictionless formulation in the tangential direction were set as the contact properties.

The friction between the contacting surfaces was modelled using a Coulomb friction model. This friction model assumes that no relative sliding occurs if the equivalent frictional stress:

$$\tau_{eq} = \sqrt{\tau_1^2 + \tau_2^2} \tag{5.18}$$

is less than the critical stress. The critical stress, τ_{crit} is defined as:

$$\tau_{crit} = \mu p \tag{5.19}$$

where μ is the coefficient of friction and p is the contact pressure between the two surfaces. The term 'frictionless' refers to a friction coefficient of zero, i.e. surfaces free to slide across one another.

The hard contact property allows for contact pressures between two surfaces when the clearance is zero, and there is no pressure when the clearance is greater than zero, as illustrated in Figure 5.2. This contact property also minimises the penetration of the slave surface (the core) into the master surface (platen) at the constraint position and does not allow the transfer of tension stresses across the interface.

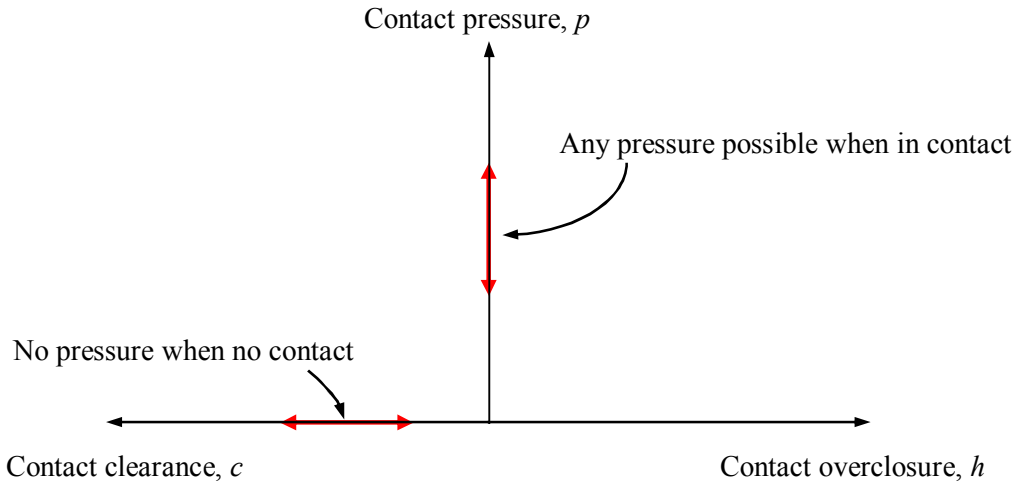

Figure 5.2: Contact pressure-overclosure relationship for hard contact [1].

5.4.1.4 Mesh Generation and Control

A mesh was then generated at a corrugated-core based on five unit cells using the meshing tools in Abaqus/CAE. Figure 5.3 shows the model used in the compression simulation study, comprising 25 linear shell elements across the width direction and 14 elements along the length of the struts, giving a total of 3500 elements. For the platen, there is no mesh required for an analytically rigid surface.

Figure 5.3: Typical meshes used in numerical modelling.

The default form of hourglass control available for the S4R element was used as well as reduced integration. Hourglass control attempts to minimise spurious modes [14] without introducing excessive constraints on the physical response of the element.

5.4.1.5 Modelling Data Output

The data output from the numerical models was specified by creating output requests. The Abaqus solver calculates the values of many variables at every step of increment. The user may control and manage the data output so that only data

required to interpret the results of the analysis is produced. An output request defines which variables are selected and outputted during the simulation step, from which region or integration points of the model and the rate at which the variable are written to the output database. There are two types of the output requests, field output or history output.

Field Output Request

Field outputs are generated from data that are spatially distributed over the whole model or over a portion of it. This output presents images of the specimen at each requested interval. In this numerical analysis, the displacement, the reaction force, the status, stress and strain field outputs were requested from the entire corrugated-core model. For the composite materials, failure was also requested.

History Output Request

History outputs are generated either from the whole model or specific points in the model. The frequency of data output depends on the users interest, and can be very high if necessary. When creating a history output request, the individual components of variables can be specified. In this study, the displacement and reaction forces for the relevant direction of the platen were requested in a history output at the specific reference point of the platen.

5.4.1.6 Model Sensitivity

The accuracy of the model can be improved in several ways. Sensitivities of the mesh refinement, imperfections from uneven cell wall thickness, the contact stiffness between the platen and the core can contribute to the inaccuracy of the analysis. Finally is the selection of the appropriate type of shell element for the model is clearly important.

a) Mesh Refinement

A mesh sensitivity study was carried out by varying the element size of the shell element throughout the core geometry. Figure 5.4 shows the variation of the peak load and CPU time with element size for the corrugated-core specimen.

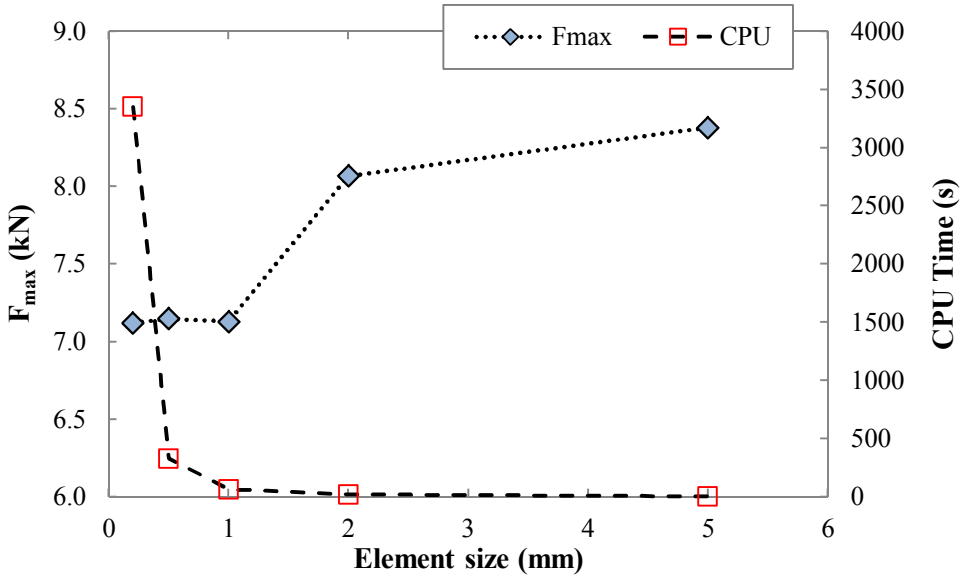

Figure 5.4: Typical mesh-sensitivity analysis showing maximum load and CPU time versus element size for the AL corrugated-core specimen with shell thickness of H = 0.5 mm.

Form Figure 5.4, the mesh sensitivity analysis shows that the maximum load in the model is dependent on element size. Here, a 1 mm element size was selected due to the optimum CPU time, and it was essential that the same size elements were used in all the specimen models. Therefore the combined effect of material property and element size was consistent throughout the study.

b) Contact stiffness

In the actual specimen preparation, the corrugated-core was bonded to the skins, and therefore there is a softening associated with the epoxy adhesive. To account for such effects, a linear softened contact pressure-overclosure formulation was employed during the initial stage of contact between the sharp edge of the core and the platen. The softened contact pressure-overclosure relationships might be used when modelling a soft, thin layer on one or both surfaces [2]. This relationship is useful for numerical reasons to make it easier to resolve the contact condition. Figure 5.5 shows the softened contact pressure relationship defined in linear form, where the contact stiffness, k_c is defined as:

$$k_c = \left.\frac{dp}{dh}\right|_{h=-0.9999c} \qquad 5.20$$

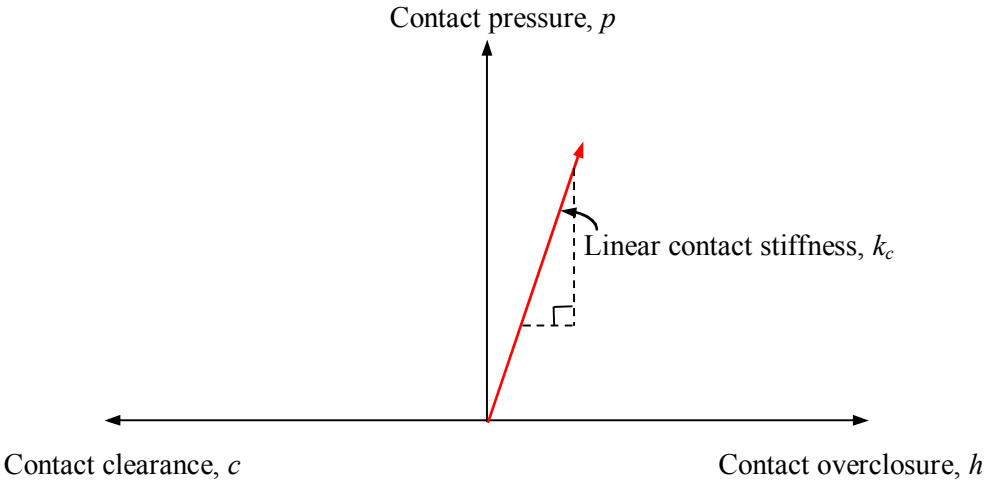

Figure 5.5: Softened contact pressure-overclosure relationship defined in linear form [1].

Figure 5.6 shows the contact stiffness sensitivity analyses for the AL corrugated-core specimen. It is evident that when the contact stiffness factor decreases, initial softening takes place and the initial stiffness of the global struts reduces.

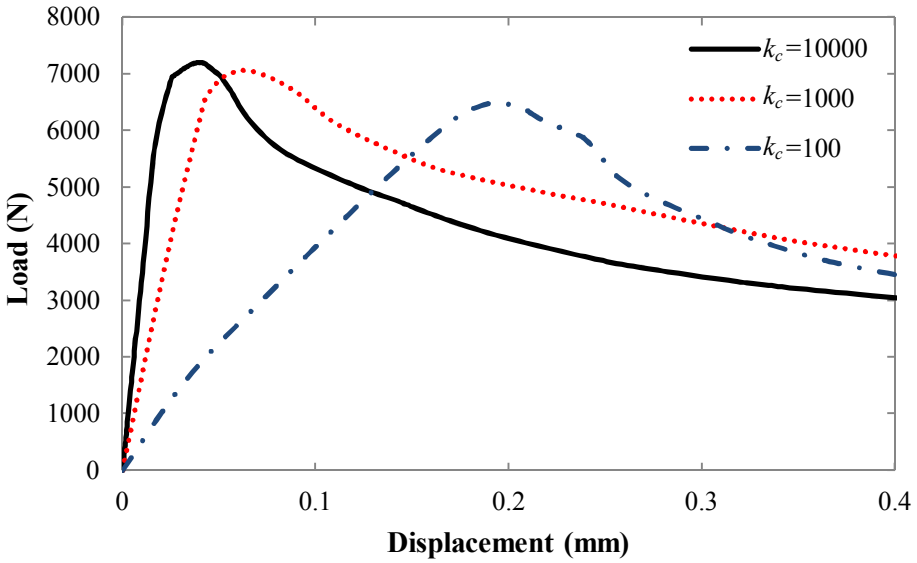

Figure 5.6: Typical contact stiffness sensitivity analyses, if the case when $k_c > 10000$ N/mm^3, is equivalent to a hard contact condition.

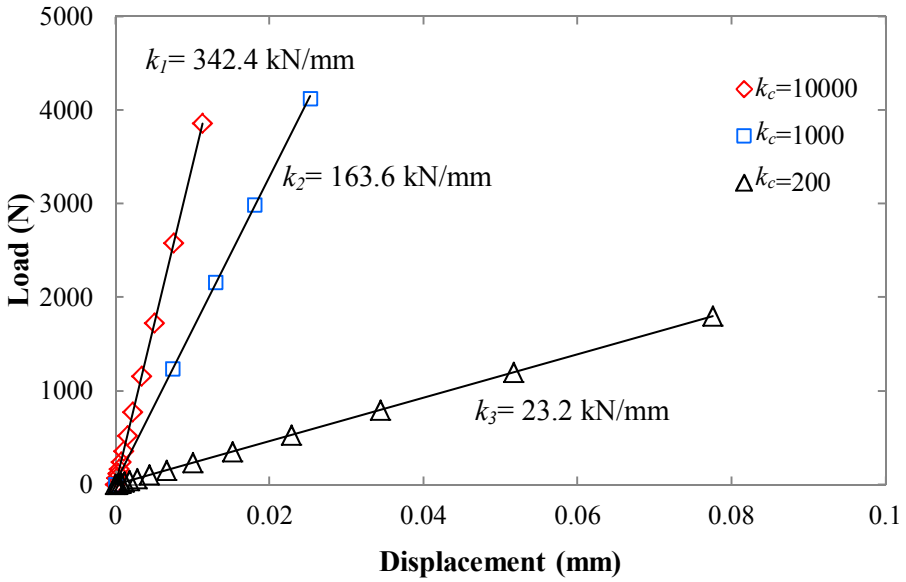

Figure 5.7: The effect of the contact stiffness k_c on the slope (P/δ) of the AL corrugated-core model.

Figure 5.7 presents the elastic stiffness (P/δ) analyses for the AL corrugated-core model. From the figure, the appropriate value k_c = 200 N/mm^3 was used as the contact stiffness for the AL corrugation, since it results in the same stiffness value as the experimental result. The above approach was repeated for the different materials, and the contact stiffness values for the GFRP and CFRP corrugation models were taken as 50 kN/mm^3 and 100 kN/mm^3, respectively.

c) Geometry Imperfection

Most manufacturing routes result in some form of 'small defect' or imperfection in the finished structure. In fabricating a corrugated-core, such flaws may be associated with geometrical imperfections resulting from spring-back following moulding, local variations in the fibre volume fraction as well as voids introduced during the compression moulding process. FE models that do not account for structural imperfections are likely to overestimate both the peak load and the stiffness of the whole structure. For example, Côté *et al.*[15] and Kazemahvazi and Zenkert [16] introduced imperfections in their numerical models to accurately predict the load-displacement trace of corrugated-core geometries.

The initial imperfection, in the shape of a buckling mode, was imposed on each

corrugated strut. Here, the initial imperfection, a was defined as:

$$a(s) = \frac{\xi H}{2}\left[1 - \cos\left(\frac{2\pi s}{L}\right)\right] \qquad 5.21$$

where ξ is a dimensionless imperfection parameter and s is the arc length along the wall thickness, H measured from one end.

In Abaqus/CAE, this was achieved using the *IMPERFECTION function in the analysis step. An elastic buckling analysis was initially conducted in a linear perturbation step to retrieve the eigenmodes of the core. From the FE buckling analysis, a selected eigenmode with a similar buckling behaviour to the experiment was used to introduce a small imperfection in the straightness of the wall, which could then be used in the step procedure. In this study, the simplest buckling mode, Mode 1 was used. An imperfection sensitivity analysis was then performed, during which the imperfection amplitudes were varied systematically between 0 (a perfect corrugated geometry) and 0.5. The imperfection parameters take the form of:

$$\Delta\chi_i = \sum_{i=1}^{M} w_i \phi_i \qquad 5.22$$

where ϕ_i is the i^{th} mode shape and w_i is the associated scale factor.

An Abaqus non-linear analysis, *STATIC, RIKS was then used to trace the full response of the structure past the buckling point and into the post-buckling region. The Riks method [17] is generally used to predict unstable, geometrically nonlinear collapse of a structure, and can be used to speed convergence of snap-through problems that do not exhibit an instability.

Figure 5.8 shows the results of four sensitivity simulations on the GFRP corrugated-core specimen with H = 0.19 mm (GF2U5). It is clear that a perfect model will overestimate the peak load. In contrast, with increasing imperfection factor, ξ the peak load gradually reduces.

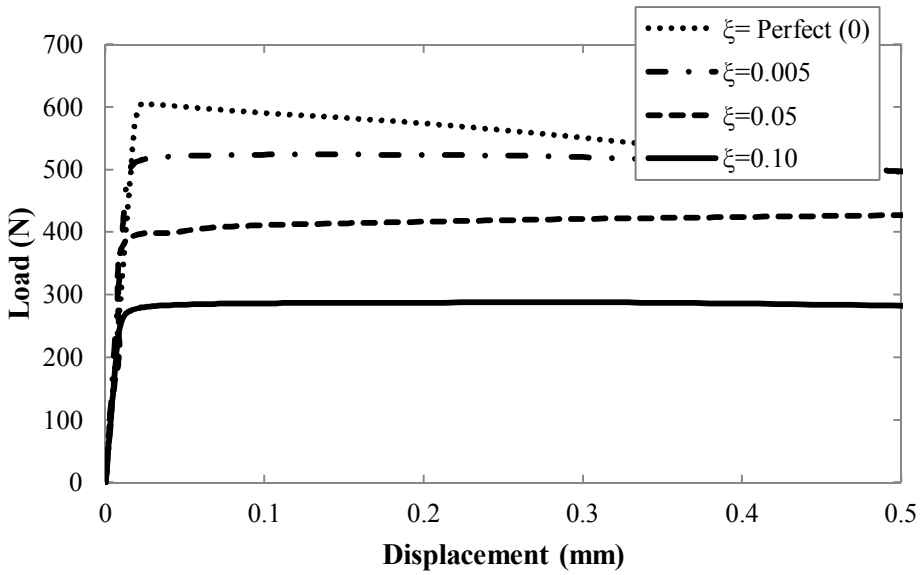

Figure 5.8: An imperfection sensitivity analysis study for the GFRP corrugation model, with a thickness of H = 0.2 mm. Note that the maximum load from the experimental test was 413 N.

d) Elements

An investigation into the effect of element formulation was also undertaken. The S4R element is a general purpose element used for thin or thick shell geometries. It was initially used to analyse the behaviour of all specimens with different cell wall thicknesses, η_H. A specific formulation for thick elements in Abaqus is S8R. This element is an 8-noded doubly curved thick shell using reduced integration to minimise run time. The definition of 'thick' is when the thickness of the element is more than approximately 1/15 of the surface length of the shell [3]. Since some of the composite corrugations were thick, this investigation was to identify which element should be used in the numerical modelling, either S4R or S8R.

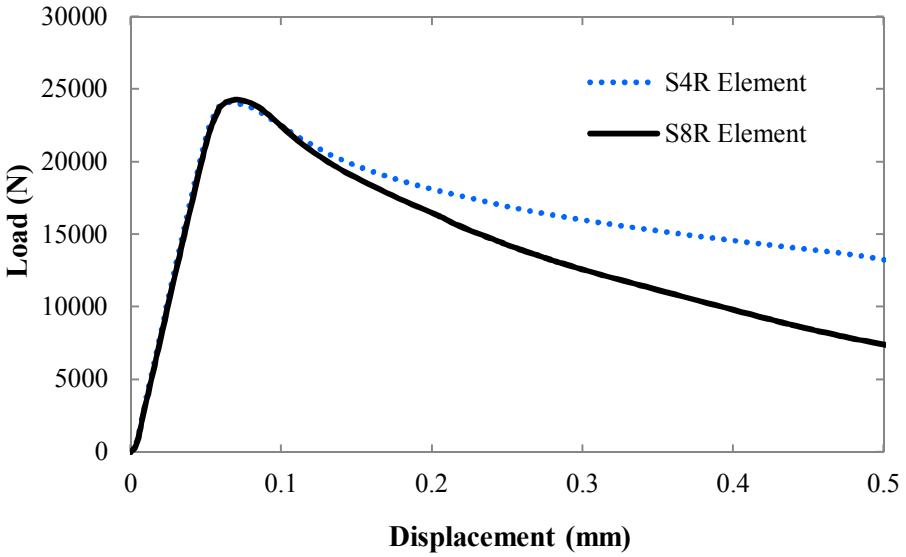

Figure 5.9: Comparison of the effect of different shell elements, S4R and S8R. The analysis was conducted on the CFRP corrugation, with a thickness of H = 1.10 mm. Note that the maximum load in the experiment was 23 kN.

Figure 5.9 shows the load-displacement traces for two different shell elements for the CFRP corrugated-core model with an aspect ratio H/L > 1/15. Both shell elements show a similar pattern in the elastic region, where the elastic stiffness and the peak load are equal. However, beyond the elastic region, the S8R element drops gradually compared to the S4R element. The S8R element is required for cases where the transverse shear flexibility is required in the calculation, for example delamination of the plies. Therefore, all the numerical analyses for composite with aspect ratio of H/L > 1/15 were undertaken using the S8R shell element.

5.4.1.7 Results from the Numerical Analysis

Figure 5.10 compares the compression load-displacement traces for the aluminium corrugations based on five unit cells, with the predictions from the finite element model. It should be noted that the initial FE predictions, based on imperfection-free corrugations (FE-Perfect), grossly over-estimated both the strength and stiffness of this AL material. Following a detailed imperfection sensitivity analysis, the FE model was modified to introduce initial imperfections of amplitude ξ = 0.01 for the aluminium corrugation. This amplitude was obtained via an imperfection sensitivity procedure, as discussed above, whereby the amplitude was varied until the predicted

peak load agreed with the experimental data. Applying this initial imperfection yields good agreement between the numerical and experimental data.

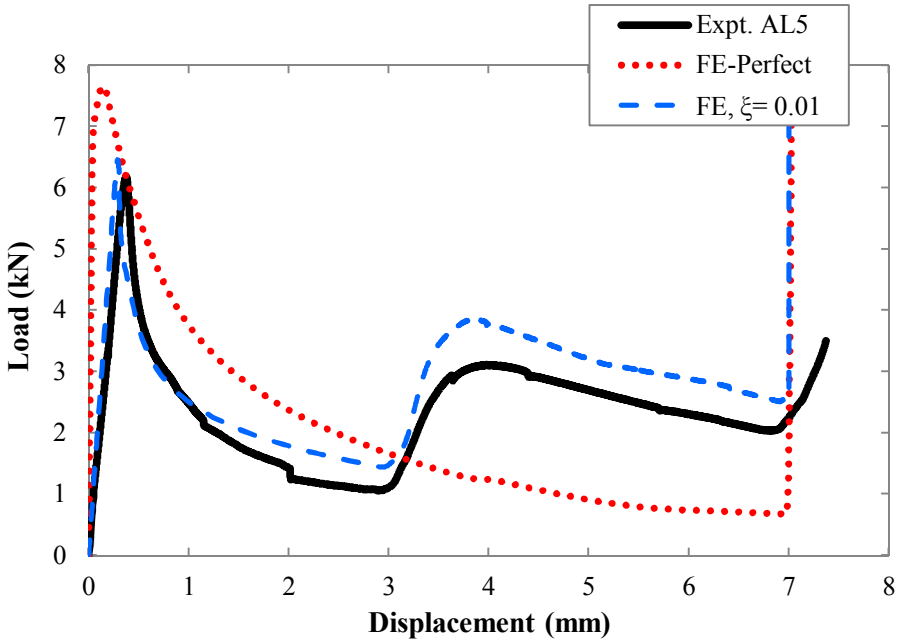

Figure 5.10: The measured response and the predictions of the load-displacement response for AL corrugated-core sandwich structure. The load-displacement responses of the structures with FE predictions with $\xi = 0.01$ show good agreement with the measured response.

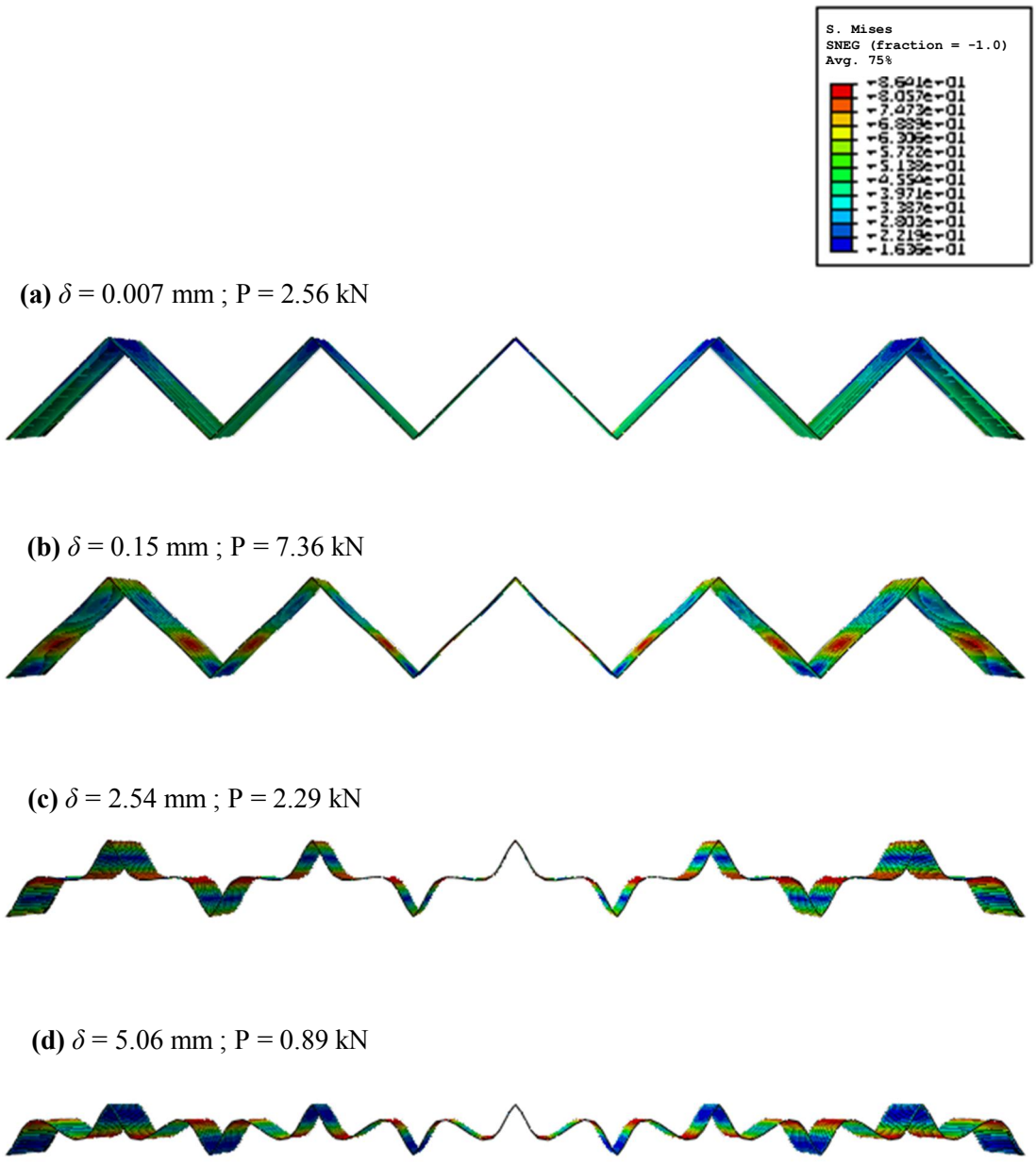

Figure 5.11: Predicted deformation modes for a perfect AL corrugation; (a) initial loading, (b) peak loading, (c) symmetrical plastic hinges due to bending and (d) progressive collapse. Note that the inset gives the Mises stress.

Figure 5.11 shows the deformation of a perfect AL corrugation. It is clear that plastic hinges dominated the collapse behaviour of the structures. After peak load, the load drops gradually until densification occurs. The figure shows that there is no contact between the upper platen and middle of struts half way through the analysis.

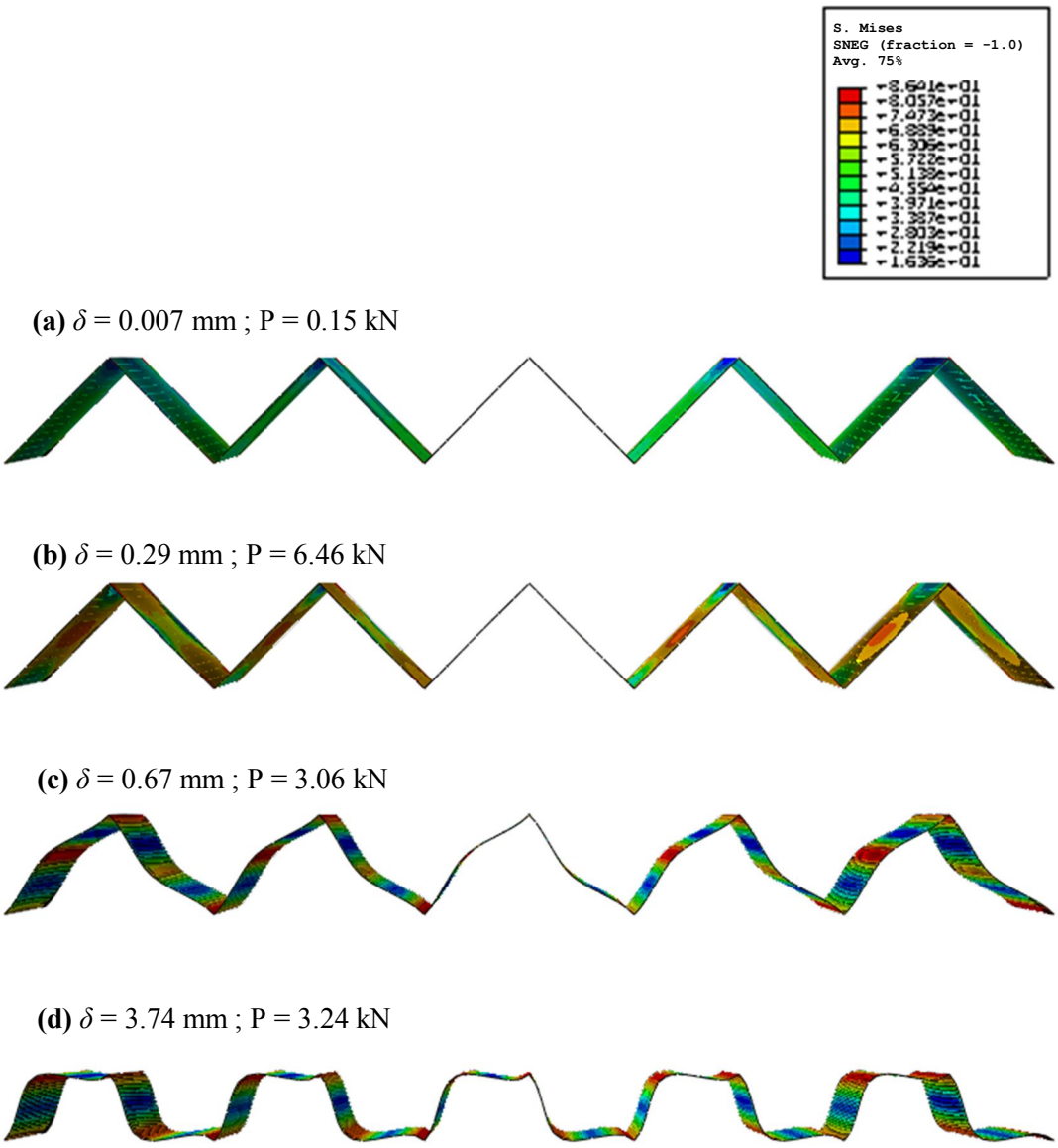

Figure 5.12: Predicted deformation modes for an imperfect AL corrugation; (a) initial loading, (b) peak loading, (c) buckling behaviour and (d) initial contact between upper platen and middle of struts. Note that the inset gives the Mises stress.

Figure 5.12 show the buckling shapes for the model of the imperfect AL corrugation. The buckling pattern in the model shows good agreement with the photographic images from the experimental result, as shown in Figure 4.13(b). Contact between the upper platen and struts is presented in Figure 5.12(d) where the load increases due to contact interaction.

Figure 5.13 compares the initial portions of the compression load-displacement traces for composite corrugations based on five unit cells, with the numerical predictions from the FE model.

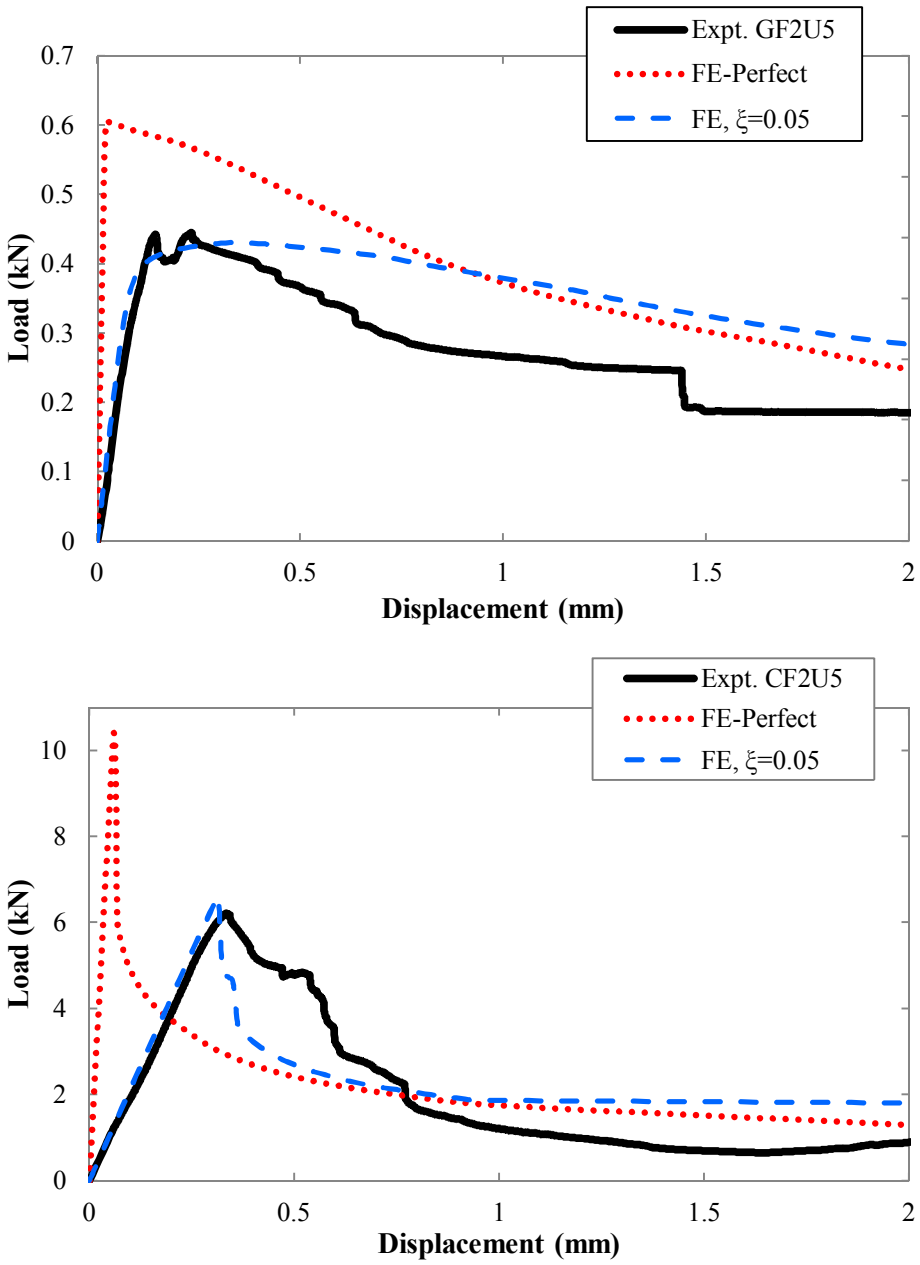

Figure 5.13: The measured response and the predictions of the peak load for composite corrugated-core structures; (a) GFRP and (b) CFRP. FE simulations for both GFRP and CFRP with $\xi = 0.05$ show reasonable agreement with the measured responses.

It should be noted that for the initial numerical predictions, based on FE-Perfect model, the predicted peak load and stiffness are higher for all types of composites corrugation. From the imperfection-sensitivity procedure and the analysis data, an initial imperfection with an amplitude of 0.05 was introduced into both the GFRP and CFRP models. Following this, the comparison between the numerical and experimental results was reasonably good. It is evident that the numerical models for of the GFRP and CFRP corrugations fail to predict the early instabilities in the load-displacement trace. Beyond peak load, the GFRP model over-predicts while CFRP under-predicts the softening phase of the deformation process. This occurs due to Abaqus/Standard being unable to eliminate the failed elements, giving over-predictions of the behaviour. Element deletion can only be activated in Abaqus/Explicit. The predicted deformation mode is presented and compared with the experimental deformation mode in Figure 5.15. The figure highlights good agreement in terms of the failure mode shapes.

Figure 5.14 shows the deformation process for the numerical model of a perfect composite corrugation. Again, for this perfect condition, plastic hinges dominated the collapse behaviour of the structures. There was no contact between the upper platen and the middle of struts during the simulation, as the load gradually drops until the compaction occurs.

Figure 5.15 show the buckling response of an imperfect GFRP composite corrugation model. The buckling pattern in the model shows good agreement with the images from the experimental test, as shown in Figure 4.15(b). Similar failure modes were observed in the model of the CFRP corrugation model. Note that the buckling phenomena only occurred in the thin cell wall structures. Although the damage criteria for the composite were inputted into the numerical model, delamination between the composite plies was not predicted in the thick struts model, as the shell element is assumed from the beginning as a one whole part (shell element is not divided ply by ply).

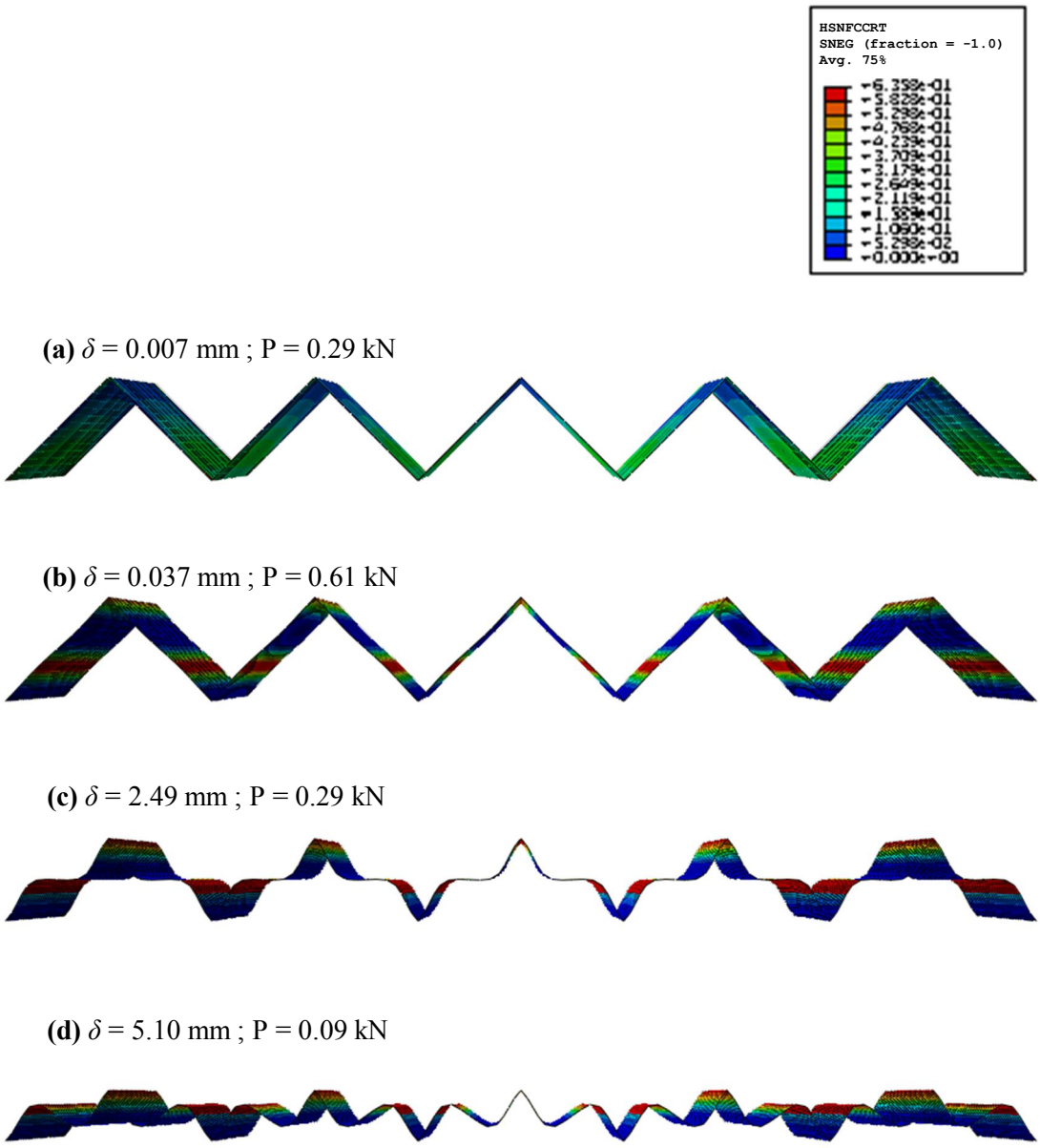

Figure 5.14: The initial modelling behaviour of the composite corrugation (perfect condition); (a) initial loading, (b) peak loading, (c) plastic hinges and (d) model progressively compressed to the lower platen. Note that this is an example for a GFRP corrugation with H = 0.19 mm. The colour spectrum represents Hashin's fibre compression damage initiation criterion.

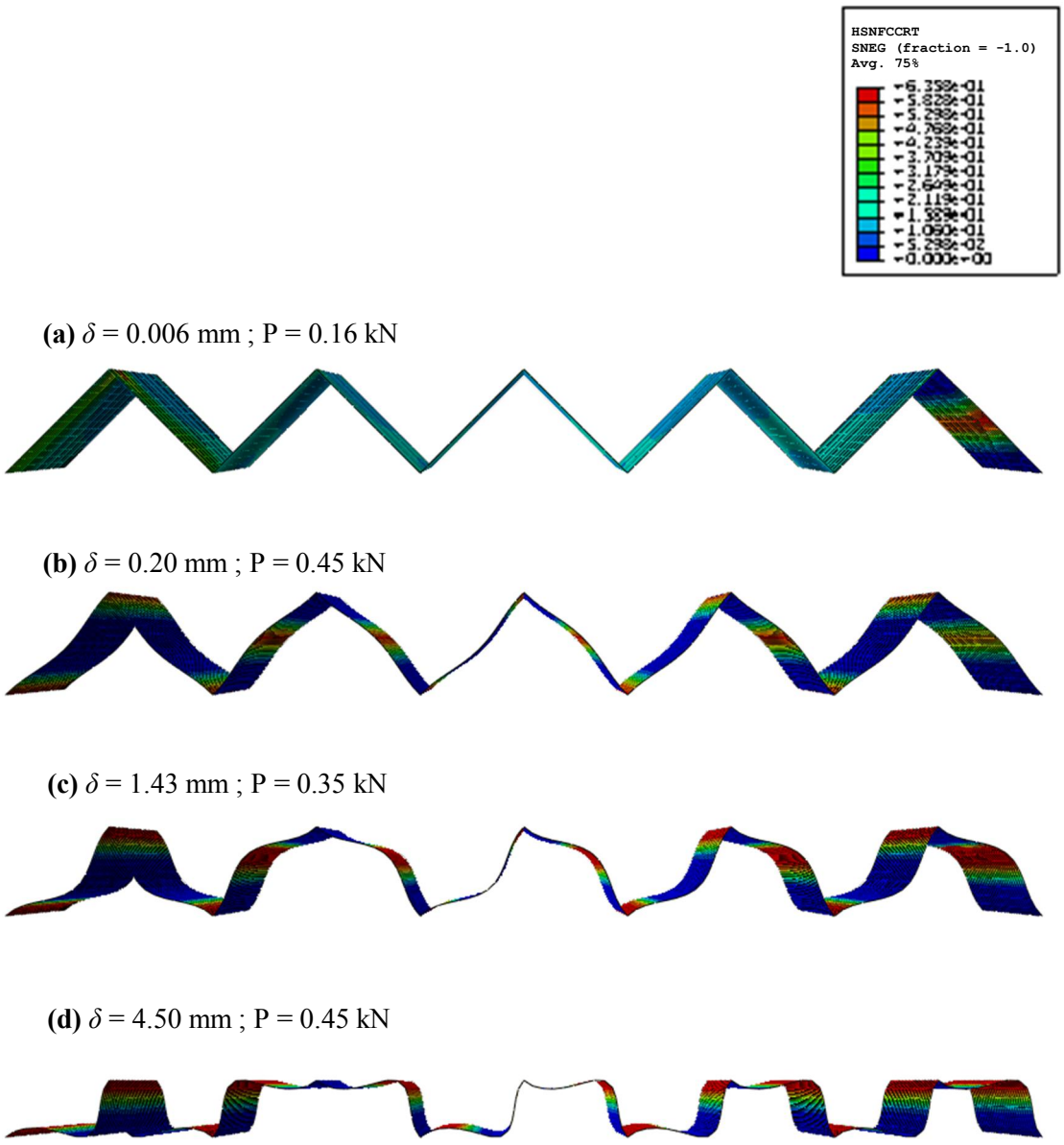

Figure 5.15: The modelling behaviour of a composite corrugation with a geometrical imperfection; (a) at initial contact, the right-end of the strut is initially bent, (b) peak loading, (c) buckling-dominated behaviour as three of the unit cells buckled and (d) initial contact between upper platen and centre of the struts. Note that this is an example for a GFRP corrugation with H = 0.19 mm. The colour spectrum represents Hashin's fibre compression damage initiation criterion.

In comparing the experimental results and the numerical predictions with the theoretical analysis, based on Equation 4.21, the analytical calculation accurately predicts the peak load for the GF2U5 corrugated-core structure with built-in ends (λ = 2). The model is 3% higher than the experimental value. Similarly, for the CF2U5 corrugated-core specimen, the equation gives a very close approximation, P_E ~6.5 kN to the experimental result if λ = 1.42, representing a clamped-hinged condition at the ends. In contrast, the pinned-ended boundary condition (λ = 1) gives the closest theoretical prediction P_E ~6.4 kN for the AL5 corrugated-core structure with the value being approximately 3% higher than the measured data. For this reason, the theoretical equation tends to over-predict the critical load. This is because the analytical model does not take into account imperfection issues as well as the inconsistency of the end condition, given that localised shear deformation may occur in the bonding area during testing.

5.4.2 Modelling of Compression Rigid Foam Core

An FE analysis on the foam was carried out to model the behaviour of the rigid polyurethane (PUR) foam numerically. A static compression test on the foam that was used to fill the corrugated-core sandwich structures is simulated with the experimental input data. The aim of this exercise was to confirm the validity of the foam input data to be used in the model corrugated-core filled foam sandwich structures. The next section presents the numerical procedures for modelling this foam core under static compression loading.

5.4.2.1 Geometry and Element

In simulating the compression test, the foam was modelled accordingly to the experimental dimensions. For this PUR foam, dimensions of 25 mm x 25 mm x 25 mm were used, i.e. the dimensions in Section 3.4.4. The foam was modelled using eight-noded linear continuum elements, with reduced integration and hourglass control (C3D8R). The element mesh was of 10 x 10 x 10, which consists of a total of 1000 elements as presented in Figure 5.16. A mesh-sensitivity study was conducted and further refinements did not change the prediction appreciably.

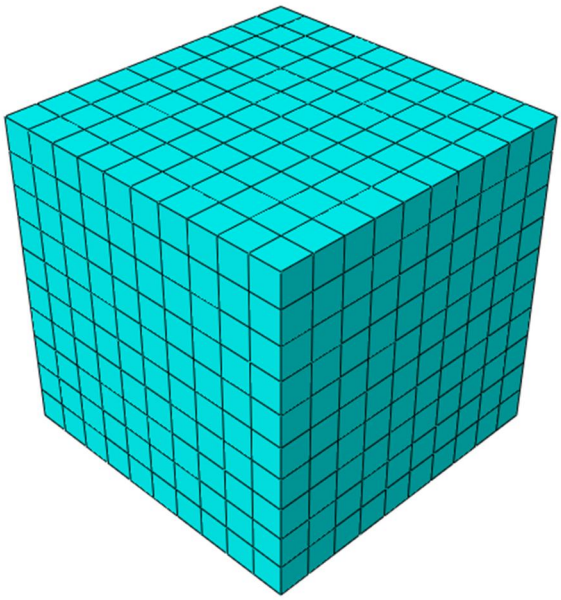

Figure 5.16: The 3D brick element mesh used in the foam modelling.

5.4.2.2 Interaction Property, Boundary and Loading Conditions

In modelling the foam, Figure 5.17 shows the foam interacts with the rigid platens with a hard contact property, hard in the normal direction and frictionless in the tangential direction. The bottom of the core was fixed to the bottom surface of the platen while at the top, the translation in the *y*-direction was free to allow downward movement of the top surface of the core. A displacement boundary condition, assigned to a reference point placed at the centre of the circular rigid platen, was then applied to crush the model. The reference point also was used to record the contact load and displacement for the foam model.

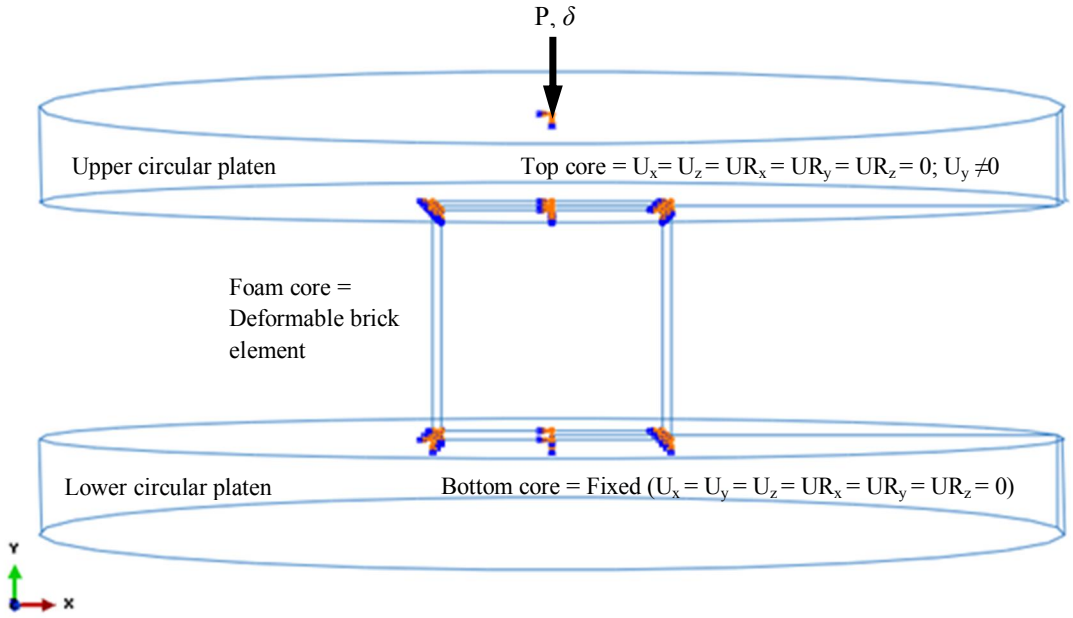

Figure 5.17: Loading direction, boundary conditions and assembly for the foam core model between the two rigid platens.

5.4.2.3 Material Model and Input Data

The foam material model requires more data than the standard metal elastic-plastic properties. To define the elastic response of the model, a linear isotropic elasticity model was used. The input data required in elastic region were Young's modulus, E = 4.12 MPa and the Poisson's ratio. The Poisson's ratio, υ was assumed to be zero. From experimental observations during the compression test and the reducing volume characteristics of the foam during crushing as reported by Alias *et al.* [18], the effect is insignificant.

To predict the plastic behaviour, a crushable foam material model with isotopic hardening was used. The model assumes similar behaviour in tension and compression, where the yield ellipse is centred at the origin in the *p-q* stress plane, evolving in a geometrically self-manner, governed by the equivalent plastic strain. This model was developed for metallic foam structures by Deshpande and Fleck [19].

The yield surface represents the von-Mises circle in the deviatoric stress plane. The yield surface in the meridional stress plane is presented in Figure 5.18. The shape factor, $\dot{\alpha}$ can be calculated using the initial yield stress during uniaxial compression, $\sigma_c^{\,0}$ and the initial yield stress in hydrostatic compression, $p_c^{\,0}$ using relationship below:

$$\dot{\alpha} = \frac{3\mathrm{K}}{\sqrt{9-\mathrm{K}^2}} \text{ where } \qquad \mathrm{K} = \frac{\sigma_c^0}{p_c^0} \tag{5.23}$$

K is the compression yield stress ratio, and this value defines the shape of the yield ellipse.

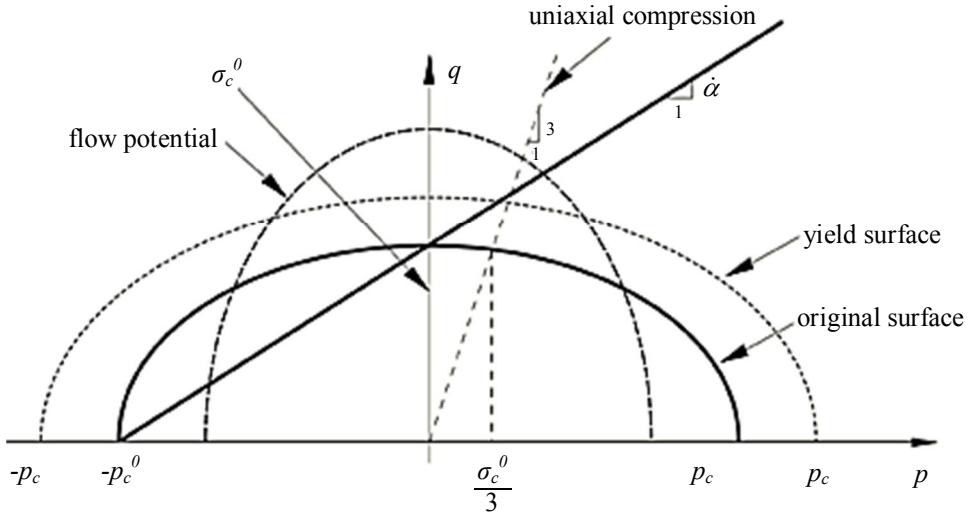

Figure 5.18: The yield surface and flow potential in the *p-q* stress plane for the isotropic crushable foam model [2].

From Figure 5.18, the flow potential in the isotropic hardening model is given by:

$$\dot{G} = \sqrt{q^2 + \beta^2 p^2} \qquad 5.24$$

where β represents the shape of the flow potential ellipse in the p-q stress plane. The term β is related to the plastic Poisson's ratio, υ_p as:

$$\beta = \frac{3}{\sqrt{2}} \sqrt{\frac{1 - 2\upsilon_p}{1 + \upsilon_p}} \qquad 5.25$$

where the υ_p is the ratio of the transverse to the longitudinal plastic strain under uniaxial compression. This value lies within the range of -1 to 0.5.

When hydrostatic data is not available, the compression yield stress ratio K can be calculated from the plastic Poisson's ratio as:

$$\mathrm{K} = \sqrt{3(1 - 2\upsilon_p)} \qquad 5.26$$

From Equation 5.26, the input properties for υ_p and K are 0 and 1.732, respectively. The crushable strain hardening data, used in the FE model, are presented in Table 5.4

Table 5.4: The strain hardening data used to define the hardening characteristics of the crushable foam model.

Yield stress (MPa)	Plastic strain
0.153859	0.0
0.153859	0.1
0.153859	0.2
0.153859	0.3
0.153859	0.4
0.161142	0.5
0.181109	0.6
0.201876	0.7
0.220871	0.8
0.250201	0.9
0.301219	1.0
0.350138	1.1
0.450678	1.2

5.4.2.4 Modelling Data Output

In this numerical analysis, stress, strain, reaction force and the displacement field output were requested for the entire foam model. In the history output, the displacement and reaction force data in the *y*-direction were obtained at the rigid platen reference point.

5.4.2.5 Results from the Numerical Analysis

Figure 5.19 compares the full experimental response of the compression-load displacement traces with the numerical analysis. It is clear that as a result of the use of the crushable foam material model, the FE data give a good prediction from the linear elastic and plateau regions up to densification zone.

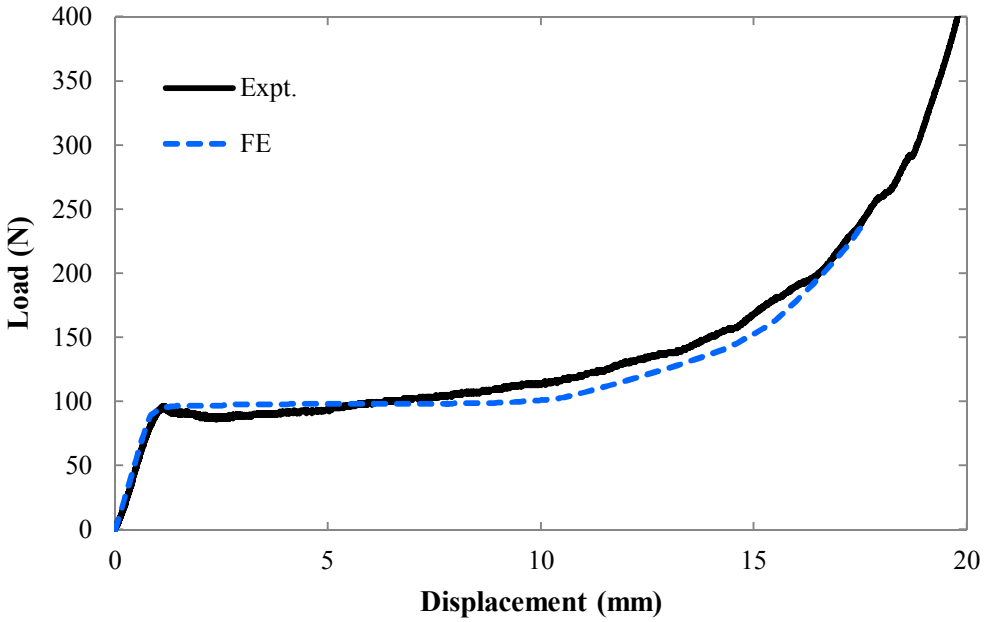

Figure 5.19: The measured mechanical response of the PUR foam. The FE simulation shows good agreement with the experimental data.

Figure 5.20 shows the progressive deformation modes in the foam model in the compression direction. The crushing pattern in the model is in a good agreement with the experimental data, as shown in Figure 4.11.

(a) δ = 0.2 mm ; P = 22.13 N

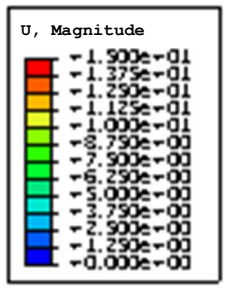

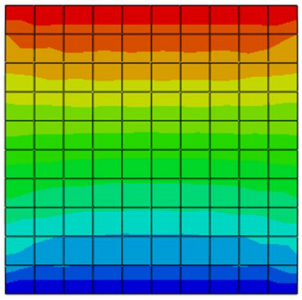

(b) δ = 2.2 mm ; P = 96.84 N

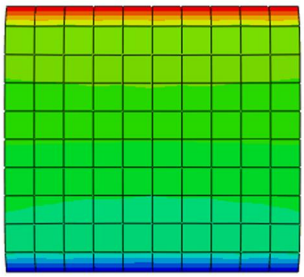

(c) δ = 7.6 mm ; P = 98.36 N

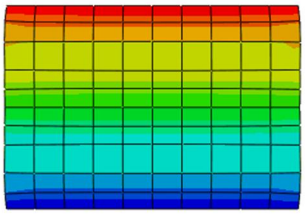

(d) δ = 15 mm ; P = 152.92 N

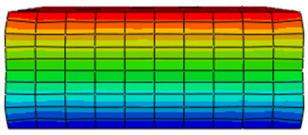

Figure 5.20: The modelling behaviour of a foam core; (a) at initial contact, (b) peak loading, (c) plateau region and (d) the initial densification region. Note that the colours represent the deformations.

5.4.3 Modelling of Bi-axial Loading of Corrugated-core Structure

This section presents the numerical simulation procedure for modelling the corrugated-core structures under combined compression-shear loading. The procedure is similar to the procedure used for static compression modelling, as discussed in Section 5.4.1, except for a few steps especially loading direction. The objective of this modelling procedure is to determine the linear stiffness responses for different loading angles.

5.4.3.1 Geometry and Element

The compression-shear behaviour of the corrugated-core structure was modelled according to the experimental dimensions. For the corrugated-core, nine thin plates were modelled using S4R shell elements. Each of the shell plates consisted of 25 x 14 element mesh, to give a total of 3024 elements, as presented in Figure 5.21. The figure also shows that the loading platens were modelled using a four-noded 3D bilinear rigid qaudilateral element (R3D4). Each of the platens was modelled exactly with the dimension taken from the Arcan test rig, i.e. dimensions of 100 mm x 80 mm x 10 mm, with 6 holes.

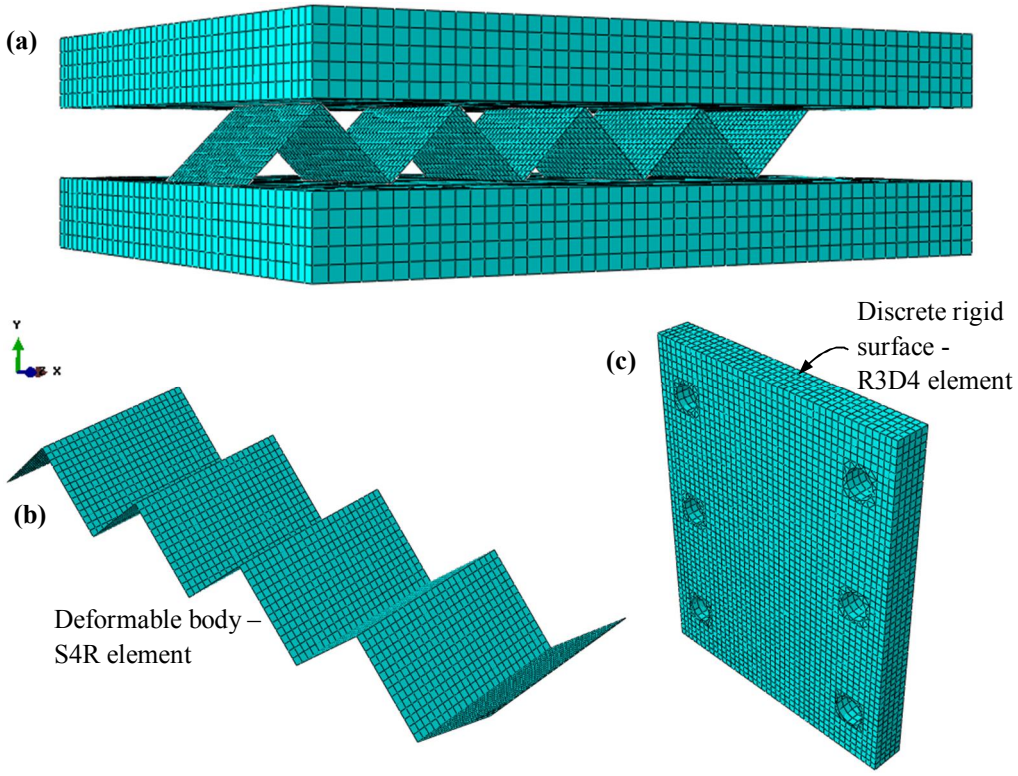

Figure 5.21: (a) Meshing of the loading platens and corrugated-core, (b) meshed corrugated-core, and (c) meshed loading platen.

5.4.3.2 Interaction Property, Boundary and Loading Conditions

With respect to modelling bi-axial loading, Figure 5.22 shows how the corrugated-core interacted with the rigid platens with a hard contact property, hard in the normal direction and frictionless in the tangential direction. Since this is an ideal case to simulate the behaviour in the linear elastic region, the edges of the corrugations were modelled as perfectly sharp, and the nodes along the upper and lower edges were tied to represent the case of perfect bonding. The tied contact formulation constrains only translational degrees of freedom in the simulations. A displacement boundary condition, assigned to a reference point placed at the centre of the square rigid platen, was then applied in two positions; x and y-directions, to collapse the corrugated-core structure model under compression and shear loads simultaneously. The reference point was also used to record the contact load and displacement data from the corrugated-core model.

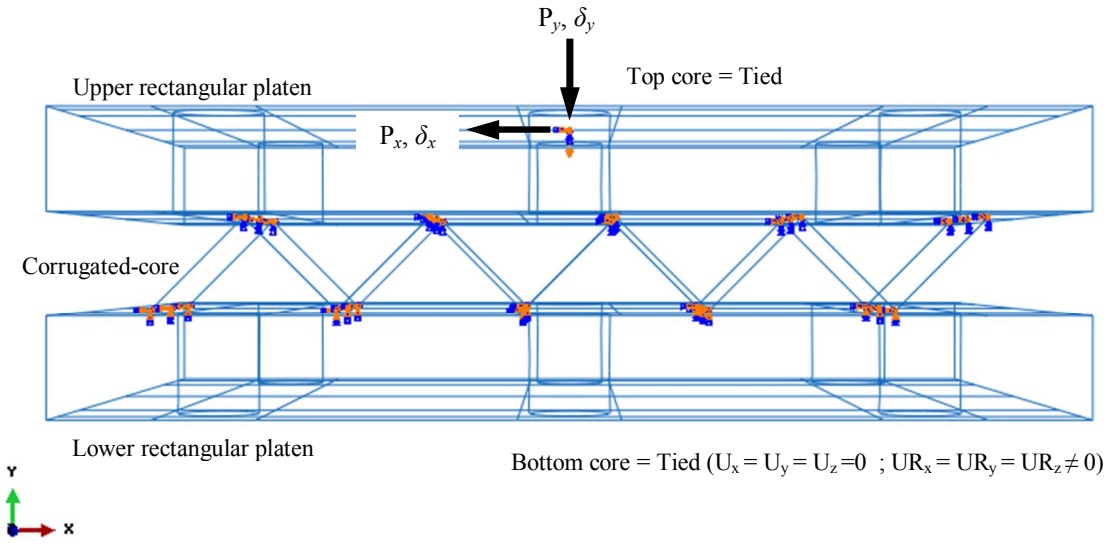

Figure 5.22: Loading direction, boundary conditions and assembly of the foam core model between two rigid platens.

5.4.3.3 Material Model and Input Data

To define the elastic response of the model, a linear isotropic elasticity model was used for the aluminium system, and orthotropic engineering constants for the composite materials. The input data for the aluminium and composite materials are given in Sections 5.2 and 5.3, respectively.

5.4.3.4 Modelling Data Output

In this numerical analysis, stress, strain, the reaction force and the displacement field output were requested for the whole corrugated-core model. In the history output, the displacement and reaction force data in x and y-directions were requested at the rigid platen reference point.

5.4.3.5 Results from the Numerical Analysis

Figure 5.23 shows the resulting load-displacement curves for an aluminium alloy corrugation for five values of loading angle, α. An examination of the figure indicates that the predictions of the FE model agree well with those offered by Equations 4.28 and 4.29. Both equations were used to predict the elastic response of the composite materials, and give a good correlation with the numerical results. Figure 5.23 also confirms the predictions of the analytical approach that state that the initial stiffness of the corrugated structure is independent of the loading angle α, except for values close to and equal to 0° and 90°, for which cases there is a small increase in the initial stiffness.

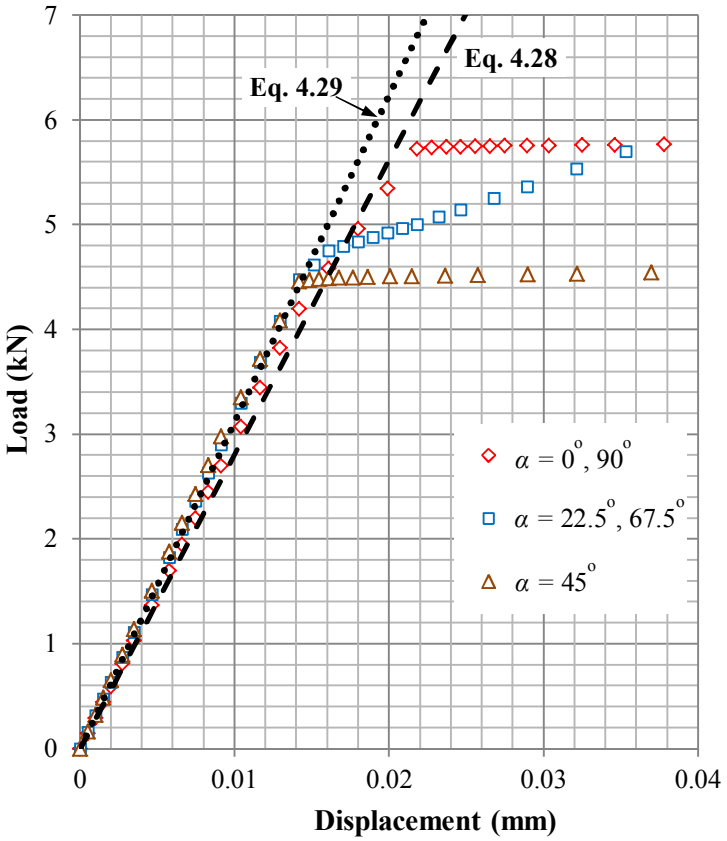

Figure 5.23: Comparison between the analytical solutions and the numerical analysis in the form of load-displacement traces for loading angles from 0° to 90°.

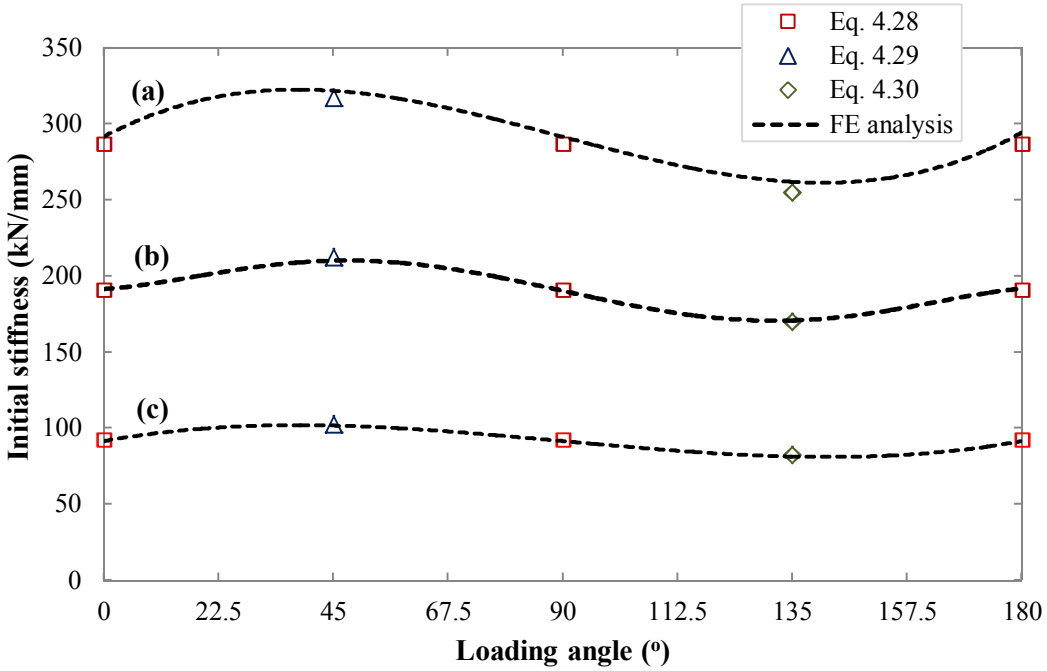

Figure 5.24: Prediction of initial stiffness (P/δ) from analytical methods compared to numerical analysis, from $0° \leq \alpha \leq 180°$: (a) AL, (b) CFRP, and (c) GFRP.

Meanwhile, Figure 5.24 shows the influence of loading angle, $0° \leq \alpha \leq 180°$ on the initial stiffness of the structure. Interestingly, based on the geometry of the above corrugated structure, the initial stiffness is the same in pure compression ($\alpha = 90°$), and pure shear ($\alpha = 0°$ and $180°$) while the overall response is a gentle sinusoidal function with a maximum peak at $\alpha = 45°$ and a minimum at $\alpha = 135°$. The maximum and minimum values of the initial stiffnesses are influenced by the number of inclined struts that are in line with the applied load, either at $\alpha = 45°$ or $135°$, respectively. Further investigation into Figure 5.24 shows that the variation of initial stiffness is less than 10% (AL with an average stiffness of 292 kN/mm and a 7.6% variation), and the average initial stiffness of the AL corrugation is higher than the composite corrugations with the same geometry and cell wall thickness, $H = 0.5$ mm.

Figure 5.25 show the progressive deformation of the corrugated-core model under combined compression-shear loading at an angle of $\alpha = 67.5°$. Here, the collapse pattern in the AL corrugation model shows good agreement with the images from the experimental result in Figure 4.32.

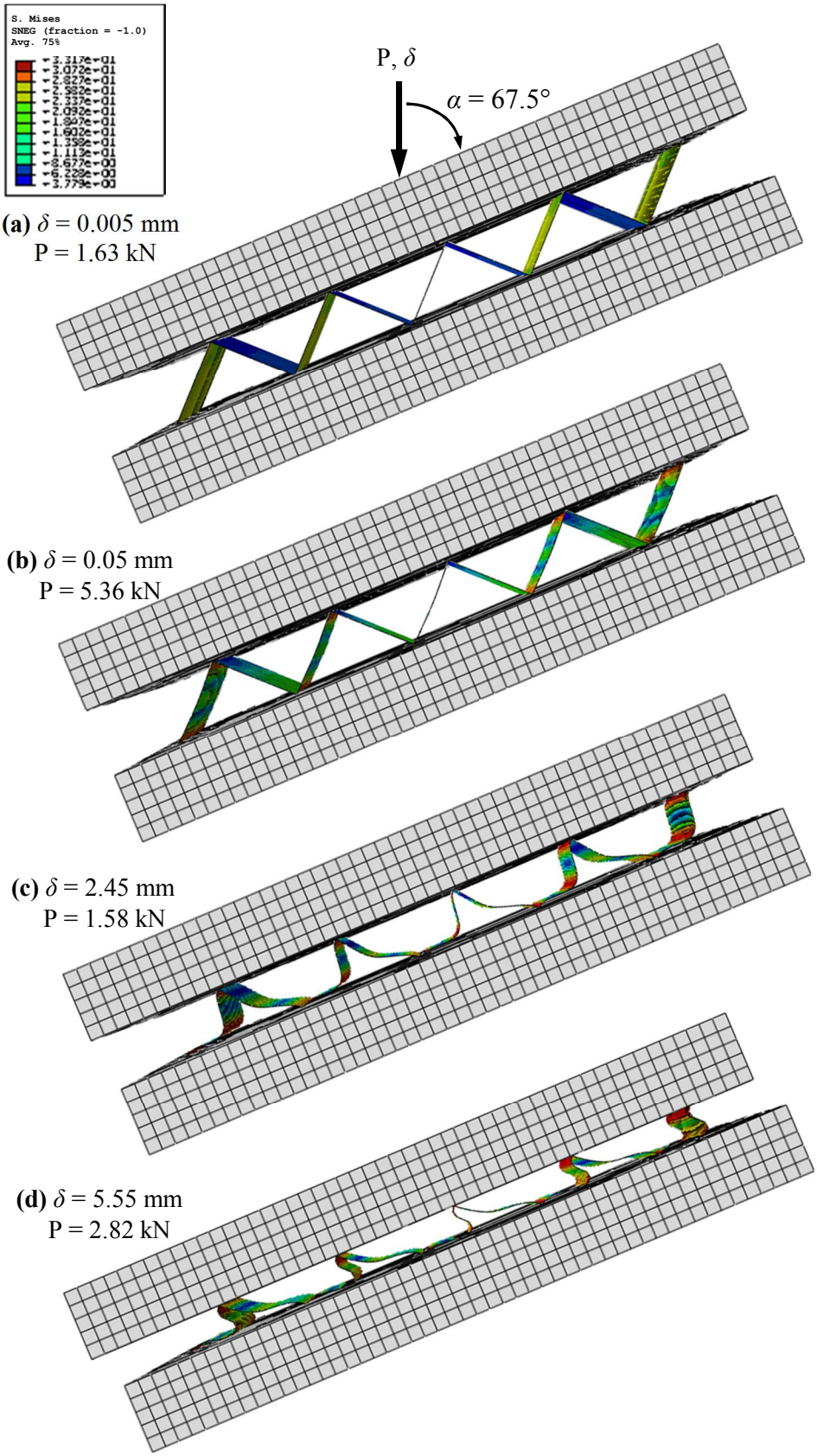

Figure 5.25: The modelling behaviour of the Arcan test for the AL corrugation at a loading angle of 67.5^{o} (a) at initial contact, (b) peak loading, (c-d) progression of buckling and collapse of the unit cells. Note that the colours represent the Mises stress.

5.4.4 Modelling the Compression Response of the Corrugated Foam-filled Core Structure

This section presents the FE modelling procedures for the composite corrugated-core sandwich structures filled with two different insertion configurations of foam, under compression loading.

5.4.4.1 Geometry and Element

For this modelling procedure, the foam core was modelled using the brick element, C3D8R, and the corrugated-core was modelled using eight-noded hexahedron, finite membrane strain elements (SC8R). The reason of choosing the continuum shell element (SC8R) instead of the conventional shell element (S4R) was to avoid over-constraint at kinematic relationship of displacement between the interface of the shell and solid elements [3]. All the geometries in the model were drawn in 3D solid for the foam and the corrugated-core sandwich structures.

An early attempt of the 3D solid modelling with perfect sharp edge corner had shown that the corner of the core was penetrating the upper skin of the model. This was believed to be due to stress concentration at the apex of the sharp edge, and therefore the sharp edge of the core penetrated the nodes between the elements in the upper skin. Figure 5.26 shows the deformation as well as penetration of the apex of the core into the upper skin.

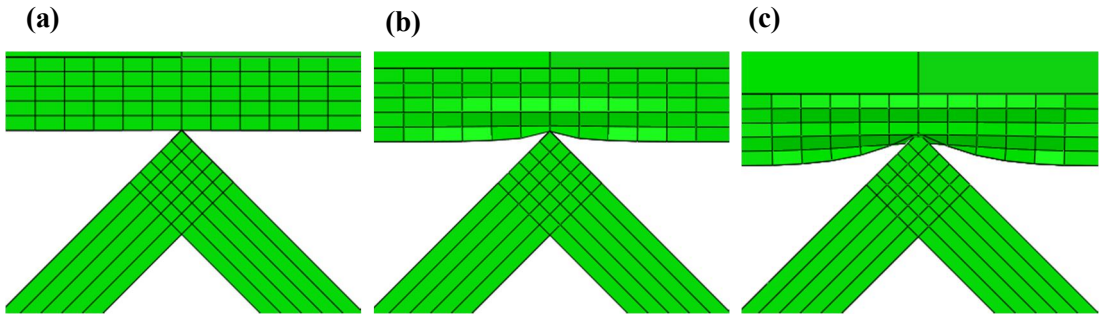

Figure 5.26: The sharp edge contact between the corrugated-core and the upper skin; (a) contact set-up, (b) initial deformation and (c) progression and penetration of the sharp corner.

To overcome this problem, the geometry of the corrugated core was modified, as shown in Figure 5.27(a). The sharp edge was modified to become a flat surface in contact, where 0.354 mm was cut from the tip from each edge. Consequently, the overall thickness of the core was reduced from 10 mm to 9.29 mm, with a small reduction of 7 % in the total thickness.

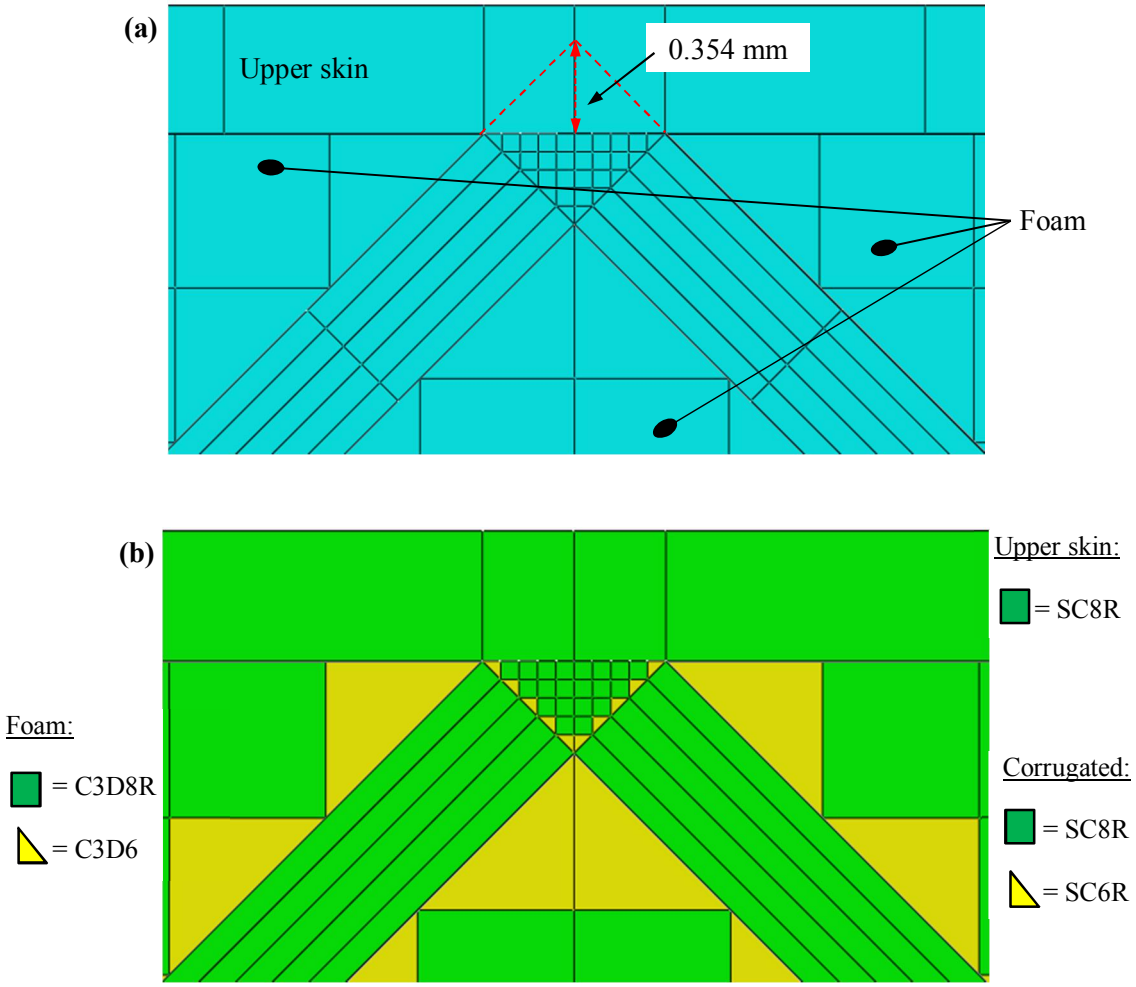

Figure 5.27: The corrugated-core sandwich structures filled with foam; (a) dashed-line is the cut area, and (b) types of elements used in the modelling.

Figure 5.27(b) shows the elements used in the modelling. Structured and sweep techniques in mesh control were implemented, to generate uniform and correct meshing, based on element shapes, i.e. for triangular shapes; SC6R is a 6-node triangular element for continuum shell wedge and C3D6 is a 6-node linear triangular

prism element. Meshes of the structures are shown in Figure 5.28. Note that the circular compression platen was modelled using the analytical rigid surface.

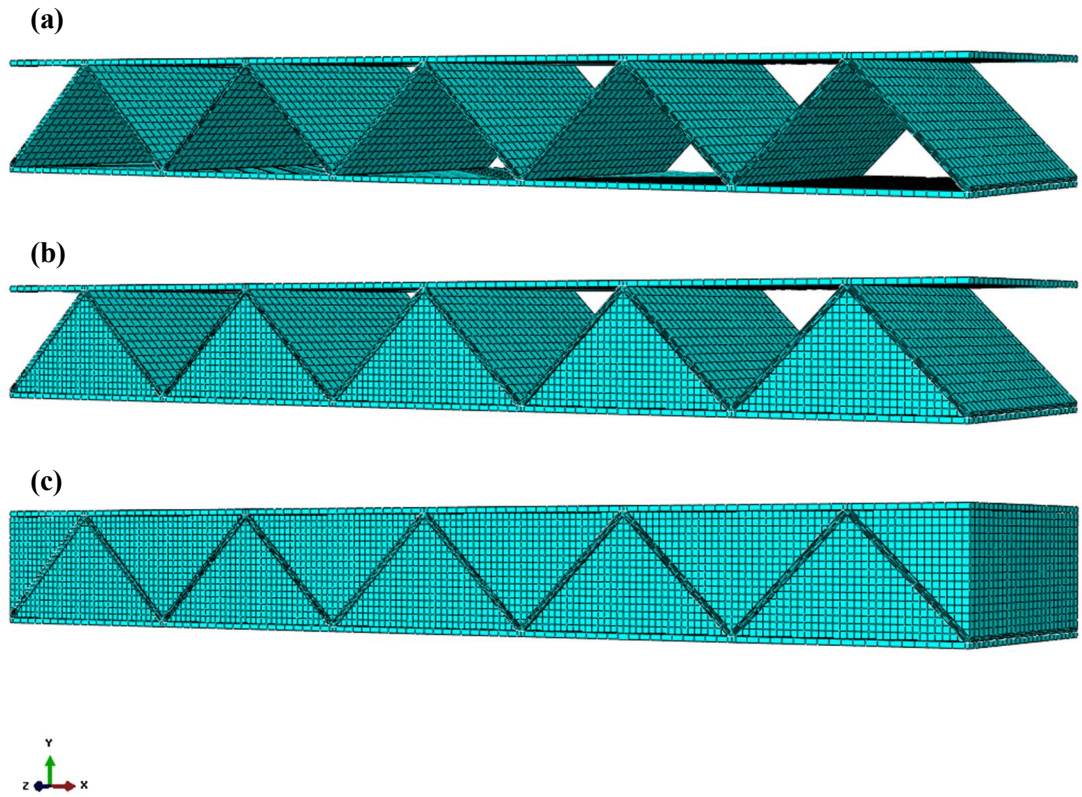

Figure 5.28: The meshes for modelling; (a) conventional corrugated-core, (b) semi-filled core and (c) fully-filled with foam core.

To summarise, the number of elements used in the study were 25000 elements for the corrugated-core, 2650 elements for the top and bottom skins and a total of 68000 elements for the fully-filled foam core. A mesh-sensitivity study was conducted and further refinements slightly changed the results of the numerical analysis.

5.4.4.2 Step, Interaction Property, Boundary and Loading Conditions

The step procedure for a quasi-static loading in this FE analysis was changed from *STATIC,General (Abaqus/Standard) to *DYNAMIC,Explicit (Abaqus/Explicit), due to explicit integration has more capabilities in solving nonlinear contact problem.

In this modelling, Figure 5.29 shows the upper surface of the sandwich structure was interacted with the rigid platens with penalty-softened contact property, where a

linear pressure overclosure contact in normal direction and frictionless contact in the tangential direction. All nodes along the upper and lower core edges were tied to the skins, to represent the case of perfect bonding. An initial imperfection was also introduced in the modelling to accurately predict the buckling behaviour, as mentioned in Section 5.4.1.6. The surface contact between the foam and the core-corrugated core was assumed to have a good bonding, and tied constraint was implemented to the surfaces. A comparison between the model with and without foam in tied constraint will be discussed later. The lower surface of the bottom skin was fixed, to prevent from any displacement and rotation movements.

A displacement boundary condition, assigned to a reference point placed at the centre of the circular rigid platen, was then applied in *y*-direction, to press the corrugated-core structure model in a compression mode. The reference point was also used to record the contact force and displacement in the model.

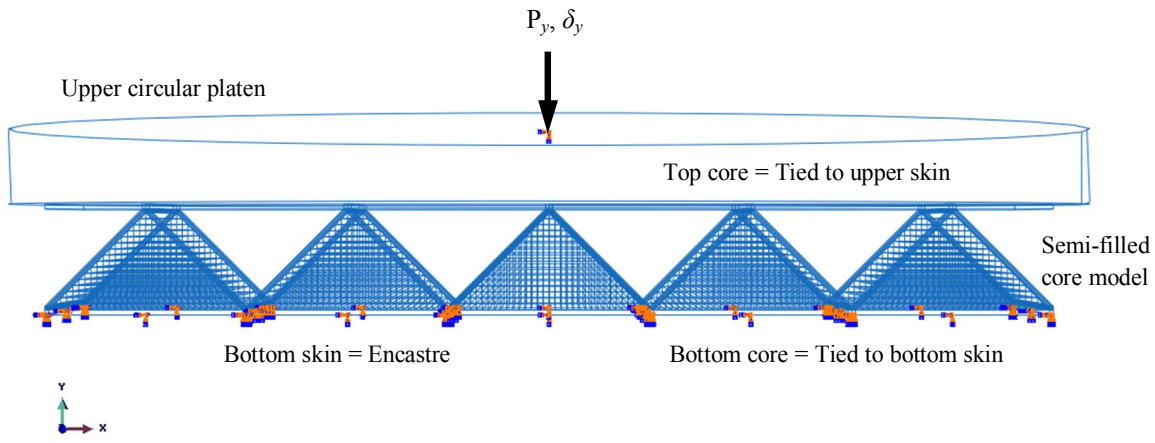

Figure 5.29: Loading direction, boundary conditions and assembly of the corrugated-core with foam model.

5.4.4.3 Material Model and Input Data

The input data for elastic property and progressive damage development in this model, were used as described in Section 5.3 for the composite corrugated-core and in Section 5.4.2.3 for the foam core.

5.4.4.4 Modelling Data Output

In this analysis, stress, strain, contact force and displacement field output were requested for the whole sandwich structure model. In the history output, the displacement and contact force data in the *y*-direction were obtained at the rigid platen reference point.

5.4.4.5 Results from the Numerical Analysis

The FE data for the structures were compared to the experimental results to verify the numerical model. Figure 5.30 shows plots of the load-displacement traces of experimental (GF5U5) and FE data, for a conventional corrugated-core structure. It is clear from the figure that the FE result indicates a good agreement with the corresponding experimental result. This level of good agreement is obtained between the numerical simulation and the experimental result in terms of initial stiffness, the peak load and the subsequent buckling behaviour. Beyond the peak load, the predicted load-displacement traces correlate well with the experimental data, exhibiting similar trends of reducing resistance to the crushing. In general, the numerical model offered reasonably good predictions of the essential features of the experimental load-displacement traces.

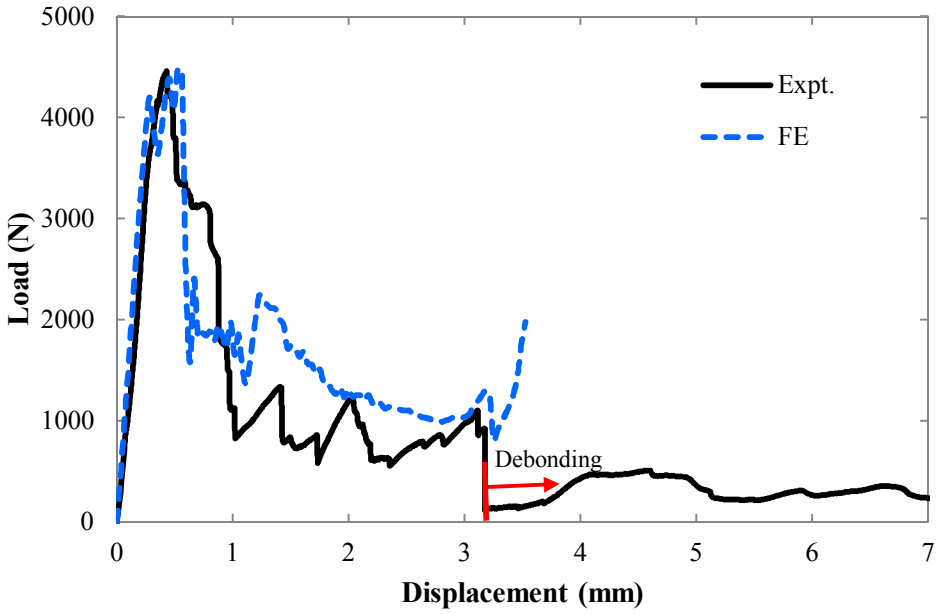

Figure 5.30: The measured response and the predictions of the load-displacement response for conventional GFRP corrugated-core structure. Note that in this FE analysis, the platen was displaced by 3.5 mm.

Figure 5.31 shows the deformation of the GFRP corrugation model in this analysis. The buckling pattern in the model shows a good agreement with the images from the experimental result, as shown in Figure 4.13(b).

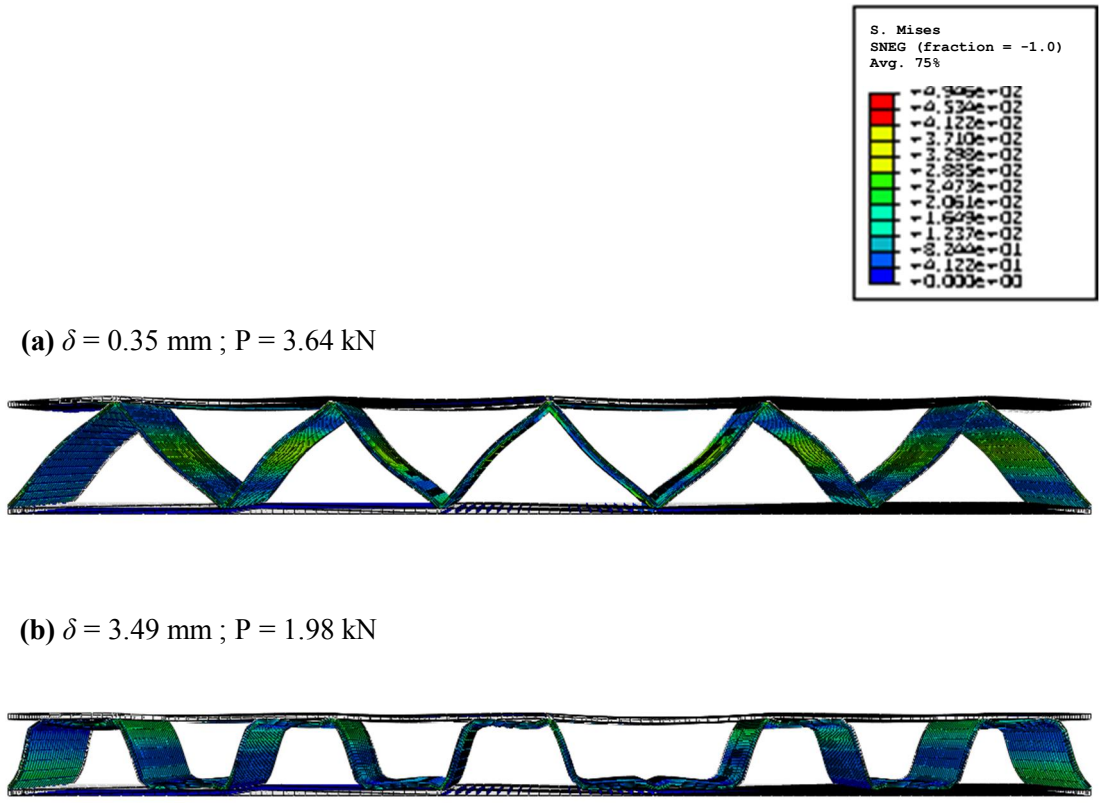

Figure 5.31: Predicted deformation modes for the composite corrugated-core structure; (a) initial buckling and (b) contact between the upper skin and middle of the struts. Note that the inset gives the Mises stress.

The FE responses of the corrugated-core structures filled with the foam are shown in Figures 5.32 and 5.36 with those determined experimentally during the compression test. Figure 5.32 compares the experimental response of the compression-load displacement traces with the two different contact conditions in the numerical analysis. The first condition (FE_Tied) is where the foam is assumed to have a good bonding with the surfaces of the corrugated-core. The second condition (FE_Untied) is vice versa, where untied between the foam and corrugated-core.

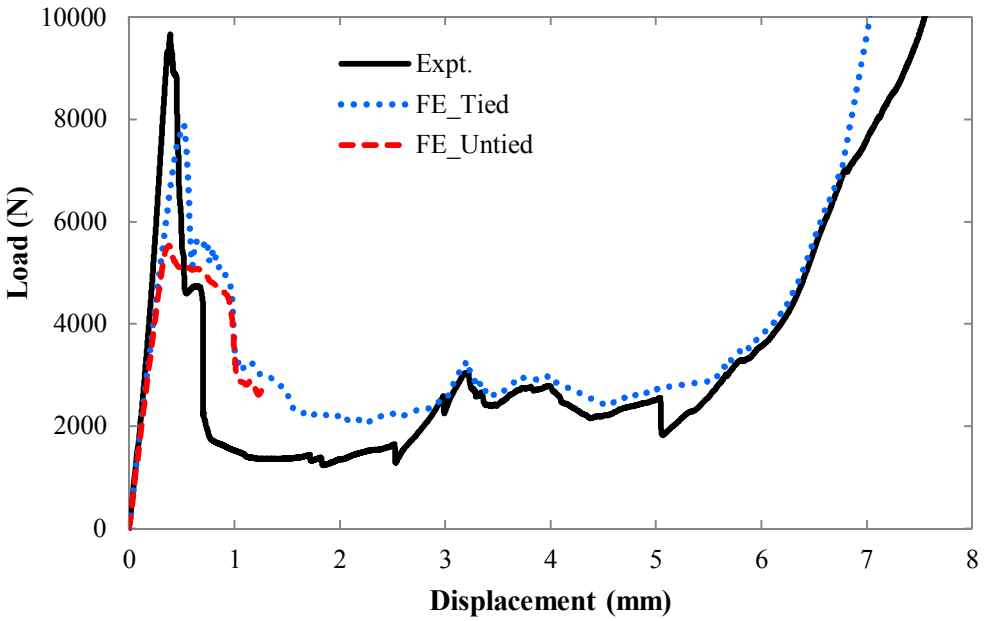

Figure 5.32: The measured response for a GFRP corrugated-core with a foam-filled structure and compared with two numerical simulations, the corrugated-core tied or untied with the PU foam.

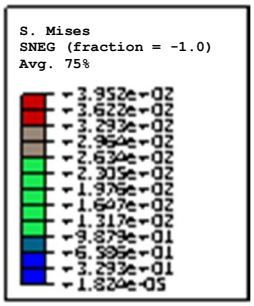

(a) δ = 0.39 mm ; P = 5.53 kN

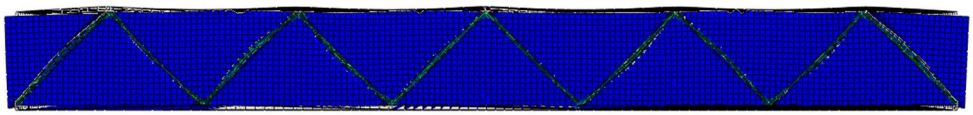

(b) δ = 1.25 mm ; P = 2.69 kN

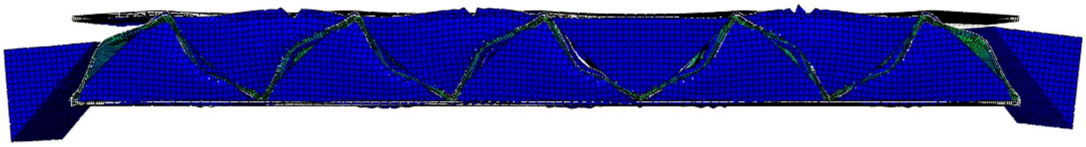

Figure 5.33: Predicted deformation modes for a corrugated-core structure with untied foam; (a) initial buckling and (b) both sides of foam went out from the core. Note that the inset gives the Mises stress.

The FE_Untied model shows a good relationship in stiffness responses, however the model predicted the maximum load is 44% lower compared than the experimental value. The simulation was deliberately stopped at 1.25 mm due to both sides of the foam extending out from the corrugated-core, as in Figure 5.33. Apparently, less contact between the core, and therefore foam reduces the peak strength of this model.

In the FE_Tied model, it is clear that the numerical result gives a good prediction for stiffness of the core, and just about 18% lesser of the peak strength compared to experimental result. However, the model is progressively and well-deformed for both corrugated-core and foam. The numerical interaction between the core and foam slightly increases by 30% of the contact load just after the peak compared to experimental data, but it is a reasonable prediction beyond that until the densification region. Interestingly, due to the fact that the PU foam is a compressible structure with a low density, almost all of the compression loads are carried by the corrugated-core structure and the foam insignificantly a load carrier in this sandwich configuration, as can be confirmed in Figure 5.34. Progressive deformations of this model are shown in Figure 5.35, and the collapse behaviour in the model is showing a good agreement with the experimental images, as in Figure 4.26.

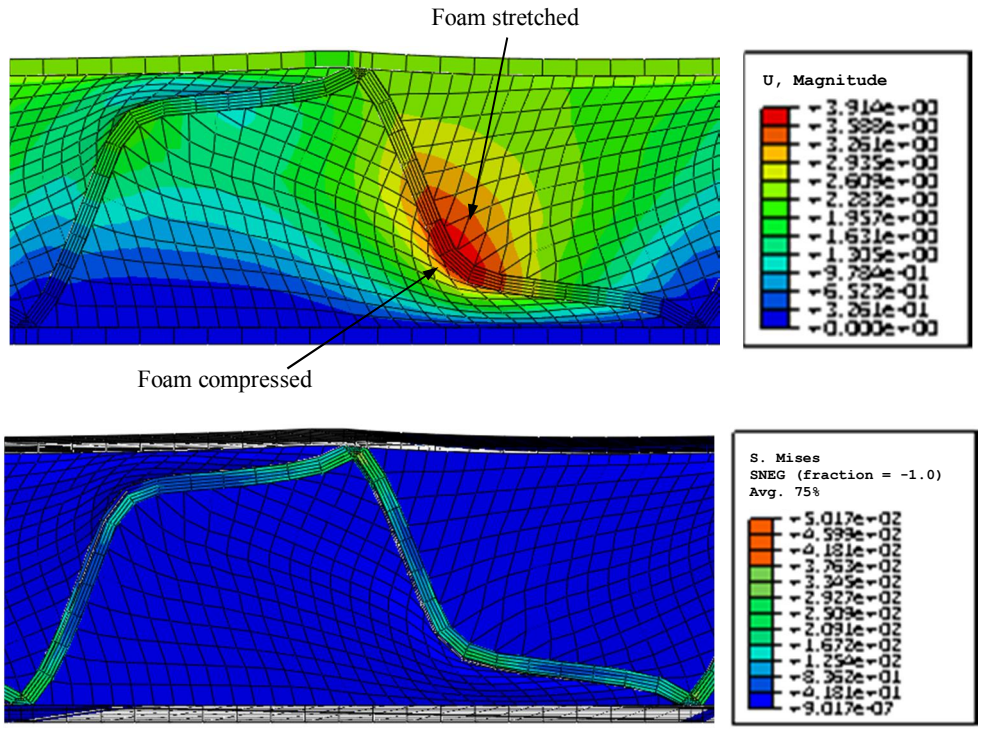

Figure 5.34: Comparison of a unit cell in the corrugated-core structure with fully-filled at different magnitudes; (a) deformation and (b) stress.

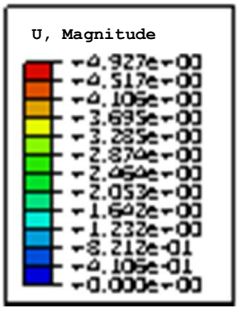

(a) δ = 0.035 mm ; P = 0.606 kN

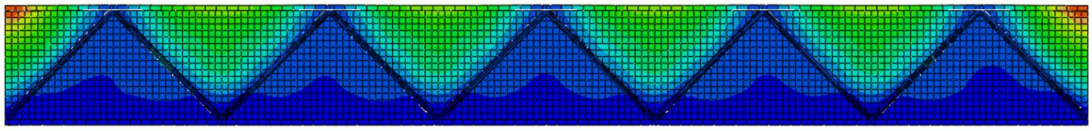

(b) δ = 0.53 mm ; P = 7.88 kN

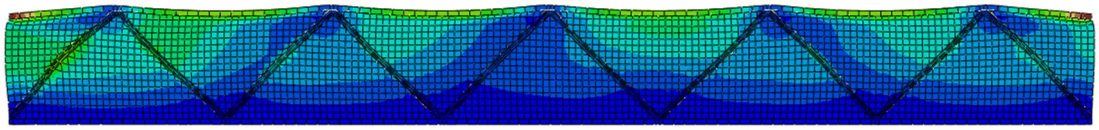

(c) δ = 1.50 mm ; P = 2.63 kN

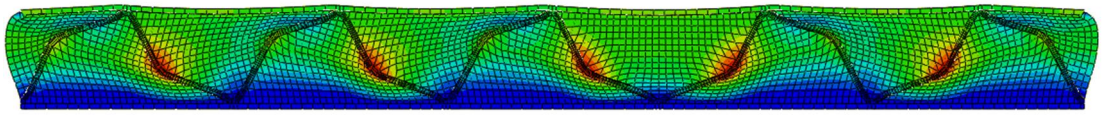

(d) δ = 3.19 mm ; P = 3.24 kN

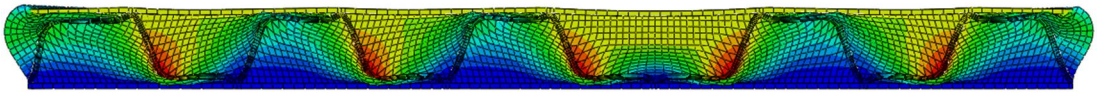

Figure 5.35: Predicted deformation modes for a corrugated-core structure with fully-filled foam; (a) initial loading, (b) peak loading, (c-d) deformation in progress as the corrugated-core buckled and the foam been compressed. Note that the inset gives the deformation values.

Figure 5.36 shows the measured response and predictions of the load-displacement trace for the corrugated-core structures with semi-filled foam core. Here, the numerical value slightly overestimates the peak load by 18% than the experimental result. However, in Figure 5.37 shows the deformation pattern of the structure agreed well with the experimental results.

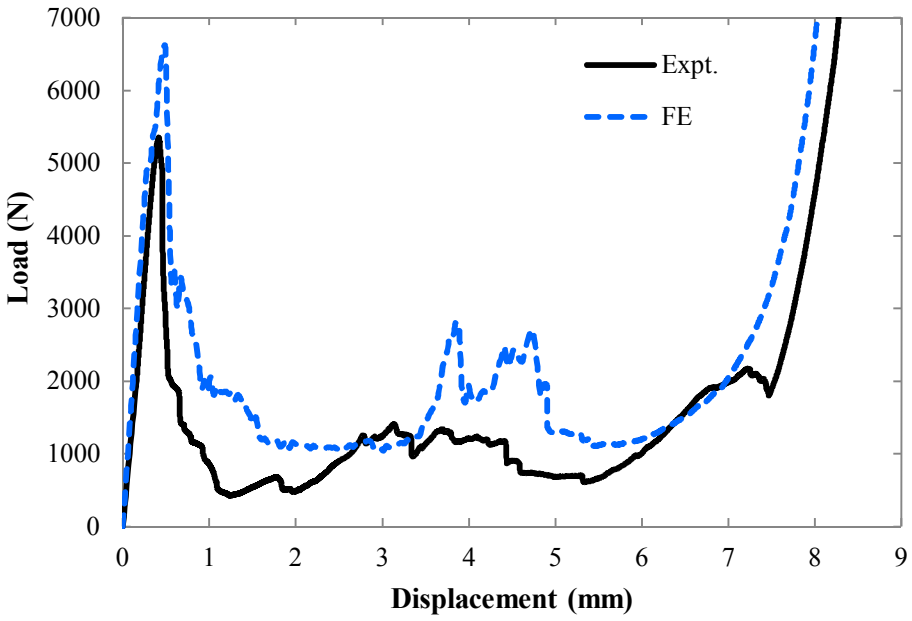

Figure 5.36: The measured response and the predictions of the load-displacement response for a corrugated-core with semi-filled structure. Note that this is GFRP sandwich structure with semi-filled core (GFPUS).

(a) δ = 0.45 mm ; P = 6.49 kN

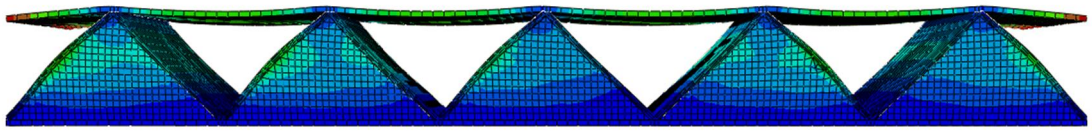

(b) δ = 4.91 mm ; P = 1.95 kN

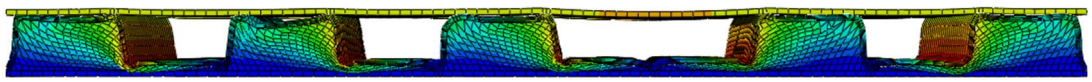

Figure 5.37: Predicted deformation modes for a corrugated-core structure with semi-filled foam; (a) peak loading and (b) collapse of corrugated-core sandwich structure. Note that the inset gives the deformation magnitude.

5.5 Dynamic Finite Element Modelling

This section presents details of the numerical modelling procedures for the metal and composite corrugated-core sandwich structures under dynamic compression loading. These three dimensional numerical simulations with six degrees of freedom were performed using Abaqus/Explicit. At the end of this section, the numerical data will be compared using experimental results.

5.5.1 Model Geometry and Element

The response of the corrugated-core sandwich structure under dynamic compression loading was modelled using the conventional shell element, S4R. As in the quasi-static modelling in Section 5.4.11, the corrugated-core was modelled together with upper and lower skins, as in Figure 5.38. The element size for each of the skins was of 12 x 50, giving a total of 600 elements. A total of 3500 elements were generated in the corrugated-core, as same as used in the quasi-static FE models. Overall, the total number of 4700 element meshes was used in this sandwich structure model.

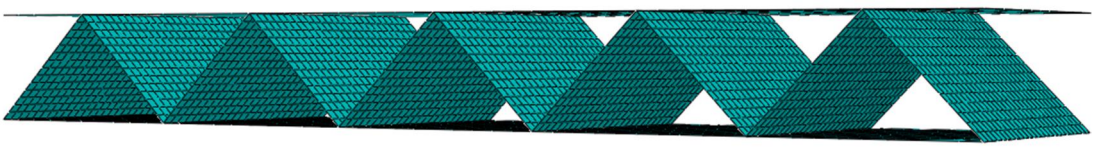

Figure 5.38: The meshes of the sandwich structure modelling.

The impactor was modelled as a flat plate using the discrete rigid surface, R3D4, and positioned above the sandwich model with a 1 mm offset. The small offset was introduced so that the impactor and the sandwich model were not in contact at the beginning of the simulation.

5.5.2 Interaction Property, Boundary and Loading Conditions

Figure 5.39 shows the model assembly used to simulate the dynamic compression test. A point mass, equal to the mass of the experimental impactor, was assigned to a reference point located at the centre of the flat plate. The reference point also was used to record the displacement from this model.

An initial velocity was prescribed to the rigid plate, was equal to the impact velocity engaged in the experiments. An initial imperfection was also introduced in the sandwich structure modelling to accurately predict the buckling behaviour, as mentioned in Section 5.4.1.6. A surface-to-surface contact algoritham was used to define contact between the impactor and the sandwich model. Self-contact within the corrugated-core was also modelled. The interaction properties were set to 'softened' in the normal direction and a friction coefficient of 0.15 was assumed in the tangential direction. All nodes along the upper and lower core edges were tied to the skins. The lower surface of the bottom skin was fixed, to restrain from any movements.

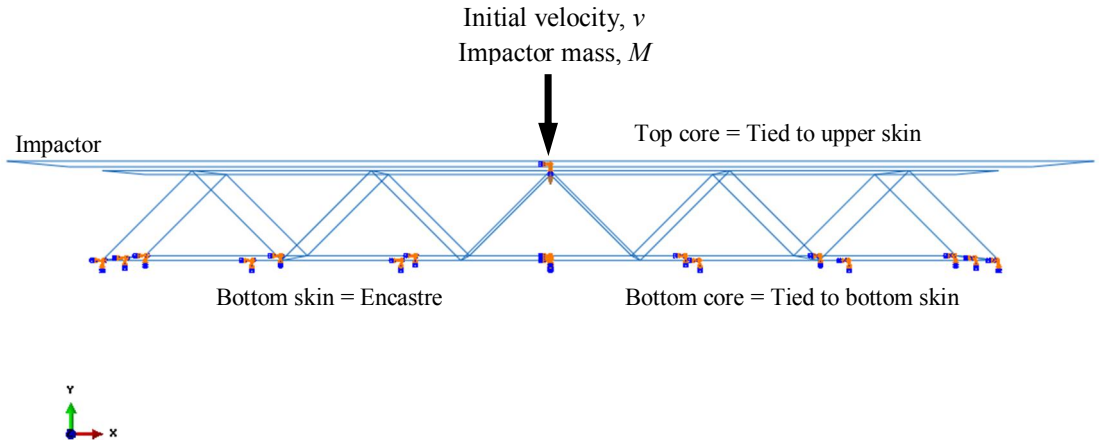

Figure 5.39: Loading direction, boundary conditions and assembly for the dynamic compression model.

5.5.3 Material Model and Input Data

The input data for the elastic property and progressive damage development in this model, were used as described in Sections 5.2 and 5.3 for the aluminium and composite materials, respectively.

Rate-dependent plasticity, based on a scaling function, was used in the analysis. This rate-dependent hardening curve in terms of static relation can be expressed as [2]:

$$\sigma_D(\bar{\varepsilon}^{pl}, \dot{\bar{\varepsilon}}^{pl}) = \sigma_S(\bar{\varepsilon}^{pl}) R(\dot{\bar{\varepsilon}}^{pl}) \qquad 5.27$$

where R is a yield stress ratio between the dynamic and static strengths. The equivalent plastic strain, $\bar{\varepsilon}^{pl}$:

$$\bar{\varepsilon}^{pl} = \int_0^t \sqrt{\frac{2}{3}\dot{\varepsilon}^{pl} : \dot{\varepsilon}^{pl}}\, dt \qquad 5.28$$

$$R = \frac{\sigma_D}{\sigma_S} \qquad 5.29$$

The yield stress ratio for the AL 2024-0 material was set as R = 1.0 , 2.5 at $\dot{\bar{\varepsilon}}^{pl} = 0$, 40 s^{-1} , and the data were taken from reference [20].

5.5.4 Modelling Data Output

In this analysis, the stress, strain, contact force and displacement field output were requested for the whole sandwich structure model. In the history output, the displacement data in the *y*-direction were obtained at the rigid platen reference point, while the contact force data were measured form the interaction between the impactor and upper skin. The acquisition frequency was set to 1 x 10^{-5} s^{-1}.

5.5.5 Results from the Numerical Analysis

The FE results for the structures were compared to the experimental results to verify the numerical model. Figure 5.40 shows the force-displacement traces of experimental and FE results, for an aluminium system. The Figures 5.40(a) and (b) show the impact response at low and beyond the energies to break the structures, respectively. In general, a small imperfection with a scale factor of 1% as used in quasi-static FE model, was applied to the thickness of the model, the FE results indicate good agreement with the corresponding experimental results. The deformation trends in the dynamic FE models mirror those observed in the quasi-static FE models, where buckling was dominating the initial damage mechanisms of the structure, as shown in Figure 5.41.

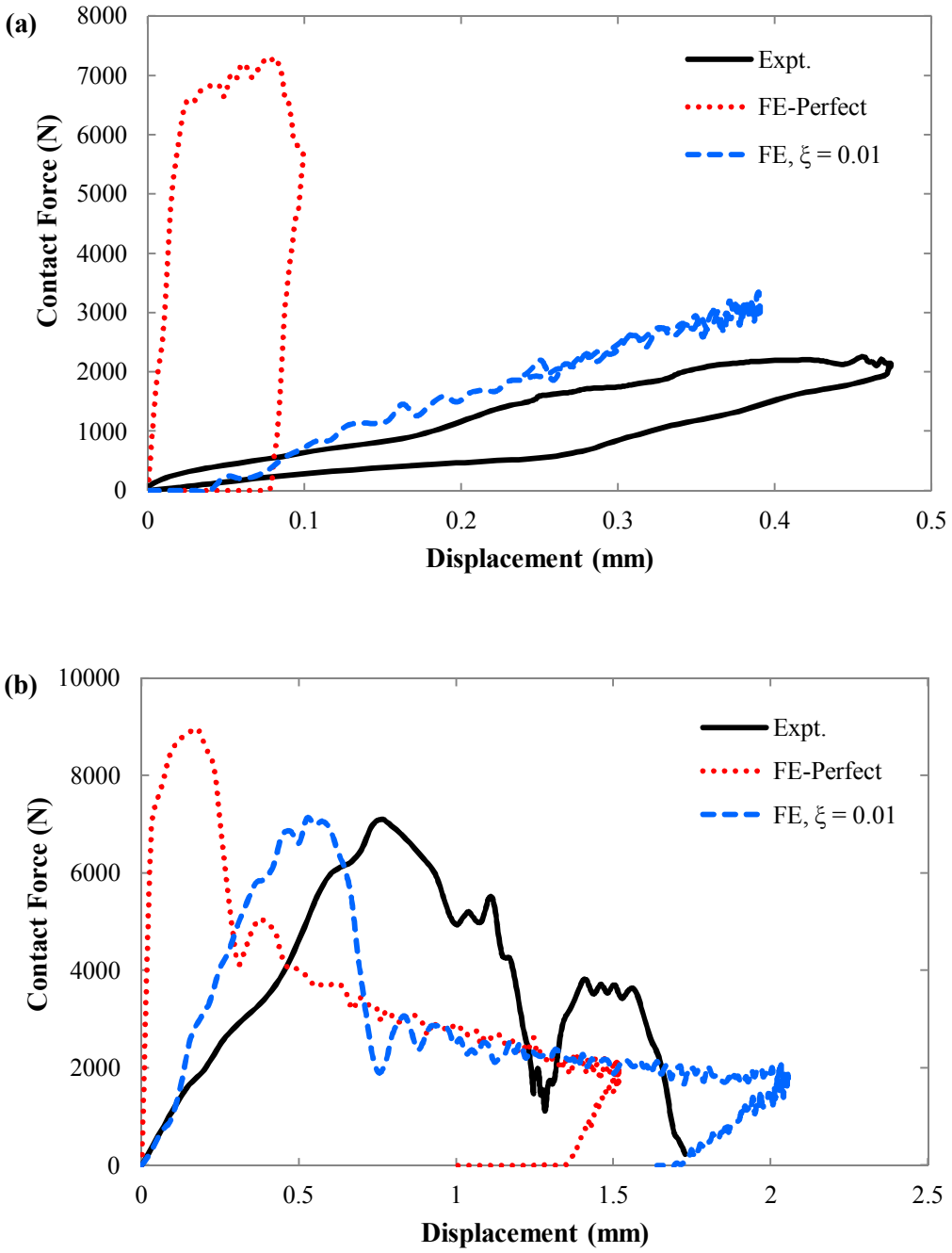

Figure 5.40: The measured response for an aluminium corrugated-core structure compared to the numerical simulation. The force-displacement responses for the model with FE–ξ = 0.01 show reasonable agreement with the measured response. Note that in this FE analysis, an initial velocity of (a) 0.99 m/s and (b) 3.13 m/s has been applied.

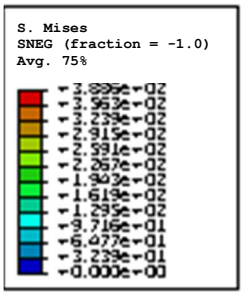

(a) t =20 μs ; δ = 0.062 mm ; F = 0.69 kN

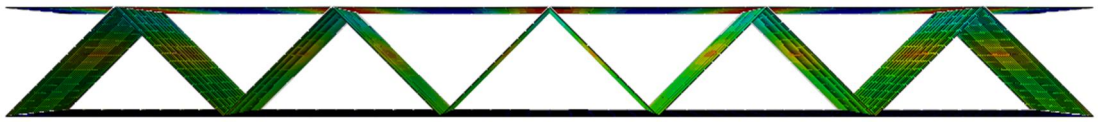

(b) t =250 μs ; δ = 0.689 mm ; F = 4.19 kN

Figure 5.41: Predicted deformation modes for an aluminium corrugated-core structure at a velocity of 3.13 m/s; (a) initial contact and (b) buckling of the struts. Note that the inset gives the Mises stress.

Figure 5.42 shows the force-displacement traces for the experimental and FE results, for typical composite corrugated-core structures. Figures 5.42(a) and (b) show the impact response at low and beyond the energies to break the structures for GFRP corrugated-core specimens, respectively. With an imperfection amplitude of 5% was applied to the thickness of the model, the FE results indicate reasonable agreement with the corresponding experimental results. The deformation trends in the dynamic FE models were observed similar in the quasi-static FE models, where buckling and followed by fibre fracture were the typical damage mechanisms of the structure, as shown in Figure 5.43.

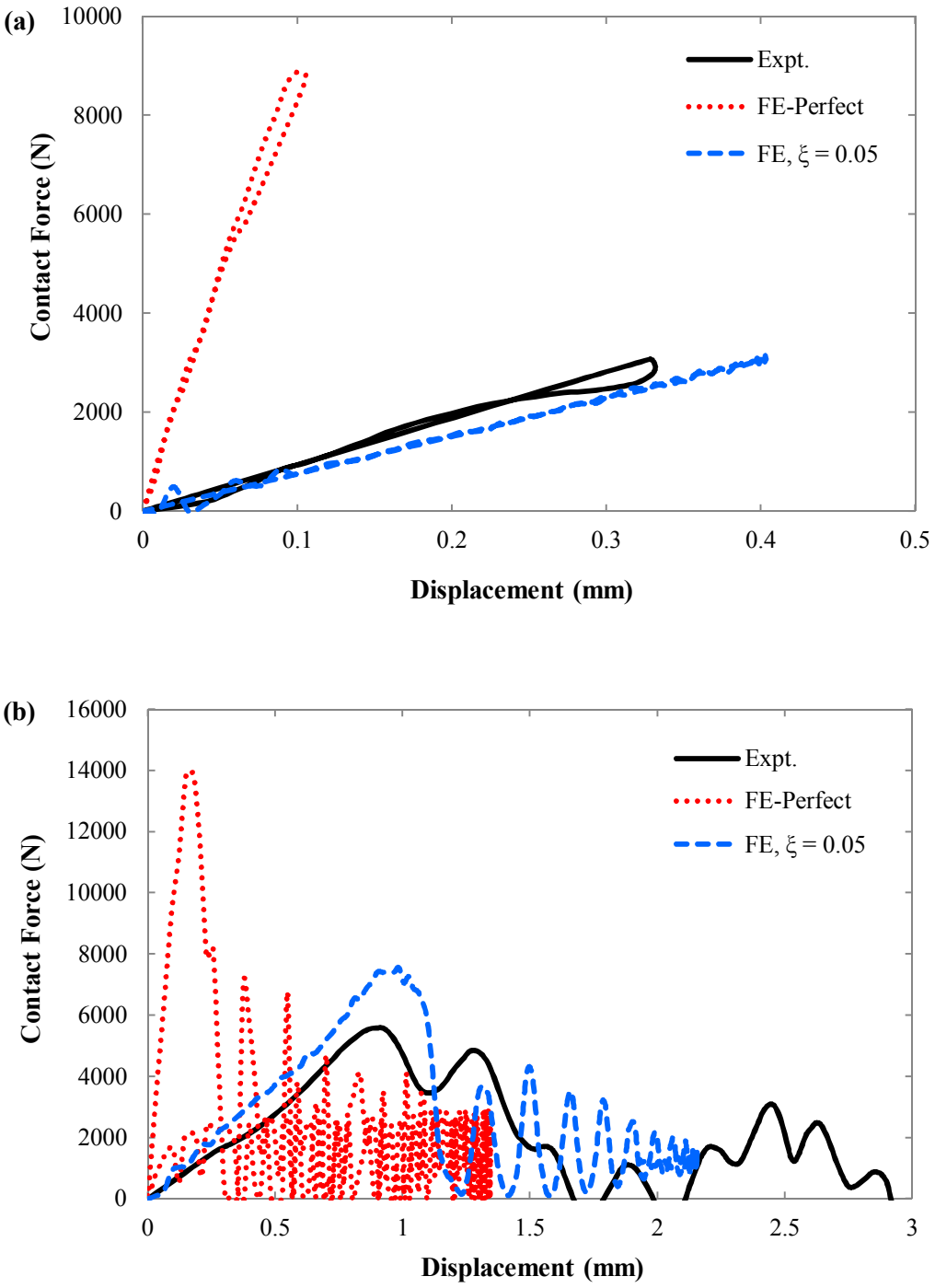

Figure 5.42: The measured response for the GFRP corrugated-core structure compared to the numerical simulation. The force-displacement responses of the model with FE–ξ = 0.05 show reasonable agreement with the measured response. Note that in this FE analyses, an initial velocity of (a) 0.99 m/s and (b) 3.13 m/s has been applied.

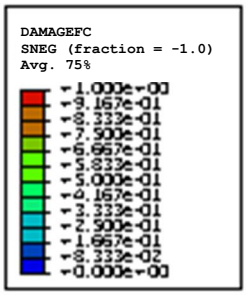

(a) t = 20 μs ; δ = 0.062 mm ; F = 0.24 kN

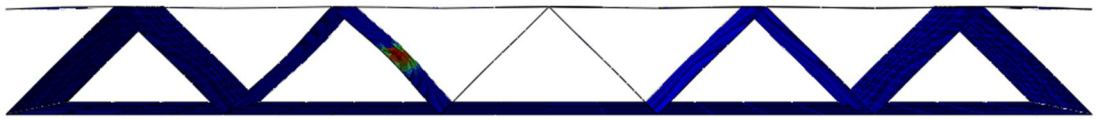

(b) t = 430 μs ; δ = 1.11 mm ; F = 4.86 kN

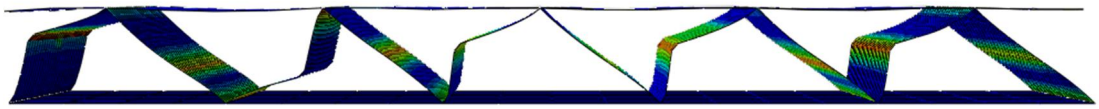

Figure 5.43: Predicted deformation modes for a corrugated-core structure at a velocity of 3.13 m/s; (a) initial buckling and (b) fibre fracture in the struts. Note that the inset gives the magnitude of fibre damage in compression.

5.6 Summary of Chapter V

Chapter V presented details of the FE modelling procedures and discussions on validating the results between the experimental and numerical data. Abaqus/Standard was used to predict the quasi-static response while an explicit dynamic solver, Abaqus/Explicit was used in simulating the low velocity impact test results. In general, the numerical models offered good agreement in terms of the essential features of the experimental load-displacement traces, as listed in Tables 5.5 and 5.6. The evidence suggests that the FE modelling procedures used to create the model could be used to model corrugated-core sandwich structures with different material properties.

Table 5.5: Predicted peak loads compared to the experimental results for the corrugated-core sandwich structures subjected to lateral compression loads.

Specimen	**Imperfection amplitude, ξ**	**Experiment - Ave. P_{max} (kN)**	**FE Prediction - P_{max} (kN)**	**Percentage different (%)**
AL1	0.01	1.503	1.496	-0.43
AL2	0.01	2.635	2.592	-1.63
AL3	0.01	3.724	3.888	4.42
AL4	0.01	4.829	5.184	7.36
AL5	0.01	6.320	6.480	2.53
GF2U1	0.05	0.107	0.097	-9.35
GF2U2	0.05	0.178	0.194	8.99
GF2U3	0.05	0.263	0.291	10.65
GF2U4	0.05	0.375	0.388	3.47
GF2U5	0.05	0.460	0.485	5.55
GF3U5	0.05	1.191	1.281	7.56
GF4U5	0.05	2.582	2.995	16.00
GF5U5	0.05	4.126	4.727	14.57
GF7U5	0.05	11.23	13.02	15.93
GF10U5	0.05	21.52	23.96	11.37
CF2U1	0.05	1.169	1.198	2.52
CF2U2	0.05	2.183	2.396	9.78
CF2U3	0.05	3.187	3.594	12.77
CF2U4	0.05	4.514	4.792	6.17
CF2U5	0.05	5.965	5.990	0.43
CF3U5	0.05	6.068	6.320	4.15
CF4U5	0.05	7.747	8.812	13.75
CF5U5	0.05	8.759	9.960	13.71
CF6U5	0.05	15.55	15.60	0.29
			Average	**6.69**

Table 5.6: Predicted peak contact forces compared to the experimental results for the corrugated-core sandwich structures (H = 0.5 mm) under the low velocity impact.

Specimen	**Imperfection amplitude, ξ**	**Velocity, v (m/s)**	**Experiment - Ave. F_{max} (kN)**	**FE Prediction - F_{max} (kN)**	**Percentage different (%)**
AL5_I1	0.01	0.99	2.51	3.03	20.72
AL5_I2	0.01	1.40	6.31	6.02	-4.60
AL5_I3	0.01	1.98	7.09	7.21	1.69
AL5_I4	0.01	3.13	7.37	7.13	-3.26
AL5_I5	0.01	4.43	6.24	7.15	14.58
GF5U5_I1	0.05	0.99	3.47	3.11	-10.37
GF5U5_I2	0.05	1.40	3.99	4.15	4.01
GF5U5_I3	0.05	1.98	6.11	6.5	6.38
GF5U5_I4	0.05	3.13	5.89	7.01	19.02
GF5U5_I5	0.05	4.43	5.83	6.80	16.64
CF2U5_I1	0.05	0.99	3.18	3.24	1.89
CF2U5_I2	0.05	1.40	7.35	6.98	-5.03
CF2U5_I3	0.05	1.98	7.54	7.67	1.72
CF2U5_I4	0.05	3.13	6.53	7.42	13.63
CF2U5_I5	0.05	4.43	6.74	7.31	8.46
				Average	**5.70**

5.7 References

[1] Hibbitt, Karlsson, Sorensen. Abaqus/CAE User's Manual (6.12): Dassault Systèmes Simulia Corp., Providence, RI, USA; 2012.

[2] Hibbitt, Karlsson, Sorensen. Abaqus Theory Manual (6.12): Dassault Systèmes Simulia Corp., Providence, RI, USA; 2012.

[3] Hibbitt, Karlsson, Sorensen. Abaqus/CAE Analysis Manual (6.12): Dassault Systèmes Simulia Corp., Providence, RI, USA; 2012.

[4] Hooputra H, Gese H, Dell H, Werner H. A xomprehesive failure model for crashworthiness simulation of aluminium extrusions. International Journal of Crashworthiness. 2004;9:449-463.

[5] Fan J. Investigation of the Behaviour of Fibre Metal Laminates subjected to Low Velocity Impact. PhD Thesis. University of Liverpool, 2010.

[6] Hashin Z, Rotem A. A fatigue failure criterion for fiber reinforced materials. Journal of Composite Materials. 1973;7(4):448-464.

[7] Hashin Z. Analysis of Properties of Fiber Composites With Anisotropic Constituents. Journal of Applied Mechanics. 1979;46(3):543-550.

[8] Hashin Z. Failure Criteria for Unidirectional Fiber Composites. Journal of Applied Mechanics. 1980;47(2):329-334.

[9] Hashin Z. Analysis of Composite Materials—A Survey. Journal of Applied Mechanics. 1983;50(3):481-505.

[10] Matzenmiller A, Lubliner J, Taylor RL. A Constitutive Model for Anisotropic Damage in Fiber-Composites. Mechanics of Materials. 1995;20:125–152.

[11] Camanho PP, Davila CG. Mixed-Mode Decohesion Finite Elements for the Simulation of Delamination in Composite Materials. NASA/TM-2002–211737. 2002:1-37.

[12] Kaw AK. Mechanics of Composite Materials: Second Edition: CRC Press; 2005.

[13] Smith MIH. The Compressive Response of Novel Lattice Strcutures Subjected to Static and Dynamic Loading. PhD Thesis. University of Liverpool, 2012.

[14] Winkler JR, Brian Davies J. Elimination of spurious modes in finite element analysis. Journal of Computational Physics. 1984;56(1):1-14.

[15] Côté F, Deshpande VS, Fleck NA, Evans AG. The compressive and shear responses of corrugated and diamond lattice materials. International Journal of Solids and Structures. 2006;43(20):6220-6242.

[16] Kazemahvazi S, Zenkert D. Corrugated all-composite sandwich structures. Part 1: Modeling. Composites Science and Technology. 2009;69(7–8):913-919.

[17] Riks E. An incremental approach to the solution of snapping and buckling problems. Journal of Solids Structures. 1979;15:529-551.

[18] Alias A, Mines RAW, Birch RS, Li QM, Close JA. On the measurement of the crush behaviour of structural foams. 11th International Conference on Experimental Mechanics, Oxford, 1998.

[19] Deshpande VS, Fleck NA. Isotropic constitutive models for metallic foams. Journal of the Mechanics and Physics of Solids. 2000;48(6–7):1253-1283.

[20] Guan ZW, Cantwell WJ, Abdullah R. Numerical modeling of the impact response of fiber–metal laminates. Polymer Composites. 2009;30(5):603-611.

CHAPTER VI: DISCUSSION

6.1 Introduction

This chapter discusses the experimental and numerical results from the tests on the corrugated-core sandwich structures subjected to different testing conditions. For the quasi-static compression tests, the effect of varying the number of unit cells, cell wall thickness, width and the configuration of the foam in foam-filled sandwich structures will be analysed. For bi-axial loading, strength-to-failure criteria for the corrugated-core structures were determined. For low velocity impact tests, the responses of the specimens will be analysed and compared with quasi-static data. Following a discussion of progressive damage development in the specimens, the fracture modes in the corrugated-core structures will be presented and characterised. Finally, these novel corrugated-core structures will be compared to existing cores.

6.2 The Effect of Varying the Number of Unit Cells

One would instinctively expect the performance of a multiple unit cell corrugation to accurately reflect that of a single cell system. However, difficulties associated with the manufacture of small single cell specimens, as well as problems with test alignment, may introduce unwanted irregularities into the test data. In order to establish this more accurately, tests were undertaken on corrugated specimens based on between one and five cells.

The effect of varying the number of unit cells on the compression strength of the aluminium and composite sandwich structures is shown in Figure 6.1(a). A comparison of the numerical analyses and the experimental results indicates that the influence of the cell number is accurately predicted. Clearly, the compression strength, σ_{max} , of the aluminium corrugation is much higher than that of the GFRP structure, due to the fact that the aluminium alloy is significantly thicker than its composite counterpart. Figure 6.1(b) shows the variation of the strength and modulus of the CFRP-based corrugations as a function of cell number. Here, the model accurately estimates the experimental strength and modulus values between one and five unit cells, for the metal and composites corrugations, with there being a linear relationship for both compression strength and modulus.

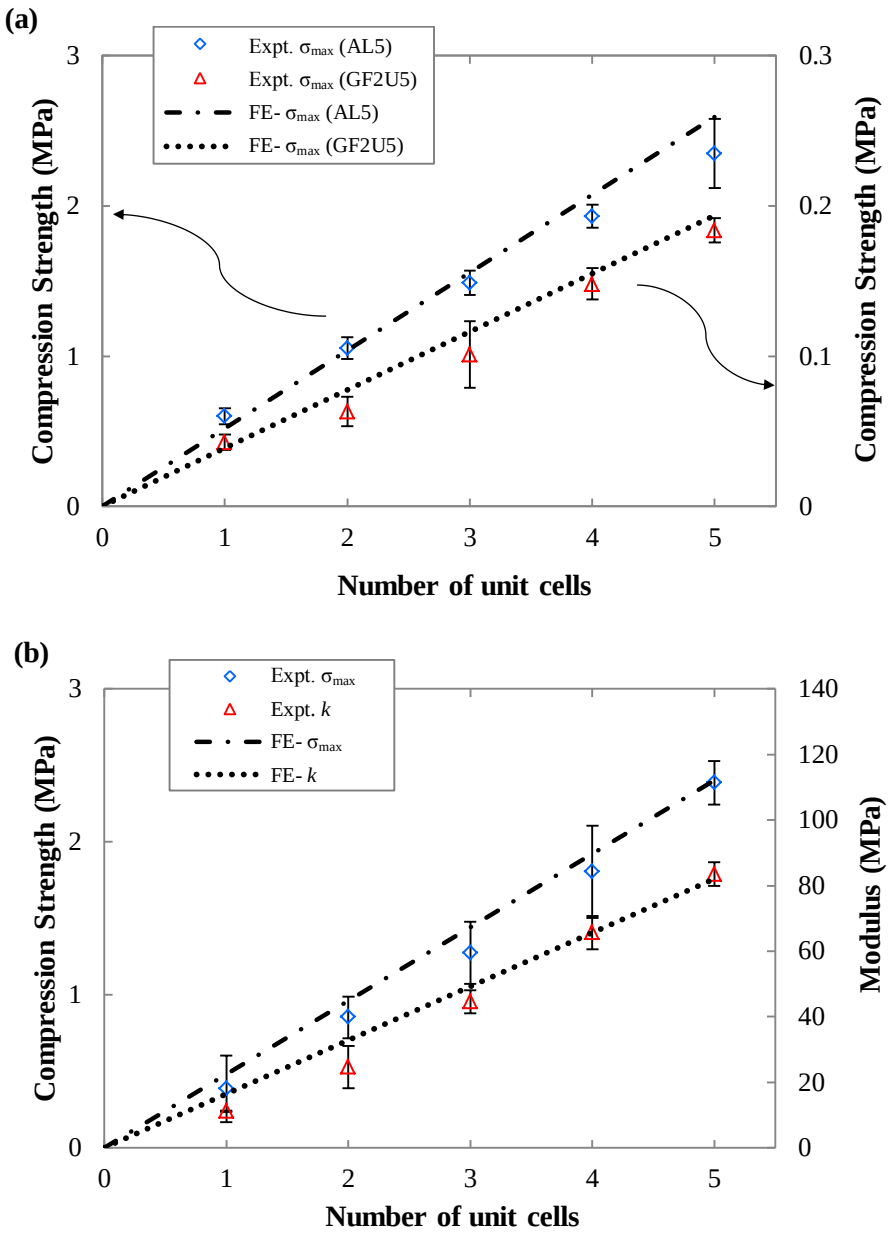

Figure 6.1: (a) Comparison of the measured and numerical data for compression strength of the AL5 and GF2U5 corrugated-core sandwich structures, and (b) compression strength and modulus properties as a function of the number of unit cells for the CF2U5 corrugated-core sandwich structures.

A comparison of Figures 6.1(a) and (b) indicates that the strengths of the aluminium and carbon fibre corrugations (AL5 and CF2U5) are similar, in spite of the fact that the density of the composite is significantly lower than that of the alloy.

All of the corrugated-core specimens were deformed to a similar level of crosshead displacement, and initial failure was dominated by instability of the struts or buckling. Figure 6.2 shows the deformed shapes of the GFRP corrugated structures based on between one and five unit cells. An examination of the photographs indicates that the failure modes are similar in all five specimens, with buckling and subsequent fracture of the cell walls being in evidence.

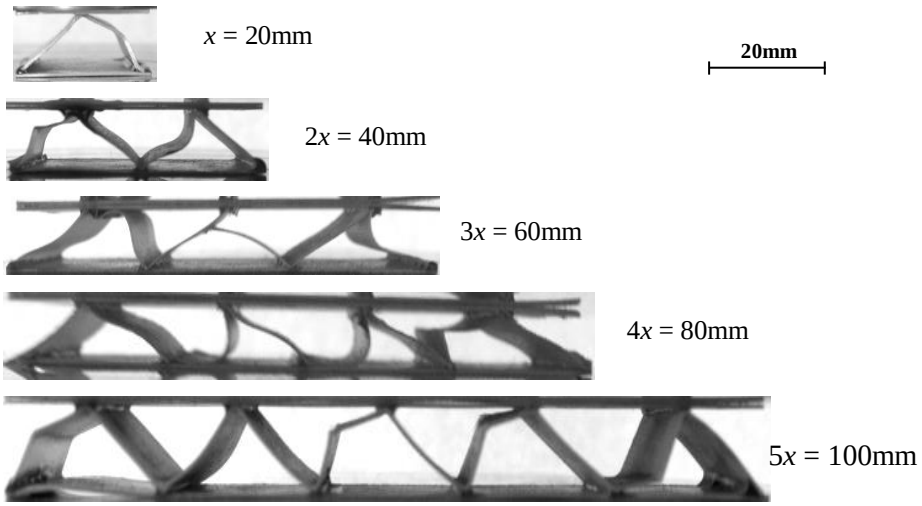

Figure 6.2: Photographs of damage in GFRP corrugated-core specimens based on an increasing number of unit cells.

6.3 The Effect of Varying the Cell Wall Thickness

Figure 6.3 shows the variation of compressive strength and modulus of the GFRP and CFRP corrugations as a function of wall thickness. As expected, the strength increases in a highly non-linear fashion with wall thickness. The compression strength of the CFRP corrugated-core with a wall thickness, H = 1.25 mm is impressive, with a value in excess of 18 MPa being recorded. The modulus property of the corrugations also increases rapidly with wall thickness. Further analysis of Figures 6.3(a) and (b) indicates that the properties associated with the thickest cores tend to be lower than expected. These discrepancies are associated with difficulties in manufacturing thicker corrugations. It was observed that once the wall thickness of the GFRP system exceeded one millimetre, the apexes became progressively rounded and defects were introduced at the bends in the corrugation. This is shown schematically in the top right hand corner of the figures. The presence of these

manufacturing defects greatly reduced both the strength and modulus of the corrugations. The vertical dashed line indicates the thickness beyond which the apex in the corrugation becomes rounded. It is worth noting that transition thickness geometry for GFRP and CFRP corrugations is 0.98 mm and 1.25 mm, respectively.

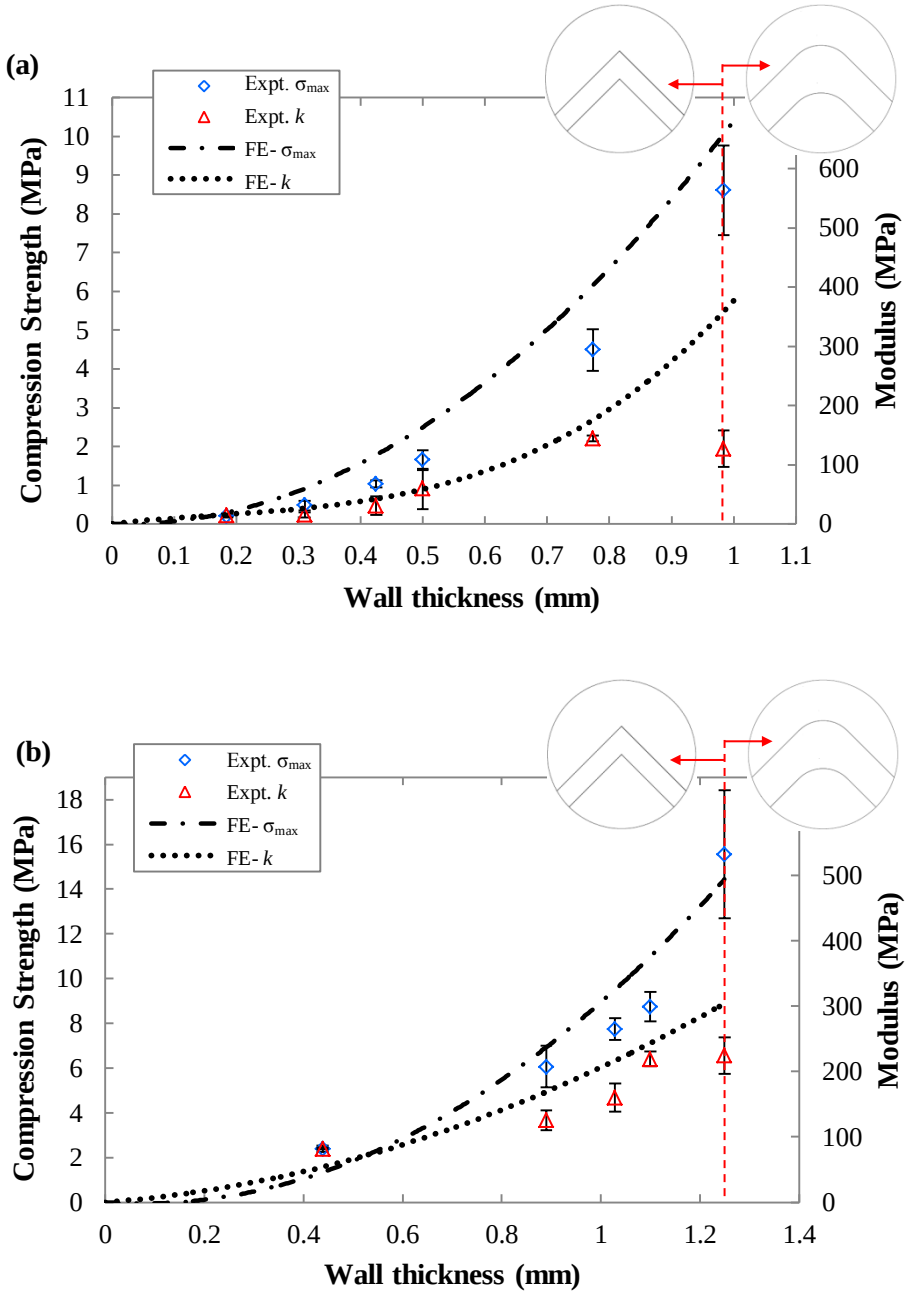

Figure 6.3: Comparison of the experimental data and numerical predictions of the compression strength and modulus as a function of cell wall thicknesses for sandwich structures based on: (a) GFRP and (b) CFRP.

In order to facilitate an appropriate comparison of the compression properties of the corrugations, the data in Figure 6.3 were normalised by the density of the core, ρ_c , to yield specific compression strength properties, σ_{sp} , and these values are shown as a function of cell wall thicknesses in Figure 6.4. The specific strength was calculated by;

$$\sigma_{SP} = \frac{\sigma_{\max}}{\rho_c} \tag{6.1}$$

The ρ_c , can be approximated as:

$$\rho_c = v_{c-c}\rho_{c-c} + \rho_f(1 - v_{c-c}) \tag{6.2}$$

where $\rho_{c\text{-}c}$ and ρ_f are the densities of the corrugated-core and the foam, respectively. Also, $v_{c\text{-}c}$ is the volume fraction of the core occupied by the corrugated-core member which is [1]:

$$v_{c-c} = \frac{H/t}{H/t + \cos\theta} \tag{6.3}$$

Note that for the unfilled corrugated-core sandwich panel, $\rho_f = 0$.

An examination of the figure indicates that the specific strength increases rapidly with wall thickness with the specific strength of the 1.25 mm panel being roughly three times that of the 0.4 mm thick structure. The figure suggests that the CFRP composites out-perform their GFRP and aluminium counterparts at a relative density of $\rho^* = 0.07$, whereas there appears to be little difference between the two composite systems as the wall thickness increases.

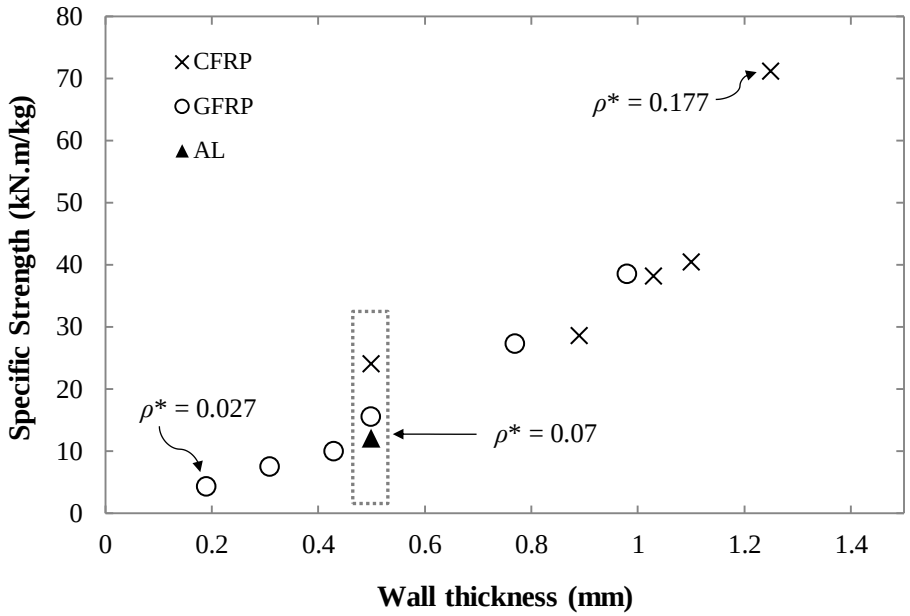

Figure 6.4: Comparison of the specific strength as a function of cell wall thickness for the GFRP, CFRP and aluminium corrugated-cores.

6.4 The Effect of Varying Specimen Width

A study was conducted on the 2-ply GFRP and CFRP sandwich structures to investigate the effect of varying the specimen width. The data from the compression tests are shown in Figure 6.5. Here, it is clear that both composite materials exhibit similar trends, with the maximum compression load as well as the stiffness increasing with specimen width.

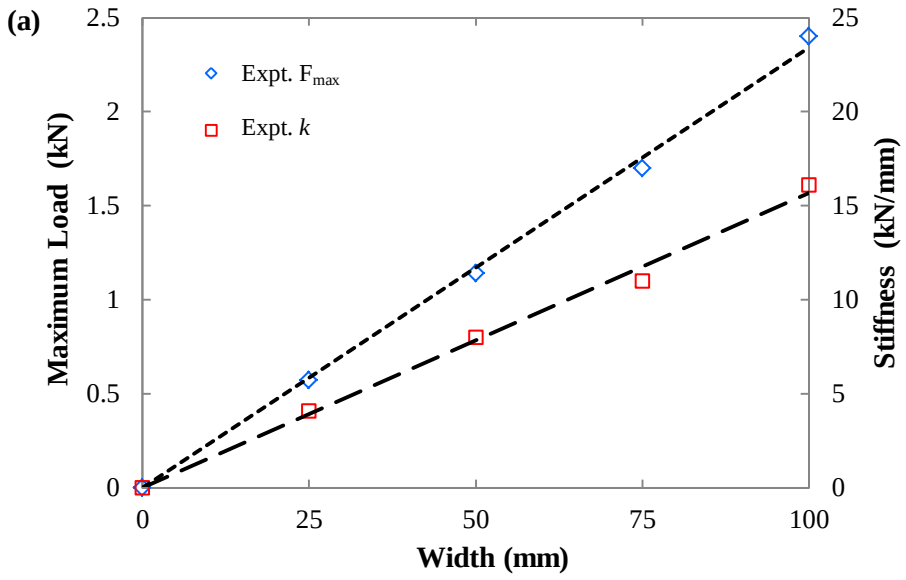

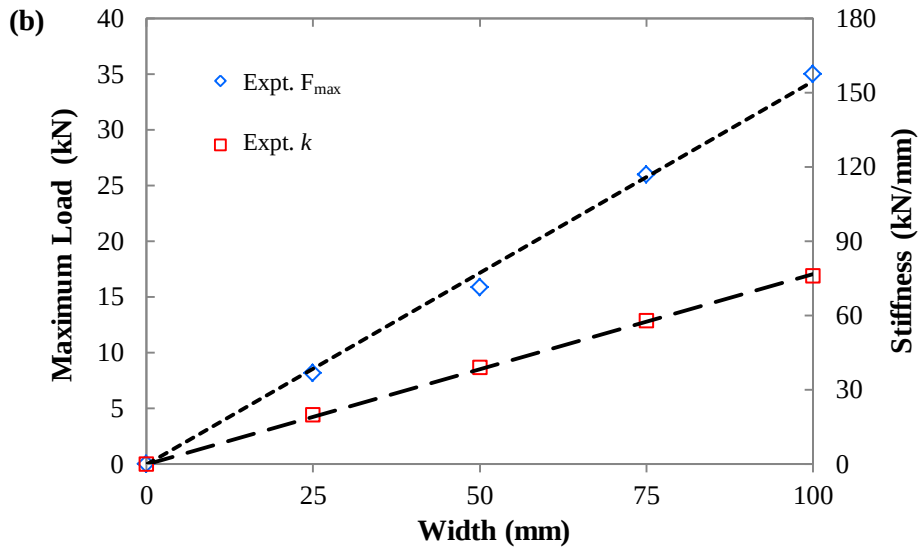

Figure 6.5: Comparison of the maximum compression load with stiffness as a function of width (a) the GFRP and (b) the CFRP sandwich specimens.

Figure 6.6 shows the compressive strength and modulus of the GFRP and CFRP corrugations as a function of normalised specimen width, η_w. The figure shows that the compression strength and modulus is unaffected by increasing width, i.e. it is independent of the specimen width. As indicated in Figure 6.6(a), the average compressive strength of the 2-ply GFRP specimen is 0.23 MPa and the modulus is 15.74 MPa. The dashed line corresponds to the FE prediction of the quasi-static compression test model. The results predicted by the model agree well with the experimental data.

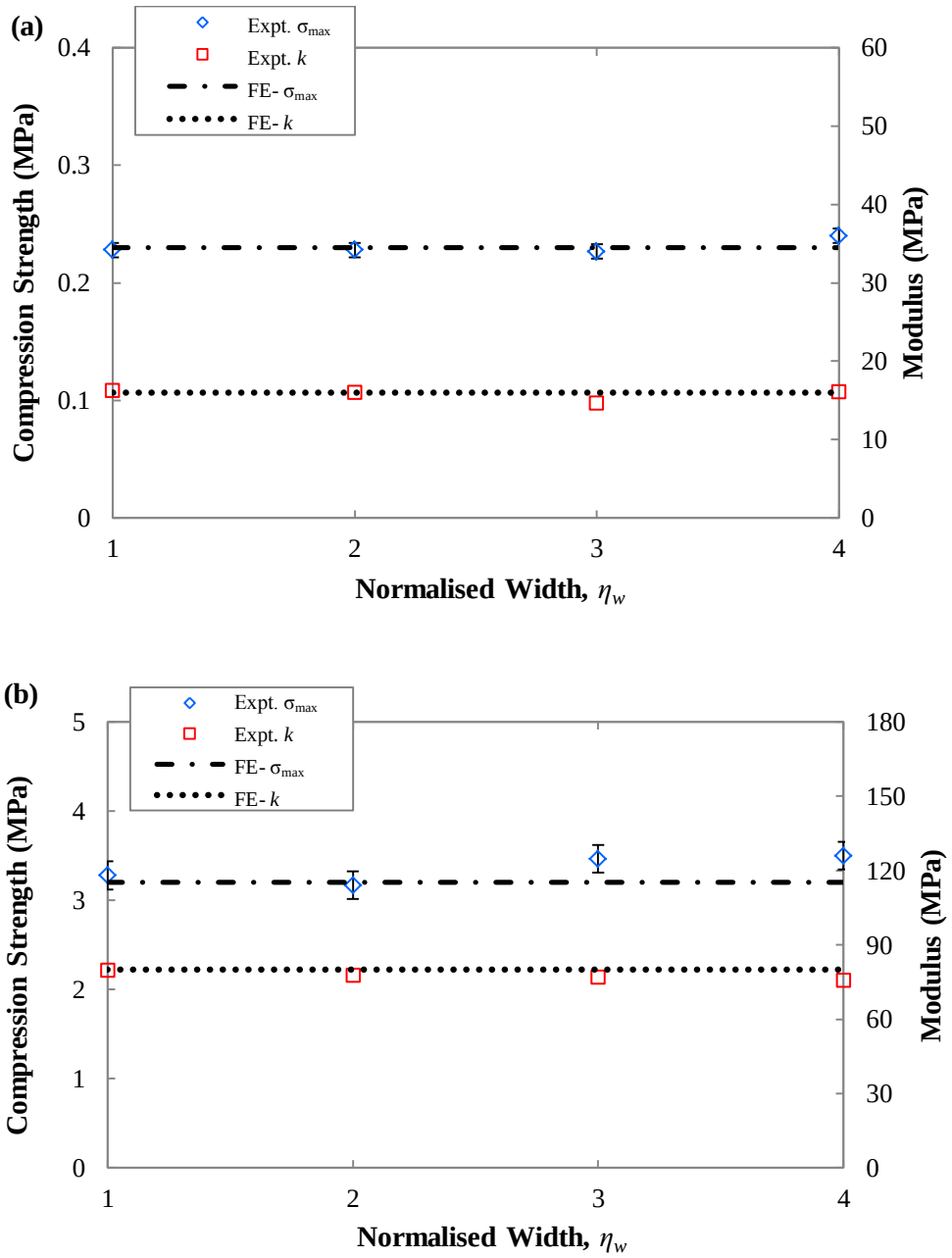

Figure 6.6: Comparison of the experimental data and numerical predictions of the compression strength and modulus as a function of normalised width of (a) the GFRP and (b) the CFRP sandwich specimens.

An examination of Figure 6.6(b) highlights a slight increase in compression strength, while the modulus was unaffected by increasing width. The slight increase in load was probably due to the uncontrolled buckling mode shape observed experimentally. This analysis increases the critical buckling load above that predicted by the FE analysis. Here, the average compressive strength for the 2-ply CFRP specimen is 3.55 MPa and the modulus is 77.78 MPa.

6.5 The Effect of Foam-filled Core

The measured compression stress versus strain responses of the foam-filled sandwich structures and the conventional sandwich structures (unfilled panel) are shown in Figure 6.7. For reference, the compression stress-strain curve for the rigid PU foam as the filler is also included. It can be seen that the foam-filled core sandwich structure offers a much improved compression strength compared to the sum of the conventional structure and the foam alone (by curve A+B).

As shown in Figure 6.7(a), foam filling in the GFRP sandwich structure had the effect of initially stabilising the corrugated-core member against buckling, resulting in a much enhanced compression strength and modulus compared to the conventional structure. As a result, the peak compression stress, σ_{max}, was two times greater than the conventional panel or even by the sum of its constituents A+B (foam and unfilled specimen tested separately).

For the CFRP sandwich structure in Figure 6.7(b), the compression strength in the fully-filled specimen has increased by over 50% compared to the conventional specimen. As the strain increased beyond the peak stress, the stress in the fully-filled specimen gradually decreased, in contrast to the much more rapid stress drop in the GFRP fully-filled specimen. However, both the GFRP and CFRP fully-filled specimens recovered from this stress drop at strains of 0.21 and 0.13, respectively. Subsequently, the compression stress in the fully-filled structure was constant and the energy absorption clearly increased as the conventional specimen crushed before both ends of the corrugated-core debonded. This improvement was believed to be due to the constraint effect between the PU foam and the corrugated-core member.

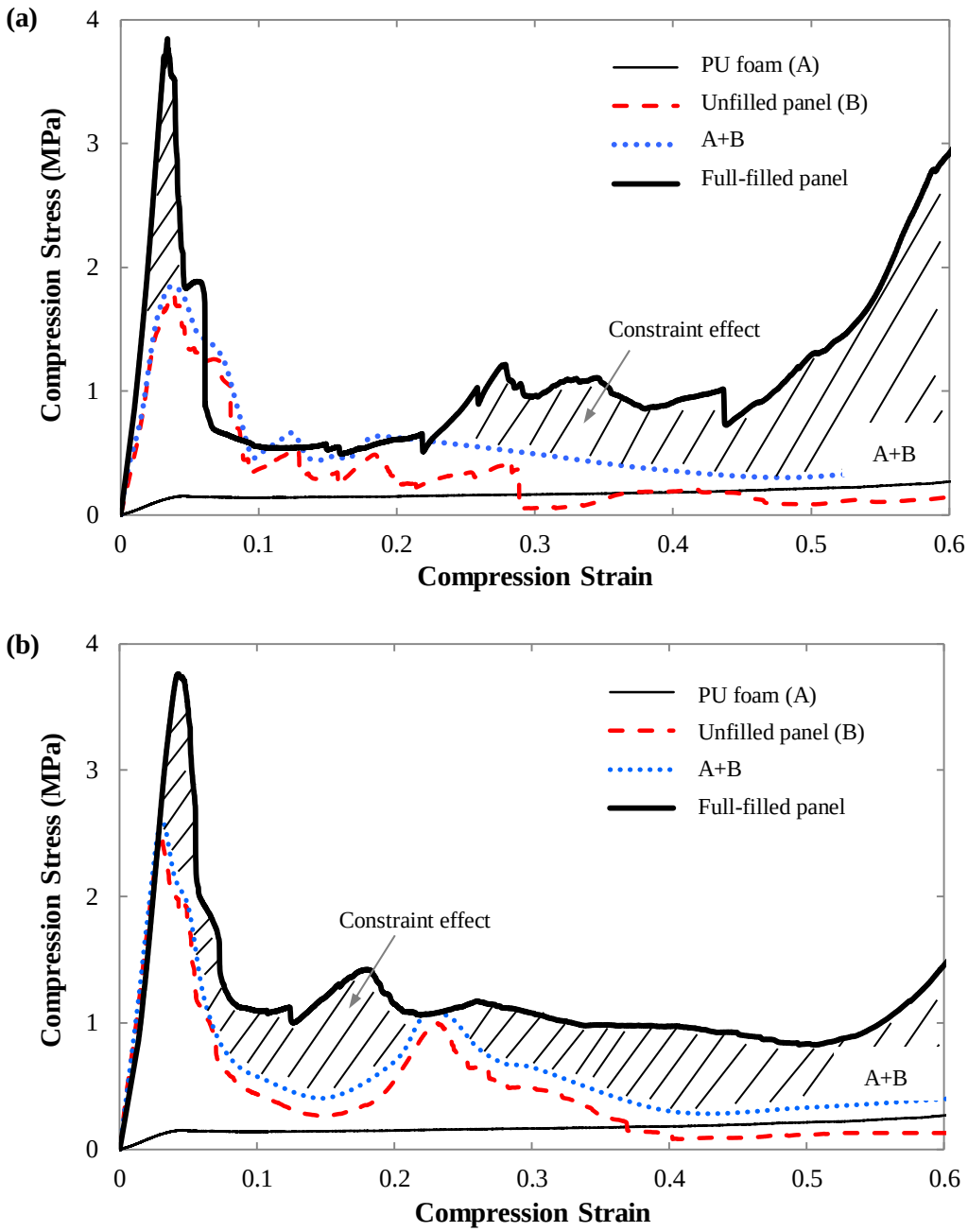

Figure 6.7: Comparison of the plain compression stress-strain behaviour of the PU foam, conventional corrugated-core (unfilled foam) and foam-filled core of (a) GFRP and (b) CFRP sandwich structures.

In order to further study the effect of filling the corrugated-core sandwich structure with the foam, the energy absorption capacity was characterised from the area under the stress-strain curve. The energy per unit volume, E_v, is defined as:

$$E_v = \int_0^{\varepsilon} \sigma . d\varepsilon \qquad 6.4$$

where the calculation of the value of E_v for the structure in the study was calculated up to a strain of $\varepsilon = 0.6$. The energy absorbed in the structure was then calculated as:

$$E_a = E_v \,.\, V \tag{6.5}$$

In addition, since mass is critical for energy absorbers destined for use in weight-sensitive applications, the specific energy absorption was another important parameter used in the study. The specific energy absorption, *SEA* , is defined as:

$$SEA = \frac{E_a}{W} \tag{6.6}$$

Table 6.1 summaries the results for the properties of the rigid PU foam, the GFRP and CFRP sandwich structures. It can be clearly seen that placing PU foam into the unfilled corrugated-core structure increases specific strength from 28.2% (semi-filled) to 63.5% (fully-filled) for the GFRP sandwich specimens. For the CFRP fully-filled sandwich structure, the specific strength shows a slight increase up to 15% relative to the conventional structure. Given that foam is a good energy absorption device, and filling the foam inside the corrugated specimen also increased the total mass of the structure, the results in table reveal that the *SEA* for the GFRP and the CFRP fully-filled sandwich structures improved by 160% and 105%, respectively. Therefore, the effect of injecting the foam is significant in improving the specific strength and *SEA* of the corrugated-core sandwich structures.

Table 6.1: Summary of the rigid PU foam, the GFRP and the CFRP corrugated-core sandwich structures. The composite sandwich structures are divided into three categories; conventional, semi-filled and fully-filled foam core.

Properties	**Foam**	**GFRP**			**CFRP**		
		Conventional	**Semi-Filled**	**Fully-filled**	**Conventional**	**Semi-Filled**	**Fully-filled**
Average Panel Density, ρ (kg/m^3)	-	261	280	310	244	260	281
Core Density, ρ_c (kg/m^3)	40	115.5	134.2	152.9	98.3	110.4	129.1
Compression Strength (MPa)	0.15	1.78	2.65	3.85	2.49	3.31	3.76
Compression Modulus (MPa)	4.12	68.49	85.01	138.89	88.11	113.04	115.4
Energy Absorbed, E_a (J)	1.42	5.75	10.64	19.86	7.56	11.79	20.44
Energy Density, E_d (J.m^3/kg)	0.04	0.05	0.08	0.13	0.08	0.11	0.16
Specific Strength, σ_{sp} (kN.m/kg)	3.85	15.41	19.75	25.19	25.33	29.98	29.12
SEA (kJ/kg)	2.27	1.99	3.17	5.20	3.08	4.27	6.33

6.6 The Effect of Strain-Rate

In order to investigate the effect of strain-rate, the geometry of the corrugated-core was set to $\rho^* = 0.07$ with an aspect ratio of $H/L = 0.035$. Figure 6.8 shows the variation of the compression strength as a function of the logarithm of strain-rate, for the aluminium, GFRP and CFRP corrugated-core sandwich structures. As expected, the compression strengths of the corrugated-core materials increased with increasing crosshead speed up to 100 mm/minute. The figure clearly shows the strengths of the corrugated-core sandwich structures are dependent on applied strain-rate at these very low rates. Note that applied strain-rate, $\dot{\varepsilon} = v/h_s$, is a strain-rate of the corrugated-core sandwich specimen (not a nominal strain-rate for parent material), where v is the applied crosshead speed and h_s is the height of specimen.

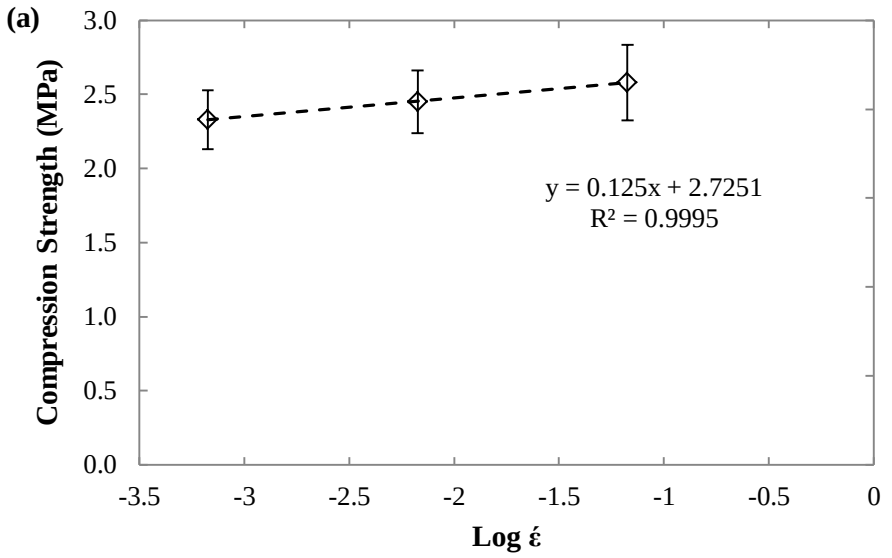

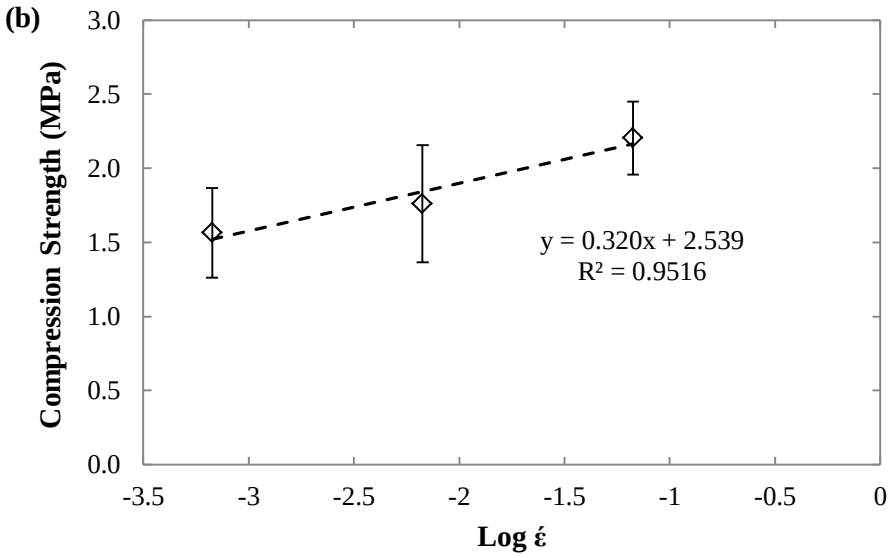

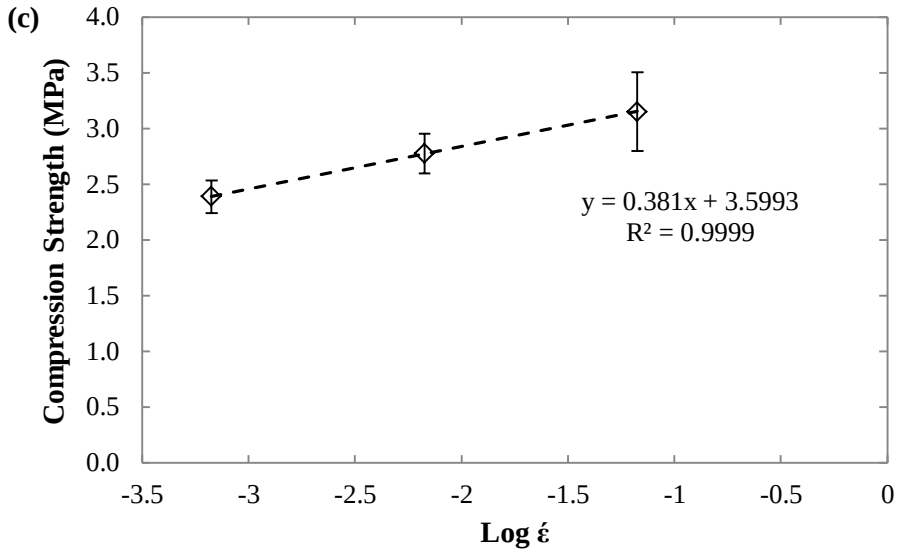

Figure 6.8: The variation of strain-rate of the compression strength of the corrugated-core (a) AL (b) GFRP and (c) CFRP sandwich structures.

The study of the low velocity impact responses was divided into incident impact energies below and above the threshold energy required to break the specimens. The maximum contact force, F_{max} , as a function of the striking velocity is shown in Figure 6.9. In Figure 6.9(a), the data are well-represented by a bi-linear curve with F_{max} increasing linearly with velocity for $v \leq 1.98$ m/s, and is reasonably rate-independent at higher values of v. Meanwhile in the composite corrugated-core structures, an examination of Figures 6.9 (b) and (c) indicates that the trend in the bi-linear curve is very similar, suggesting that the figures are divided into strain-rate sensitive and insensitive regions. For the GFRP and CFRP specimens, the transition velocity between the sensitivity regions is approximately 2.0 m/s and 1.5 m/s, respectively. These bi-linear curve fits agree with the work of Russell *et al.* [2] who also measured the peak stress in E-glass specimens over a range of impact velocities.

Here, the impact velocity at the transition between the rate-sensitive and insensitive regions is influenced by the impact energy, E_i. At lower incident impact energies, no damage was observed as the impactor bounces back following the initial strike. Above the threshold energy to fracture the specimen, the corrugated-core was buckled and crushed before rebound. Since the corrugated-cores are buckling-dominated, inertial effects can delay the onset of buckling load, and change the wavelength of buckling mode [3].

Figure 6.9 shows the relationship between the incident and absorbed energies. An inspection of the figure indicates that almost all of the impact energy, E_i is absorbed by the sandwich structures, E_a. The small energy loss was expected, due to friction between the impactor and guide rails.

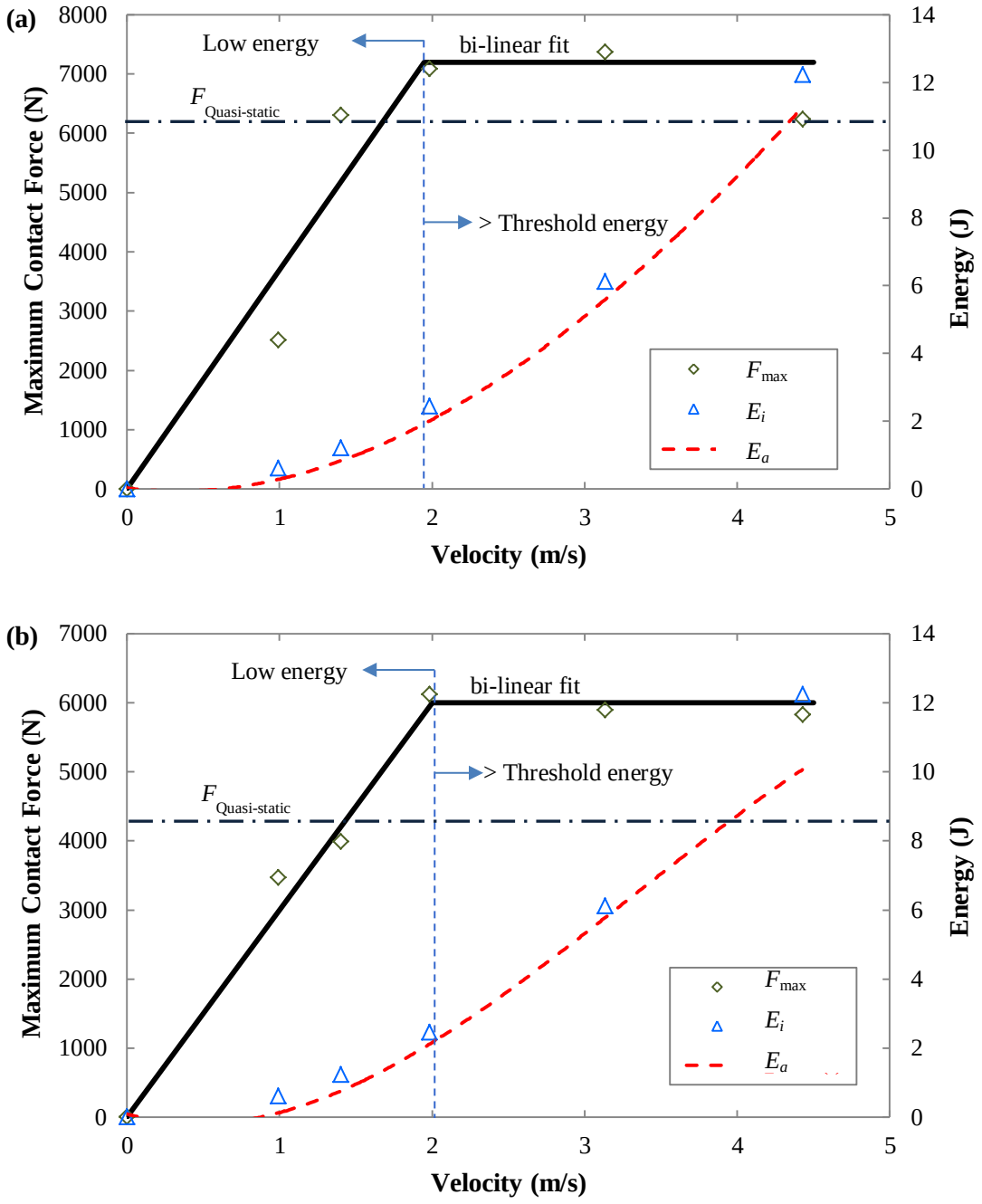

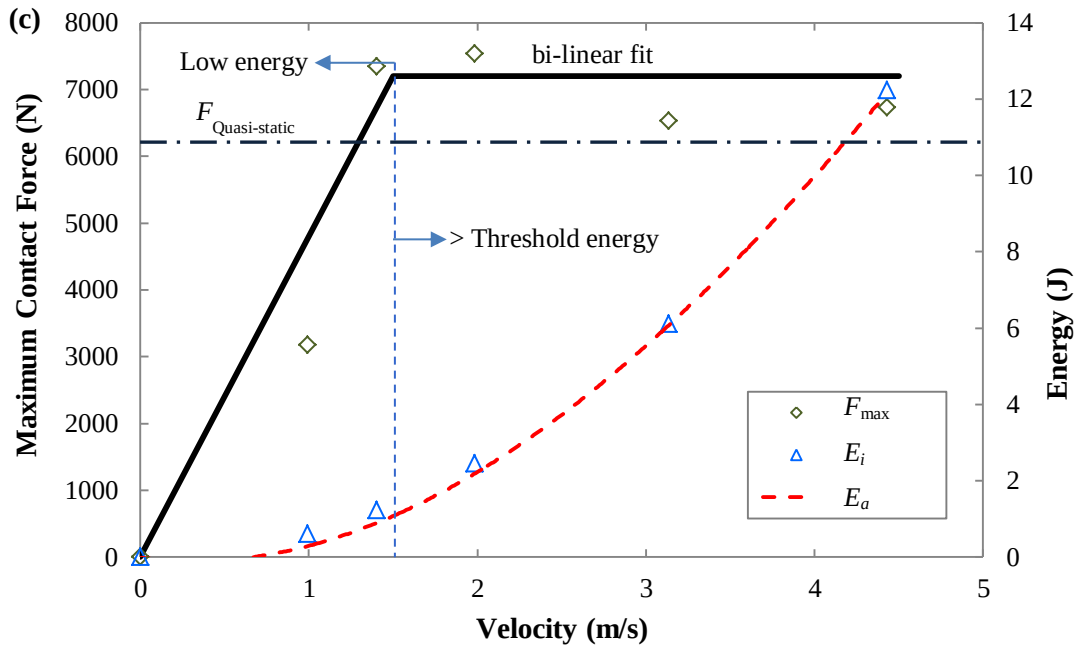

Figure 6.9: The measured maximum contact force and energies as a function of impact velocity, for (a) AL, (b) GFRP and (c) CFRP sandwich panels. Note that the impactor mass ratio, **m***, to AL, GFRP and CFRP is 98, 170 and 173 respectively.

The data presented above also show that the maximum dynamic out-of-plane compressive strength is higher than the quasi-static value. Figure 6.10 shows the dynamic strength enhancement, σ_D/σ_S , as a function of impact velocity, for all three specimens. The dynamic strength enhancement is defined by the maximum dynamic stress, σ_D normalised by the quasi-static strength, σ_S for the same aspect ratio *H*/*L*. An examination of the figure indicates that in spite of the fact that there is some scatter in the data, the GFRP specimens are more sensitive to dynamic effects than the AL and CFRP specimens. The strength of the GFRP specimen increased by 50% compared to quasi-static value. Interestingly, the strength of both the AL and CFRP specimens is about the same, increasing by approximately 22% from the quasi-static value. This suggests that the GFRP specimen is more rate-sensitive than the AL and CFRP specimens in low velocity impact event.

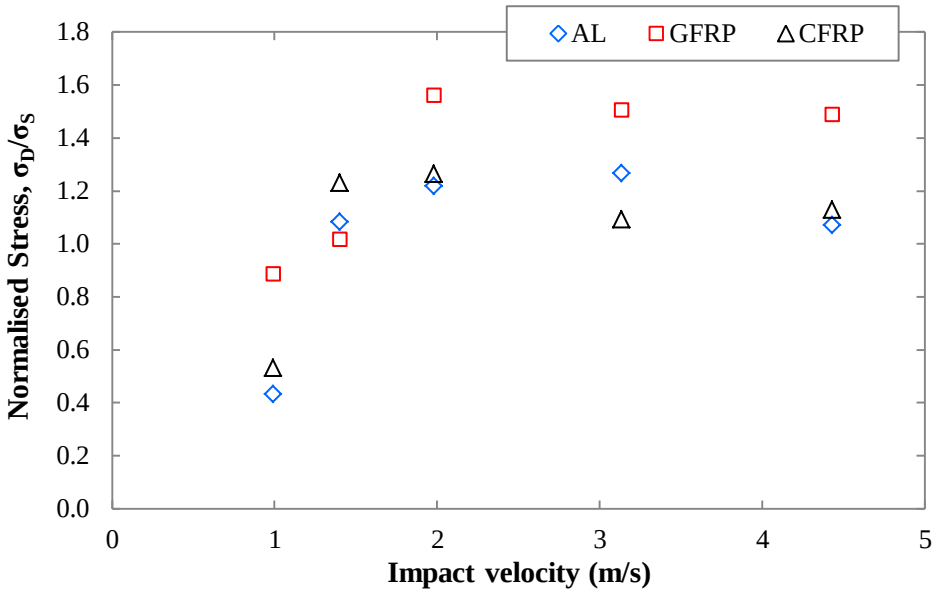

Figure 6.10: The dynamic strength enhancement factor obtained by normalising the maximum dynamic stress by the quasi-static strength, plotted as a function of the impact velocity.

6.7 The Effect of Mixed-mode Loading on the Failure Strength

It was noted in Section 4.4 that failure in these corrugated-cores is due to compression, global buckling, debonding or delamination, with failure being associated with one or more of these. Table 4.3 summarises the average failure loads (and associated standard deviations), as well as the average compression and shear stresses at failure (calculated using Equations 4.31 and 4.32, respectively) in the first quadrant-space. For all loading conditions, it is evident that the CFRP corrugation offers failure loads that are higher than those measured on the GFRP and AL systems. However, there is less scatter in the data for the AL and GFRP specimens.

Figures 6.11(a), 6.12(a) and 6.13(a) show the maximum stresses for the AL, GFRP and CFRP corrugations as a function of loading angle, α. The figures show that the maximum compression stress increased linearly with α, while the shear stress drops in a parabolic fashion with loading angle, as expected,. The evidence in these figures highlights that significant interaction exists between the shear and compression stresses under mixed-mode loading conditions. Initially, a quadratic failure criterion of the following form was applied:

$$\left(\frac{\sigma_\alpha}{\sigma_\mathrm{f}}\right)^2+\left(\frac{\tau_\alpha}{\tau_\mathrm{f}}\right)^2=1 \qquad 6.7$$

where σ_α and τ_α are the compression and shear stresses at a given angle α, and σ_f and τ_f are the compression and the shear strengths at failure. This failure criterion is only valid for compression-shear loading conditions where the material is subjected to a state of plane stress. This equation accurately predicts the failure response of the ductile aluminium corrugations as shown in Figure 6.11(b). However, it does not appear to be suited to predicting the data of the composite corrugations shown in Figures 6.12(b) and 6.13(b), where the model over-predicts the experimental data. This information suggests that an additional term may be required to accurately capture the mechanical response of the corrugated-cores. Indeed, a closer examination of the CFRP corrugated-core specimen during loading highlighted the presence of a complex three-dimensional buckling mode, leading to delamination in the individual struts during loading. Evidence of localised delamination was also observed in the GFRP corrugation specimen during the initial loading phase, where a small drop in load was observed during loading. Therefore, an additional component, similar to that used previously by Besant *et al.* [4] to characterise complex failure in an aluminium honeycomb, was introduced in Equation 6.8 to account for the occurrence of delamination in the struts as well as through-the-thickness buckling effects. This modified criterion takes the form:

$$\left(\frac{\sigma}{\sigma_u}\right)^n+\left(\frac{\tau_l}{\tau_{lu}}\right)^n+\left(\frac{\tau_t}{\tau_{tu}}\right)^n=1 \qquad 6.8$$

where σ, τ_l and τ_t are the compressive stress and the through-thickness shear stresses in the longitudinal and transverse directions, and σ_u, τ_{lu} and τ_{tu} are the corresponding yield stresses. Here, the value of n required to force the model to fit the experimental data was found to be dependent on the corrugation type, with values of n = 1.5 and 1.2 being required to predict the trends in the failure surface of the GFRP and CFRP corrugation, respectively. Determination of the n values are shown in Figure 6.14 and a valid value of n provides a good fit to the experimental data, suggesting that the yield surface criteria is elliptical.

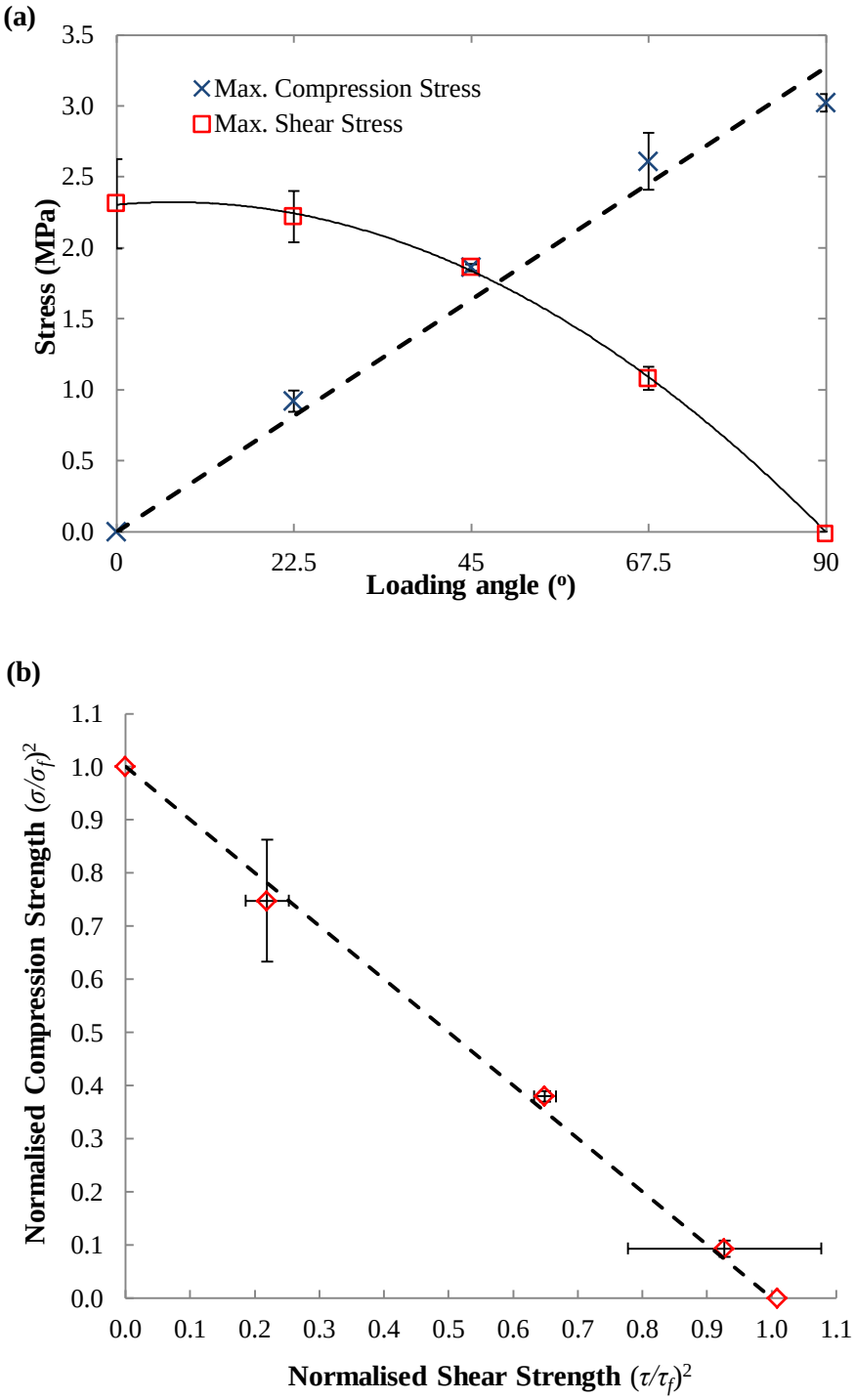

Figure 6.11: (a) Variation of the maximum compression and shear stresses with loading angle, (b) strength-failure criterion for the AL corrugated-core structure.

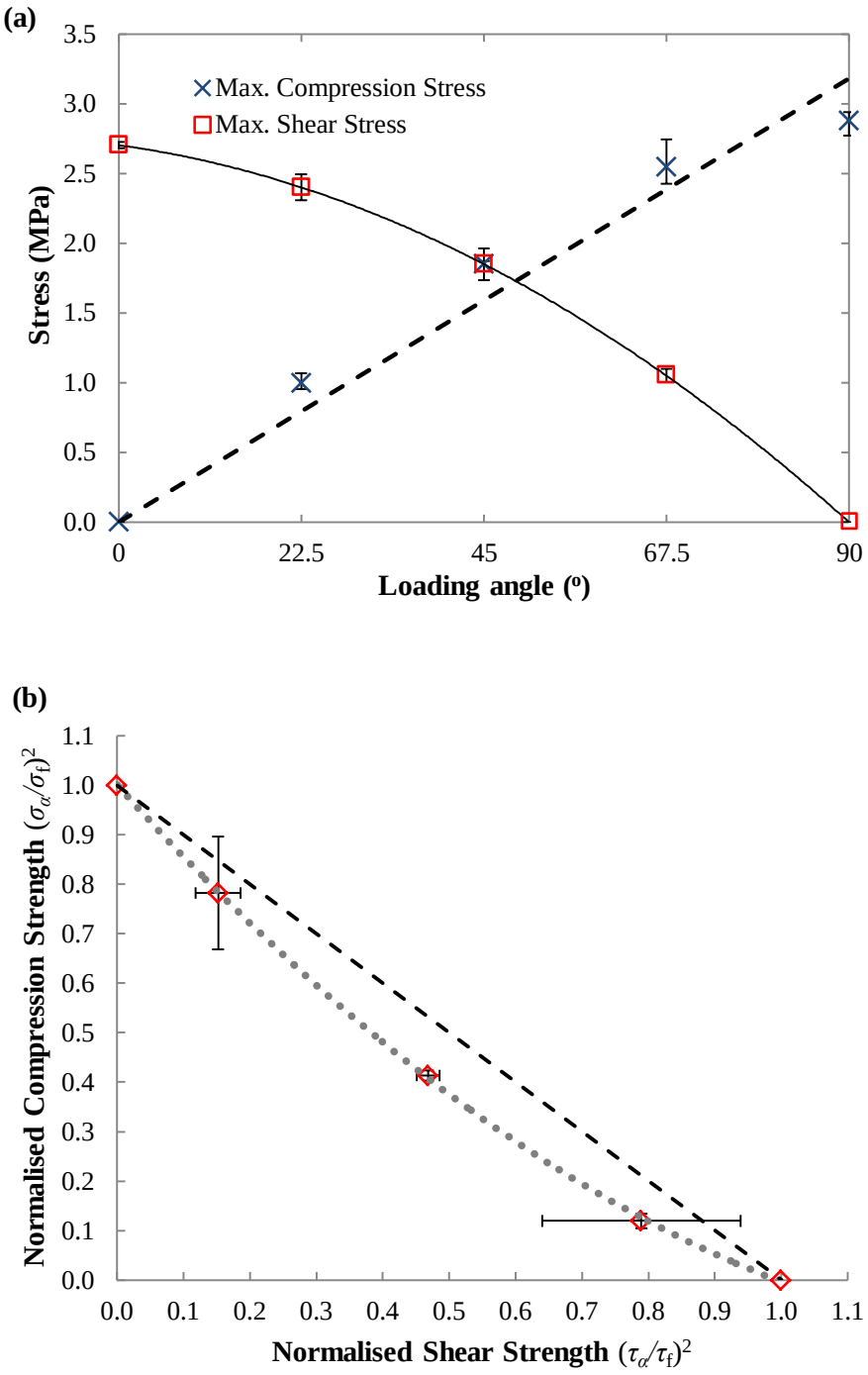

Figure 6.12: (a) Variation of the maximum compression and shear stresses with loading angle, (b) strength-failure criterion for the GFRP corrugated-core specimen.

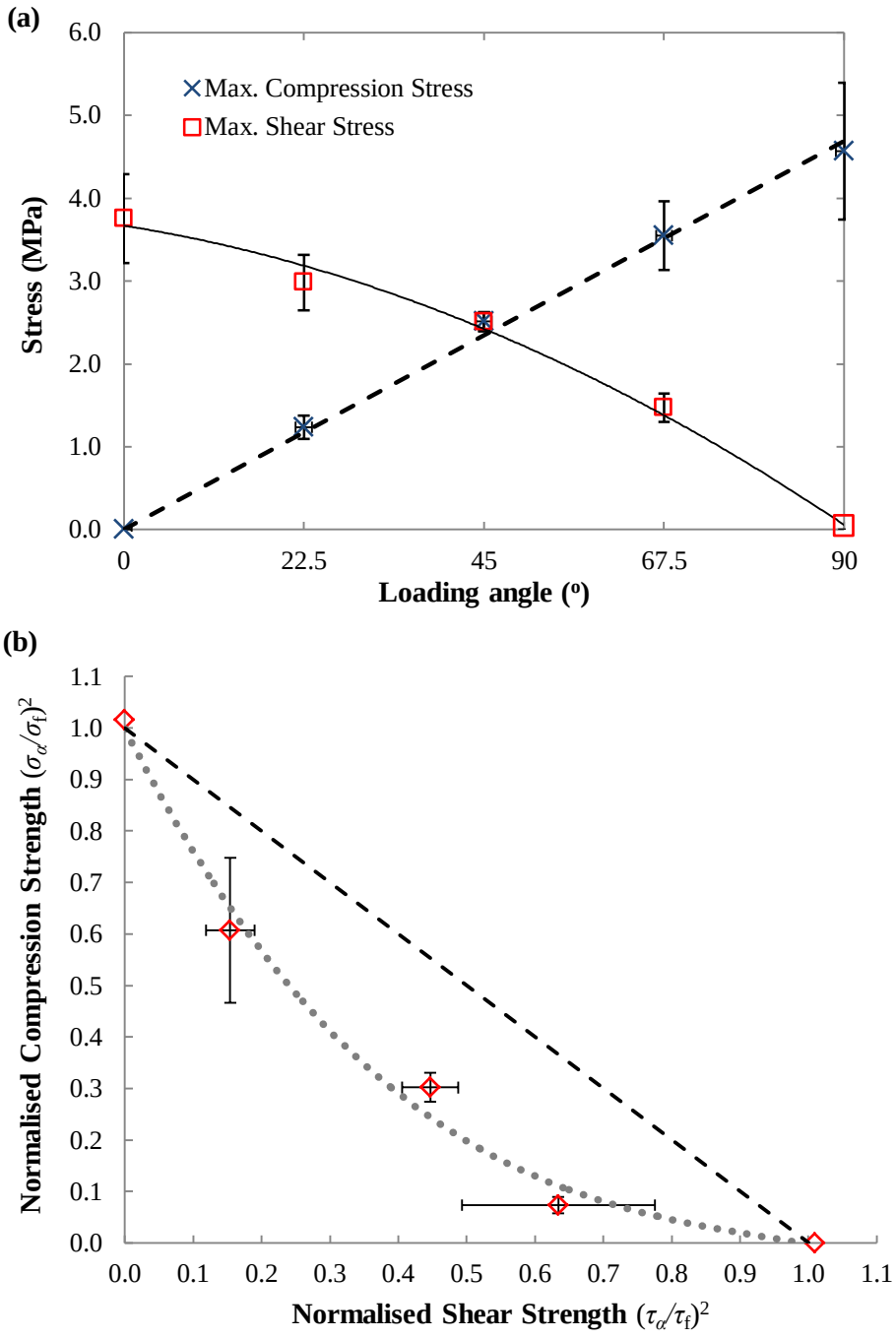

Figure 6.13: (a) Variation of the maximum compression and shear stresses with loading angle, (b) strength-failure criterion for the CFRP corrugated-core structure.

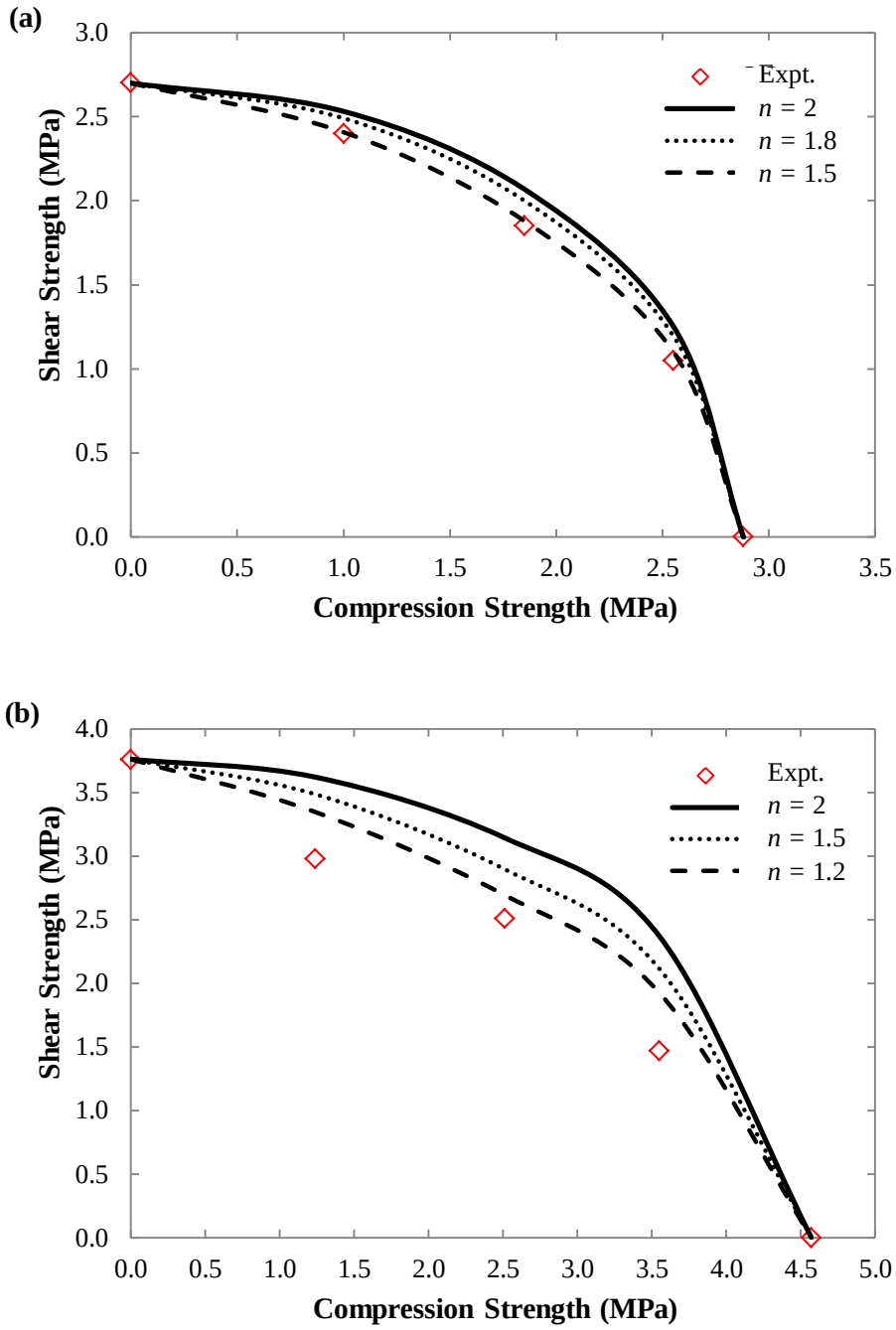

Figure 6.14: Determination of *n* values to fit the yield surface criteria of (a) GFRP and (b) CFRP corrugated-core structure.

6.8 Investigation of the Damage Mechanisms in the Corrugated-core Sandwich Structures

Figure 6.15 shows the damage mechanisms for the two different composite materials, for the same aspect ratio of H/L = 0.035 (H = 0.5 mm and ρ^* = 0.07). Damage initiated due to buckling. Damage mechanisms, such as buckling, fibre fracture, matrix cracking, delamination and debonding, were identified as dominant failure modes during the quasi-static and dynamic compression loading. However, in Figure 6.16, different modes of damage were observed in the metal system and the composite specimens. Damage in the metal system was due to an instability in the strut, followed by global buckling and then crumpling at the end of the compression loading. Plastic deformation occurred in the metal system, rather than fibre failure, as in the case for the composite material. This is due to the greater strain to failure of the metal, as previously discussed in Section 4.2, the strain to failure of the plain AL is approximately ten times greater than of the composite plain. Due to their lower strain to failure, the GFRP and CFRP corrugated-core specimens failed due to fibre fracture and matrix cracking (see Figures 6.15 (a-ii) and (b-ii)), after the instability of the struts.

A closer examination of the both ends of the AL sandwich structure showed debonding between the strut and the lower skin. It is believed that due to initial fracture in the adhesive, the transverse load in the strut, pushed the strut sideways from the centre, and therefore debonding occured as the shear strength of the adhesive was unable to resist the load. In the low magnification optical micrograph, no debonding at the joints between the corrugated-core and the upper and lower was skins observed in either composite structures. However, some delamination was generated which propagated in the corner of the unit cell of the GFRP corrugated-core. As mentioned previously, both composites have the same thickness, H, but the greater number of plies in GFRP specimen increase the possibility of delamination [5].

Similar failure mechanisms were observed in the corresponding semi-filled and fully-filled specimens, as shown in Figure 6.17. A careful examination of the filled specimens indicated that the foam was compressed and became thinner.

As already stated, the failure mechanisms in the metal and the composite at a velocity of 4.43 m/s were similar to the quasi-static damage mechanisms, as shown in Figure 6.18. Conversely, as the impactor mass ratio was higher, **m*** = 98, symmetrical and asymmetrical buckling modes in the metal were triggered, due to stabilising effect of inertia on buckling. Despite this inertia effect, a combination of the higher initial axial compression and bending loads in the strut suddenly changed the buckling sine wave, as well as increasing the maximum contact force in the sandwich structures.

The failure modes in the corrugated-core specimens were further investigated by polishing and examining the specimens under an optical microscope. The subsequent development of damage with increasing aspect ratio (*H/L*) in the GFRP and CFRP corrugated-core specimens are summarised and presented in Tables 6.2 and 6.3, respectively.

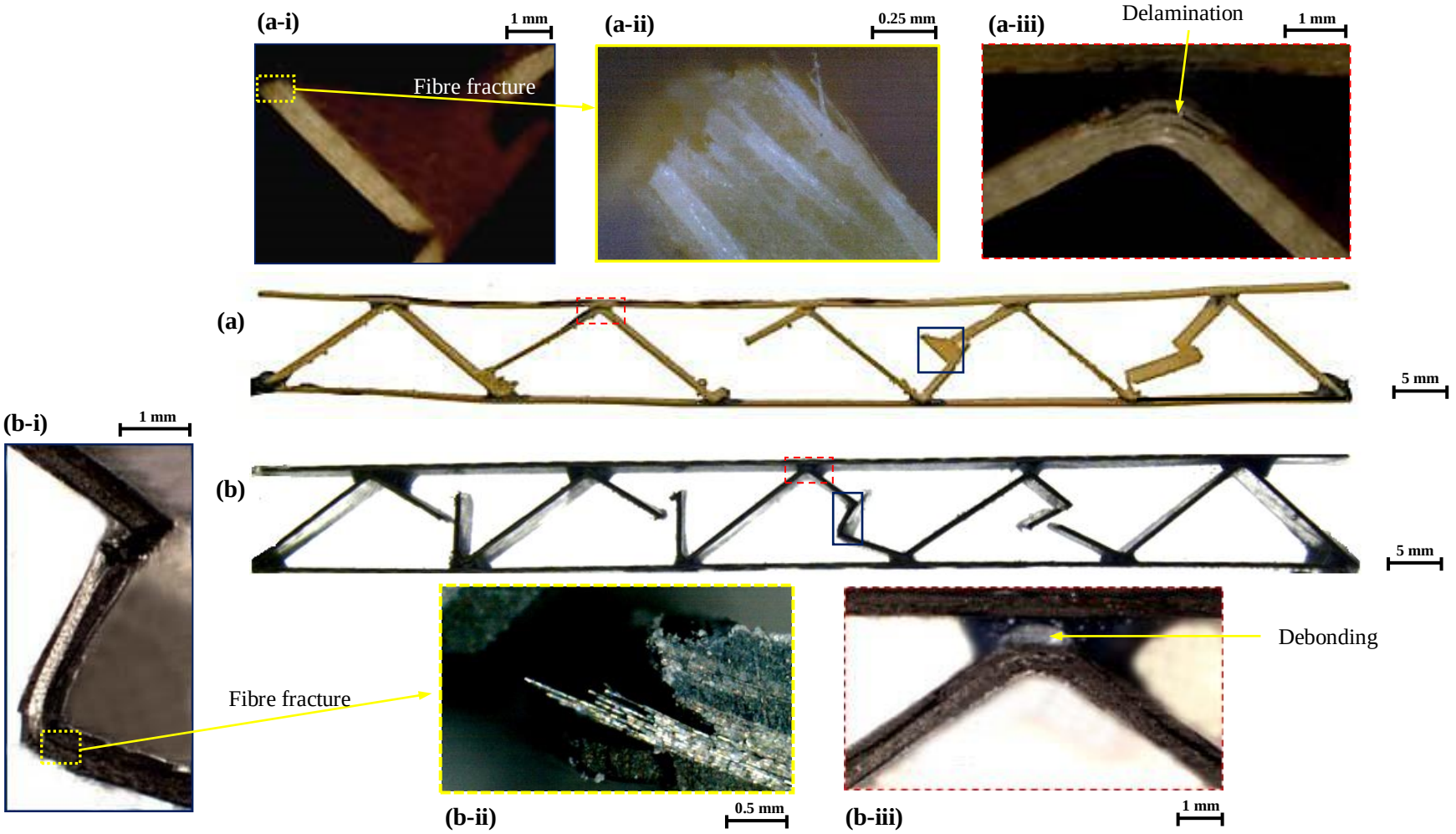

Figure 6.15: Low magnification optical micrographs of polished sections of the corrugated-core sandwich structures at H/L = 0.035; (a) GFRP and (b) CFRP specimens. Fibre fracture, delamination and debonding are typical failure modes in quasi-static and dynamic loadings.

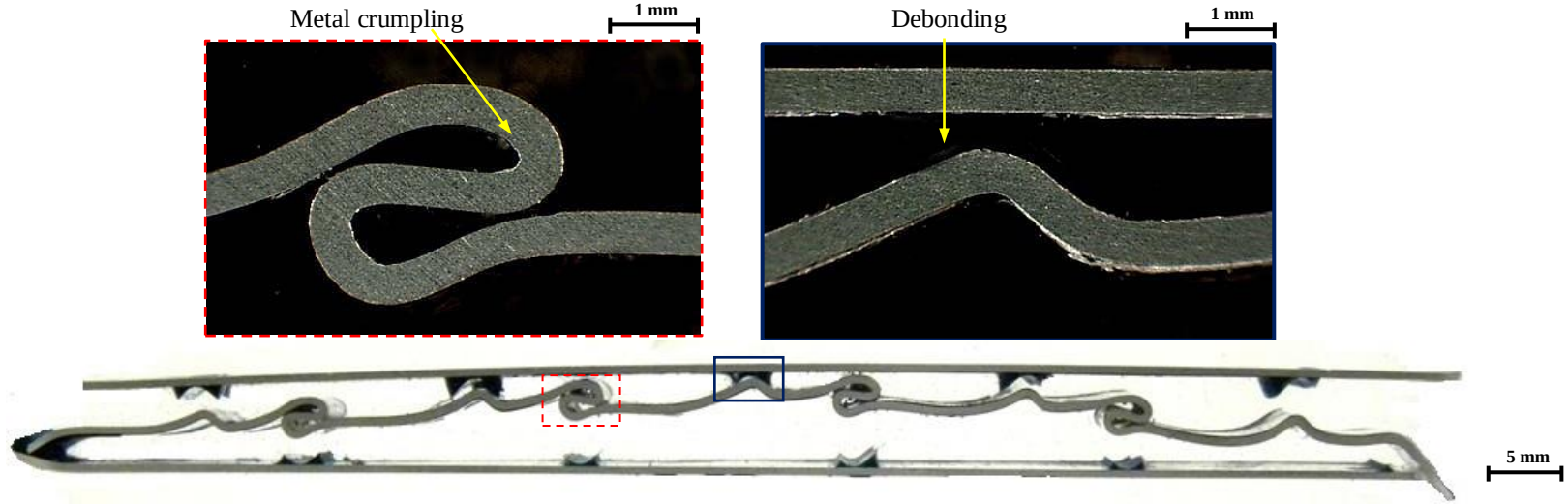

Figure 6.16: Post-damage photos of the AL corrugated-core sandwich structures for an aspect ratio of *H/L* = 0.035.

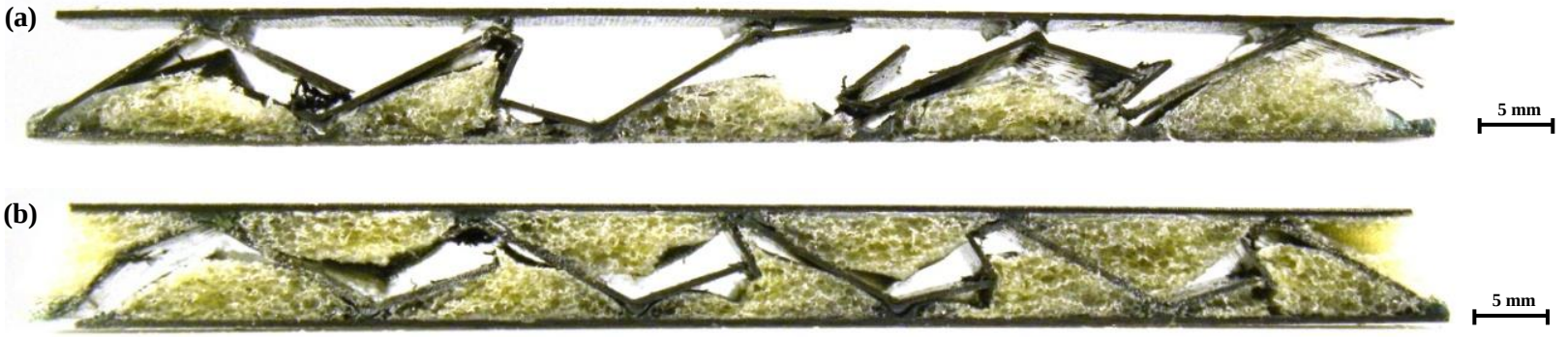

Figure 6.17: Post-test photos of the composite sandwich structures for an aspect ratio of *H/L* = 0.035; (a) Semi-filled and (b) Fully-filled.

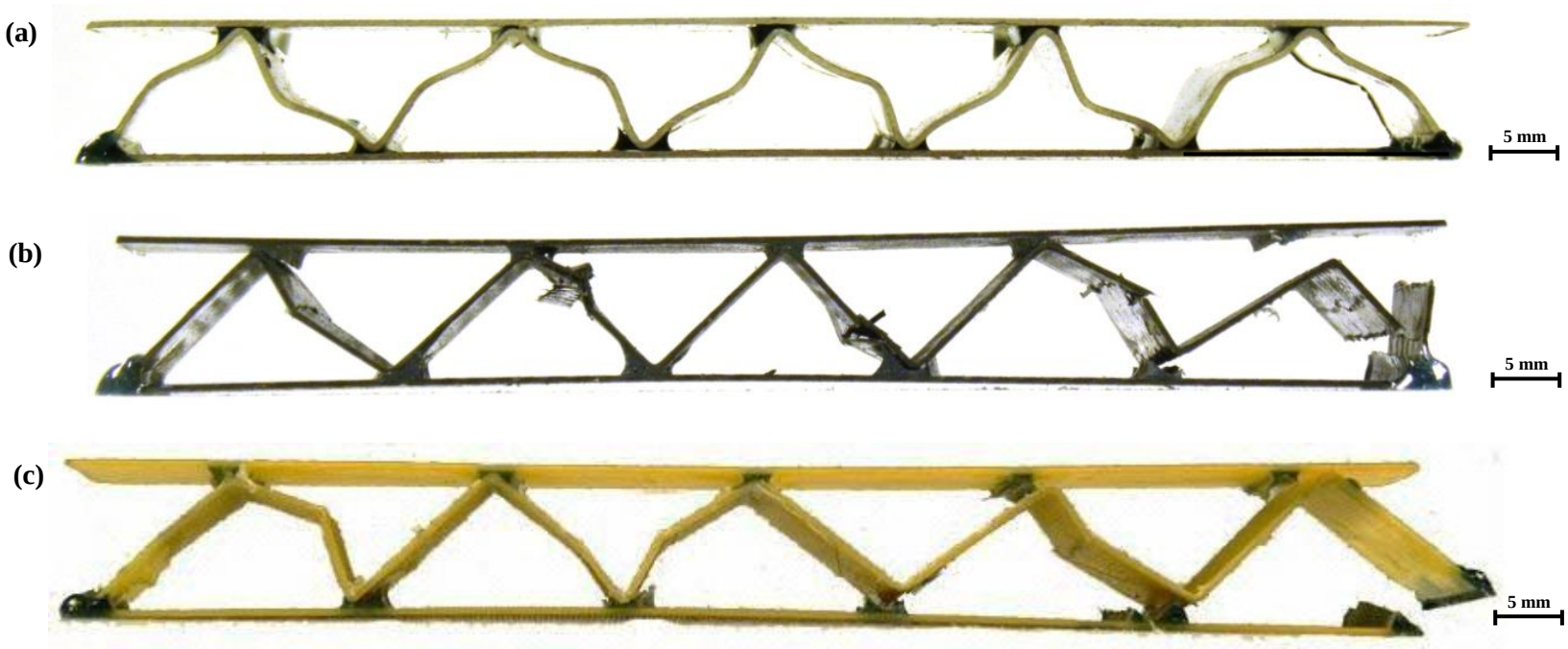

Figure 6.18: Photographs of impacted specimens beyond the threshold energy to initiate fracture, at velocity of 4.43 m/s; (a) AL, (b) CFRP and (c) GFRP materials.

Table 6.2: Post-failure examinations of the GFRP corrugated-core structures for various aspect ratios (*H/L*).

H/L	Micrograph Observations
0.013	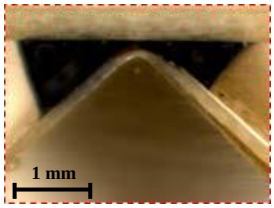 GF2U5 with an average *H* = 0.19mm, failure starts with buckling followed by hinges and fibre fracture, debonding at the end of test.  
0.022	 GF3U5 with an average *H* = 0.31mm, failure starts with buckling followed by hinges and fibre fracture, debonding at the end of test. 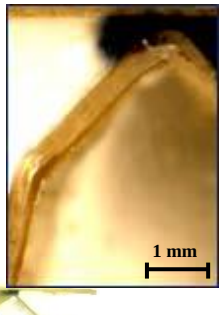 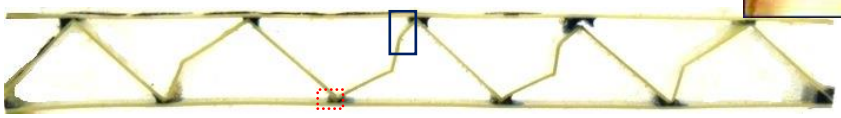
0.030	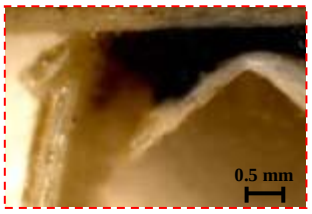 GF4U5 with an average *H* = 0.43mm, failure starts with buckling followed by fibre fracture, debonding at the end of test.  
0.054	 GF7U5 with an average *H* = 0.71mm, failure starts with buckling followed by fibre fracture and delamination around the corner, and debonding at the end of test.  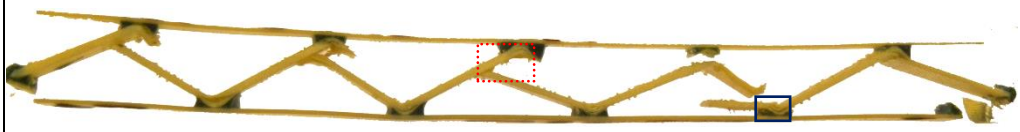

0.069	 GF10U5 with an average H = 0.98mm, failure mode is dominated by delamination damage in the corner of the unit cell.  

In the GFRP corrugated-core for an aspect ratio $H/L < 0.035$, failure initiates with buckling followed by the formation hinges and fibre fracture, finally with debonding at the end of test. Further for aspect ratios $H/L \geq 0.035$, initial failure is still dominated by buckling, however since the thicker composites contain more layers of fibres and a higher possibility of interfacial defect [5], delamination occurs before debonding at the end of the loading process. Here, delaminations are generated that propagate not only in the corner of the unit cell, but also in the inclined members of the core. The generation and propagation of the delaminations in the corner of the unit cell is due to a bending moment that causes high interlaminar stresses.

Similar failure mechanisms were observed in the corresponding CFRP corrugated-core. For aspect ratios $H/L \geq 0.073$, delamination was observed and debonding occurred at end of the loading. A closer examination shows that delamination is more pronounced in the GFRP specimens than in the CFRP corrugated-core specimens.

Table 6.3: Post-failure examinations of the CFRP corrugated-core structures for different aspect ratios (*H/L*).

H/L	Micrograph Observations
0.063	CF3U5 with an average *H* = 0.89 mm, failure starts with buckling followed by fibre fracture and debonding at the joints. 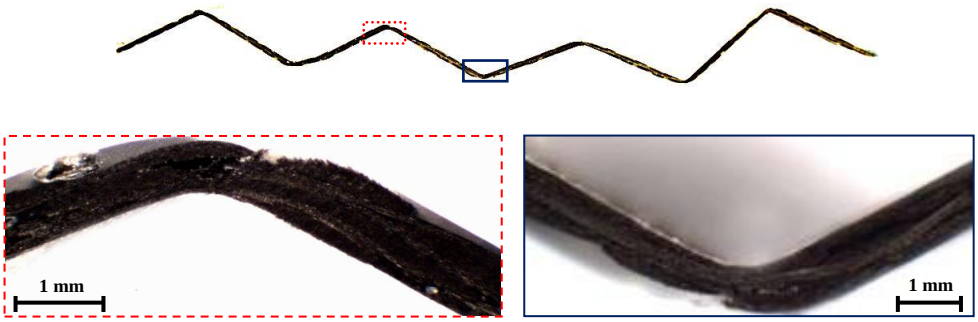
0.073	CF4U5 with an average *H*=1.03mm, failure starts with buckling followed by delamination at the corners. 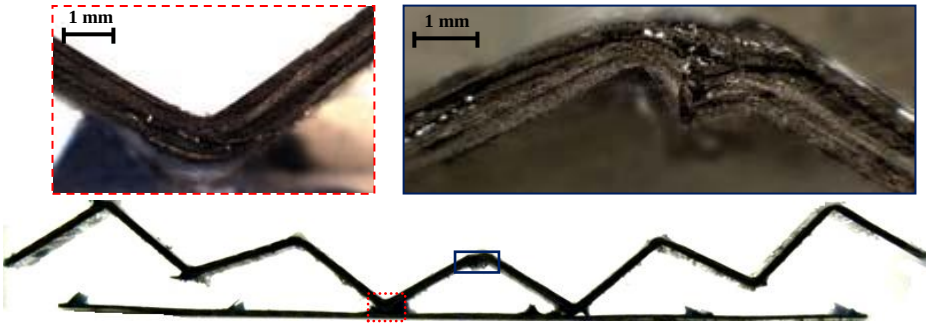
0.078	CF5U5 with an average *H*=1.10mm, fibre delamination occurs in cell wall and debonding. 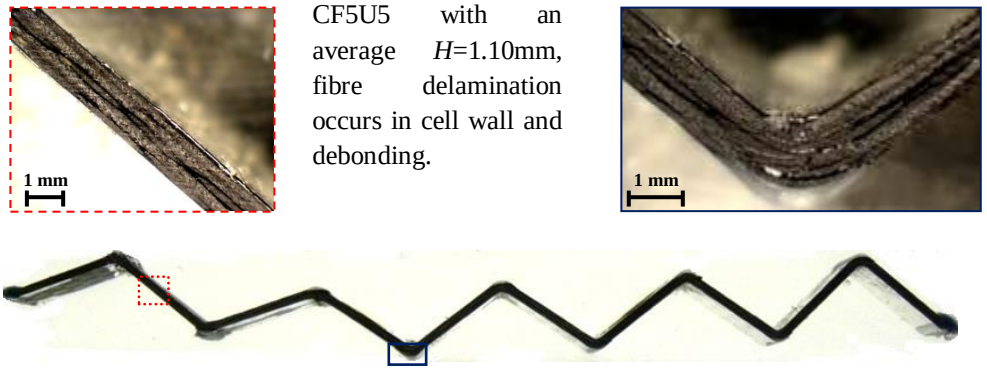
0.088	CF6U5 with an average *H*=1.24mm, fibre delamination occurs in cell wall and debonding suddenly takes place. 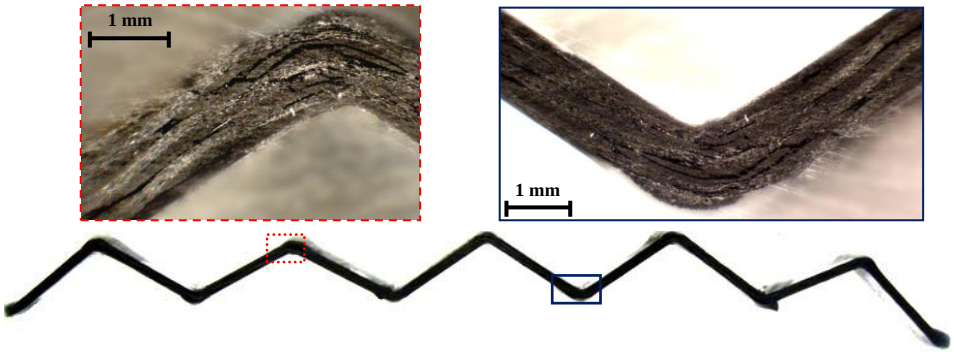

6.9 Triangular Corrugated-cores and the Competing Core Structures

Figure 6.19 summarises the values of the compression strength and the energy absorbed by all the AL, GFRP and CFRP corrugated-core sandwich panels. In general, it was found that the compression strength and energy absorption increases with increasing thickness of the struts, *H*. An examination of the figure highlights the impressive compression strength and energy absorption of the 6-ply CFRP specimen (CF6U5) with values in excess of 18 MPa and 35 J, respectively. It is believed that the extensive delamination in the composite plies has made a significant contribution to the energy-absorbing process in the laminate. Indeed, Abdullah [6] and Liu and Raju [7] reported that large amounts of delamination can result in a higher damage threshold energy in a composite.

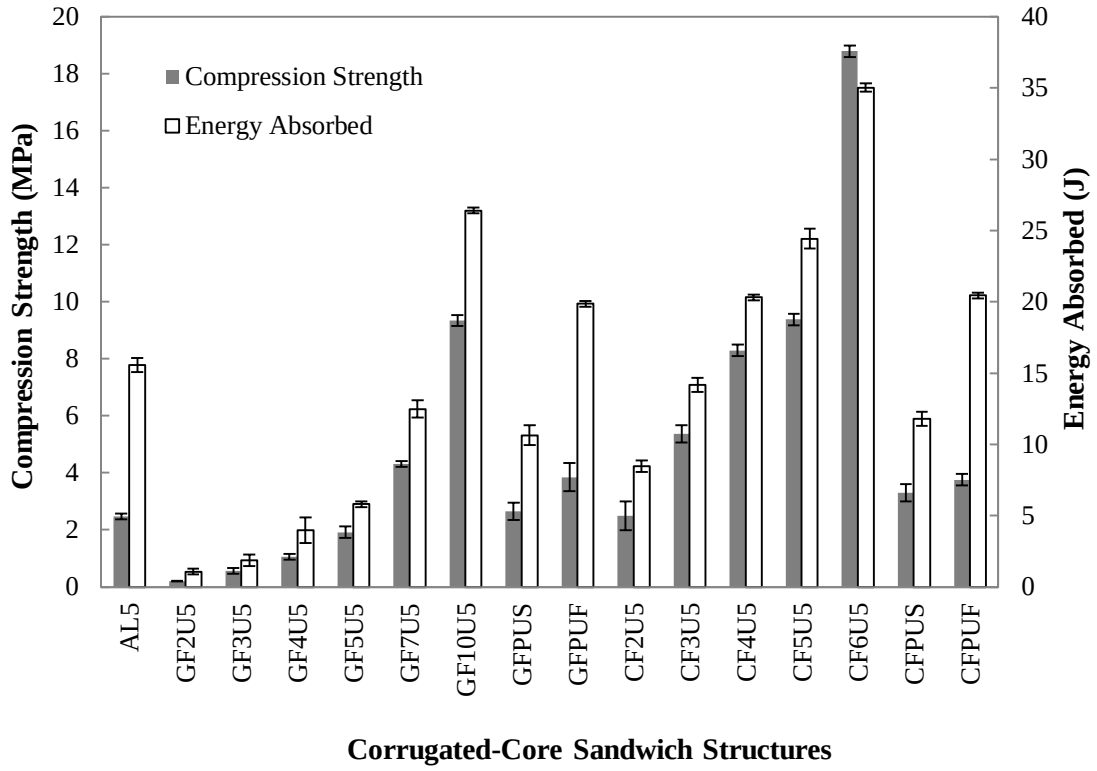

Figure 6.19: Values of compression strength and energy absorbed for all the tested corrugated-core sandwich structures.

It is interesting to note that the aluminium corrugated-core, having the same geometry (H = 0.5 mm) as a corrugated-core composite, is capable of absorbing more energy and offers a higher compression strength. Here, the energy absorbed by the AL5 is three times greater than the GF5U5, and also 50% higher than CF2U5.

This supports the evidence from the work of Qin *et al.* [8] that the aluminium corrugated-core offers sufficient ductility to sustain loading, therefore increasing its energy absorption capability.

In order to facilitate a comparison of the performance of the specimens, the specific properties of the core for the same geometry, $\rho^* = 0.07$, are shown in Figure 6.20. A closer examination shows the specific strength of the AL5 was lower than that for both composites, i.e. the GF5U5 and CF2U5. Interestingly, the specific energy absorption of the CF2U5 corrugated-core is a slightly higher than the aluminium system, however the *SEA* of the GF5U5 corrugated-core is still lower by approximately 50% compared to the AL5. This suggests that the conventional corrugated composite core structures offer higher compression strength to weight ratios but lower energy absorption than the corrugated metal core.

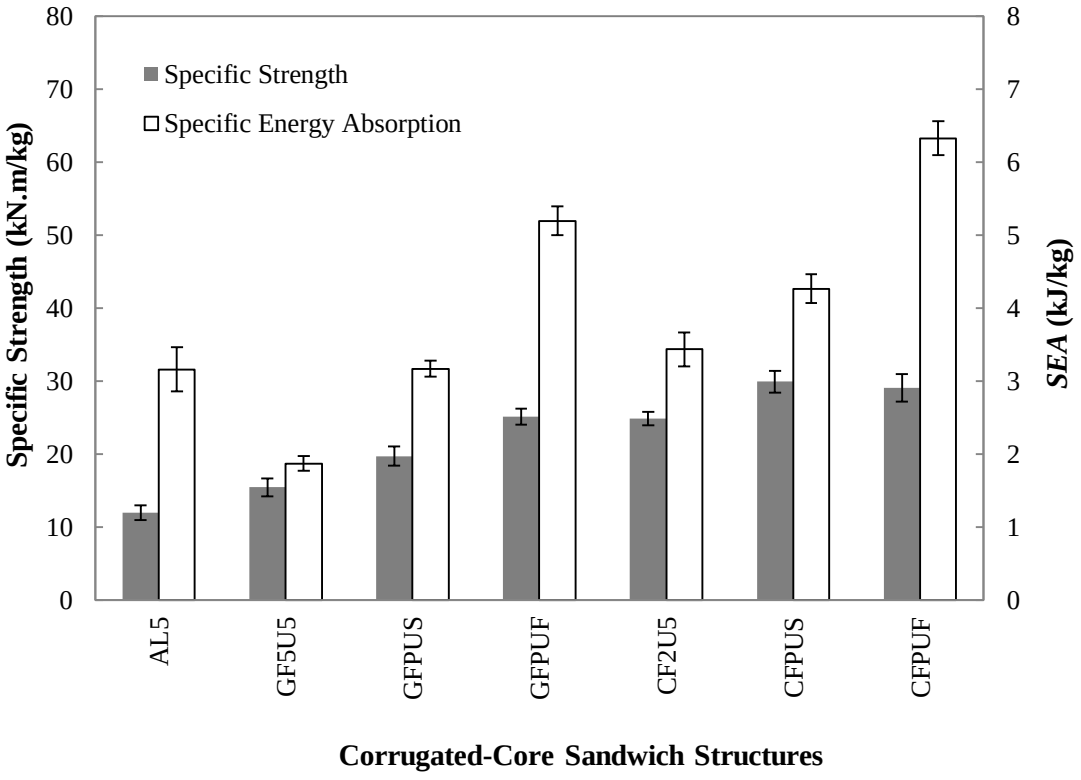

Figure 6.20: Comparison of the specific strength and specific energy absorption values of the corrugated-core sandwich structures for an aspect ratio of $H/L = 0.035$.

For the foam-filled core, it was found that the low density PU foam makes a significant contribution to the energy-absorbing process in the corrugated structures. For example, by comparing the semi-filled GFRP specimen (GFPUS) with the conventional GFRP corrugated-core specimen (GF5U5), it can be seen that the *SEA* of the GFPUS specimen is up to 58% greater than the GF5U5 specimen. It is worth noting that with semi-filled foam in the GFRP corrugation system, the *SEA* value is equivalent to the aluminium system, AL5. Furthermore, the fully-filled foam in the GFRP corrugated-core specimen (GFPUF) the *SEA* increased by approximately 70% compared to the AL5 specimen. Here, the CFPUF specimen offers the highest absorbed energy to weight ratio, whereas the AL system exhibits the lowest strength to density ratio. However this structure is good for absorbing energy.

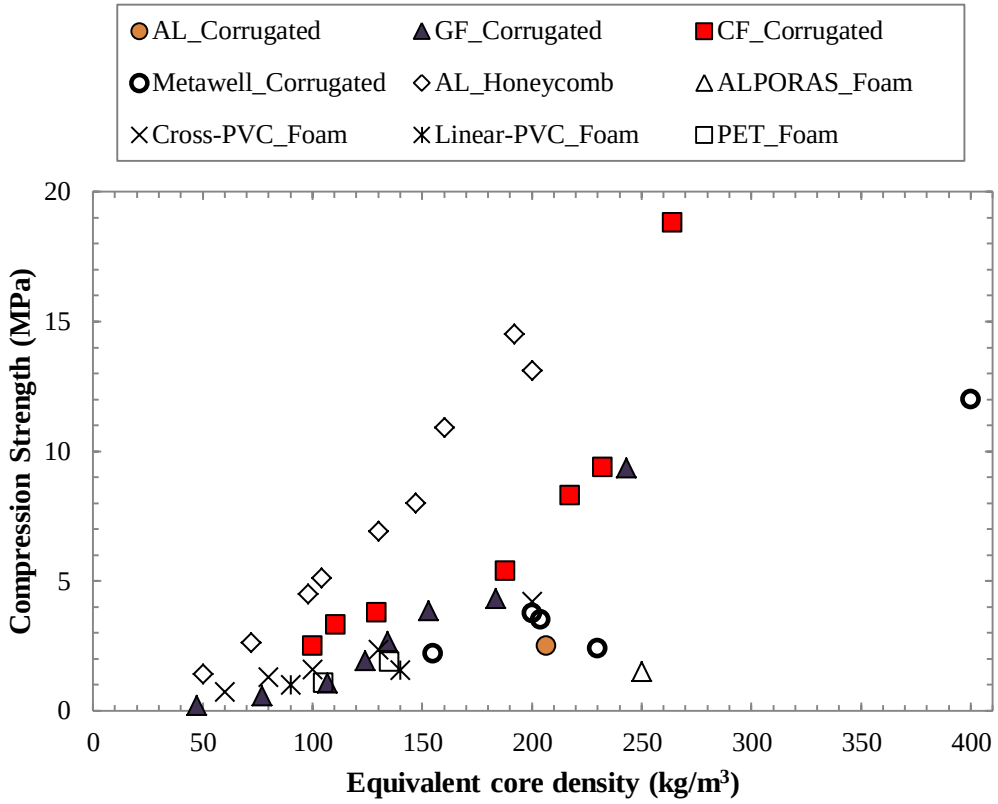

Figure 6.21: Comparison of the compression strength of the experimental data with commercially available sandwich core types for lightweight applications, as a function of equivalent core density.

Figure 6.21 compares the compression strength of the triangular corrugated-cores investigated in this study with other commercial core types, including an aluminium

sinusoidal corrugated-core from Metawell [9], Hexcel aluminium honeycomb [10], polymeric foams from Divinycell [11] and a metal foam. Clearly, the established aluminium honeycombs out-perform the remaining cores, including the corrugated-core structures discussed herein. However, closer inspection suggests that the thickest CFRP corrugated-core should offer compressive properties that are comparable to those of the honeycomb systems. It is also interesting to note that the composite corrugated-cores out-perform the Metawell corrugated material as well as both the metal and polymeric foam cores.

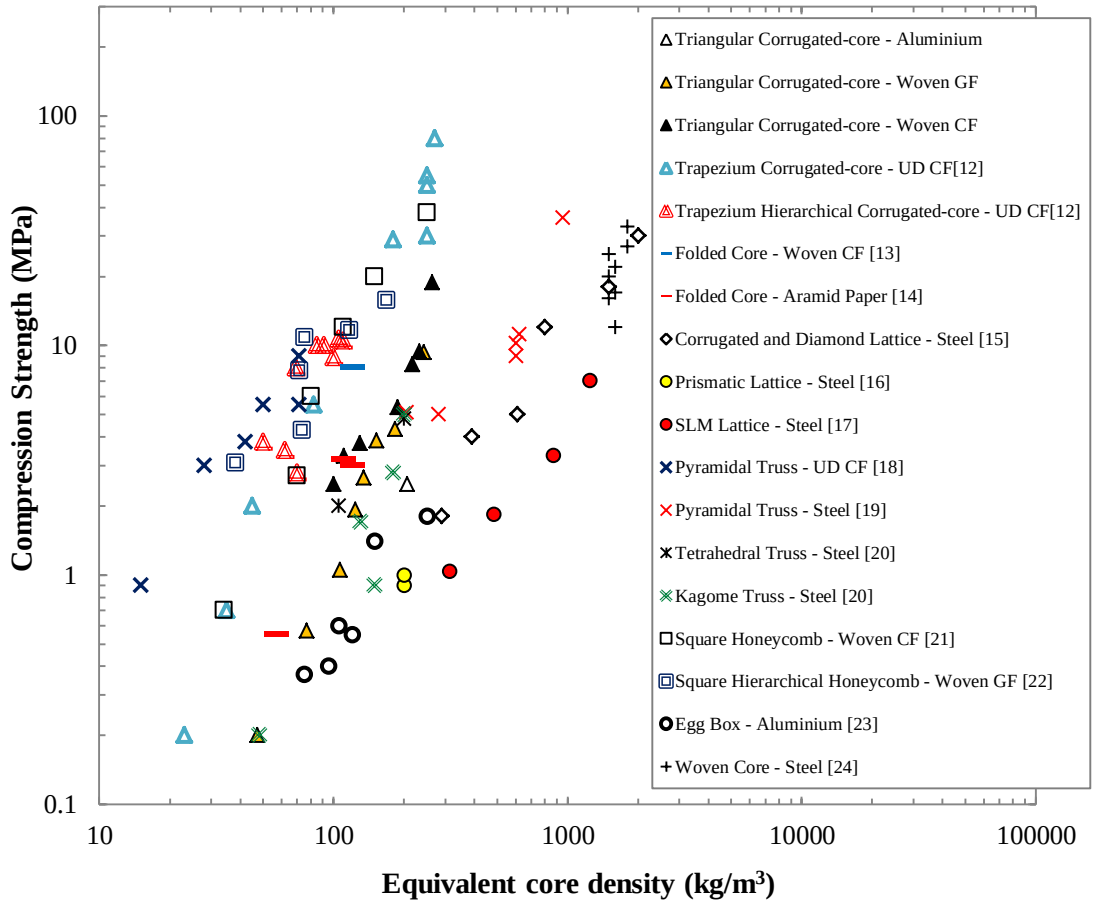

Figure 6.22: Collection of experimental data summarising the compression strength of current core types design developed by researchers in recent years, as a function of equivalent core density.

To evaluate the performance of the triangular corrugated-core developed in the current research work, Figure 6.22 shows the compressive properties of various cellular cores and designs that are presented in the literature [12-24]. Overall, the

compressive properties of the triangular corrugated-cores exhibit a moderate performance, situated between the metal and composite regions. However, the triangular corrugated-core based on the woven CFRP material can compete with current sandwich core configurations. For example, for a density of approximately 200 kg/m^3, it can be seen that the CFRP triangular corrugated-core exhibits the highest design performance, behind the trapezium corrugated-core and the square honeycomb core. This indicates that a combination of core design and lightweight materials e.g. carbon fibre, can play an important role in determining structural performance. This suggests that the triangular corrugated-core could offer an impressive performance, if manufactured from a unidirectional carbon/epoxy composite.

6.10 Summary of Chapter VI

Chapter VI discussed the experimental and numerical results for the aluminium alloy 2024-O, the GFRP and CFRP corrugated-core materials. Firstly, varying the number of unit cells, the cell wall thickness and the specimen width has shown that the properties of the core material have a significant influence on the compression behaviour of the sandwich structure. It has been shown that the compression strength and modulus increases with increasing numbers of unit cells and cell wall thickness. In contrast, the compression strength and modulus was unaffected by increasing specimen width. The numerical results predicted by the model agree well with the experimental data.

Secondly, the effect of foam filling inside the corrugated-core structures has been investigated. The findings show that the presence of the foam filler improves the specific strength as well as specific energy absorption characteristics of the structure.

Next, the out-of-plane compressive properties under quasi-static and dynamic loading indicate that the dynamic strength enhancement increased significantly, and also the GFRP corrugated-core is more rate-sensitive than the other two materials. The damage mechanisms in evidence following both the quasi-static and dynamic events have been examined.

The yield surface criteria for the corrugated–cores have then been constructed from the mixed-mode loading data. The failure response of the aluminium corrugated-core was accurately predicted by a quadratic failure criterion. In contrast, the composite corrugated-cores were accurately predicted using a modified failure criterion.

Finally, the sandwich structures based on a triangular corrugated geometry evaluated in this study have been compared to commercially-available sandwich cores.

6.11 References

[1] Vaziri A, Xue Z, Hutchinson JW. Metal sandwich plates with polymer foam-filled cores. Journal of Mechanics of Materials and Structures. 2006;1(1):97-127.

[2] Russell B, Malcom A, Wadley H, Deshpande V. Dynamic compressive response of composite corrugated cores. Journal of Mechanics of Materials and Structures. 2010;5(3):477-493.

[3] Kazemahvazi S, Russell BP, Zenkert D. Impact of carbon fibre/epoxy corrugated cores. Composite Structures. 2012;94(11):3300-3308.

[4] Besant T, Davies GAO, Hitchings D. Finite element modelling of low velocity impact of composite sandwich panels. Composites Part A: Applied Science and Manufacturing. 2001;32(9):1189-1196.

[5] Lee J, Soutis C. Thickness effect on the compressive strength of T800/924C carbon fibre–epoxy laminates. Composites Part A: Applied Science and Manufacturing. 2005;36(2):213-227.

[6] Abdullah MR. The High Velocity Impact Response of Novel Fibre-Metal Laminates. PhD Thesis. University of Liverpool, 2006.

[7] Liu D, Raju BB. Effects of joining techniques on impact perforation resistance of assembled composite plates. Experimental Mechanics. 2000;40(1):46-53.

[8] Qin QH, Zhang JX, Wang TJ. Low velocity impact response of lightweight metal sandwich panel with corrugated core. Materials Research Innovations. 2011;15(s1):s198-s200.

[9] Metal Sandwich Technology - www.metawell.de.

[10] HexWeb Honeycombs Cores - www.hexcel.com.

[11] Hassan MZ, Cantwell WJ. Strain rate effects in the mechanical properties of polymer foams. International Journal of Polymers and Technologies. 2011;3(1):27-34.

[12] Kazemahvazi S, Tanner D, Zenkert D. Corrugated all-composite sandwich structures. Part 2: Failure mechanisms and experimental programme. Composites Science and Technology. 2009;69(7–8):920-925.

[13] Heimbs S. Virtual testing of sandwich core structures using dynamic finite element simulations. Computational Materials Science. 2009;45(2):205-216.

[14] Heimbs S, Middendorf P, Kilchert S, Johnson AF, Maier M. Experimental and numerical analysis of composite folded sandwich core structures under compression. Applied Composite Materials. 2007;14(5-6):363-377.

[15] Cote F, Deshpande VS, Fleck NA, Evans AG. The compressive and shear responses of corrugated and diamond lattice materials. International Journal of Solids and Structures. 2006;43(20):6220-6242.

[16] Tilbrook MT, Radford DD, Deshpande VS, Fleck NA. Dynamic crushing of sandwich panels with prismatic lattice cores. International Journal of Solids and Structures. 2007;44(18):6101-6123.

[17] Smith M, Guan Z, Cantwell WJ. Finite element modelling of the compressive response of lattice structures manufactured using the selective laser melting technique. International Journal of Mechanical Sciences. 2013;67:28-41

[18] Finnegan K, Kooistra GW, Wadley HNG, Deshpande VS. The compressive response of carbon fiber composite pyramidal truss sandwich cores. International Journal Materials Research. 2007;98(12):12.

[19] Zok FW, Waltner SA, Wei Z, Rathbun HJ, McMeeking RM, Evans AG. A protocol for characterizing the structural performance of metallic sandwich panels: application to pyramidal truss cores. International Journal of Solids and Structures. 2004;41(22):6249-6271.

[20] Lim J-H, Kang K-J. Mechanical behavior of sandwich panels with tetrahedral and Kagome truss cores fabricated from wires. International Journal of Solids and Structures. 2006;43(17):5228-5246.

[21] Russell BP, Deshpande VS, Wadley HNG. Quasistatic deformation and failure modes of composite square honeycombs. Journal of Mechanics, Materials and Structures. 2008;3(7):1315-1340.

[22] Russell BP, Deshpande VS, Fleck NA. The through-thickness compressive strength of a composite sandwich panel with a hierarchical square honeycomb sandwich core. Journal of Applied Mechanics. 2009;76(6):1004.

[23] Zupan M, Chen C, Fleck NA. The plastic collapse and energy absorption capacity of egg-box panels. International Journal of Mechanical Sciences. 2003;45(5):851-871.

[24] Zupan M, Deshpande VS, Fleck NA. The out-of-plane compressive behaviour of woven-core sandwich plates. European Journal of Mechanics-A/Solids. 2004;23(3):411-421.

CHAPTER VII: CONCLUSIONS

7.1 Introduction

The aim of this research work was to manufacture and investigate the mechanical properties of triangular corrugated-core sandwich structures made from aluminium and composite materials. A range of quasi-static tests from out-of-plane compression to combined compression-shear loading have been conducted to understand the mechanical response, energy absorption and failure modes in the structures. An analytical model and a finite element model have been used to predict the strength and stiffness of the structures, either under quasi-static or low velocity compression loading. Based on the findings of this work, the following conclusions can be drawn.

7.2 Conclusions of the Research Work

i) To design and manufacture triangular corrugations and sandwich structures.

- In the open literature, no investigations have been conducted on the mechanical properties of triangular corrugated-core made from composite materials. Novel lightweight structures based on corrugated-cores have been fabricated using a special mould that has been designed and fabricated with a corrugation angle of 45^{o}.
- The compression moulding technique has been used to manufacture composite corrugation specimens where the quality control procedures were put in place. The metal corrugations were folded to form a triangular shape. Note that the mould could only produce specimens up to one millimetre thickness or 10 plies of GFRP, above this, the apex in the corrugation became too rounded.
- Sandwich structures were fabricated using an adhesive bonding technique, where an epoxy adhesive for the metal and composite systems was used to bond the skins and the core.

ii) To investigate the mechanical performance of the corrugated-core sandwich structures subjected to static compression, bi-axial loading, and dynamic compression loading.

- The key mechanical properties under static compression, such as compression strength, stiffness and energy absorption characteristics have been recorded for each corrugated-core sandwich specimen. The structures have shown excellent repeatability in terms of their mechanical response. The mechanical response in compression increases with specimen thickness.
- Bi-axial loading conditions, from pure shear to pure compression loading, (loading angles: 0^o, 22.5^o, 45^o, 67.5^o and 90^o) were investigated. Two pre-calibration tests were conducted to eliminate the effect from the machine stiffness and the horizontal force due to the mounting configuration, leading to a high degree of confidence in the overall experimental results and good repeatability in their mechanical response. For the 0.5 mm wall thickness, the failure loads for CFRP specimen were three times higher than the AL and GFRP specimens at a loading angle of 45^o.
- The impact response at low energies and above the threshold energy to fracture the specimens was investigated, for selected specimens with a relative density of $\rho^* = 0.07$. Virtually all of the impact energy was absorbed by the specimens. The dynamic strength enhancement factor for the GFRP specimens was approximately 50%, suggesting that the GFRP specimens are more rate-sensitive than the AL and CFRP specimens under low velocity impact loading.

iii) To characterise the failure mechanisms in corrugated-core sandwich structures subjected to different loading conditions.

- Under static compression loading, the strength of the strut was controlled by Euler buckling, or by compression failure. In the metal system, after initial buckling, plastic deformation progressively occurred in the system and crumpling was exhibited at the end of the loading regime. In contrast, the composite corrugated-core specimens failed due to fibre fracture and matrix cracking after the initial instability in the struts. Delamination was observed in those composites with greater numbers of plies.
- Under bi-axial loading conditions, the strength was also controlled by Euler buckling, and for some case in CFRP specimens, the specimens failed in a three-dimensional buckling mode, leading to a reduction in failure load.

- No sign of damage was observed at low impact energies. For metal and composite systems, increasing the impact energy resulted in a change in buckling mode shape due to inertia stabilisation effects.
- Debonding was observed at the end of most loading cases.

iv) To model the mechanical response of corrugated-core sandwich structures using finite element techniques.

- The deformation process in those structures with the five unit cell was accurately modelled in Abaqus finite element package. The FE response with an initial imperfection (AL : $\xi = 0.01$, GFRP and CFRP : $\xi = 0.05$) showed good agreement with the measured response. The mechanical properties were predicted with reasonable accuracy, with small discrepancies of 6.7% and 5.7% for the static and impact loading cases, respectively.

v) To study the effect of varying geometrical parameters (unit cell, thickness, width) and the properties of foam-filled structures.

- Varying the number of unit cells, cell wall thickness and widths has a significant influence on the compression behaviour of the corrugated-core sandwich structures. The compression strength and stiffness relatively increases with increasing numbers of unit cell and cell wall thickness. However, the compression strength and stiffness was unaffected by increasing the specimen width. The specific strength of CFRP specimen was two times greater than the AL and GFRP specimens, at the same relative density of $\rho^* = 0.07$. The numerical results predicted by the model agree well with the experimental data.
- Filling the inside of the corrugated-core sandwich structures with foam significantly improved the specific strength as well as the specific energy absorption characteristics of the structures. The *SEA* for the GFRP and the CFRP fully-filled specimens improved by almost 160% and 105%, respectively. This improvement was due to the constraint effects between the foam and the corrugated-core members.

- The semi-filled foam structure offered a moderate specific strength and *SEA* values. The foam configuration increased the performance of the empty corrugated-structure, without sacrificing the air flow exchange characteristic.

vi) To propose suitable failure criteria to predict the failure strength of corrugations under combined compression-shear loading.

- From the bi-axial loading data, the failure strength in the aluminium corrugated-core was accurately predicted by a two dimensional quadratic failure criterion equation. In contrast, due to the initation of delamination within the composite struts, an additional component in the failure criterion was required to accurately capture the response of the composite systems.

vii) The triangular corrugated-core based on the woven CFRP material can compete with current sandwich core configurations. The CFRP triangular corrugated-core exhibited the best design performance behind the trapezium corrugated-core and the square honeycomb core. This indicates that a combination of the correct core design and appropriate lightweight materials can play an important role in determining the overall structural performance.

viii) Finally, it is believed that this study filled the gap between various aspect of research on cellular core materials, design and manufacture, mechanical properties as well as failure modes in the composite corrugated-core sandwich structures.

7.3 Recommendations for Future Work

It has been shown that the performance of triangular corrugated-core sandwich structures compares well with other cellular cores. Here, some recommendations for future work are given:

- Fibre metal laminates (FML) are increasingly being used in an aerospace industry. It would be interesting to study the mechanical properties of novel

FML corrugated-core, as the FML system are known to be blast resistant structures.

- Further testing should be carried out to fully characterise the behaviour of corrugation structures under tensile, bending and torsion loading conditions.
- The corrugated-core should be optimised to achieve the ideal ratio of weight and mechanical properties. The use of other materials, such as unidirectional carbon fibre, fibre metal laminates or 3D woven textiles (weft tow, warp tow and z-yarn), should be investigated.
- The FE simulation work that has been presented in this study has assumed perfect bonding between skins and core. Even though good results were obtained, using a cohesive element to represent the adhesive layer could give better results and simulate debonding between the skins and the core.
- Further study should be taken in the buckling resistance of the corrugated-core sandwich structure with higher density foam cores in order to increase compression strength of the struts.

APPENDICES

Appendix A

Technical Drawing: Corrugation Moulds

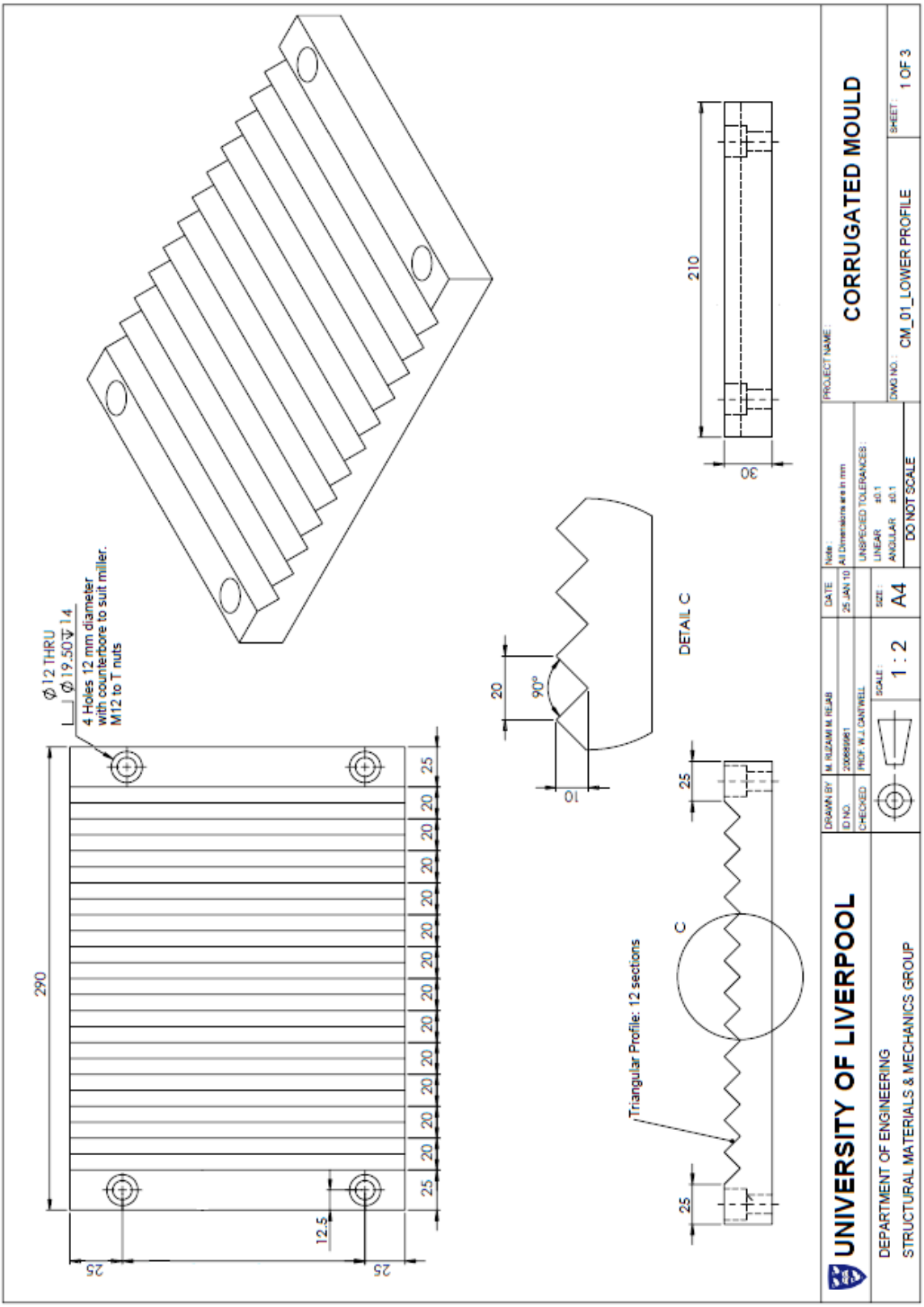

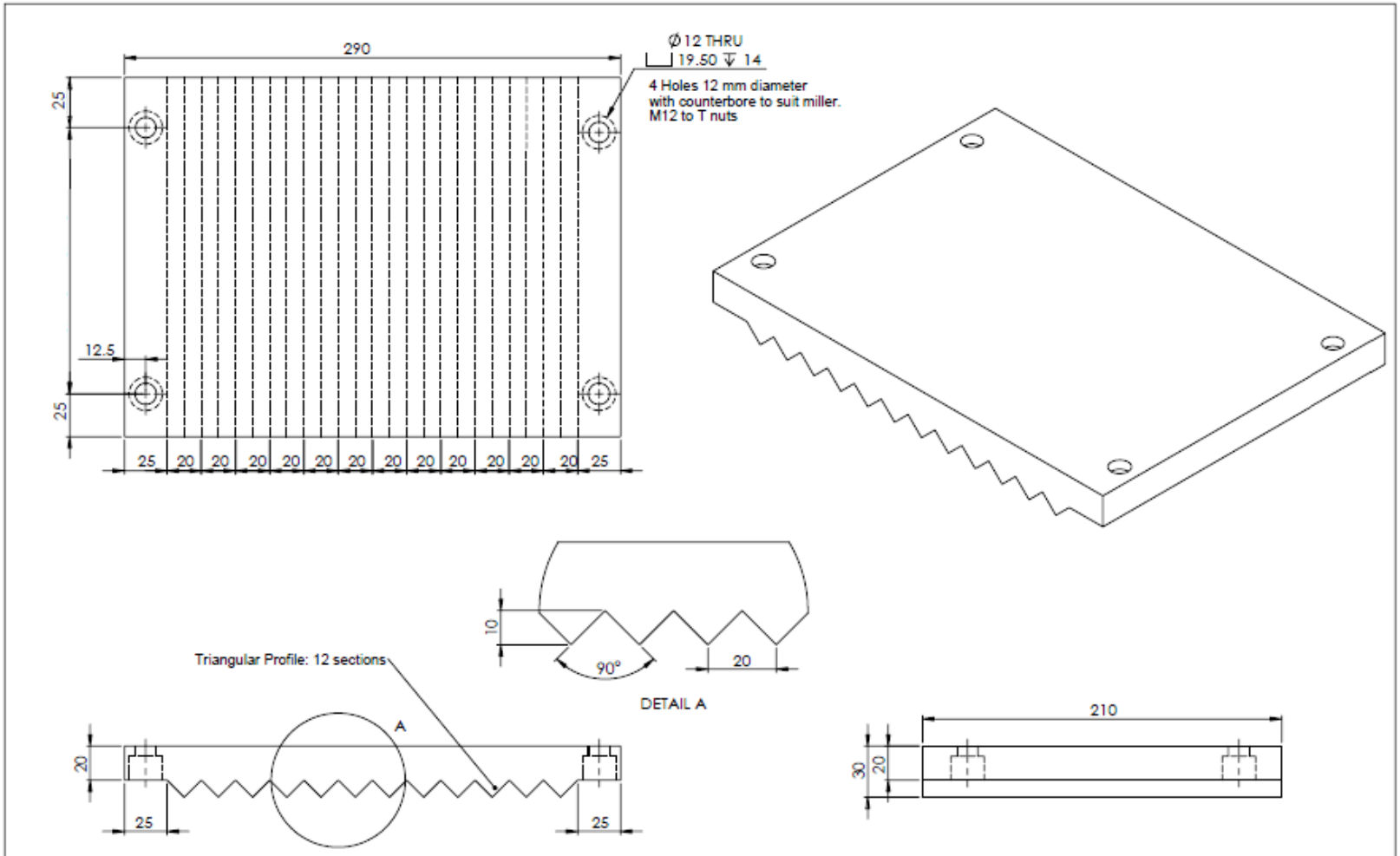

UNIVERSITY OF LIVERPOOL

DEPARTMENT OF ENGINEERING
STRUCTURAL MATERIALS & MECHANICS GROUP

DRAWN BY	M. RIZAMI M. REJAB	DATE	25 JAN 10
ID NO.	200889961		
CHECKED	PROF. W.J. CANTWELL		
SCALE :	1 : 2	SIZE :	A4

Note : All Dimensions are in mm
UNSPECIED TOLERANCES :
LINEAR ±0.1
ANGULAR ±0.1
DO NOT SCALE

PROJECT NAME : **CORRUGATED MOULD**

DWG NO. : CM_02_UPPER PROFILE

SHEET : 2 OF 3

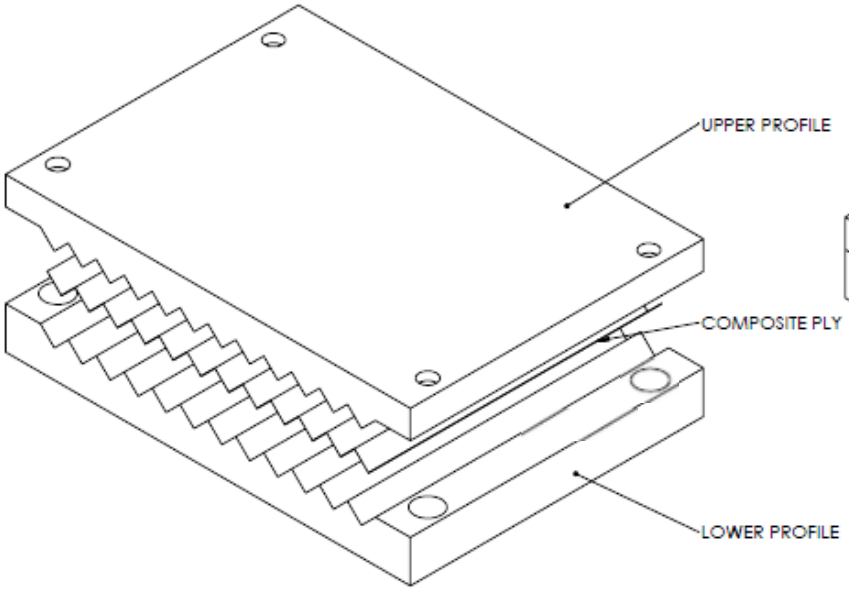

EXPLODED VIEW

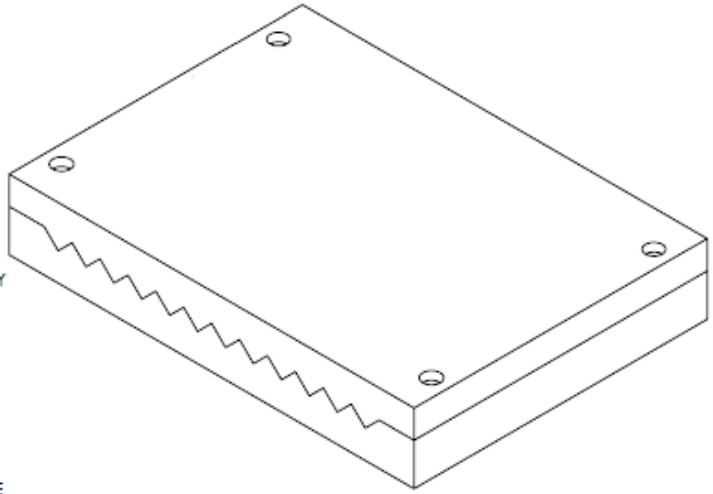

ASSEMBLED VIEW

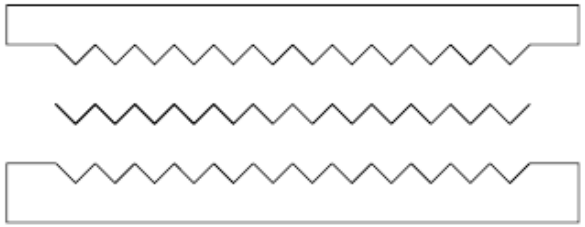

UNIVERSITY OF LIVERPOOL	DRAWN BY: M. RIZAIMI M. REJAB	DATE: 25 JAN 10	Note: All Dimensions are in mm	PROJECT NAME: CORRUGATED MOULD	
DEPARTMENT OF ENGINEERING	ID NO.: 200689981		UNSPECIED TOLERANCES: LINEAR ±0.1, ANGULAR ±0.1		
STRUCTURAL MATERIALS & MECHANICS GROUP	CHECKED: PROF. W.J. CANTWELL	SCALE: 1 : 2	SIZE: A4	DWG NO.: CM_03_ASSEMBLY DWG	SHEET: 3 OF 3
			DO NOT SCALE		

Appendix B

A FORTRAN program for Compliance Correction Procedure

```
      PROGRAM COMPLIANCE TEST
      REAL M,C,X(5000),DF(5000),S(5000),N,Y(5000)
      INTEGER TD
C     GRAPH EQUATION; Y=MX + C
C     WHERE M=SLOPE AND C=INTERCEPTION OF GRAPH
      PRINT*, 'VALUES OF SLOPE AND INTERCEPTION ON THE GRAPH'
      READ*,M,C
      PRINT*, 'NUMBER OF DATA'
      READ*, TD
C     OPEN THE DATA FILE
      OPEN(1,FILE='CF45.dat', STATUS='OLD')
      OPEN (2, FILE='XCF45.dat', STATUS='OLD')
      WRITE(*,100)
      WRITE(2,100)
C     LOOP TO CALCULATE THE DATA
      DO 10 L=1,TD
        IF(L.EQ.1)READ(1,*)
          READ(1,*)N,X(L),Y(L)
          S(L) = (Y(L)-C)/M
          DF(L)=X(L)-S(L)
          WRITE(*,102) L, DF(L), Y(L)
       WRITE(2,102) L, DF(L), Y(L)
10    CONTINUE
100   FORMAT(6x,'No.',5x,'Displacement (mm)',4x,'Force (kN)')
102   FORMAT(2x,I7,8x,F12.8,8x,F12.8)
      CLOSE (UNIT=1)
      END FILE(UNIT=2)
      CLOSE (UNIT=2)
      STOP
      END
```